HAL
open science

Phase transitions and oxygen ordering in La2CoO4+δ and (T, T')-La2CuO4 : single crystal growth and structural studies using synchrotron and neutron diffraction methods

Loïc Le Dréau

To cite this version:

Loïc Le Dréau. Phase transitions and oxygen ordering in La2CoO4+δ and (T, T')-La2CuO4 : single crystal growth and structural studies using synchrotron and neutron diffraction methods. Chemical Sciences. Université Rennes 1, 2011. English. NNT : 2011REN1S072 . tel-00634848

HAL Id: tel-00634848

https://theses.hal.science/tel-00634848v1

Submitted on 24 Oct 2011

HAL is a multi-disciplinary open access archive for the deposit and dissemination of scientific research documents, whether they are published or not. The documents may come from teaching and research institutions in France or abroad, or from public or private research centers.

L'archive ouverte pluridisciplinaire **HAL**, est destinée au dépôt et à la diffusion de documents scientifiques de niveau recherche, publiés ou non, émanant des établissements d'enseignement et de recherche français ou étrangers, des laboratoires publics ou privés.

N° d'ordre : 4366 ANNÉE 2011

THÈSE / UNIVERSITÉ DE RENNES 1

Sous le sceau de l'Université Européenne de Bretagne

Pour le grade de

DOCTEUR DE L'UNIVERSITÉ DE RENNES 1

Mention : Chimie

École doctorale Science de la matière (SDLM)

Présentée par

Loïc Le Dréau

Préparée à l'UMR CNRS 6226, Sciences Chimiques de Rennes

et au

Paul Scherrer Institute, Laboratory of Neutron Scattering (LNS, PSI, Villigen, Suisse)

Phase transitions and oxygen ordering in $La_2CoO_{4+\delta}$ and (T, T')-La_2CuO_4: single crystal growth and structural studies using synchrotron and neutron diffraction methods

Thèse soutenue à Rennes
Le 6 juillet 2011
devant le jury composé de :

M. Antoine MAIGNAN
Directeur de CRISMAT, Caen / rapporteur

M. Olivier MENTRÉ
UCCS, Lille 1/ rapporteur

M. Jean-Marc BASSAT
ICMCB, Bordeaux/ examinateur

M. Philippe PAPET
C2M ICG Montpellier 2/ examinateur

M. Olivier HERNANDEZ
MICDR, Rennes 1/ examinateur

M. Carmelo PRESTIPINO
MICDR, Rennes 1/ examinateur

M. Werner PAULUS
C2M, ICG Montpellier 2/ directeur de thèse

M. Jürg SCHEFER
LNS, PSI Suisse/ co-directeur de thèse

4366

Phase transitions and oxygen ordering in $La_2CoO_{4+\delta}$ and (T, T')-La_2CuO_4: single crystal growth and structural studies using synchrotron and neutron diffraction methods

A dissertation submitted to

University of Rennes 1 (France)

For the degree of

Doctor of science

Presented by

Loïc Le Dréau

2011

Contents

General introduction 11

Chapter 1 13

Non stoichiometric oxides: structure and reactivity of perovskite derivatives 13

1. From Perovskite to Brownmillerite and Ruddlesden-Popper phases 13

1.1. Flexibility of Perovskite-type structure: 13

1.1.1. Basic ABO_3 structure 13

1.1.2. Effect of cation substitution on structure and properties 14

1.1.3. Variation of ABO_3 stoichiometry: possible derivatives 15

1.2. Variation of oxygen content: From perovskite to Brownmillerite 17

1.2.1. Intermediate phases 17

1.2.2. The Brownmillerite phase 18

1.2.3. Reducing the Brownmillerite to ABO_2 20

1.3. Cation doped perovskite: Ruddlesden-Popper phases and derivates 21

1.3.1. General structure of Ruddlesden Popper phases 21

1.3.2. La_2MO_4 T-type structure (n = 1) 23

1.3.3. T' type structure and associated T'' 24

1.3.4. T-type structure: hybrid phase between T and T'* 26

1.3.5. Oxygen deficiency in Ruddlesden-Popper derivatives: S-phase 28

1.3.6. A new tolerance factor adapted to A_2BO_4 stoichiometry 30

1.4. Properties of Ruddlesden-popper phases and derivatives 31

1.4.1. General case of rare earth-doped Ruddlesden-popper $La_{2-x}RE_xCuO_4$ 31

1.4.2. Coexistence of two polymorph states of La_2CuO_4 at RT with different properties 32

1.4.3. Intercalated $La_2CuO_{4+\delta}$: mixture of T and T' 33

2. Phase transitions in $La_2MO_{4+\delta}$ depending on temperature and oxygen content ... 35

2.1. Structural phase transitions with temperature for stoichiometric La_2MO_4 35

2.1.1. Doubling of the unit-cell at ambient temperature: LTO phase 35

2.1.2. Phase transitions at lower temperatures: LTT and LTLO phases 38

2.2. Effect of oxygen doping on structure and properties 40

2.2.1. Historical background: from superconductivity to oxygen conduction properties 40

2.2.2. Oxygen intercalation 41

2.2.3. Local disorder induced by interstitial oxygen 44

2.2.4. Coming back of ordering for higher values of δ: modulated structures 47

Chapter 2 53

Synthesis and qualitative characterizations of highly pure poly- and single-crystal samples of $La_2MO_{4+\delta}$ (M = Co, Cu) 53

1. Synthesis of polycrystalline La_2MO_4 (M = Co, Cu) T-phase 53

1.1. Solid state synthesis 53

1.1.1. Generalities 53

1.1.2. Synthesis procedure for T-$La_2CuO_{4+\delta}$ 54

1.1.3. Synthesis procedure for $La_2CoO_{4+\delta}$ 54

1.1.4. Difficulties encountered for the synthesis 55

1.2. Coprecipitation method 56

1.2.1. Generalities and experimental procedure 56

1.2.2. Results of sol gel tentative on La_2MO_4 57

1.2.3. Problem of sol gel method for synthesis of perovskite derivatives 58

1.3. Characterization of polycrystalline products by X-ray diffraction 58

1.3.1. As-prepared La_2CuO_4 59

1.3.2. As-prepared $La_2CoO_{4+\delta}$ by solid state reaction 61

1.3.3. Spontaneous oxidation of $La_2CoO_{4.00}$ under air 63

2. Synthesis of La_2CuO_4 T'-phase 64

2.1. Synthesis of polycrystalline samples from T-phase, followed *in situ* by thermogravimetry and *ex situ* by X-ray diffraction 64

2.2. Synthesis of single crystal samples by molten salt technique 68

2.3. Compositional characterizations of T' single crystal samples by SEM 69

3. Growth of $La_2CoO_{4+\delta}$ single crystal samples 71

3.1. Choice of adapted synthesis procedure 71

3.2. Image furnace 72

3.3. Travelling Solvent Floating Zone technique for incongruent melting phases 75

3.4. Key process parameters 78

3.4.1. High quality feed rod 79

3.4.2. Solvent ratio 80

3.4.3. Sharpness of the temperature gradient 80

3.4.4. Growth rate and power of lamps 82

3.4.5. Molten zone shape and dynamics 83

3.4.6. Gas flowing 85

3.5. Detailed procedure for growth of high quality single crystals of La_2CoO_4 86

3.5.1. Preparation of rods 87

3.5.2. Special settings of the system for a very steep temperature gradient 87
3.5.3. Setup and stabilization of the molten zone 88
3.5.4. Qualitative characterizations and orientation of as grown crystals 91

Chapter 3 95

Strategy of experimental analyses adapted to the study of twinned $La_2MO_{4+\delta}$ crystals with modulated structures 95

1. Twinning in $La_2MO_{4+\delta}$ single crystals 95
1.1. Generalities on twinning 95
1.2. Twinning law for the basic unit-cell of $La_2MO_{4+\delta}$ system 98
1.3. Implications of pseudo symmetry 102
2. Introduction to crystals with modulated structures 103
2.1. Generalities 103
2.2. Complexity induced by the coexistence of twinning and structural modulation 108
3. Choice of adapted method for characterizing modulated structures 109
4. Reconstruction of reciprocal space planes and intensity integration from single crystal X-ray diffraction experiments. 114
4.1. X-ray diffraction apparatus 114
4.2. Key process parameters and data treatments 115
5. Single crystal neutron diffraction experiments and Maximum Entropy Method 117
5.1. Neutron diffraction apparatus 117
5.2. Maximum entropy method (MEM) 118

Chapter 4 121

Crystal structures of stoichiometric La_2CuO_4 T and T', and oxygen rich $La_2CoO_{4+\delta}$ phases with δ = 0.14, 0.19, 0.25, at ambient temperature 121

1. Introduction 121
2. Stoichiometric La_2MO_4 compounds at RT: single crystal structures of basic T and T'-phases. 123
2.1. Stoichiometric phase for M = Co and Cu, combination of static and dynamic displacements 123
2.2. Single crystal structure of T'-La_2CuO_4, only static contribution 127
3. *As grown* $La_2CoO_{4.14}$ single crystal 129
3.1. Average basic structure, anisotropic displacements of all atoms 131
3.2. First modulation vector q_1 in a^*-b^* plane, attribution of satellites, second twinning effect 137
3.3. Second modulation vector q_2 with a supplementary component along c^* 141

3.4. Conclusions about the real structure of $La_2CoO_{4.14}$ 146

4. Atomic structure of oxygen rich $La_2CoO_{4.25}$ at RT 147

4.1. Basic structure explored by synchrotron diffraction 148

4.2. Modulation in the *a-b** plane** 150

4.2.1. Determination of the supercell 150

4.2.2. Structural refinements 153

4.2. Order/disorder along *c in $La_2CoO_{4.25}$** 158

5. Atomic structure of intermediate oxygen-rich $La_2CoO_{4.19}$ at RT 162

5.1. Basic structure 162

5.2. Commensurate modulation in three dimensions, symmetry of supercell. 163

5.3. Structural refinements 165

Chapter 5 171

Phase transitions with temperature: Irreversible transformation of T' to T La_2CuO_4, Thermal evolution of $La_2CoO_{4+\delta}$ accompanied with variation of δ 171

1. Transitions between T' and T-phase by La_2CuO_4, migration pathway between interstitial site and apical site. 172

1.1. Motivations of the studies 172

1.2. Reconstructive phase transition from T' to T-phase 174

1.2.1. First sample: complete destruction of the T'-type single crystal into polycrystalline T-phase around 1000 K. 174

1.2.2. Second sample: continuous transformation of T'-phases into T-phase by crystal intergrowth, starting at 900 K. 181

1.3. Global outcomes about the transformation from T' to T-phase. 187

2. Successive structural phase transitions undergone by the *as grown* $La_2CoO_{4+\delta}$ as function of temperature 189

2.1. Low temperatures: in the range of 10K to RT 190

2.2. Transitions from RT to 773 K 193

2.2.1. Reversible transitions with δ constant from (3+2) incommensurate LTO to HTT phase, via intermediate (3+1) incommensurate HTLO phase. 196

2.2.2. Transition from HTT to (3+2) commensurate HTO phase with increase of δ from 0.14 to 0.19, at 580 K. 209

2.2.3. Irreversible transition from (3+2) commensurate HTO to (3+1) incommensurate HTO phase with δ ~ 0.2, at 653 K on heating. 212

2.2.4. Transition on cooling from (3+1) incommensurate HTO phase to commensurate $La_2CoO_{4.19}$ LTO phase at 610 K. 215

2.2.5. Global thermal evolution of significant parameters, from RT to 773 K. 217

3. Successive phase transitions in the oxygen-rich $La_2CoO_{4.25}$ 226

3.1. Magnetic structure at low temperature 226
3.2. Structural evolution in the range of RT-800 K 228
3.2.1. Experimental procedure and thermogravimetry 228
3.2.2. Transition from $La_2CoO_{4.25}$ to $La_2CoO_{4.19}$ around 480 K 229
3.2.3. First tentative of structural refinements of the (3+1) INC HTO phase via superspace approach. 231
3.3. Global outcomes concerning the thermal evolution of $La_2CoO_{4.25}$ 238
General conclusion 240
APPENDIX A: Structural model for $La_2CoO_{4.25}$ at RT 244
APPENDIX B: Structural model for $La_2CoO_{4.19}$ 245
Bibliography 248
Acknowledgments 257

General introduction

The origin of oxygen mobility at moderate temperatures in non-stoichiometric oxides, together with its underlying mechanisms in terms of diffusion pathways and associated activation energies, are presently of great scientific interest. A better understanding of these diffusion mechanisms on a microscopic scale, would considerably contribute to enhance the tailoring of new materials for the use of *e.g.* oxygen sensors, oxygen membranes and electrolytes in Solid Oxide Fuel Cells, etc. In particular, lowering the operating temperature of such technological devices at enhanced oxygen ion conductivity must be considered as an important breakthrough, which would decisively contribute to solve important problems essentially linked to the thermal instability of the components currently used, *e.g.* aging, cracking, lowering of efficiency, apparition of impurities, etc.

Only a few oxides are known today, showing oxygen-ion conductivity at moderate temperatures or even at ambient. Among them, two Perovskite-derivative varieties, the Brownmillerite[1] $ABO_{2.5+\delta}$ and the Ruddlesden-Popper[2,3] $A_2BO_{4+\delta}$ phases are of particular interest, as they are non-stoichiometric and are able to accommodate an important amount of oxygen on interstitial or regular lattice sites. More precisely, the oxygen content (δ) of $SrMO_{2.5+\delta}$ (M = Fe, Co) and $La_2MO_{4+\delta}$ (M = Co, Ni, Cu) can be varied in a controlled way by topotactic red/ox reactions, already proceeding at ambient temperature *via* electrochemical methods in an aqueous alkaline electrolyte[4,5,6,7,8]. Beside this, $La_2CoO_{4+\delta}$ is highly reactive and surprisingly this phase is able to take up oxygen spontaneously under ambient conditions[9]. While the uptake of oxygen for Brownmillerite-type compounds goes along with the filling up of 1D oxygen vacancy channels, *i.e.* regular lattice sites, the intercalation of oxygen in K_2NiF_4 type oxides leads to a partial occupation of interstitial lattice sites. This implies a principal difference in terms of diffusion pathways and mechanisms for both types of oxides. One astonishing aspect in this regard is the formation of complex superstructures occurring during the intercalation of oxygen in $SrCoO_{2.5}$ and La_2CoO_4, accompanied in both cases by strong distortions of the host crystal lattice[8,10,11]. The superstructures are related to oxygen ordering and increase the unit-cell volume in case of $La_2CoO_{4+\delta}$ to about 25,000 $Å^3$ [8]. The condition to realize low temperature oxygen mobility in solid oxides thus seems to be contradictory with the generally accepted concept that disorder commonly favours ion mobility.

As a consequence, the topic of this thesis highlights the relation of complex oxygen ordering in Brownmillerite and K_2NiF_4 type oxides and aims at investigating its influence on low temperature oxygen mobility. La_2CoO_4 has been chosen as the primary compound because of its ability to take up a huge quantity of oxygen up to $La_2CoO_{4.25}$ [8,9,12]. Thus structural changes should be detected more easily, but also the fact that an important quantity of oxygen can be intercalated allowing easy access to different ordered states. The understanding of oxygen ordering as a function of temperature should then enable to conclude on the stability of the underlying phases and, more generally, the phase diagram of $La_2CoO_{4+\delta}$. In the same context the quantity of intercalated oxygen atoms should allow the tuning of physical properties, and especially magnetism. For stoichiometric La_2CoO_4, cobalt is in a divalent state, changing to equal amounts of Co^{2+} & Co^{3+} when oxidized to $La_2CoO_{4.25}$, giving rise to a non-magnetic state for low spin $3d^6$ configuration for Co^{3+}. Antiferromagnetic ordering has been found to set in at 36 K for $La_2CoO_{4.25}$[8].

One obstacle to overcome during this thesis concerns the availability of large and high quality single crystals, as La_2CoO_4 is known to melt incongruently. This part of the thesis must therefore be regarded as a proper thematic itself. It is also the reason why only few studies on this compound have been reported in literature related to work on single crystals so far.

Structure analysis of $La_2CoO_{4+\partial}$ were investigated essentially using neutron and X-ray (classical and synchrotron) diffraction methods in order to determine precisely the underlying structures and symmetry as a function of temperature and δ.

In the course of the thesis also single crystals of T'-La_2CuO_4 became available, which were investigated to determine the thermodynamical stability of both T and T' polymorphs of La_2CuO_4[13,14,15,16,17]. The relation of the T and T' structure is essential for the understanding of the oxygen diffusion pathway in K_2NiF_4 type oxides.

The structural investigations, importantly including the use of large scale facilities, should also enable the estimation of the influence of lattice dynamical aspects for low temperature oxygen diffusion in these compounds, which have been formulated for Brownmillerite type oxides in terms of a phonon-assisted diffusion model[18], and equally postulated for K_2NiF_4 type oxides[19]. In this aspect the point of direct interest is the change in the lattice dynamics of La_2CoO_4 with different oxygen content.

Chapter 1

Non stoichiometric oxides: structure and reactivity of perovskite derivatives

1. From Perovskite to Brownmillerite and Ruddlesden-Popper phases

1.1. Flexibility of Perovskite-type structure:

1.1.1. Basic ABO_3 structure

Materials having the ABO_3 perovskite-type structure are famous in the field of crystal-chemistry for their very wide panel of varieties, for their different physical and chemical properties, with respect to their applications in recent technologies. Perovskites can be considered to be the basic structure from which many types of compounds are derivatives, and thus symbolizes a starting model to the introduction of the family of materials constituting the subject of this thesis. The atomic structure of perovskites consists in a 3D network of BO_6 octahedra connected by apex, which are maintained by a cubic lattice of A atoms of coordination 12. The ideal atomic arrangement, usually adopted at high temperatures, is shown in Figure 1.1, with a cubic unit cell of space group $Pm\bar{3}m$.

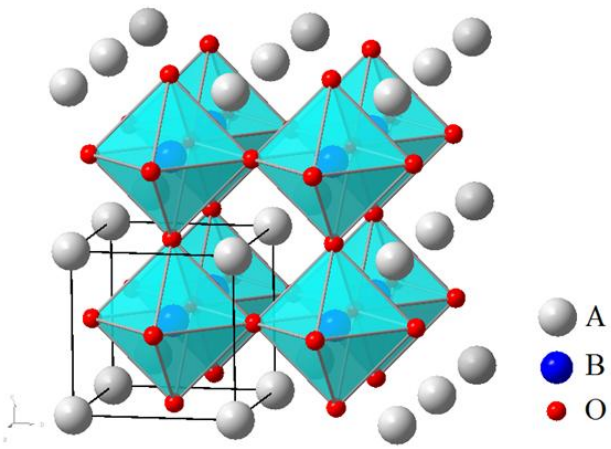

Figure 1.1: *Perovskite-type structure in its cubic form, the unit-cell edge is shown in black, the space group is $Pm\bar{3}m$.*

The name "perovskite" was firstly referring to $CaTiO_3$ before being enlarged to the group of oxides of ABO_3 stoichiometry[20]. Several combinations are possible for A and B cations, leading to different possible respective valence states, as for instance I-V for $KNbO_3$, II-IV for $CaFeO_3$ or III-III for $LaCoO_3$. Other compounds also exist containing Fluor or Sulphur instead of oxygen as ligand, but the present study is only dedicated to oxides. Indeed perovskite oxides are famous for their oxygen ion conduction properties, stoichiometry variations and physical properties.

1.1.2. Effect of cation substitution on structure and properties

The perovskite phases are well known for their reactivity and flexibility not only in terms of oxygen stoichiometry but also with regards to A and B cation substitutions. They undergo various types of phase transitions as function of the thermodynamic conditions[21]. Different properties ensue from these structural changes, *e.g.* ferroelasticity[22] for $SrTiO_3$, ferroelectricity[23] for $BaTiO_3$, ferromagnetism[24] for $YTiO_3$, piezoelectricity[25] for PZT ($PbZr_xTi_{1-x}O_3$), pyroelectricity[26] for $LiTaO_3$, etc. From the crystallographic point of view, structural phase transitions imply different distinct phenomena taking place at the atomic level. For instance, the piezoelectric PZT is sensitive to external pressure which provokes a positional shift of the B cation together with a delocalization of the surrounding oxygen atoms in opposite directions, responsible for a symmetry breaking. In this particular case, the BO_6 octahedra are deformable and they can switch between different shapes depending on the external pressure. Other types of excitations can lead to similar effects; for example when applying external electromagnetic fields in the case of ferroelectric/magnetic materials. However when temperature plays the role of excitation field, several structural transitions succeed to one another on cooling (or heating) involving different phenomena, *e.g.* the cubic $BaTiO_3$ at high temperature (HT) successively becomes[27] tetragonal, orthorhombic and finally rhombohedral at low temperature (LT). These transitions do not imply major modifications of the shape of polyedra but are induced by a distortion of the rigid TiO_6 octahedra arrangement from their perfectly aligned configuration at HT. These few examples between many others depict the diversity of effects entering the game, which are sometimes combined, at the origin of phase transitions. To sum up, perovskites can deviate from the cubic state for different reasons being: *i*) a shift in the position of A or B cation from their respective site, *ii*) a rotation of the octahedra around one axis, *iii*) a deformation of the octahedra, *iv*) a distortion of the whole unit-cell *e.g.* by elongation in particular directions.

More generally, symmetries of ABO_3 perovskites can theoretically be directly determined from the ionic radii of A and B cations, which govern strains inside the materials, since the size mismatch is responsible for the distinct stacking. The Goldschmidt tolerance factor[28] (t) is conventionally used to quantify these internal strains in the perovskite structures as function of ionic radii or as function of inter-atomic bond lengths:

$$i)\ t = \frac{r_A + r_O}{\sqrt{2} * (r_B + r_O)} \quad \text{or} \quad ii)\ t = \frac{d_{AO}}{\sqrt{2} * d_{BO}} \qquad \text{equation 1}$$

If $t = 1$, strains are minimal and the structure is cubic as shown in Figure 1.1, but for $t \neq 1$, the strains are not negligible and are compensated by atomic shifts, which usually lower the symmetry. For instance, when $t > 1$, A-O bond distance increases and the symmetry is rhombohedral, whereas when $t < 1$ the structure is compressed and, the symmetry is tetragonal (or orthorhombic). It is admitted that below the value of $t = 0.86$, the perovskite structure is no longer stable and the atomic arrangement adopts a layered configuration. Internal strains can be relaxed through rotations of octahedra around the axis of the highest symmetry. Angles and directions of tilt strongly depend on the combination of chemical elements composing the materials. As stated above, octahedra are generally considered to remaining rigid while they tilt, instead of being deformed. However, some special cases necessitate the assumption of B-O bond length variations for depicting the real structure[29,30].

1.1.3. Variation of ABO_3 stoichiometry: possible derivatives

In addition to the flexibility of their structure, perovskite phases are also flexible in terms of stoichiometry. Indeed, many ABO_3 phases accept in one hand the substitution of A or B sites by other cations and on the other hand oxygen vacancies. Besides, the perovskite-type structure can be intergrown with other building blocks forming layered structures. If doped with AO, the stoichiometry of perovskite can turn to A_2BO_4. It is for instance the case of Ruddlesden-popper phases, which are made of alternating layers of perovskite-type and rock salt type (NaCl). This state is called T-phase; it corresponds to K_2NiF_4-type structure. Derivates of this structure also exist, like T'-phase for which the AO layers is of fluorine type (CaF_2). By taking these possibilities into account, the chemical formula of such materials can be generalized as $(A_xA'_{1-x})_n(B_yB'_{1-y})_mO_{3\pm\delta}$. Figure 1.2 shows a non-exhaustive scheme of some possible derivates from the central ABO_3 compound: vertically, the possible intergrowths of ABO_3 and AO or BO_2 building blocks, and horizontally the intermediate

phases obtainable by variation of oxygen content through oxidation/reduction process. Resulting from these structural and compositional modifications, different ionic mixed-valence states with different coordinations become available, conferring various features to the ensuing compounds. This enlarges considerably the structural possibilities and associated physical and chemical properties.

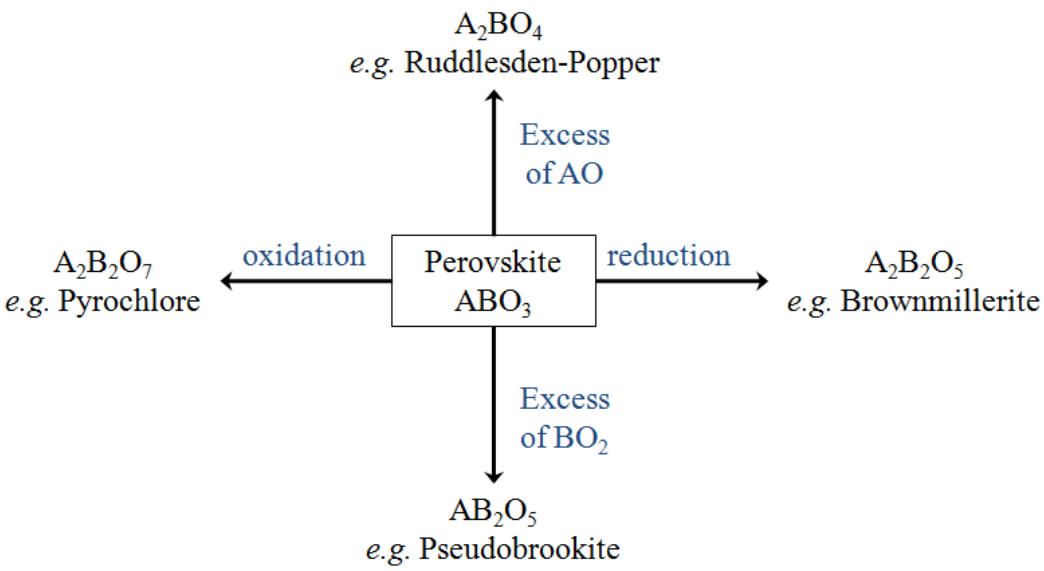

Figure 1.2: *Perovskite derivatives reachable by changing the stoichiometry of A or B cation (vertical) and O anion (horizontal).*

One interesting feature of perovskites is their capacity to be reversibly transformed into Brownmillerite phase $A_2B_2O_5$ (also written $ABO_{2.5}$) by red/ox reaction, passing through intermediate metastable states $ABO_{2.5+\delta}$ of different oxygen content δ. The most surprising aspect of this particularity is that, for some specific compounds, namely $SrMO_{2.5+\delta}$ (M = Co, Fe), oxygen content can be modified already at room temperature (RT) by soft chemistry techniques, implying oxygen diffusion performing far away from temperatures where the phenomenon usually occurs, as outlined in the general introduction. The $La_2MO_{4+\delta}$ (M = Co, Ni, Cu) compounds, which belong to the Ruddlesden-Popper-type phases, share this feature and present several similarities in terms of reactivity with oxygen. The $La_2MO_{4+\delta}$ system is nothing else than an alternation of perovskite and rock salt layers. That is why the reactivity, together with the structural features of the 3D perovskite structure to Brownmillerite, will be introduced as a preamble to the description the intergrowth of perovskite layers with rock salt layers.

1.2. Variation of oxygen content: From perovskite to Brownmillerite

1.2.1. Intermediate phases

The reduction of perovskite compounds to oxygen-deficient phases can be obtained by diverse techniques, like thermal treatment, partial pressure of different oxidizing or reducing gases, or electrochemistry. It allows controlling the oxygen content in the structure. As shown in Figure 1.2, reducing the stoichiometric ABO_3 perovskite phase leads to the $ABO_{2.5}$ Brownmillerite–type structure. Between the two latter states, ABO_{3-x} intermediate phases can be stabilized for different values of x due to the ordering of oxygen vacancies. The structural evolution of the non stoichiometric $SrFeO_{3-x}$ as function of oxygen content x can be outlined as follows[31]. At relatively high temperature, *i.e.* above the temperature of transition depending on oxygen content, $SrFeO_{3-x}$ forms a vacancy-disordered solid-solution with perovskite structure. But at lower temperatures, the $SrFeO_{3-x}$ system can be stabilized into four distinct phases from $x = 0$ to $x = 0.5$, depending on the oxygen concentration. The two intermediate phases which have been isolated, correspond to vacancy contents $x = 0.125$ and $x = 0.25$, leading respectively to $SrFeO_{2.875}$ and $SrFeO_{2.75}$; both presented on Figure 1.3. The two latter phases are preferentially stabilized, on the contrary purely stoichiometric $SrFeO_3$ compound is extremely difficult to synthesize; it always tends to lose oxygen.

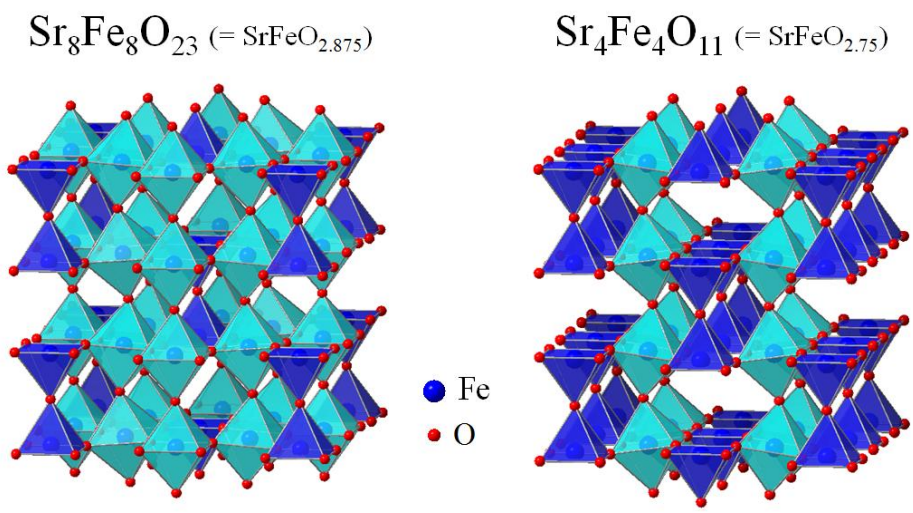

Figure 1.3: *Polyhedra arrangement of the $SrFeO_{3-x}$ intermediate phases from perovskite to Brownmillerite, with x = 0.125 and x = 0.25. The space groups are respectively I4/mmm and Cmmm. The A atoms are not shown for the sake of clarity.*

These intermediate phases can be obtained reversibly by successive electrochemical topotactic reduction/oxidation at ambient temperature. In fact, the reduction process, consisting in removing O^{2-} anions from the ABO_{3-x} lattice, introduces vacancies which

partially modify the coordination number of B ions as well as their valence state. Consequently, after reduction, different types of polyedra BO_x can replace some octahedra of the starting perovskite. One remarkable fact is that oxygen ions are not randomly removed from the host structure but they follow an anisotropic diffusion pathway in the [110]-type direction of the perovskite unit-cell. As a consequence, the alternation of oxygen vacancies takes various configurations creating different orders between BO_6 octahedra and BO_5 square-based pyramids as a function of oxygen content. These transfers of oxygen ions *via* anisotropic diffusion pathways imply a specific ion conduction mechanism which is subject of great attention in the literature[32,18,33].

1.2.2. The Brownmillerite phase

Originally, the chemical formula of the Brownmillerite mineral[1] is $Ca_2(Al,Fe)_2O_5$, but distinctive compounds can be obtained with the same general stoichiometry $AMO_{2.5}$, depending on the synthesis technique and on the type of cations. In the search of improved oxygen ion conduction, Brownmillerite structure has always played an important role; $BaInO_{2.5}$ compound can be for instance regarded as one of the most prominent example of these series[34]. The crystal structure is composed of MO_6 octahedral layers (perovskite-type) sandwiched between slabs of MO_4 tetrahedral chains. One-dimensional vacancy channels separate the tetrahedral chains, which have themselves an average diameter of about 3.5 Å. The $A_2MM'O_5$ Brownmillerite-type structure can thus be described by a sequence of AO-MO_2-AO-M'O□-AO- layers where □ symbolizes oxygen vacancy, as presented on Figure 1.4*a*. These vacancies are ordered in rows along the $[110]_P$ direction of the perovskite subcell. Two different sites are possible for transition metal atoms, called M and M', with different coordination number, namely 6 and 4, respectively. Consequently, M sites correspond to octahedra whereas M' sites refer to tetrahedra. The $M'O_4$ tetrahedra are connected by corners and form one-dimensional chains lying in the [110] direction of the perovskite cell. In the M'O□ layers, both M' and O atoms are shifted from their ideal position in the perovskite structure; these displacements are due to cooperative rotations of tetrahedra within the chains. Two switching orientations are available for the tetrahedra, allowing two types of chains arbitrarily called R and L (for Right and Left) as shown on Figure 1.4*b*. These two configurations differ only by small atomic displacements, and the transformation from L to R chains does not modify the first coordination sphere and consequently does not create any significant structural deformations.

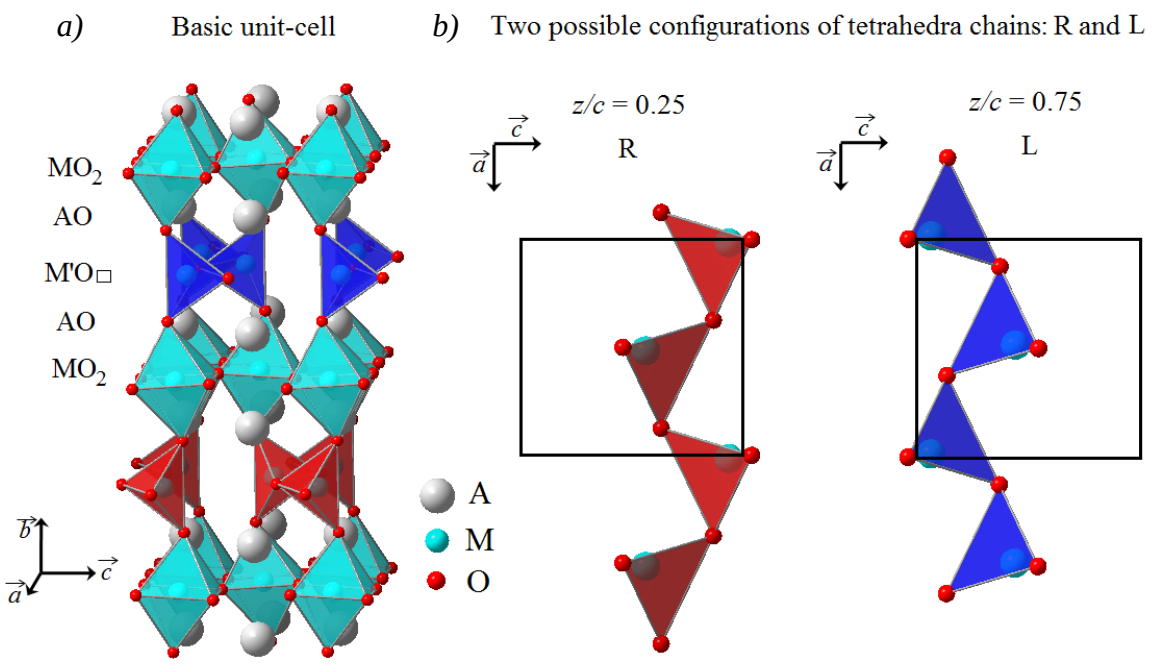

Figure 1.4: *a) Basic unit-cell of Brownmillerite-type structure, space group, Pnma made of layers of octahedra separated by layers of tetrahedral chains, b) the different R and L configurations of MO_4 tetrahedral chains, respectively colored in red and blue.*

However different arrangements between L and R chains lead to different possible structural configurations. Three space groups are generally considered: *i*) if all tetrahedral chains are identical (*e.g.* only L-type), the space group of the unit-cell is *I2mb*; *ii*) if tetrahedral chains alternate between L and R configuration along the *b*-axis, creating an interlayer ordering, the space group is *Pnma*; *iii*) if both R and L chains coexist but are randomly distributed, or if different domains exist, the space group is *Imma* (average symmetry). The three latter space groups are valid for the same unit-cell, *i.e.* $a \sim 5.5$ Å, $b \sim 15.5$ Å, $c \sim 5.6$ Å (values depending on different studies), but particular investigations dedicated to the elucidation of tetrahedral chains arrangements finally revealed that L and R ordering can extend at longer range and form super-orderings in certain cases, implying enlargements of the unit-cell volumes up to 8 times the volume of the basic one[35]. The real structure is thus much more complex than the basic model, and the apparent disorder of the tetrahedral chains described with the space group *Imma* is nothing else than an average of the real structure. The depiction of the real structure which can be commensurately modulated, *e.g.* for $SrFeO_{2.5}$[35] and Sr_2MnGaO_5[36], or incommensurately modulated, *e.g.* for $CaFe_{2.5}$, can be more generally achieved thanks to the centrosymmetric (3+1) superspace group *Imma*(00γ)*s*00 permitting to take into account both 3D usual space groups *Pnma* and *I2mb* together in the same model, instead of averaging the structure with the *Imma* space group. Subsequent crenel Functions allow to rationalize the L

and R-type chains long-range ordering in some particular directions of the lattice. Super-ordering can be stable until high temperature, *e.g.* for Sr_2MnGaO_5 and $CaFeO_{2.5}$. The structural complexity is of first importance and cannot be neglected in the course of oxygen diffusion studies at moderate temperatures; furthermore, it must be a criterion driving the phenomena. As mentioned previously, it has been recently reported that the vacancy channels of $SrCoO_{2.5}$ and $SrFeO_{2.5}$ can be filled up completely already at RT in reversible topotactic oxidation. Consequently, the oxygen diffusion mechanism, usually depicted in terms of disordered and isotropic atomic hoping from site to site *via* vacancies at high *T*, is not valid for Brownmillerite-type compounds. Thus, the classical concept of oxygen migration must be reconsidered when occurring at such low temperature in highly ordered structure. Recently, a phonon assisted diffusion model has been proposed[18] to be at the origin of fast oxygen diffusion at moderate temperature. It has been shown that lattice instabilities were responsible for low-energy phonon modes consisting in dynamic switching of tetrahedra chains which amplify oxygen mobility. The correlation between ionic conduction and dynamic fluctuations of atoms between different positions allow conceptualizing oxygen diffusion at moderate temperatures. Extending this notion to other ionic conductors at moderate temperature could provide a better understanding of the properties.

1.2.3. Reducing the Brownmillerite to ABO_2

Although the Brownmillerite phase was historically assumed to represent the lower limit of oxygen stoichiometry, the compound $SrFeO_2$ has recently been obtained by topotactic reaction *via* CaH_2 reduction already around 400 K[37]. $SrFeO_2$ is isostructural with $CaCuO_2$[38,39,40] and consists only in BO_2 planes separated by A atoms, yielding to a so-called "infinite-layer" structure. However, the particular case of the two-dimensional $SrFeO_2$ attracts much attention due to the resulting square-planar oxygen coordination around Fe^{2+}. Surprisingly $SrFeO_2$ remains free from the structural instabilities that could be expected at low temperature owing to twofold orbital degeneracy in the Fe^{2+} ground state. The oxidation/reduction process from perovskite to infinite layer-type has been shown to proceed *via* the Brownmillerite intermediate phase. Ideally, the atomic structure of ABO_2 system adopts a *P4/mmm* symmetry as shown on Figure 1.5 where all apical sites are empty (⅓ of all oxygen sites). In some cases a distortion of the BO_2 square-planes from the perfectly aligned configuration has been observed. It is for instance the case for $CaFeO_2$ compound[41] in which the FeO_4 units unprecedentedly distort from square-planar toward tetrahedra and rotate along the *c*-axis.

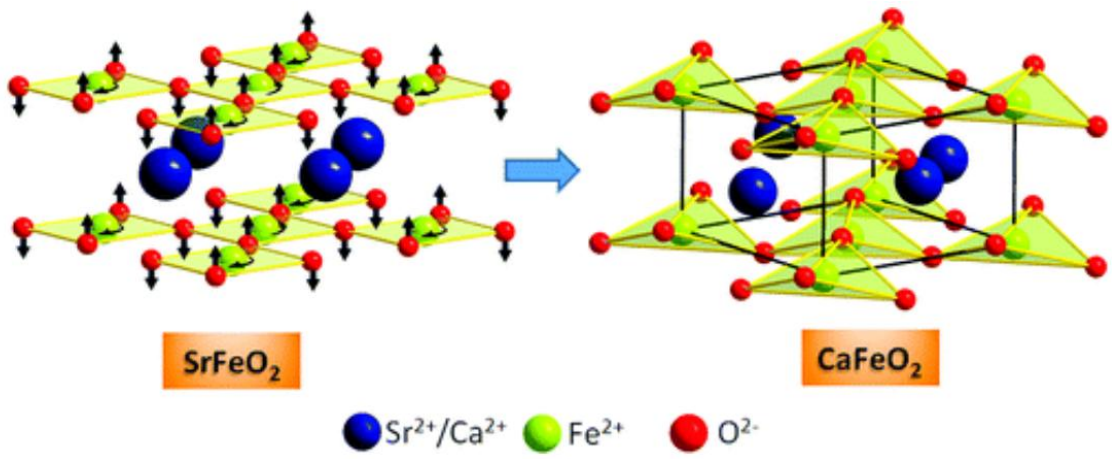

***Figure 1.5**: Crystal structures of $SrFeO_{2.5}$ and $CaFeO_{2.5}$ in which FeO_4 units respectively adopt either a perfect square planar geometry or take a tetrahedral configuration*[41].

It is noteworthy that recently, *c*-axis oriented thin films of $CaFeO_2$ and $SrFeO_2$ have been obtained on $KTaO_3$ substrate[42] by removing oxygen ions topotactically through CaH_2 chemical reduction, starting from perovskite material. This gave unprecedented results concerning the mechanism of oxygen migration in this oxide and it also demonstrates that unexpected states can be obtained, highlighting the complexity of the phase diagram of perovskite derivatives.

1.3. Cation doped perovskite: Ruddlesden-Popper phases and derivates

1.3.1. General structure of Ruddlesden Popper phases

The Ruddlesden-Popper phases of general formula $A_{n-1}A'_2B_nO_{3n+1}$ can be considered as a stacking of n $A_{1/n}A'_{1-1/n}BO_3$ perovskite layers alternatively with one AO rock salt layers (NaCl-type) along the *c*-axis[2,3]. Figure 1.6 presents the ideal tetragonal unit-cells for n = 1, 2 and 3, which correspond to the stoichiometric compounds all of same space group *I4/mmm*. It shows the additional ABO_3 blocks introduced for the structure when $n > 1$. The A' cations are characterized by their cuboctahedral anionic coordination, corresponding to a coordination number of 12 and they belong to the perovskite-like stack. On the contrary the A cations are located at the boundary between layers and have a coordination number of 9. The B cations are located at the centroid of octahedra formed by 6 oxygen anions. Two consecutive perovskite-like layers are displaced with respect to each other of a half diagonal of the base of the unit cell (shift of ½, ½, 0). If A and A' cations are identical, which is frequently the case,

the formula becomes $A_{n+1}B_nO_{3n+1}$ which is often written $(AO)\bullet(ABO_3)_n$ to symbolize the two types of layers. Other structures exist with oxygen vacancies which lead to different polyhedra arrangements[43]. It is for instance the case of the $YBa_2Cu_3O_{7-x}$ high T_c superconductor which is made of alternation of CuO_5 pyramids and CuO_4 along the *c*-axis.

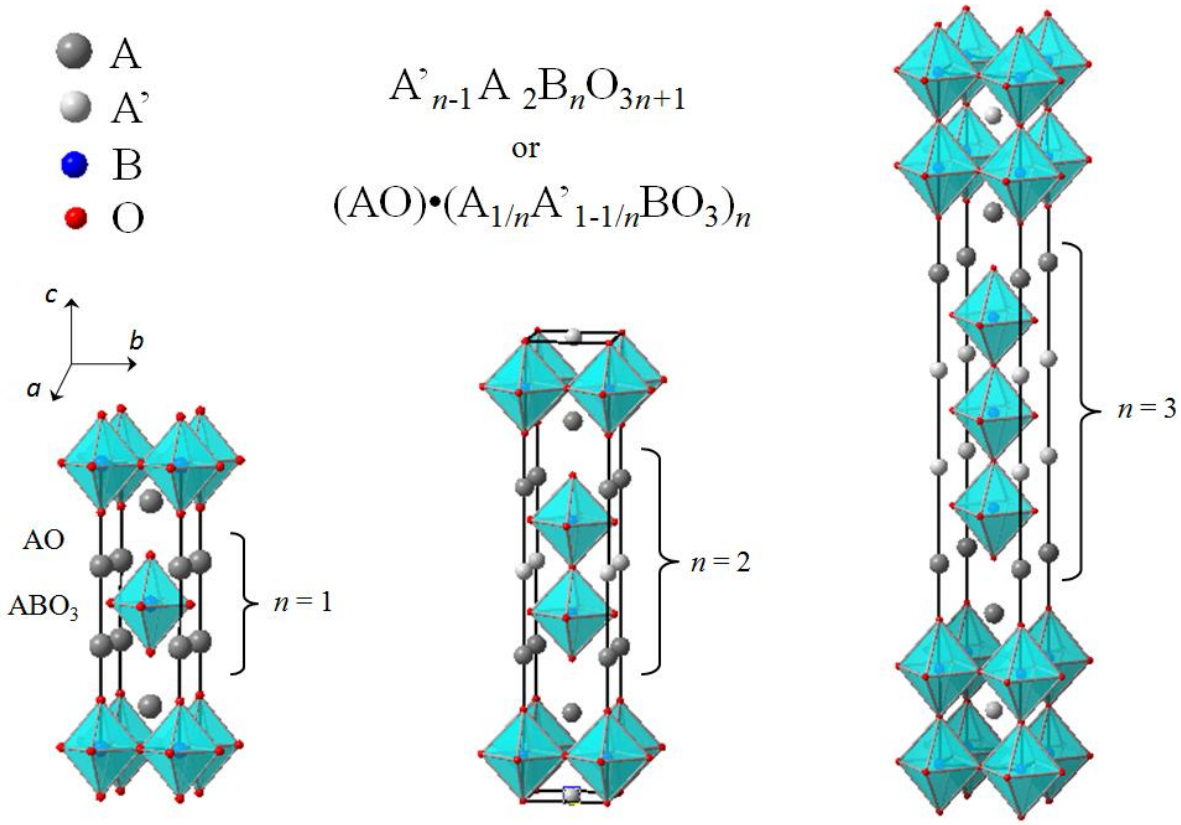

Figure 1.6: *Typical unit-cells of Ruddlesden-Popper phases with different thickness of perovskite layers.*

Similarly to perovskites, Ruddlesden-Popper phases show a rather high structural flexibility, and more particularly the cuprate compounds. Copper-oxides exist with atomic structures derived from the original K_2NiF_4-type, with different coordination numbers for Cu and subsequent various CuO_x polyhedra geometries. The structural changes do not systematically affect the stoichiometry: although oxygen deficient phases exist, the A_2BO_4 stoichiometry can stabilize in distinct structures differing only by the position of oxygen atoms in the unit-cell. The A-site can be shared by diverse rare earth (*RE*) element or alkaline metal (*M*) of different valences (mainly Sr and Ba), yielding distinct physical properties to the subsequent $Ln_{2-x-y}RE_xM_yCuO_4$ compounds depending on the substitution coefficient *x*. The discovery[44] of high-*Tc* superconducting properties in such materials has notably created a strong interest for structural investigations.

1.3.2. *La_2MO_4 T-type structure (n = 1)*

The La_2MO_4 system corresponds to the case of n = 1 for $A_{n+1}B_nO_{3n+1}$, *i.e.* A_2BO_4 with A = La and B is a transition metal M. This system consists of three isostructural compounds with M = Co, Ni, Cu. In the high temperature phase, the stoichiometric $La_2MO_{4.00}$ structure adopts the tetragonal K_2NiF_4-type structure above 535 K for Cu[45], 770 K for Ni[46] and 850 K for Co[47]: they are in the High Temperature Tetragonal phase (HTT) of space group *I4/mmm*, as shown on Figure 1.7.

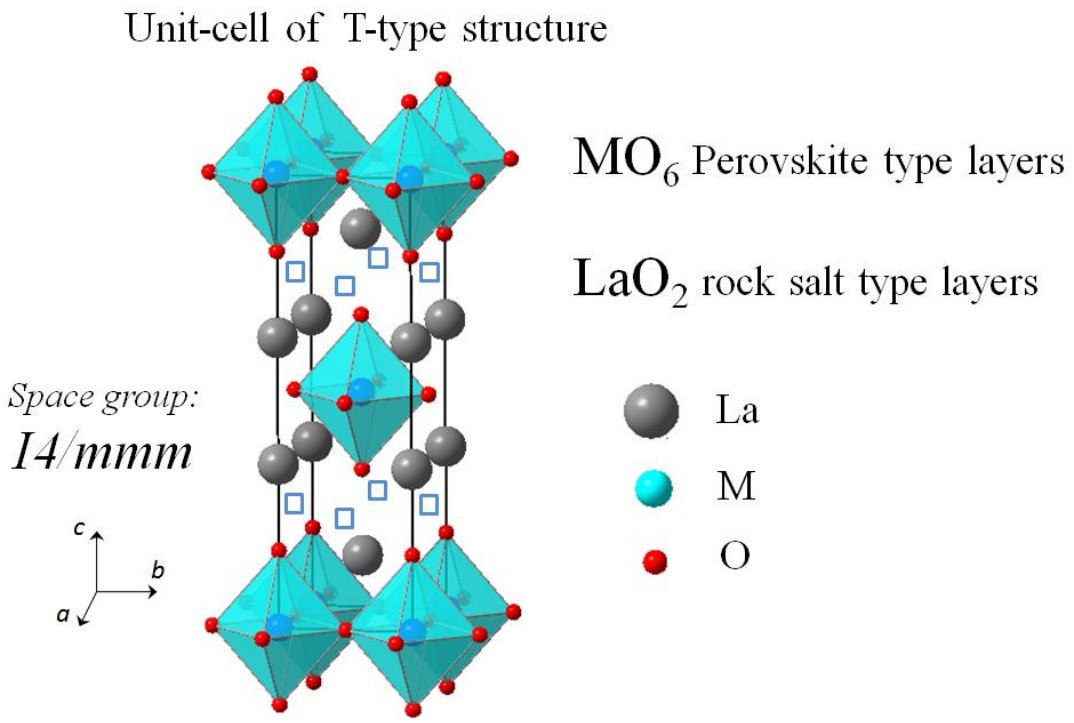

***Figure 1.7**: Three different sites for oxygen in the basic unit-cell of the HTT phase (space group: I4/mmm).*

The structure is strongly anisotropic, almost bi-dimensional since the thickness of perovskite layers is minimal; the octahedra share corners but are not interconnected between layers. The fact that n = 1 implies that each MO_6 octahedral layer is sandwiched between two slabs of rock salt LaO. La ions occupy a single site at the boundary between the two types of layers, corresponding to the A site of coordination number 9, *i.e.* 4 + 4 + 1 oxygen ions with different bond lengths of, for instance, 2.35 Å, 2.64 Å and 2.75 Å in La_2CuO_4. The M cations are in coordination 4 + 2 of equatorial (O_{eq}) and apical oxygen (O_{ap}) respectively, but M-O_{ap} bond lengths vary with the type of M cation. Indeed, although they are almost equivalent for Co and Ni, the Cu-O_{ap} bond length is elongated by the Jahn-Teller effect due to the valence state of Cu^{2+}. This has an impact on the *c*-axis which is equal to 13.15 Å for La_2CuO_4 whereas it is

comprised in the range of 12.55 Å < c < 12.70 Å for La_2CoO_4 and La_2NiO_4[48,12,49]. In the ideal HTT state, MO_6 octahedra are perfectly aligned toward the c-axis. The distance between oxygen apical site and interstitial site (O_{int}) is 2.1 Å which is normally too low to allow the presence of extra oxygen on interstitial sites. The interstitial sites are consequently marked by an empty square (□) on the figure since they are all empty.

Even if it is mainly used for perovskites, the Goldschmidt factor t (equation 1) can be extended to Ruddlesden-Popper phases to quantify internal strains. For La_2MO_4, t = 1 corresponds to the tetragonal HTT state described above. However, for 0.86 < t < 1, strong strains are present in the structure, the MO_2 planes endure compression and the unit-cell is either tetragonal or orthorhombic. For t < 0.86, the atomic structure is different and corresponds to the T'-type structure, adopted by Nd_2CuO_4 for example[50]. The T' structure will be described in more details in the next section. Internal strains can be compensated in several ways, one of them being the partial substitution of La by alkaline metals of smaller ionic radius. For instance, t passes from the value of 0.88 for La_2NiO_4 to 0.94 for $LaSrNiO_4$, and similarly from 0.86 to 0.97 for La_2CoO_4 and $LaSrCoO_4$ respectively. It has to be noticed that Sr-doping stabilizes the tetragonal HTT structure even at ambient temperature. Doping with divalent cations also provokes the localization of holes on orbitals which encourages decreasing the compression of MO_2 planes. An alternative way to doping for the relaxation of strains at ambient temperature in La_2MO_4 is a cooperative tilt of octahedra from the c-axis leading to structural distortion. This also results in structural phase transitions with temperature.

1.3.3. T' type structure and associated T''

The ionic radius of rare earth elements composing Ln_2MO_4 oxides is a critical criterion driving the type of structure adopted by the material. Among the family of lanthanide cuprate of stoichiometry Ln_2CuO_4, all compounds stabilize in T'-structure at RT when synthesized by usual solid state procedure, excepted for Ln = La which adopts the T-structure. This difference is due to the big size of La ions, preventing stabilization of T'-type structure because of size mismatch. However, smaller ionic radii of the other lanthanides favors crystallization in T'-configuration. The common prototype for T' phase is the Nd_2CuO_4 compound[51], which has been mainly studied since it represents the basic structure for electron-doped superconductors, similarly to La_2CuO_4 for hole-doped ones. It was initially assumed that La_2MO_4 could exclusively stabilize in T phase, but surprisingly, synthesis

techniques operating at lower temperature than usual solid state route have recently permitted to synthesize pure T' lanthanum copper oxide, remaining stable at RT. Indeed, recent researches[52] have allowed to synthesize polycrystalline T'-La_2CuO_4 by molten salt technique[53].Other studies[54] have furthermore shown the possibility to obtain T'-La_2CuO_4 through a more classical procedure in terms of synthesis technique, namely a two-step process: *i*) hydrogen reduction of T-phase yielding an intermediate oxygen deficient phase (pseudo oxygen deficient S phase of structural model Sr_2CuO_3) and *ii*) oxidation at relatively low temperature to finally reach T' state. Recently, different procedures have been also elaborated[55] allowing to synthesizing epitaxial thin films of T'-La_2CuO_4 by molecular beam epitaxy. The synthesis of T'-La_2CuO_4 have to be carried out at relatively low temperature, which is mandatory for obtaining this particular compound. At RT, La_2CuO_4 oxide exists in the two polymorph states. The basic structural difference between T and T' structure consists only in one oxygen position in the unit-cell. In T' structure, the apical site is empty whereas interstitial site is completely full and *vice-versa* for T-structure. However the space group remains the same for both models: *I4/mmm.* Figure 1.8 shows the T'-tetragonal unit-cell with vacant apical oxygen sites indicated by empty squares.

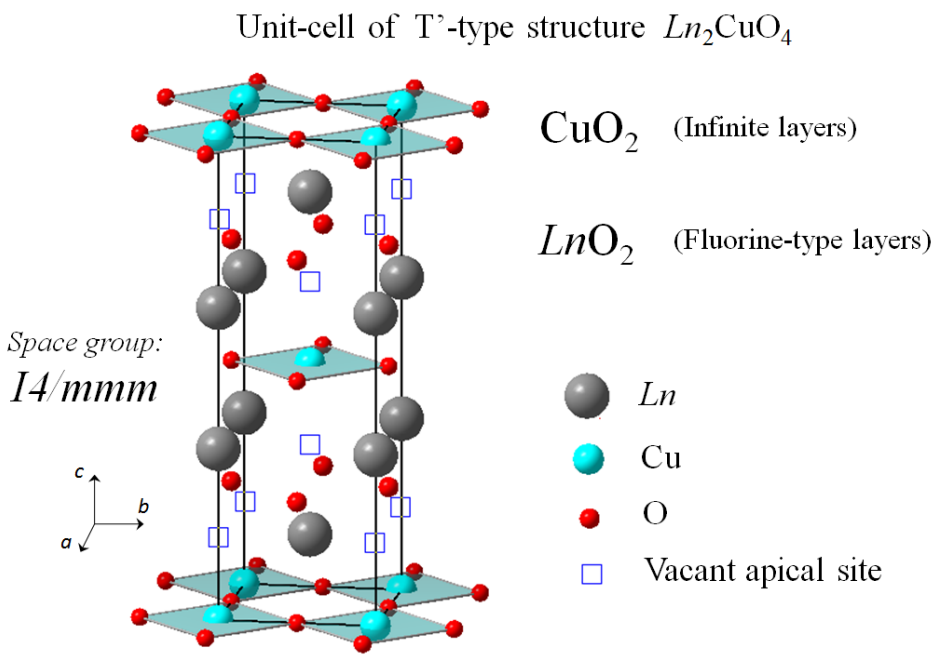

***Figure 1.8**: Unit-cell of the T'-type structure made of corner-shared CuO_4 square planes layers. Empty apical oxygen sites are represented by empty squares.*

Instead of occupying this site, oxygen ions are located in the interstitial planes (z = 0.25 and z = 0.75). Therefore, copper layers consisted of planar array of corner-shared CuO_4 square-planes, form infinite CuO_2 layers. The resulting arrangement can be depicted as an intergrowth of infinite transition metal oxide layers ABO_2 with AO_2 fluorine-type layers. The coordination number of Cu is 4 instead of 6 for the T-phase, and the one of La is 8 instead of 9. The absence of apical oxygen releases structural frustrations induced by the Jahn-Teller effect occurring for CuO_6 octahedra responsible for the high value of *c*-parameter of 13.15 Å for T-phase in comparison with the one of the T' unit-cell is smaller and takes the value of 12.53 Å. Conversely, the *a*-parameter enlarges to 4.02 Å (instead of 3.88 Å for T-phase). The volume of the T'-unit-cell (202.48 $Å^3$) is larger than the one of T-unit-cell (197.96 $Å^3$).

Different deviations from the ideal T'-structure have been observed in certain cases. As a first example, a reduced symmetry has been observed[56] in the Gd_2CuO_4 oxide (space group *Acam*), induced by a rotation around the *c*-axis of oxygen squares surrounding the Cu sites. This structural distortion has been used as an argument to explain the non-existence of superconductivity in $Gd_{2-x}Ce_xCuO_4$. As a second example, the special case of $La_{2-x}Nd_xCuO_4$ can be given. Substituting La by Nd has a direct impact on the Goldschmidt tolerance factor since the average ionic radius for the *Ln* site is modified. Investigations[57] concerning the structural evolution of this compound as function of Nd content have permitted to build a phase diagram as function of the Goldschmidt tolerance factor, showing the emergence of the intermediate T''-state for t = 0.864 at the boundary between T and T' structure. This tolerance factor precisely corresponds to the $La_{1.5}Nd_{0.5}CuO_4$ stoichiometry. The *a*- and *c*-axes of the T'' unit-cell are elongated and an order between Nd^{3+} and La^{3+} ions has been presumed to occur within *Ln*-O layers. Furthermore, the compound of composition $La_{1.5}Nd_{0.5}CuO_4$ can be stabilized as single phase T', T or T'' depending on the synthesis temperature[58]. T''-phase is created only at high temperatures since it needs sufficient cation mobility and stabilization to occur. Until now, T''-phase has only been observed in *RE*-doped lanthanum cuprates.

1.3.4. T-type structure: hybrid phase between T and T'*

According to the large amount of studies reported in the literature, several types of structure are available for the $La_{2-x-z}Ln_xSr_zCuO_4$ oxides, depending on *Ln* substitution. Among them, the T*-type structure is probably the simplest system with Cu-O square pyramidal sheets; it consists of alternation of T and T'-type 2D layers along the *c*-axis and thus represents a hybrid system. As shown in Figure 1.9, the resulting stacking is of -ABACABAC-type, with

A = layers of CuO_5 square based pyramids, B = (La,Sr)O rock salt-type layers and C = LnO_2 fluorine type layers (CaF_2-type). It is worth noting that even if all Cu-O layers have been chosen to be identified as A-type, the CuO_5 pyramids are oriented antiparallely between two consecutive layers (called "up" and "down" in the figure).

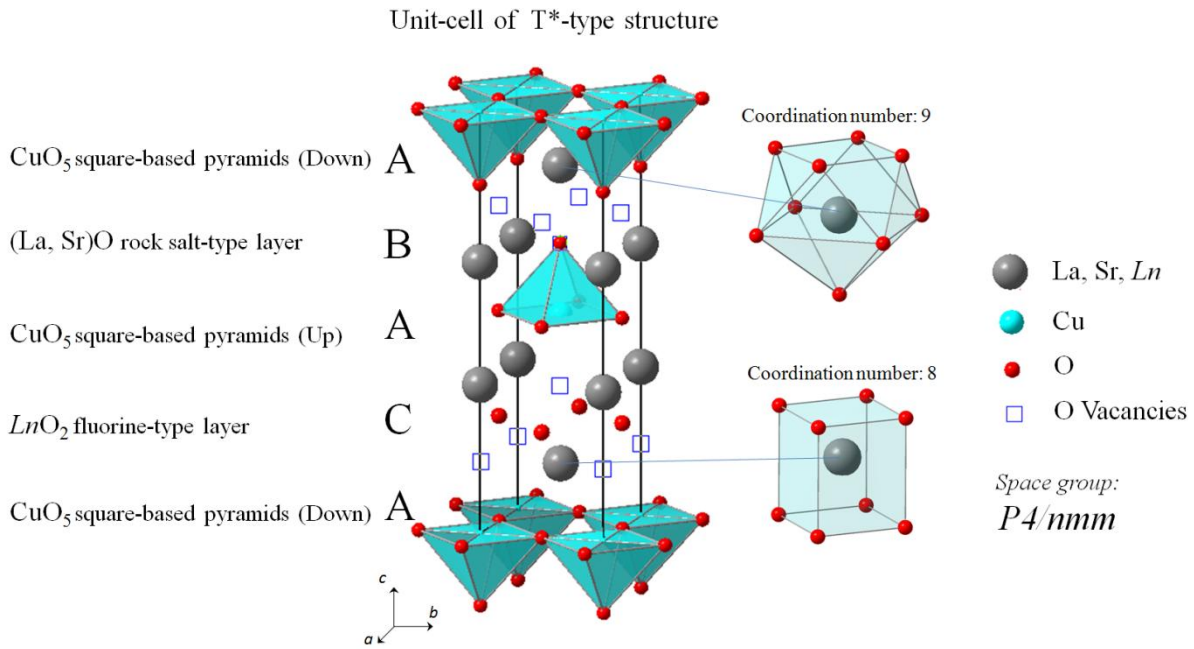

***Figure 1.9**: Unit-cell of the T*-type layered structure, where the alternation of T and T'-type layers induces the appearance of CuO_5 square-based pyramids, as well as two different coordinations for (La,Sr) and Ln.*

La and Sr cations are located in the rock salt layers (coordination 9), in accordance with their tendencies to form the T-phase, whereas smaller *Ln* cations permit the stabilization of the fluorine-type layers (coordination 8). Generally, the relatively large *Ln* ions (*e.g.* Pr, Nd) can easily form a solid solution with the largest La ions over the whole composition range, but remain either in T or in T' configuration. On the other hand, large La ions can hardly be dissolved in smaller ion sites (Sm, Eu, Gd, Dy …) in the T'-structure, and *vice versa* in the T-structure. The key to obtain the intermediate T*-structure is to mix the large and small cations, which are mutually insoluble, approximately with the 1:1 ratio. A small amount of Sr is necessary, supposedly due to the condition of the stable Cu valence, slightly above two. This results in the sequential ordering of the large and small cations, as in the case of the famous $YBa_2Cu_3O_7$, with small Ba and large Cu. Superconductivity has been observed in few T*-type compounds (*e.g.* $SmLa_{0.75}Sr_{0.25}CuO_4$) when post annealed under high oxygen pressure, suggesting that intercalation of oxygen ions within the rock salt layers is possible for T*. The temperature dependence of resistivity has been shown to be strongly sensitive to the

post annealing temperature[59]. But in addition to the physical and chemical properties, the existence of T*-type compounds demonstrates the promiscuity between T and T'-structures and their possible intergrowth. When chemical constituents are chosen appropriately, and when synthesis conditions are adapted for stabilization of cation ordering, T and T'-layers order themselves in the same bulk. Reflecting the hybrid character between T and T', the tetragonal T* shows intermediate values of unit-cell parameters: a ~ 3.9 Å and c ~ 12.6 Å. However, even if T and T'-structures have the same space group (*I4/mmm*), the body-centering is lost in T*-structure, the symmetry is lower and the space group is *P4/nmm*.

1.3.5. Oxygen deficiency in Ruddlesden-Popper derivatives: S-phase

Besides the ability of $Ln_2MO_{4+\delta}$ compounds to be oxidized by accepting overstoichiometric oxygen atoms, they can also be reduced, yielding oxygen deficient phases Ln_2MO_{4-x}. Taking off oxygen from these compounds can be achieved by different reducing techniques which are depicted in the next chapter. Herein are introduced the repercussions of oxygen deficiency on atomic structure, and particularly on the oxygen sublattice. In general, non-stoichiometries result in complex arrangements derived from ideal structures, and similarly to excess of oxygen in the case of intercalation, the deficiency of oxygen induces symmetry breaking, local disorder, re-ordering at long range, structural defects, etc. However, the main characteristic remains that the structure does not collapse but undergoes topotactic transformations when anionic stoichiometry evolves, showing the high flexibility of such phases. Oxygen-poor phases of lanthanum copper La_2CuO_{4-x} have been shown to be decisive since they constitute an intermediate step mandatory for the transformation from T to T' structure, as mentioned before. Because the deficiency rate x is hard to estimate, the different models suggested could correspond to different oxygen contents. Nevertheless, even if the atomic structure is strongly depending on the amount and position of oxygen vacancies, different prototypes are available for describing La_2CuO_{4-x}, depending on which kind of oxygen is lacking, namely apical or equatorial. It has been firstly assumed that reducing La_2CuO_4 would stabilize a deficient phase whose atomic structure is similar to Sr_2CuO_3-type. The latter has been studied, once again, in the course for high-T_C superconductors, and it has been conventionally named S-type structure[60,61,62,63]. Contrary to T, T', T'' and T*, the S-phase possesses lacks of oxygen on equatorial sites, which are only half occupied. Vacancies are ordered in such way that Cu adopts a square planar coordination. However, contrary to the T'-structure, the CuO_4 square planes are lying toward the c-direction, as shown on Figure

1.10, and not within the *a-b* plane. In brief, copper atoms are surrounded by 2 O_{ap} and 2 O_{eq} in their first coordination sphere instead of 4 O_{eq} in T'. This is a major difference, since the resulting arrangement of square planes in S-type structure do not form 2D-layers but 1D-chains sharing corner oriented along [100] direction. As a consequence, the strains are decreased in the direction perpendicular to the planes and the unit-cell becomes orthorhombic, space group *Immm*.

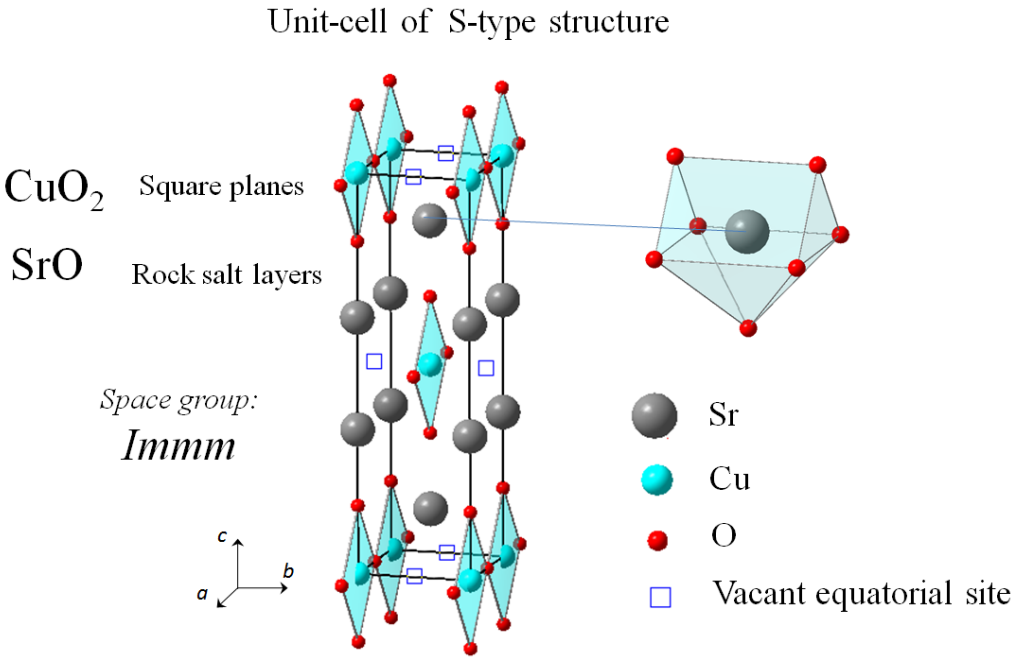

***Figure 1.10**: Ideal unit-cell of oxygen deficient S-type phase; CuO_4 square planes form parallel chains, and the coordination number of Ln is 7.*

However, the ideal S-type unit-cell cannot perfectly match with the real Ln_2CuO_{4-x} structure since in reality the maximum deficiency rate has been found, until now, to be x_{max} = 0.33 for La and x_{max} = 0.5 for *Ln* = Pr, Nd, Sm, Eu, and Gd[13], which is far from the value of x = 1 in the theoretical model. Consequently, there are less vacancies and the coordination of copper is in fact closer to 5 than 4, yielding to the existence of CuO_5 pyramids in addition to the CuO_4 square planes. Besides, positions of vacancies in the unit-cell are controversy; although equatorial sites have been found to be good candidates, apical sites have also been shown to be only partially occupied. Even if the temperature dependence of magnetism in oxygen-deficient La_2CuO_{4-x} has attracted much attention, its real atomic structure has not been the subject of many studies. One particular work[64] dedicated to structural investigations has however permitted to determine a long-period shear structure for oxygen deficient La_2CuO_{4-x} by electron diffraction and high resolution transmission microscopy techniques. They have

shown that dislocations induces shear planes formed by edge-sharing CuO_6 octahedra, parallel with $(111)_{LTO}$ plane. A subsequent modulated structure has been determined, matching with a monoclinic unit-cell of parameters: a = 6.6 Å, b = 7.6 Å, c = 26.6 Å and β = 103°, space group *P2/c*. The resulting crystal bulk consists in domains of stripes, where $\vec{a}$ and $\vec{c}$ are interchanged from one domain to the other. These results are far from the ideal S-type model, showing the considerable lack of knowledge concerning the real structure of reduced compound La_2CuO_{4-x}.

1.3.6. A new tolerance factor adapted to A_2BO_4 stoichiometry

The T and T' structural types are commonly differentiated thanks to the Goldschmidt factor t (equation 1) as a criterion for stability. If $t < 0.86$, the atomic structure does not belong to T anymore but to T'-type. However, several exceptions to this rule persist. For instance, for the phases Ln_2CuO_4 (with Ln = Dy, Ho, Er, Tm, Y), the lower limit of t for the T' phases extends to 0.81. Other examples illustrate the deviation from such general tendency. Therefore, a second tolerance factor tf has been proposed[65] in addition to the Goldschmidt factor originally developed for ABO_3 perovskites, for a better classification of the materials with A_2BO_4 stoichiometry. Applying the same method as the one developed for the conception of the Goldschmidt factor led to the following relation:

$$tf = \frac{3\sqrt{2}r_O + 2\sqrt{6}(r_O + r_A)}{9(r_B + r_O)} \qquad \text{Equation 2}$$

The tolerance factor tf is based on the geometrical matching between *A-O*, *B-O* and *O-O* bond distances in A_2BO_4 and has been shown to be perfectly appropriated for the differentiation of T, T' and T* phases. The T' phase exhibits a tolerance factor in the range $0.96 < tf < 1.00$ while T phase occurs for $1.00 < tf < 1.14$. The T* phase exists in a very narrow range between T and T', *i.e.* for $tf \sim 1.00$. The fact that T and T'-phases are separated by an ''ideal'' tolerance factor tf = 1.00 suggests that the model relates accurately to the ionic packing factors and clearly shows that tf is a very powerful classification parameter.

1.4. Properties of Ruddlesden-popper phases and derivatives

1.4.1. General case of rare earth-doped Ruddlesden-popper $La_{2-x}RE_xCuO_4$

Up to now, all the known copper-oxide superconductors have an intergrowth structure of superconductively active layers and inactive layers. The simplest structures of this class are illustrated by the two following prototypes, T-$La_{2-x}Sr_xCuO_4$ and T'-$Nd_{2-x}Ce_xCuO_4$, being respectively *p*-type and *n*-type superconductors[66,67,68]. The superconducting properties have motivated studies about the crystal chemistry of cuprates having these two structures, which differ by their inactive layers, of rock salt type in the case of T phase (as extensively described in the previous section), and of fluorine-type for T'. The latter layers are sandwiched between CuO_2 active layers in both cases. However, the coordination number of Cu differs, being equal to 6 in T phase (CuO_6 octahedra) whereas it is equal to 4 in T'-phase (CuO_4 square planes). When doping T-phase with Strontium (+II), holes are introduced in the copper slabs, identically to what happens by oxygen intercalation. On the contrary, doping the T'-phase with Cerium (+IV) pushes electrons as charge carrier in the copper layers. After the preliminary studies concerning these two prototypes, investigations have been extended to other compositions showing many possibilities for each T and T'-structures depending on the rare earth used for doping. One singular behavior has been recently reported[69] concerning doping $La_{2-x}RE_xCuO_4$ with a *RE* of +III valence states which astonishingly turns the compounds to superconductors even if no effective dopants are theoretically introduced, which are normally indispensable for the apparition of superconductivity in copper oxides. The substitution of isovalent *RE* for La was essentially performed to stabilize the T'-phase of La_2CuO_4 instead of the T-phase. Incredibly, the maximum T_c has been found to be remarkably high ~ 25 K. However the structure of this compound was idealized; since minor oxygen defects would be sufficient to create electrons in CuO_2 layers, the knowledge of the real stoichiometry is crucial. This example nicely shows how the depiction of the real structure is essential for understanding the physical properties of these materials. Oxygen content is always hard to estimate, it generally deviates, even slightly, from ideal stoichiometry which is in fact rarely respected. Even if not all of $La_{2-x}RE_xCuO_4$ compounds show superconducting properties, they exhibit a large panel of other interesting features, and they offer an opportunity for structural investigations with respect to oxygen migration.

Oxygen deficiency in T'-structure has been found to be responsible for serious damages on superconductivity, and thus further studies have been focused on stoichiometric compounds yielding to the discovery of new structures with the same ideal stoichiometries A_2BO_4. For

instance, within the phase diagram of the $La_{2-x-z}Ln_xSr_zCuO_4$ system, the hybrid T*-phase has been isolated[70,71,59,72,73] for some specific values of *x*. As explained before, the T* phase can be depicted as an intergrowth of T and T' layers, forming a structure of space group *P4/nmm*. The great attention dedicated to phase diagram investigations also permitted to discriminate the T''-phase, appearing rarely and showing resemblance with T' but with a larger volume of unit-cell (presented in section 1.3.3 of this chapter). Indeed, $La_{2-x}Ln_xCuO_4$ (with *Ln* = Pr, Nd, Sm, Tb, Dy) has been shown to stabilize in T''-type structure for specific *x* values depending on *Ln*, suggesting cation ordering within the *Ln*O layers. The T'' phase appears to be an ordered variant of the T' phase, but could neither be doped with *n*-type nor *p*-type charge carrier. To sum up, the four distinct types of structure: T, T', T'' and T* have been differentiated for $La_{2-x-z}Ln_xSr_zCuO_4$ compounds, but they exhibit different physical properties depending on their atomic structure.

1.4.2. Coexistence of two polymorph states of La_2CuO_4 at RT with different properties

One particular feature of the T'-La_2CuO_4 is to show metallic temperature dependence of resistivity down to 50 K, contrary to the stoichiometric T-La_2CuO_4, famous for its insulating properties. Indeed the latter belongs to the family of Mott insulators, meaning that it should theoretically conduct electricity, but an electron-electron interaction not considered in the conventional band theory makes it insulating. This feature has motivated many theoretical studies until recently[74,75]. The disappearance of insulating character with carrier doping has also been studied[76] in detail. The two distinct behaviors of T and T' lanthanum copper oxides involve an essential difference in the electronic structure between the two phases, due to distinct oxygen coordination. This implication is consistent with new state-of-the-art band calculation results[77,78,79], which propose a metallic solution to T'- La_2CuO_4 but an insulating one to T- La_2CuO_4, *i.e.* in agreement with experimental behavior.

But more generally, the co-existence of two polymorph states of La_2CuO_4 at RT remains decisive since it directly asks the question to know which state is the most stable under atmospheric conditions. According to the ionic radius[80] of La^{3+}, Cu^{2+} and O^{2-}, the Goldschmidt tolerance factor (equation 1) of T-La_2CuO4 is t = 0.869, and the tolerance factor (equation 2) is tf = 1.009; they are both close to the T/T' limit, but still in the T region. However, when calculating these coefficients with the ionic radius corresponding to the coordination numbers of T'-La_2CuO_4, the resulting values are: t = 0.92 and tf = 1.008, which surprisingly still correspond to T-phase, and thus are in discordance with the usual tendency;

it seems that the T'-La_2CuO_4 constitute an exception to the rule for both classification parameters. This is also why T'-La_2CuO_4 has always been considered to be unstable at RT; and therefore the actual existence of pure lanthanum copper oxide with this structure calls the fundamental statements into questions.

A major difference that persists between T and T'-phases is the apparent impossibility to over-oxidize the compounds with T'-structures. Only oxygen defects are conceivable for these phases. And correlatively, oxygen ionic diffusion in T' is insignificant in comparison with T phase. The reason of such different ionic conduction properties needs to be clarified. Indeed, considering their very close structure, the drastically different reactivity of T and T' appears to be a clue for the basic understanding of oxygen self-diffusion. In this context, investigations of structural phase transitions of La_2CuO_4 between the latter two polymorph states, depending on synthesis process, becomes a clue for the fundamental understanding of the oxygen diffusion mechanism in the La_2MO_4 family. Until now, only polycrystalline T'-La_2CuO_4 could have been synthesized, according to the studies reported in peer reviews. Nevertheless, it is clear that single crystal samples could considerably increase the possibility of studies, and provide complementary results concerning oxygen diffusion mechanism.

1.4.3. Intercalated $La_2CuO_{4+\delta}$: mixture of T and T'

It is remarkable that La_2CuO_4 is the only compound of Ln_2CuO_4 series to adopt the T-structure when obtained by usual solid state synthesis, and also the only one to exhibit fast oxygen conduction properties. The possibility to stabilize the polymorphic T'-La_2CuO_4 by soft chemistry technique at lower temperature enhances the promiscuity of the two states, both stable at RT. They differ only by one oxygen position in the unit-cell (interstitial or apical site). In this context the oxygen rich compounds $La_2MO_{4+\delta}$ can be considered as a kind of intermediate state between T and T'-phase since oxygen atoms occupy not only the apical site but also partially the interstitial site. In spite of this, the topotactic oxidation only occurs for the T-phase, although T' is full of interstitial oxygen. Several studies[81,82,83,84] result in the following statement: an anisotropic diffusion pathway of interstitial oxygen in the crystal lattice of T-$Ln_2MO_{4+\delta}$ implies the participation of apical oxygen in the process as shown on Figure 1.11.

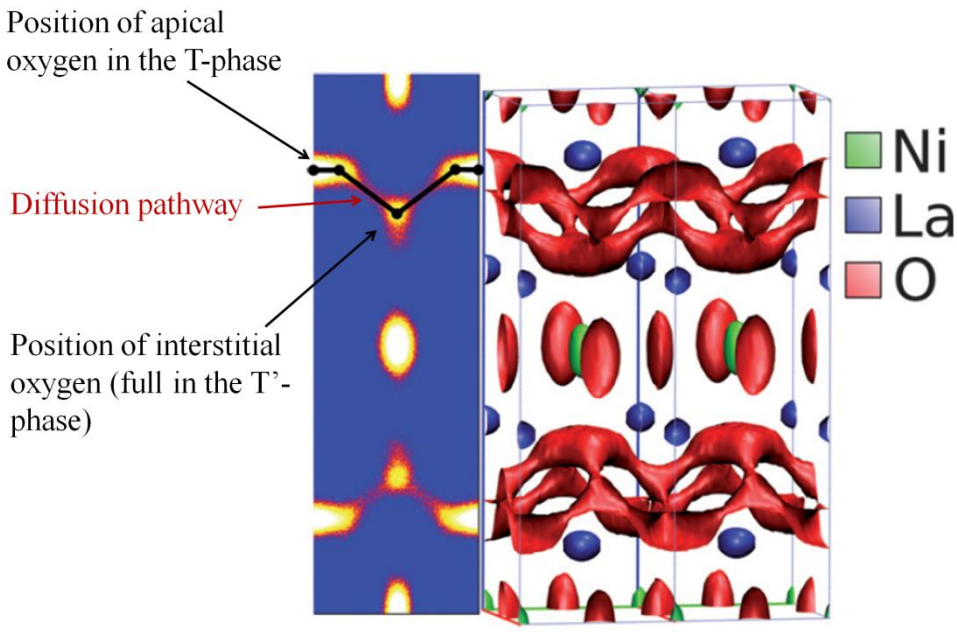

***Figure 1.11**: Pictorial view of molecular dynamics calculations carried out for La_2NiO_4[83]. The oxygen diffusion pathway links the apical site with the interstitial site, suggesting a hopping process between these two sites and enhancing the importance of apical oxygen in the global oxygen migration mechanism.*

In fact the diffusion would occur by mutual exchange of oxygen atoms between interstitial and apical sites, which permits their propagation through the material *via* hopping process between the lattice sites. Therefore, apical oxygen atoms play a decisive role in the diffusion mechanism, and furthermore their presence seems to be a condition *sine qua non* for the diffusion since oxygen conduction is blocked in the T'-phase. Nevertheless, even if this pathway can be reasonably accepted now, the underlying phenomenon responsible for such particular property remains unknown. Moreover, these results concern high temperatures, for which structural disorder is prominent. But the scenario is significantly dissimilar at lower temperatures; in this case the atomic structures of $La_2MO_{4+\delta}$ compounds are highly-ordered. As presented in the next section, long-range orders modulate the structures above certain amount of extra-oxygen (δ). In this context, the phonon-assisted diffusion model[18], recently developed for the parent compound Brownmillerite, yielding oxygen diffusion at moderate temperatures, represents a remarkable candidate for explaining the similar behavior of $La_2MO_{4+\delta}$ compounds.

2. Phase transitions in $La_2MO_{4+\delta}$ depending on temperature and oxygen content

As explained in the previous section, internal strains are relatively strong in La_2MO_4 system. At high temperatures the unit-cell is tetragonal and MO_6 octahedra are all parallel: aligned toward *c*-axis. But, on cooling the *c*-axis shrinks and the strains increase; the structure tends to relax by elongating the interatomic bond lengths. For the stoichiometric compounds, this is achieved by a cooperative tilt of MO_6 octahedra from the *c*-axis by rotation along $[110]_{HTT}$ direction, which leads to a distortion of the structure. Concomitantly, oxidation constitutes an alternative way to relax strains. Indeed, the presence of interstitial oxygen in the lattice favors the tilts by steric effect and thus goes along with the sense of structural relaxation. However, different orientations of tilts appear when $\delta \neq 0$: $[100]_{HTT}$. Relaxation of the crystal lattice induces distinct structural phase transitions in $La_2MO_{4+\delta}$, depending on three major criteria: on the transition metal of the compound, on the temperature and of course, on the extra oxygen content δ. In the first step, the structural evolution of stoichiometric compounds with temperature will be presented, followed in a second step by the effects of oxygen intercalation on the structure and properties.

2.1. Structural phase transitions with temperature for stoichiometric La_2MO_4

2.1.1. Doubling of the unit-cell at ambient temperature: LTO phase

At high temperatures the atomic structure of stoichiometric La_2MO_4 compounds is of K_2NiF_4-type but, when decreasing temperature, the material undergoes a second order phase transition to a so-called Low Temperature Orthorhombic phase (LTO) stable at RT. The interatomic bond distances are contracted due to the lowering of thermal agitation and subsequent diminution of atomic displacement factors which become less and less anharmonic. Consequently the strains are amplified and the Goldschmidt factor decreases. To counterbalance this effect and to release tenses, MO_6 octahedra tilt cooperatively in the same $[110]_{HTT}$ (or $[010]_{LTO}$) direction but in the opposite sense for two neighbor octahedra of the same layer. La ions are affected by the structural distortion and experience a slight shift toward *b*-direction in comparison with their position at high temperature. As a result, the structure transits to the LTO-phase because of the new atomic ordering which causes the appearance of superstructure reflections implying a doubling of the unit-cell volume ($\sim a\sqrt{2}$,

~$a\sqrt{2}$, c) and a *B*-centred symmetry of the lattice. Intensities of superstructure reflections arising below the transition are proportional to the square of the tilt angle between octahedra and *c*-axis, which is around 3° for Cu and Ni. The space group of the unit-cell turns to *Bmab*. Figure 1.12 shows the unit-cell of the LTO phase together with the scheme of cell transformation from HTT to LTO view perpendicularly from the *c*-axis.

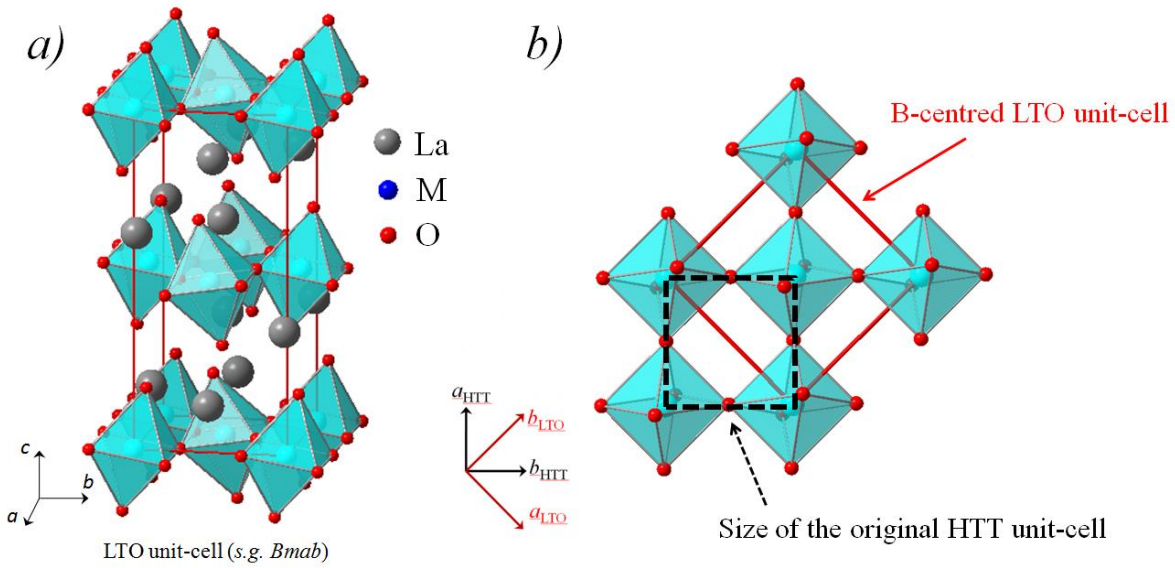

Figure 1.12: *a) B-centred unit-cell of LTO structure at RT, space group Bmab; b) the scheme of the transformation between HTT to LTO in real space viewed with c-axis normal to the plane. Only the upper layer of octahedra is represented for the sake of clarity.*

For Cu and Ni compounds, this tetragonal to orthorhombic transition on cooling has been described in terms of displacive phase transition induced by a softening of a transverse-optic-phonon modes at the *X*-point of the Brillouin zone of the *I4/mmm* HTT unit-cell[85,86,87,88]. For La_2NiO_4, the soft phonon mode (1.6 THz corresponding to ~ 6 meV) has been attributed to the coherent tilting of rigid NiO_6 octahedra[85]. The freezing of this specific mode at the transition conveys the ordered and static tilting scheme of octahedra at RT in the direction $[010]_{LTO}$ (see Figure 1.12). This interpretation of the phase transition ascribes a different character to the HTT phase which appears to be dynamically disordered. Only the average position of the apical oxygen corresponds to M-O_{ap} collinear with the *c*-axis, *i.e.* non-tilted octahedra. But in fact they are dynamically disordered around the apical site in anisotropic way.

The so-called "T/O transition", for Tetragonal to Orthorhombic transition, has been less studied for the stoichiometric cobaltate compound, certainly because it is difficult to synthesize the stoichiometric phase which is unstable. Structural transformations undergone

by this compound have been followed by neutron diffraction on a single crystals of apparently oxygen deficient[89] La_2CoO_{4-x} and also on an oxygen-rich[10] $La_2CoO_{4+\delta}$. The results indicated that a lack of oxygen corresponding to x = 0.14 leads to a different orthorhombic unit-cell at RT, of space group *Pmcb*. The phase transitions of oxygen rich compound will be detailed in the next section. The HTT to LTO transition has also been widely observed in $La_{2-x}B_xMO_4$ system (B = Ba, Sr, and M = Co, Ni, Cu) as function of B-doping, showing a rapid decrease of transition temperature with the substituent content. For instance, $La_{1.88}Sr_{0.12}NiO_4$ remains tetragonal at ambient temperature and it has been shown[90] that the temperature of transition is inversely proportional to the content of Sr. In general, the "T/O transition" causes the appearance of twin domains in single crystals. This point is developed in chapter 3.

Concerning the magnetic structures at RT, neutron diffraction studies performed on these lamellar transition metal oxides have so far revealed two types of antiferromagnetic spin structure in the LTO phase. One is the Cu-type with τ [100] and S [010] and the other is Ni-type with τ [100] and S [100], where S and τ respectively denote the spin direction and the antiferromagnetic propagation vector. The structures are interchangeable by rotation of spin by 90° about the *b*-axis. On the contrary, the cobaltate compound does not show any 3D magnetic order at ambient temperature; only a possible 2D spin correlation in the CoO_2 has been suggested from magnetic quasielastic scattering measurements[91].

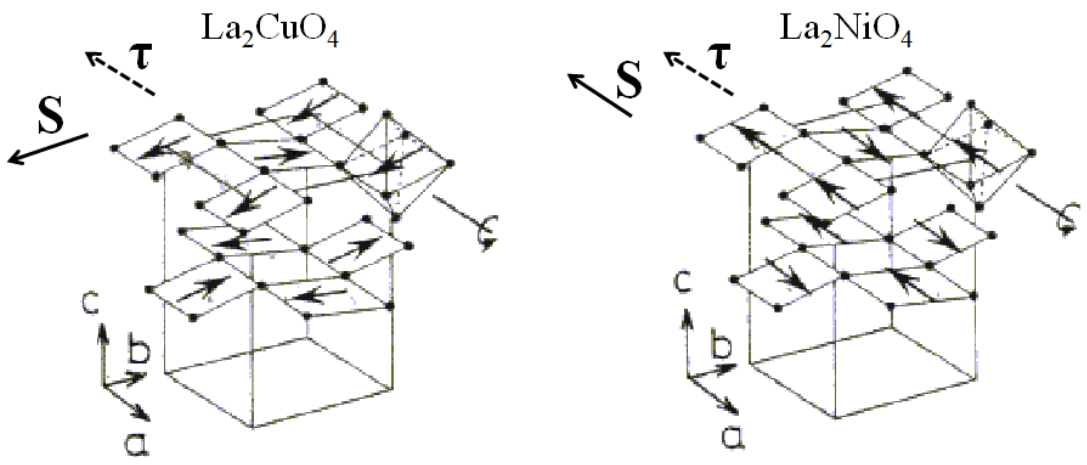

***Figure 1.13**: Magnetic structures of La_2CuO_4 and La_2NiO_4 at RT according to Tranquada et al[92]. The rotations of octahedra are represented to show the resulting small antiferromagnetic component corresponding to the vector τ; which is either perpendicular to the spin direction S in the case of Cu compound or parallel to S in the case of Ni compound.*

2.1.2. Phase transitions at lower temperatures: LTT and LTLO phases

Contrary to La_2CuO_4 which keeps the *Bmab* space group below RT, La_2NiO_4 and La_2CoO_4 compounds undergo a second structural phase transitions around 75 K[46,49] and 110 K[91,8,93] respectively. A similar phase transition has been extensively studied[94,95,96] in the Strontium doped compounds $La_{2-x}Sr_xMO_4$ as well as in Barium doped cuprate $La_{2-x}Ba_xCuO_4$ which transits from LTO to the so-called LTT (Low Temperature Tetragonal) state below RT. The LTT phase also appears at low temperatures in isostructural Nd_2NiO_4 and Pr_2NiO_4 oxides[97,98]. The unit-cell turns to tetragonal but keeps the proportions of the LTO unit-cell (*i.e.* $a_{HTT} \times \sqrt{2}$, $a_{HTT} \times \sqrt{2}$, c), however the space group changes to $P4_2/ncm$. This transition is attributed to a variation of tilt direction of octahedra which re-orients in $[110]_{LTO}$ instead of $[010]_{LTO}$. Indeed this direction of tilt permits a higher elongation of M-O bond length, which furthermore decreases the strains induced by lowering the temperature. This re-arrangement breaks the B-centering symmetry of the crystal lattice but also creates new symmetries. Consequently, the reciprocal space of the structure differs. Indeed new reflections appear by loss of the extinction condition $h + l = 2n$ of *Bmab* and others disappear due to the condition $h + k = 2n$ of the $P4_2/ncm$ symmetry. The conditions on $0kl$ is $l = 2n$, but no conditions exist for $h0l$. In parallel to the LTT phase, it has been shown that not only parent compounds[99,100] but particularly La_2NiO_4 oxide[49,46] possess in fact not a perfectly tetragonal unit cell at low T but slightly orthorhombic, of space group *Pccn*. The resulting structure is called Low Temperature Less Orthorhombic phase (LTLO). For the latter, there is a condition on the reflections $h0l$: $l = 2n$.

The *Pccn* symmetry gives more freedom to the apical and equatorial site of oxygen which allows octahedra to tilt in any direction within the 45° between $[100]_{LTO}$ and $[110]_{LTO}$ axes. Nevertheless, the coherency is kept between octahedra. To sum up, each phase HTT, LTO, LTT, LTLO and their respective space group correspond to particular arrangements of MO_6 octahedra which are either aligned with *c*-axis, tilted by a rotation along $[100]_{LTO}$ direction, $[110]_{LTO}$ direction, or along an intermediate direction (*c.f.* Figure 1.14). It has to be noted that the strong anisotropy of the structure influences drastically the physical properties. Even if it is a coincidence, it can be stressed that only the compounds which are not superconducting at low T seem to show the second structural transition at low temperature.

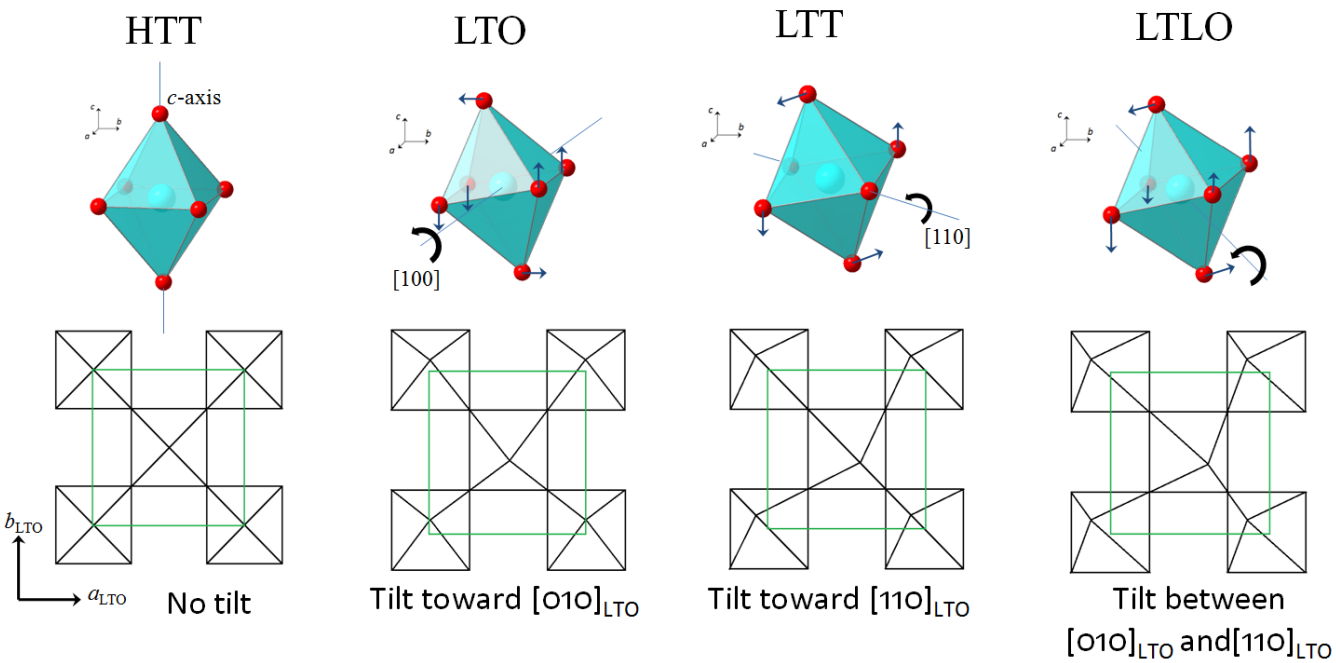

Figure 1.14: *Orientation of tilt of MO_6 octahedra for each low temperature La_2MO_4 phase. Their corresponding tilting schemes are shown below, where the upper layer of octahedra of the unit-cell is represented perpendicular to c-axis.*

The transition from LTO to LTLO has also been described in terms of displacive phase transition, as for the HTT to LTO one in Cu and Ni oxides. A softening of a second phonon mode, involving rotations of the tilt axis of the MO_6 octahedra, has been proposed as a driving mechanism for this second phase transition at low temperatures[101,102,103].

Both tetragonal $P4_2/ncm$ and orthorhombic *Pccn* allow a weak ferromagnetic spin canting with a resulting magnetic moment forming a small ferromagnetic contribution parallel to the *c*-axis (forbidden by the *Bmab* symmetry). The Nickelate compound has been shown to undergo this misalignment of spins together with the structural transition, whereas two magnetic transitions have been reported for La_2CoO_4 compound[91,93] (which is not magnetically ordered at RT). The first one occurring for T_N ~ 275 K consists in the appearance of antiferromagnetic long range order like in the LTO state of Ni-type, *i.e.* τ [100] and *S* [100] which does not imply any structural or symmetry changing. The spins orient parallel to the magnetic propagation vector and the space group remains *Bmab*. But as the temperature is lowered, the structural transition (T ~ 110 K) from LTO to LTT above mentioned is in fact accompanied by a Co^{2+} spin flip which results in a new antiferromagnetic structure with the spin oriented perpendicularly to the magnetic propagation vector as follows: τ [100] and *S* [010], *i.e.* similar to the Cu-type spin order. To sum up, in the range between 275 K and 110 K, the spin arrangement in La_2CoO_4 is similar to the one in nickelate (τ // *S*),

then below 100 K the spins rotate 90° within the CoO_2 plane and adopt the Cu-type configuration ($\tau \perp S$). However, it has to be mentioned that the tetragonal symmetry of La_2CoO_4 at LT allows a non-collinear configuration of spins between alternative CoO_2 layers, but it does not drastically change the physical properties.

2.2. Effect of oxygen doping on structure and properties

2.2.1. Historical background: from superconductivity to oxygen conduction properties

After the structural characterization of the K_2NiF_4 system[104] during the 1950s, a particular interest has been dedicated to this new class of compounds, derivatives from the famous perovskite-type. The possible layered-intergrowth of perovskite with rock salt-type structure, together with the simultaneous improvements of synthesis procedures, opened a new way of investigation in the field of solid state science since a large amount of new materials became available by building up new structures from different block-units. Taking advantage of this, S. N. Ruddlesden and P. Popper have considerably enhanced the classification of these new phases, notably with respect to their famous studies[2,3] concerning the $Sr_{n+1}Ti_nO_{3n+1}$ oxide, justifying the adoption of their names for this family of phases. During the following decades, a wide variety of compounds have ensued from intense studies carried out on these series of systems, which have significantly emphasized their structural complexity. But, it is during the 1980's that K_2NiF_4-type structures have attracted much attention due to the discovery of High-T_c superconducting properties near 30 K in La-Ba-Cu-O system by Bednorz and Müller[44]. This breakthrough has been rapidly followed by the optimization of the feature by designing materials with adapted structures and compositions, which notably yielded to $La_{1.85}Sr_{0.15}CuO_4$ compound being superconducting up to 40 K[66], and particularly to the famous $YBa_2Cu_3O_{7-x}$ with T_c = 93 K[105,106]. Then, coupling between electrons and phonons has been shown[107] to be at the origin of the creation of cooper pairs yielding superconductivity[108,109]. The investigations of high-T_c superconductivity in solid oxides are still very active; until now the highest critical temperature[110] reached is 135 K in the $HgBa_2Ca_2Cu_3O_{8+x}$ system and possibly up to 164 K under high pressure[111].

All these superconducting cuprates belong to the Ruddlesden-popper family; among them La_2CuO_4 represents the basic structural model from which the doped compounds derivate. Due to its simple character in *prima facie*, the insulating lanthanum copper oxide is considered as host structure which can be turned into hole-doped superconducting by

introducing charge carrier in the copper layers *via* cationic substitution. But contrary to all expectations, superconductive behavior has been also evidenced[112,113,114,115] in $La_2CuO_{4.07}$ (T_c = 44 K) showing that hole-doping could also be also achieved by the presence of extra-oxygen within layers[116], leading to the following generalized chemical formula $La_2CuO_{4+\delta}$. The ability of this material to allow intercalation of interstitial oxygen atoms already at room temperature by electrochemistry[117,118,5,119,6] has then been demonstrated. Furthermore, oxygen has been shown to be highly mobile also in the parent compounds[47,120] $La_2NiO_{4+\delta}$ and $La_2CoO_{4+\delta}$. Consequently, although $La_2MO_{4+\delta}$ oxides had been characterized in the framework of superconductivity, investigations concerning these materials have progressively switched to the study of fast oxygen transport at moderate temperatures with respect to their possible technological applications. Based on mathematical models[121] of ionic diffusion in solids, oxygen conduction could have been modelized[122] for $La_2MO_{4+\delta}$ (M = Co, Ni, Cu) oxides permitting to calculate diffusion coefficients from experimental results (*e.g.* oxygen tracer diffusion by the isotope exchange method), giving a scale of comparison between ionic conductors. $La_2CoO_{4+\delta}$ has been found[123] to possess the highest diffusion rate at ambient temperature ($D \sim 10^{-8}$ $cm^2 \cdot s^{-1}$) and the weakest activation energy for oxygen diffusion (E_a = 12 $kJ \cdot mol^{-1}$). In comparison, D and E_a take the following values[83,124,125]: *i)* $D \sim 10^{-8}$ $cm^2 \cdot s^{-1}$ and $E_a \sim 50$ $kJ \cdot mol^{-1}$ for $La_2NiO_{4+\delta}$, *ii)* $D \sim 10^{-9}$ $cm^2 \cdot s^{-1}$ and $E_a \sim 25$ $kJ \cdot mol^{-1}$ for $La_2CuO_{4+\delta}$. In addition, the cobaltate compound is the one which accepts[12] the highest amount of extra oxygen up to some contents of $\delta = 0.25$. But despite these advantages, $La_2CoO_{4+\delta}$ remains the less studied oxide in literature, probably because of the difficulties encountered for the preparation of pure samples (*cf.* chapter 2). However, it represents a very good candidate for the study of oxygen diffusion mechanism, which remains only partially understood when occurring at moderate temperatures with regards to theoretical expectations. The crystal structures and symmetries are of first importance for the understanding of reactivity and more particularly of oxygen intercalation.

2.2.2. Oxygen intercalation

One particularity of $La_2MO_{4+\delta}$ system is its ability to accept overstoichiometric oxygen atoms in the structure (δ). Indeed, extra oxygen can be inserted/removed in/from the lattice by several techniques which are identical to the ones previously listed for perovskite oxidation/reduction reactions. But, conversely to the transformation from perovskite to Brownmillerite and *vice versa*, oxygen ions do not propagate *via* regular vacant sites in

Ruddlesden-Popper; instead extra-oxygen ions are located on interstitial vacancy sites between layers of octahedra, *i.e.* in the rock salt type layers LaO, yielding a principal difference in terms of quality for the underlying diffusion mechanism and pathway. In $ABO_{3-\delta}$ perovskites, diffusion occurs *via* vacancies that are created by lack of oxygen whereas it is related to an excess of interstitial oxygen for $La_2MO_{4+\delta}$. These two distinct cases strongly differ in terms of structural modifications induced by variation of oxygen content although their reactivity at ambient temperature with regard to oxygen remains analogous. This astonishing similarity constitutes one of the main motivations of this work: to correlate the two types of apparently different structural behavior in the same diffusion mechanism.

As already mentioned, the discovery of superconductivity in $La_2CuO_{4+\delta}$ has revealed the importance of extra oxygen on the physical properties of this type of oxide. Further investigations[118,5,119,126] have demonstrated the possibility to oxidize and reduce $La_2CuO_{4+\delta}$ already at ambient temperature by electrochemistry up to $\delta = 0.07$, which turns the material to high-T_c superconductor (T_c = 44 K). Soon after, this oxygen conduction feature has been extended to the Co and Ni compounds[12,127,128,129]. Due to the importance of interstitial oxygen atoms and their strong influence on physical properties, the characterization of their exact positions in the unit cell, as well as their valence states, became a challenge. After a few decades of studies it appears that, among the possibilities[130], extra-oxygen ions occupy an interstitial site located exactly in the position (¼ ¼ ¼) of the LTO unit cell (corresponding to the position (½ 0 ¼) in HTT unit cell). The type of bonds between O_{ap} and O_{int} was also controversial in literature, since a "superoxide" model has been proposed[116,130] for the inter-oxygen bonds with subsequent valence state of –I. Finally this possibility has been refuted after spectroscopic measurements[131] showing that O-O type bond are due to high concentration of oxygen on the surface of the material and after neutron diffraction studies[132,91] on single crystal showing that the O_{int}-O_{ap} distance is too elongated (~2.7 Å) for this type of chemical bonding. The charge transfer induces hole-doping of the CuO_2 layers and interstitial oxygen ions are commonly considered as O^{2-}.

However, contrary to perovskites for which lacks of oxygen induces different types of polyhedra forming the structure, in the case of Ruddlesden-Popper, extra-oxygen fill the interstitial vacancy sites and do not modify the 1st coordination sphere of the transition metal atoms. However, extra oxygen atoms located on interstitial sites form tetrahedra with apical oxygen atoms. The maximum amount of extra oxygen insertable in $La_2MO_{4+\delta}$ depends on M, and is also subject of controversy. Of course δ_{max} varies against synthesis procedures and post-synthesis treatments, but in addition to this, measuring precisely the extra oxygen content

turns out to be difficult due to the low occupancy of the site. Indeed different values are available in literature for δ_{max}, which goes from 0.07 to 0.12 for $La_2CuO_{4+\delta}$[133,134] and from 0.18 to 0.25 for $La_2NiO_{4+\delta}$ [128,135,136,137], whereas δ_{max} has been measured as 0.25 for $La_2CoO_{4+\delta}$[47,12,8].

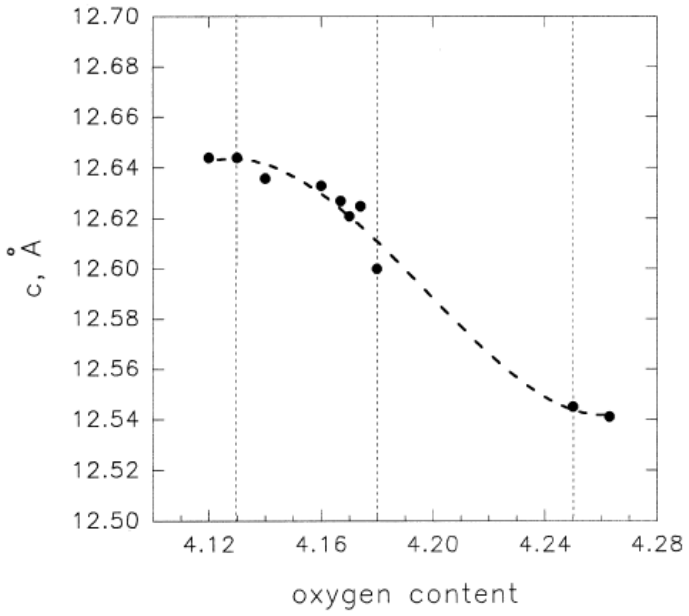

Figure 1.15: *Dependence of c parameter of $La_2CoO_{4+\delta}$ upon oxygen stoichiometry, according to Nemudry et al*[12].

Transition metal oxides exhibit fascinating physical properties which are strongly depending on whether the *d*-electrons are localized on individual transition metal sites or are delocalized throughout the solid. In the *d*-electron systems the orbital degeneracy plays an important role in the complexity and in the stability of the systems. On the crystal chemistry point of view $La_2CoO_{4+\delta}$ is of particular interest in comparison with $La_2CuO_{4+\delta}$ and $La_2NiO_{4+\delta}$ given the high stability of Co^{3+} with respect to Cu^{3+} and Ni^{3+}. Indeed, Co^{3+} is even more stable than the +II state (which is a real problem concerning the synthesis of La_2CoO_4 containing only Co^{2+}, this point is developed in details in the next chapter). Consequently, the high stability of Co^{3+} valence state of cobalt encourages the oxidation by turning the metastable Co^{2+} ions into Co^{3+} when O^{2-} is inserted in the lattice (up to 50% Co^{2+} and 50% Co^{3+} for δ_{max} = 0.25). In addition to this, $La_2CoO_{4+\delta}$ compound exhibits a particular behaviour when δ increases: contrary to the Cu and Ni compounds, the *c*-axis parameter of the unit cell of the Co oxide astonishingly decreases for high δ values[12]. Thanks to these preliminary studies, the evolution of cell parameters is known as function of oxygen content, which is very convenient since it is sufficient to measure the *c*-parameter of the unit-cell to know approximately δ. This avoids

resorting to complex techniques such as iodometry titration, for measuring directly the extra oxygen content. The evolution of *c*-parameter of the unit cell of $La_2CoO_{4+\delta}$ with δ, according to Nemudry *et al.* is shown on Figure 1.15 for $0.1 < \delta < 0.25$. It results from refinements of X-ray powder diffraction pattern recorded *ex situ* at RT, on sample obtained with thermal treatments.

2.2.3. Local disorder induced by interstitial oxygen atoms

The interstitial site is not only surrounded by 4 La atoms, but also possesses 4 apical oxygen atoms in its first coordination sphere: 2 O_{ap} from the upper layer and 2 O_{ap} from the lower one. Together they form a tetrahedral site O_{int}-4(O_{ap}), as well as the four surrounding La atoms (see figure 1.16).

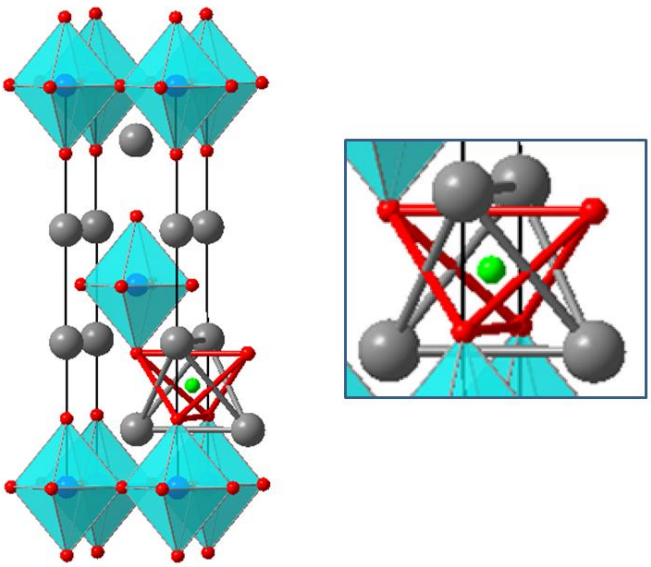

Figure 1.16*: Position and coordination of interstitial oxygen site (green) in the ideal HTT unit-cell.*

In the HTT phase, the distance between O_{int} and O_{ap} is too short (~2.1 Å) in comparison with the ionic radius[80] of O^{2-} (1.38 Å). When $\delta \neq 0$, a part of apical oxygen atoms undergo a shift from their original position in HTT unit-cell, and the O_{int}-O_{ap} distance stretches yielding the opening of interstitial tetrahedral site. Because of this, the corresponding MO_6 octahedra tilt by rotation in opposite directions. The displacements of octahedra towards [110] allow the tetrahedral sites to relax in a way to maximize the distances between the apical and interstitial oxygen atoms. The tilt angles of those MO_6 octahedra which are concerned by the apical oxygen displacements, are about 14° at room temperature, i.e., four times the value found for

the tilt angles around the [100] direction for the *Bmab* structure at ambient. As explained in the previous sections, the symmetry of the atomic structure strongly depends on octahedra arrangement, which is very specific in each case. Even if octahedra are already tilted in LTO phase, the tilting scheme of *Bmab* symmetry does not correspond to an opened interstitial tetrahedral site: two O_{int}-O_{ap} bonds (over four of the $O_{int}4(O_{ap})$ tetrahedra) are systematically shrunk (~1.9 Å). The elongation of the four of them (~2.6 Å), induced by the presence of an interstitial atom, implies higher degrees of freedom for O_{ap} and consequently the uptake of oxygen atoms is accompanied by a breaking of the original symmetry of octahedra. Interstitial oxygen disorders its close environment, but since octahedra are linked by equatorial oxygen, their tilt can propagate the disorder further than the first coordination sphere (Figure 1.17).

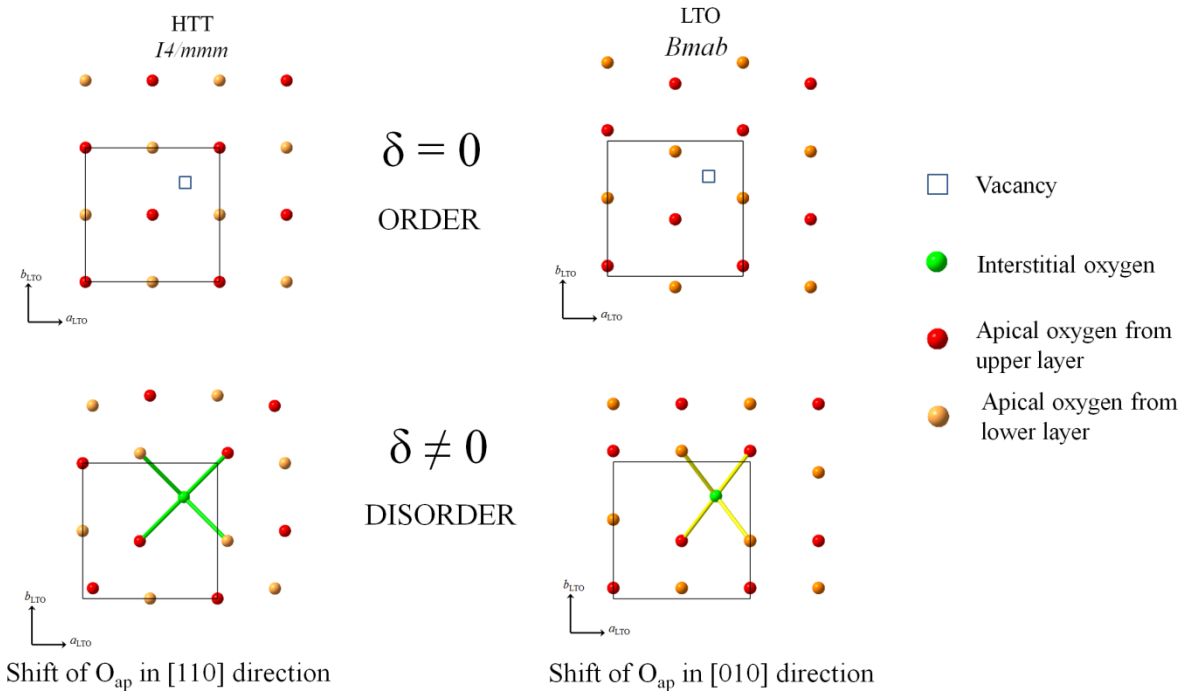

Figure 1.17: *View perpendicular to c-axis of possible local disorder induced by interstitial oxygen. Apical oxygen atoms belonging to layers below and above one interstitial site are shown in green and red respectively. When $\delta = 0$ the ordering is clear, but when $\delta \neq 0$, the structure is distorted, and locally disordered. Directions in square bracket are given with respect to LTO unit-cell.*

As a consequence, the basic unit-cell of $La_2MO_{4+\delta}$ compounds adopts several symmetries depending on δ and M at RT. For instance, the stoichiometric $La_2CuO_{4.00}$ with space group *Bmab* turns to $La_2CuO_{4+\delta}$ with *Fmmm* space group[48] when $\delta \geq 0.04$. The disappearance of superstructure reflections characteristic of *Bmab* space group has also been found when oxidizing stoichiometric $La_2NiO_{4.0}$ to $La_2NiO_{4+\delta}$, which undergoes successive structural phase transitions depending on δ, from LTO to tetragonal and orthorhombic unit-cells of space

groups $P4_2/ncm$, $F4/mmm$, $Fmmm$[49]. On the contrary, $La_2CoO_{4+\delta}$ shows, as the homologous copper phase, an orthorhombic symmetry *Fmmm* even for high extra oxygen values[10] up to $\delta \approx 0.25$. A. Nemudry *et al*[12] have also suggested the existence of an intermediate tetragonal phase for $La_2CoO_{4+\delta}$ between LTO and *Fmmm* states but without giving any further details about the structure. Figure 1.18 summarizes the symmetries adopted by the basic unit-cell of $La_2MO_{4+\delta}$ as function of δ. It is also shown on the figure that the boundary between regions of different symmetries can present a phase separation occurring in various ranges of δ. This leads to miscibility gaps and to the impossibility to obtain a homogeneous repartition of intercalated oxygen for some specific values of δ. Instead, domains of different phases coexist in the same bulk. This tendency of phase separation has been studied in details[119,137,138,139] since it was considered to be a clue for the understanding of phase stability and superconducting properties of $La_2CuO_{4+\delta}$.

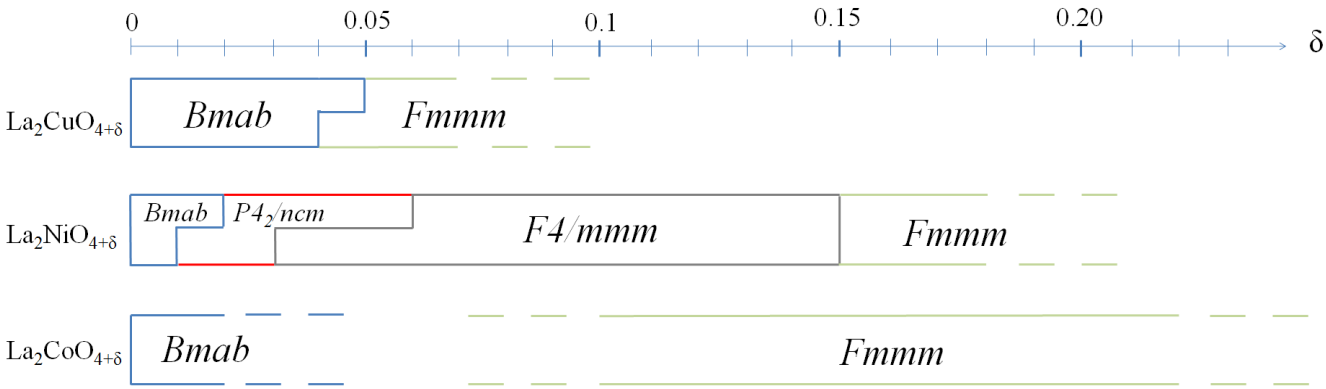

***Figure 1.18**: Space groups of basic unit-cells of $La_2MO_{4+\delta}$ (M = Co, Ni, Cu) as function of δ at ambient temperature.*

From the electrochemical investigations carried out in a galvanostatic mode, lanthanum copper oxide with $\delta \approx 0.07$ has been well investigated[48]. It corresponds to an extra oxygen occupation of 0.28/unit cell, referenced for the *F*-cell containing 4 formula units. This means that only one interstitial oxygen atom is present for about four unit-cells. As there are 8 interstitial sites per *F*-centred unit cell, the occupancy of this site is 1/32 (~0.031) for $\delta = 0.07$. Thus, quantitative analysis of the interstitial oxygen atoms in terms of site occupation and displacement behaviour is not as evident, due to the very small amount of oxygen intercalated. This low site occupancy is also the reason for the disorder created within the original stoichiometric lattice, and explains why the *F*-centred symmetry adopted when $\delta \neq 0$ is averaged on the whole crystal structure. Indeed it is easily conceivable that the local disorder induced by interstitial oxygen atoms partially breaks the 3D ordering of octahedra

and thus affects the structure at long range. That is why an average symmetry becomes necessary to depict the disorder which cannot be neglected anymore since superstructure peaks vanish; and unfortunately, it brings out the lack of knowledge concerning the microstructure, which is nevertheless extremely important with/in regards to physical and chemical properties. In *Fmmm* space group, supplementary positions are available for O_{ap} and O_{eq} allowing to taking structural distortion into account, but their occupancy is lower than 1 and are only statistically occupied. It is remarkable that the disordered state *Fmmm* is of higher symmetry than the ordered state *Bmab*. But as said before, the oxygen sites are only partially occupied and the real structure is ignored by the symmetry of the basic unit-cell. However, the phase transitions undergone by the structure for high δ suggest an underlying ordering at long-range which is the subject of the next section.

2.2.4. Coming back of ordering for higher values of δ: modulated structures

The previous section aimed to introduce the structural disorder caused by interstitial oxygen ions for rather low values of δ, and to list the resulting phase transitions to some states which can be described only by average symmetries. But for high extra oxygen contents, typically when $\delta > 0.1$, emergence of more complex orderings have been observed[10,140,141,142,143,144] in $La_2CuO_{4+\delta}$, $La_2NiO_{4+\delta}$ and $La_2CoO_{4+\delta}$, respectively for $\delta = 0.12$, $\delta \geq 0.10$ and $\delta = 0.20$. Indeed, when δ reaches such values, superlattice reflections observable by diffraction appear. The super-ordering can have different origins: structural modulation, charge ordering, and arrangements of spins at long range, but all of them result from the partial occupancy of interstitial site by extra oxygen ions. The mechanism of oxygen ordering correlated to octahedra ordering has been the subject of many studies in perovskite related compounds[145,146,147,148,149]. The first evidence of interstitial oxygen ordering in $La_2MO_{4+\delta}$ came from TEM (Transmission Electron Microscopy) studies[141] on $La_2NiO_{4+\delta}$. The latter technique is well sensitive to local arrangements and allows measuring directly zones of reciprocal planes of the structures thanks to two-dimensional electron detectors. The short wavelength of electrons corresponds to a rather big Ewald sphere whose radius is much larger than the cell parameters. Consequently, a whole reciprocal pattern of a specific crystal orientation can be obtained from one single measurement. This experimental aspect is treated in more details in chapter 3. The crucial advantage of the technique was the possibility to detect superlattice reflections even without knowing *a priori* their position in the reciprocal space, as it is always problematic with point detectors used at this time in the field of

diffraction. Consequently, several TEM studies have been carried out on Cu and Ni compounds, followed by neutron diffraction experiments. The results of these investigations showed the emergence of 3D superstructures in $La_2NiO_{4+\delta}$ with commensurate enlargements of the unit-cell, *i.e.* $na + p\ b + qc$ with n, p, and q integers, that depend on δ. The supersymmetries have been attributed to atomic long-range ordering, and several models have been proposed for which interstitial oxygen were forming a sublattice[127,141].

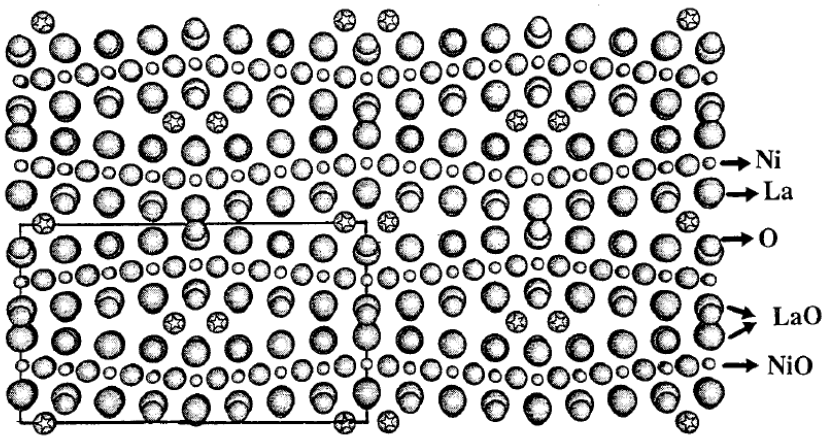

***Figure 1.19**: Pictorial view of a possible structural model of long-range ordering of interstitial oxygen atoms responsible for structural modulation in $La_2NiO_{4.125}$*[150].

The technique of electron diffraction has also been used to characterize the structural modulation of the heavily doped cuprate $La_2CuO_{4.12}$, showing incommensurate modulation in the $\vec{b}$-$\vec{c}$ plane evolving with temperature [140]. For all these studies, a vanishing of superlattice reflections has been reported to occur after short time of experiment, due to strong interaction between electron beam and oxygen ordering. Indeed, the high energy (~1×10^2 keV) and the reductive character of the beam modify the oxygen content and warm the sample enough for a loss of superstructures. These highly ordered phases are certainly weakly stable, since, for instance, just a slight modification of oxygen content is enough to create drastic structural changes. That is why it is understandable that they are very sensitive and easily perturbed by external conditions. In complement to TEM, neutron diffraction experiments have been carried out in complementary studies taking advantage of the non-destructive character of the latter technique. Besides, neutrons are famous for their sensitivity to oxygen, which is obviously beneficial in the present context. But unfortunately, reciprocal maps are not obtainable by this technique at that time, only point-detectors were used during experiments. The results concerning the Cu system[133] have shown an extraordinarily large commensurate superstructure about 10*a* 10*b* 6*c*. For the Ni compound[144], the superlattice reflections could be

indexed with a structural model of large monoclinic unit-cell of space group *C2*. It is very surprising that very few studies have been dedicated to $La_2CoO_{4+\delta}$, only Le Toquin *et al.*[10] reported the presence of modulation measured by neutron diffraction on a single crystal of $La_2CoO_{4.20}$. The structure could be indexed in *Fmmm* basic unit cell with the following incommensurate propagation vectors: $\vec{q}$ = ±0.769 $\vec{a}$* + 0.559 $\vec{b}$*. However, until now, no experimental reciprocal space map of the cobaltate compound has ever been published in literature, and consequently the structural modulation remains unknown for this compound.

For all the studies described above, only atomic ordering was considered as responsible for superstructures, and ensuing structural models did not take into account charge and spin ordering. However it is noteworthy that the detection of those types of ordering by diffraction is very delicate due to the very low intensity of the satellite reflections. While the intensity of these superlattice reflections induced by atomic ordering is of the order of 1% of the basic Bragg reflections, the intensity of charge and spin ordering is 10^{-4} times lower. The work of Tranquada *et.al*[142,151,152,153,92,154] on $La_2NiO_{4+\delta}$ and $La_2CuO_{4+\delta}$ was in this sense decisive since they could propose a mechanism of charge and spin ordering, in addition to structural modulation, by detecting the reflections of very low intensity by neutron diffraction. The two latter effects have been subjected to many studies for their hypothetical role in superconducting properties. Indeed, according to one approach, the holes introduced in the valences of Cu by O_{int} are believed to self organize into "stripes" that alternate with antiferromagnetic regions within copper oxide planes, which would necessitate an unconventional mechanism of superconductivity[155]. Concerning nickelate, neutron diffraction experiments performed on single crystal of $La_2NiO_{4.125}$ have shown a cooperative ordering of holes and Ni spins below 110 K together with the interstitial oxygen ordering already present at RT. At low *T* the magnetic moments are oriented antiparallely to nearest neighbors and they sinusoidally modulated within the NiO_2 plane, resulting in a commensurate magnetic structure of 3*a* x 5*b* x 5*c*. A corresponding modulation within the Ni layers involves breathing mode distortions consistent with modulation of charge density. In complement, atomic ordering has been approached with a staging model, previously developed for intercalated graphite[156]. Indeed a 1D incommensurate structural modulation has been observed on cooling, interpreted as a periodically ordered interstitial oxygen layers along *c*-axis. Each different phase has been differentiated by a number *n* for which "stage *n*" consists in a partially occupied interstitial layer separated by *n* M-O planes, responsible for satellites with $l \pm 1/n$. The other satellites, lying in the $\vec{a}$*-$\vec{b}$* plane, *i.e.* with $l = 0$, were attributed to hole and spin ordering. These superlattice reflections could be indexed with $h \pm p\varepsilon$, k, 0 with ε being the

magnitude of incommensurate splitting. The satellites with *p* odd were ascribed to spin ordering, whereas the ones with *p* even were attributed to hole ordering. Analysis of those features indicated that, in the same way as in the cuprate, holes were structured in domain walls forming antiphase boundaries between antiferromagnetic domains. Finally, a model with cycloid-type spin structure has been evoked[143] for the incommensurate magnetic phase observed above the transition temperature. The oxygen content dependence of the magnetic structure shows commensurability below $\delta \sim 0.10$ and incommensurability above this content. In this context, when taking into account atomic, hole and spin modulation together with basic unit-cell transformations, the phase diagram of $La_2NiO_{4+\delta}$ becomes very complex, revealing the diversity of phases and showing the significant structural flexibility. Figure 1.20 shows the revised phase diagram of $La_2NiO_{4+\delta}$ according to Tranquada *et al*. Similar models of staging has been proposed by Radaelli *et al.*[157,158] for the cuprate.

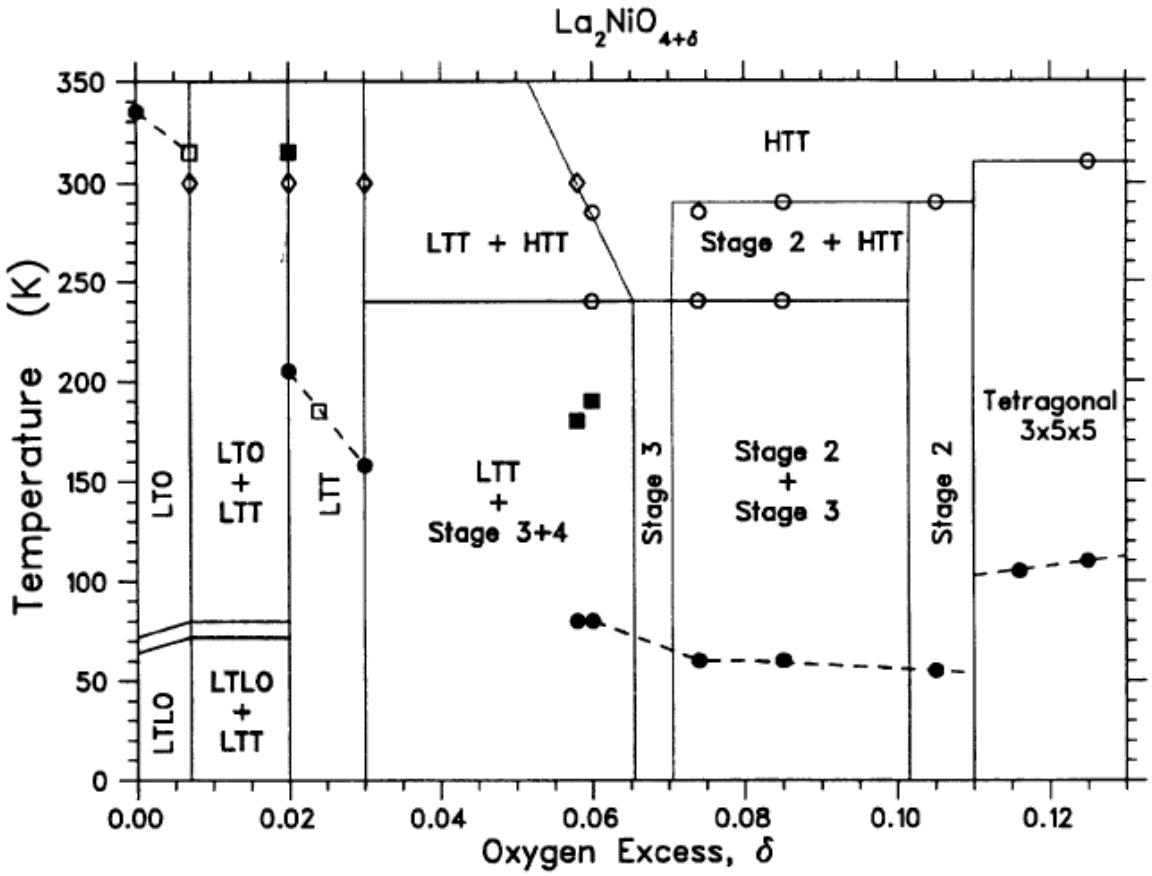

***Figure 1.20**: Revised phase diagram of the atomic structure of $La_2NiO_{4+\delta}$ as function of oxygen content, according to Tranquada et al.[142], accompanied with the Neel-temperature of the magnetic phase transitions (black spots and squares)*

As already mentioned before, the $La_2CoO_{4+\delta}$ oxide has been poorly studied, and consequently not only the atomic modulation but also the magnetic order remain unknown for low

temperatures in the non stoichiometric compounds. R. Le Toquin has given first results in the manuscript of his Ph. D thesis[8], indicating a loss of 3D magnetic ordering induced by oxygen intercalation until the value of δ = 0.19, and a possible re-arrangement for δ = 0.25 to antiferromagnetic state at low temperature (T_N = 36 K).

Chapter 2

Synthesis and qualitative characterizations of highly pure poly- and single-crystal samples of $La_2MO_{4+\delta}$ (M = Co, Cu)

1. Synthesis of polycrystalline La_2MO_4 (M = Co, Cu) T-phase

Polycrystalline samples have been synthesized for preliminary studies on one hand, *i.e.* in prelude to further investigations, and on the other hand as a first step to obtain starting materials for: *i*) the synthesis of T'-La_2CuO_4 polycrystalline samples (section 2.2) *ii*) the growth of large single crystals of La_2CoO_4 (section 2.3). $La_2CuO_{4+\delta}$ and $La_2CoO_{4+\delta}$ powder samples have been synthesized by the conventional technique of solid state reaction. The step of the experimental procedure consisting in mixing reactants has been carried out by two different techniques: grinding in mortar and sol-gel process. It has permitted to compare the two techniques for the synthesis of La_2MO_4 (M = Co, Cu) compounds, and to obtain products of high quality which are mandatory since they were then used as starting reactants for secondary synthesis or red/ox post treatments. The polycrystalline samples have been systematically characterized by X-ray powder diffraction experiments and the red/ox treatments have been followed by thermogravimetry.

1.1. Solid state synthesis

1.1.1. Generalities

High purity CuO and Co_3O_4 starting reactants were supplied by Aldrich with a minimum purity of 99.98% and 99.8% respectively (Aldrich Chemical Co., Milwaukee, WI, USA). La_2O_3 was supplied by Alpha Aesar with a minimum purity of 99.99%. For precautions, La_2O_3 reactant has been in all cases previously annealed at 1173 K for 12 h to decompose eventual traces of lanthanum hydroxide which has a tendency to materialize in presence of water from atmosphere. The powders should be stored in a dessicator. The products have been synthesized respectively by the two following chemical reactions:

$$La_2O_3 + CuO + \delta/2\ O_2 \rightarrow La_2CuO_{4+\delta}$$

$$La_2O_3 + 1/3\ Co_3O_4 \rightarrow La_2CoO_{4+\delta} + (1/6 - \delta/2)\ O_2$$

Powders have been finely grounded in proper ratios in mortar, pressed into pellets (diameter of 13 mm under 10 MPa) and then heated up several times in alumina crucibles in horizontal tubular furnace, with controlled atmosphere.

1.1.2. Synthesis procedure for T-$La_2CuO_{4+\delta}$

In a first step, reactants have been mixed in stoichiometric ratios and calcined at 1173 K for 12 hours. The resulting product has been pressed into pellets and sintered at 1373 K for 24 hours (heating and cooling rate of 10 K/min). This process has been systematically repeated 3 times to improve the grain size and to provide a better homogeneity to the final polycrystalline product. $La_2CuO_{4+\delta}$ can be synthesized under air, no special atmosphere is needed. The high purity of the as-obtained samples has been systematically checked by X-ray diffraction (section 2.1.3.1.). This synthesis procedure leads to the stoichiometric $La_2CuO_{4.00}$ compound.

The synthesis of T'-La_2CuO_4 is not possible by the solid state routine due to the high temperatures implied by this technique. However, it is possible to transform polycrystalline T-phase into T'-phase thanks to post synthesis treatments. This point is developed in section 2.2.1 of this chapter.

1.1.3. Synthesis procedure for $La_2CoO_{4+\delta}$

The synthesis of high quality $La_2CoO_{4+\delta}$ samples is more subtle than for the Cu compound, which is probably one of the reasons why there has been such few studies done on the Cobaltate. One main disadvantage of Cobalt is its elevated volatility at high temperatures. It prevents a successful synthesis from stoichiometric ratios, as explained in next section. Consequently, La_2O_3 and Co_3O_4 powders have been mixed with an overstoichiometric amount of Co of 3% in order to compensate the loss during high temperature treatment. The mixture has been firstly calcined at 1000°C for 12 hours before making pellets of it, in order to remove any traces of impurity. The resulting pellets have then been sintered at 1523 K for 24 hours under argon flux preventing the formation of $LaCoO_3$. Indeed, the latter phase stabilizes more favorably under atmospheric conditions. The sintering step under Argon has always been repeated 3 times for the same reasons as previously mentioned for the Copper

compound. But in contrary to the case of Cu, a phase separation occurs in the as-obtained polycrystalline $La_2CoO_{4+\delta}$ product between stoichiometric phase and oxygen rich phase which already possesses an overstoichiometric amount of extra oxygen of $\delta \sim 0.15$ (*c.f.* section 2.1.3.1). After several tries, it has been found that synthesizing pure stoichiometric $La_2CoO_{4.00}$ can be achieved thanks to a final reduction step, consisting in heating the sample up to 723 K under flux of H_2/Ar gas mixture (1:4) for 6 hours, followed by a slow cooling ramp of 0.5 K/min. The oxidation of polycrystalline $La_2CoO_{4+\delta}$ up to some values of $\delta \sim 0.20$ is also possible by heating the powder to 773 K under mixed O_2/Ar (1:2) flux for few hours, generally 2 or 3 hours are already sufficient for ~ 20 g of product. The final powders have been systematically checked by X-ray diffraction. It is worth noting that the phase separation occurring before the final oxidation or reduction step reveals a miscibility gap between stoichiometric and oxygen rich La_2CoO_4.

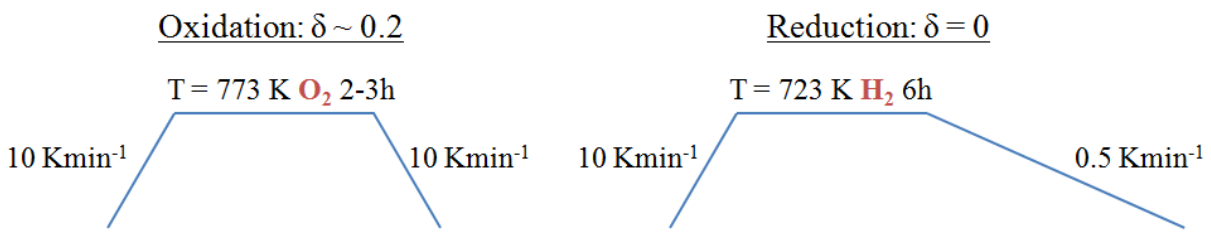

Figure 2.1*: Temperature ramps for oxidizing or reducing the powder samples.*

1.1.4. Difficulties encountered for the synthesis

First of all, for both $La_2CuO_{4+\delta}$ and $La_2CoO_{4+\delta}$ the use of La_2O_3 oxide as reactant is delicate due to its tendency to hydrolyze itself into $La(OH)_3$ accompanied with an increase of volume. If the atmosphere is not well controlled or if the reactant powders are not well weighted during the preparation, white spots of lanthanum hydroxide visible by eye appear soon after the synthesis. This effect is extremely difficult to control and has dramatic consequences on the final product since it modifies the amount of La cation which creates an imbalance in the stoichiometry: the La/M ratio will no longer be respected and the subsequent excess of transition metal will also lead to impurities (namely Co_3O_4 or CuO). In the case of La_2CoO_4, the lack of Lanthanum or the excess of Cobalt, can partially stabilize the $La_4Co_3O_{10}$ phase (Ruddlesden popper phase with n = 2), remaining at ambient temperature. The presence of $La(OH)_3$ is very constraining for the synthesis of single crystals. As explained in the

subchapter 2.3., rods of polycrystalline $La_2MO_{4+\delta}$ are used as starting materials; the presence of even few traces of lanthanum hydroxide results in pulverization of the crystal when released back to atmospheric condition after growth. This is why the La/M ratio is of first importance and must be very precisely respected. However, another fact enters into account in the case of $La_2CoO_{4+\delta}$: the high volatility of cobalt also responsible for stoichiometry mismatch. Cobalt partially evaporates at high temperatures and partially reacts with alumina crucible to form a surface layer of $CoAl_2O_4$ spinel recognizable by its blue color. Indeed, when taken out from furnace, the crucible becomes slightly blue, and completely dark-blue after several uses, until it breaks after a certain time of use. The subsequent loss of cobalt from the powder during the heating process has bad consequences on the La/Co ratio and must be overcome by adding an excess of cobalt in the starting material. Obviously, the longer the temperature treatment is, the higher the cobalt excess must be. After several tries, 3% molar excess of cobalt has been found to be appropriate for the temperatures steps described in the previous section.

The $La_2CoO_{4+\delta}$ compound is especially difficult to synthesis due to the mixed valence states of cobalt. Indeed, the +II valence state of Co is barely stable contrary to the +III valence state, and particularly at high temperature. However the stabilization of stoichiometric La_2CoO_4 necessitates exclusively Co +II for global neutrality reasons, whereas Co +III leads to $LaCoO_3$ perovskite compound. Consequently, any trace of oxygen will tend to turn Co +II into Co +III, creating the parasite $LaCoO_3$ phase during synthesis at high temperatures. This is why neutral atmosphere must be imperatively used during the process. In the present work, pure argon gas flux has been introduced constantly in the sample's environment during heating.

As a remark, the use of CoO oxide as starting reactant, containing only Co +II, should be avoided due to the same reasons as previously: the oxygen stoichiometry of this oxide is not well defined and partially decomposes into Co_3O_4 in presence of oxygen because of the transformation to highly stable Co +III. That is why, contrary to CuO, the synthesis of La_2MO_4 with CoO is difficult, Co_3O_4 being preferable.

1.2. Coprecipitation method

1.2.1. Generalities and experimental procedure

An alternative way to the grinding step of the ceramic routine for synthesis of Ruddlesden-Popper compounds is the so-called "sol-gel" method, a wet-chemical technique derived from

Pechini process. The principle is to solubilize reactants in water ("sol") and then to form an inorganic polymer of the mixture ("gel"), followed by a "firing" step during which all the impurities (hydrogen, carbon and nitrogen) are removed. The sol gel approach is a low temperature technique which allows a very fine control of the product's chemical composition. Moreover, the main advantage of this process is the extreme homogeneity of the final product provided by the solubilization and thus the complete mix of the starting element. This initial stage has systematically been followed by classical sintering in furnace at high temperature.

The sol-gel procedure starts by putting together in the solution La and Cu, or Co, with the proper ratios. It is possible to use nitrates of these elements as starting materials or carbonates, but in the latter case, few drops of nitric acid should be added for a total dissolution. For the sake of precision, the water contents of the starting compounds have always been determined by thermogravimetry in order to avoid weighting errors and to respect the La/Co ratio imposed by the wanted stoichiometry. When the reactants are dissolved, citric acid ($C_6H_8O_7$) and ethylen glycol ($C_2H_6O_2$) are added and provide the polymerization between La and M elements. The "sol" gradually evolves toward a gel-like biphasic system containing both liquid and solid phase which goes from discrete particles to polymer network. The polymerization is directly followed by a drying step accompanied by shrinkage and densification. Finally, the gel is fired by flame in order to remove all organic derivates of the polymer (CO_2, NH_3 …) until only ashes, made of micro-crystalline ceramic, remain. The last step of the synthesis, in common with the solid state process, is sintering at high temperature using the same experimental conditions than those described in the previous section. In short, sol gel process replaces the grinding step and provides a better homogeneity to the as-obtained mixture, but the whole synthesis remains solid state routine.

1.2.2. Results of sol gel tentative on La_2MO_4

The Lanthanum nitrate hexahydrate, $La(NO_3)_3.6H_2O$, was used as reactant in both cases; $Cu(NO_3)_2.3H_2O$ and $Co(NO_3)_2.6H_2O$ were independently chosen for the synthesis of La_2CuO_4 and La_2CoO_4 respectively. However the synthesis was only successful in the case of Cu compound whereas the resulting product for the Co compound undergoes a phase separation leading to a Co rich phase $La_4Co_3O_{10}$ and lanthanum oxide La_2O_3. $La_4Co_3O_{10}$ has already been observed as impurity for some tries of synthesis by solid state reaction (mentioned in section 2.1.1.4) when the cations were not in good proportions. But in the present case this

La/Co ratio was carefully respected and remained good after synthesis: the total amount of La in the final product, *i.e.* in both impurities, was calculated from X-ray diffraction results to be exactly in good ratio with Co (2:1). Several tries have been attempted with different experimental conditions and chemical concentrations but all led to phase separation, contrary to the La_2CuO_4 synthesis which was directly successful and completely reproducible, even for high amount of reactants. The quality of the obtained polycrystalline samples appeared to be even better than the samples resulting from solid state reaction (section 2.1.3.1).

1.2.3. Problem of sol gel method for synthesis of perovskite derivatives

It has to be noticed that one major problem arises with the presence of carbonates in the solution. Indeed, a carbonate group can replace a MO_6 octahedra in the structure thanks to the flexibility of the perovskite arrangement, and it has also been shown that this is even possible with borates[159]. Some planar molecules, tetrahedral or triangular like CO_3^{2-}, can partially substitute the M site. An intergrowth can thus occur like in $Sr_2CuO_2CO_3$ or the transition metal could be even totally replaced like in $LaKOCO_3$. The presence of CO_3^{2-} has obviously a drastic impact on the physical and chemical properties of the final compound.

1.3. Characterization of polycrystalline products by X-ray diffraction

X-ray powder diffraction experiments have then been carried out with a Bruker AXS D8-Advance diffractometer (Bragg-Brentano geometry). The wavelength of X-rays used was the $K\alpha_1$ of Copper (λ = 1.54056 Å). For $La_2CoO_{4+\delta}$ samples, a Sol-X energy dispersive detector has been used in order to reduce the background caused by fluorescence of Cobalt. For $La_2CuO_{4+\delta}$ samples, a linear Positional Sensitive Detector (Braun L- PSD) has been used for optimizing statistics. The latter detector induces an asymmetry of reflection profile at low angles due to axial divergence, but it can be corrected during refinement. Lebail and Rietveld refinements have been carried out with the software FULLPROF [160,161]. The strategies of refinements are not discussed for powder samples. They have been carried out for checking purity and quality; no structural considerations are drawn from these results, contrary to the results of single crystal diffraction, which are presented in the two following chapters.

1.3.1. *As-prepared La_2CuO_4*

As explained in the previous sections, La_2CuO_4 powder samples have been synthesized with two different methods for mixing starting reactants: grinding in mortar or coprecipitation method (sol-gel). For comparison, both types of samples have been characterized by X-ray diffraction with the same experimental conditions in the range of $5° < 2\Theta < 120°$. All reflections of both experimental diagrams could be refined with a single phase of *Bmab* space group with good agreement factors. It appeared that the two subsequent structural models were very similar, although the samples prepared with sol-gel process was of better quality. Therefore, La_2CuO_4 powders have been systematically synthesized the same way for further experiments.

The experimental X-ray diffraction profile of the sample prepared by sol-gel method is plotted in red on Figure 2.2. It is superimposed with the theoretical profile (black line) ensuing from Rietveld refinement; the blue line below the diagram represents the difference between observed and calculated profiles. Table 2.1 gives the resulting structural model. Both atomic positions and sizes of the unit-cell are in agreement with literature and correspond to pure phase of stoichiometric La_2CuO_4.

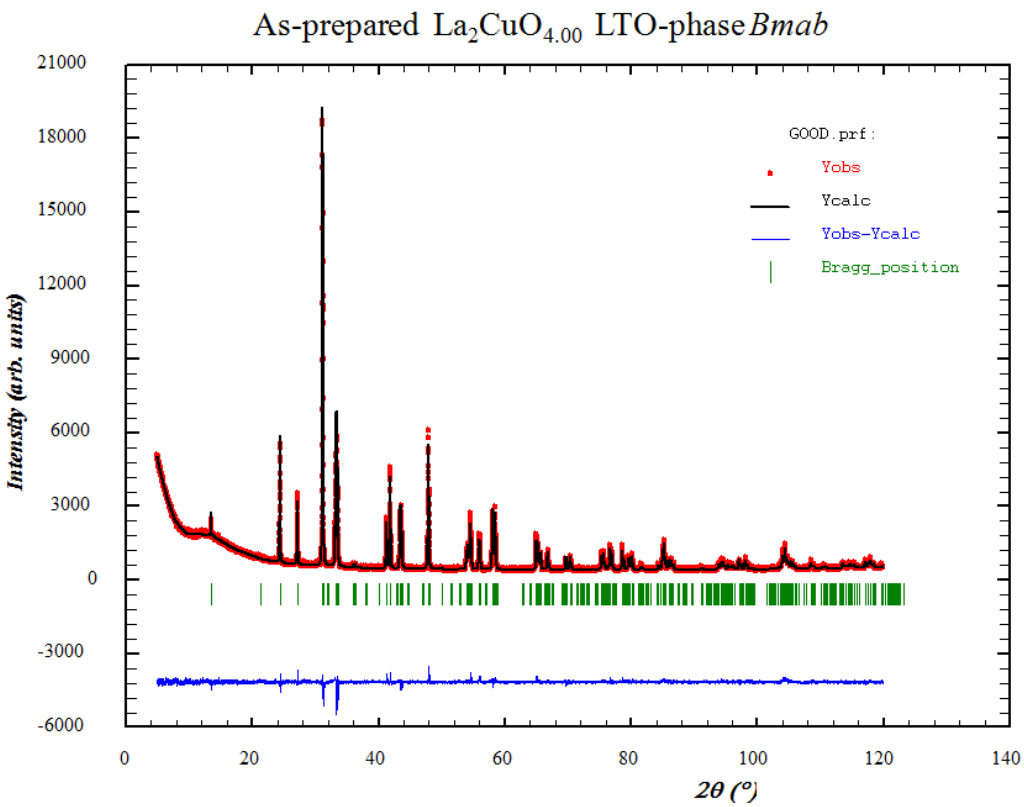

***Figure 2.2**: Rietveld refinement of X-ray diffraction pattern of La_2CuO_4 synthesized by sol-gel method. These experimental data have been refined with the LTO model (Bmab space group).*

Table 2.1: Structural model of La_2CuO_4 resulting from the Rietveld refinement shown above.

Atom	*x/a*	*y/b*	*z/c*	*Occ*	*β iso*
La	0	0.995(15)	0.3615(1)	2	0.218(8)
Cu	0	0	0	1	0.168(4)
O (eq)	¼	¼	0.990(2)	2	0.187(6)
O (ap)	0	0.043(7)	0.181(1)	2	0.225(7)

a = 5.34(5) Å, b = 5.39(2) Å, c = 13.12(2) Å, $\alpha = \beta = \gamma = 90°$. Space group: *Bmab*. Wavelength: $Cu_{k\alpha 1}$ = 1.54056 Å. Accordance factor: R-Bragg factor = 3.93 %, R_F factor = 2.47 %.

The superimposition of X-ray diagrams of the two types of samples is plotted on Figure 2.3, focused on 3 particular reflections: the reflection (113) is the most intense of the whole dataset and the interval between (020) & (200) is directly proportional to orthorhombicity. The profiles of the Bragg reflections of the sample prepared by coprecipitation (in red) are sharper than the other sample (in black), revealing a better quality of the product obtained by sol gel method, *e.g.* grain sizes, homogeneity, crystallinity… Indeed the profile in black shows a broader dispersion at the base of the peaks. The full width at half maximum of (113) is 0.078(9)° for the reflection in red, and it is of 0.091(5)° for the one in black.

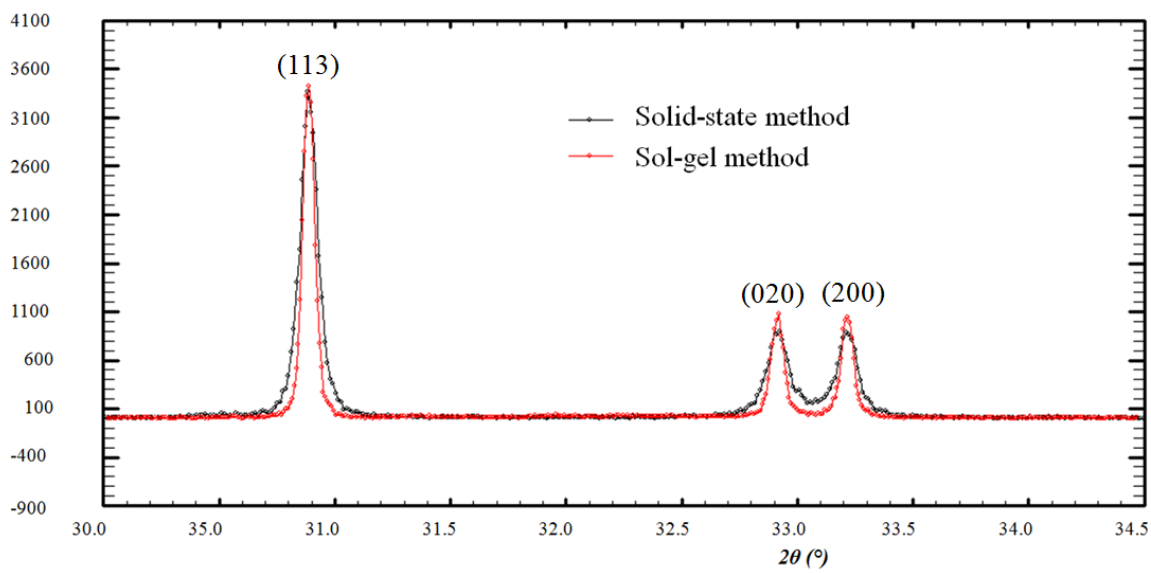

***Figure 2.3**: Superimposition of the experimental X-ray diagrams of La_2CuO_4 prepared by solid state route and by sol-gel method, zoomed on 3 particular reflections: the (113) which is this most intense, and (020) & (200) which depict orthorhombicity (they are single peak in the case of tetragonal lattice).*

1.3.2. *As-prepared $La_2CoO_{4+\delta}$ by solid state reaction*

This section concerns the first characterization of the crude $La_2CoO_{4+\delta}$ samples obtained without any oxidizing or reducing post treatment. It corresponds to the products obtained after the three steps of sintering at 1523 K. Qualitatively, the experimental X-ray diagram reveals a phase separation at RT between two distinct phases: *i)* stoichiometric phase (*Bmab* space group) and *ii)* oxygen-rich phase (*Fmmm* space group). The plot of the difference between experimental data and Rietveld refinement, carried out with the two phases, is shown on Figure 2.4. Since X-rays do not allow to determine precisely the oxygen content of interstitial site; O_{int} occupancy has been fixed to δ = 0.15 with regards to previous works[12]. This phase separation always occurs if no reducing gas is flushed in furnace during the last sintering step. Moreover, it is astonishingly very well reproducible.

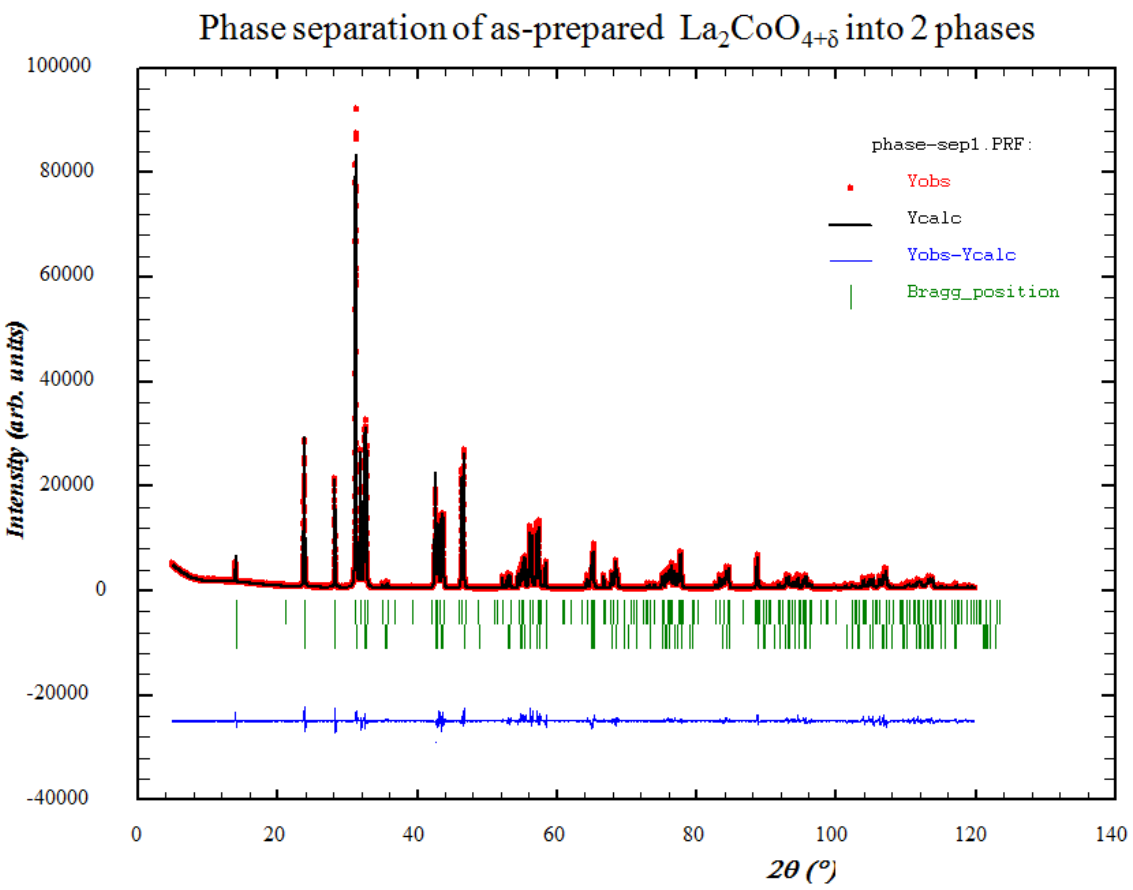

***Figure 2.4**: Rietveld refinement of X-ray diffraction pattern of $La_2CoO_{4+\delta}$. A phase separation occurs between stoichiometric (Bmab space group) and an oxygen rich phase (Fmmm).*

Table 2.2: Structural models of the two phases resulting from Rietveld refinements.
Phase 1: Stoichiometric La_2CoO_4

Atom	*x/a*	*y/b*	*z/c*	*occ*	*β iso*
La	0	0.996(8)	0.360(5)	2	0.221(8)
Co	0	0	0	1	0.174(2)
O (eq)	¼	¼	0.989(7)	2	0.187(4)
O (ap)	0	0.048(6)	0.180(1)	2	0.247(2)

a = 5.46(2) Å, *b* = 5.60(3) Å, *c* = 12.65(4) Å, *α* = *β* = *γ* = 90°. Space group: *Bmab*. Wavelength: $Cu_{k\alpha 1}$ = 1.540562Å. Accordance factor: R-Bragg factor = 4.41 %, R_F factor = 3.23 %.

Phase 2: Oxygen rich $La_2CoO_{4+\delta}$

Atom	*x/a*	*y/b*	*z/c*	*occ*	*β iso*
La	0	0	0.361(4)	2	0.227(6)
Co	0	0	0	1	0.169(5)
O (eq)	¼	¼	0	2	0.180(3)
O (ap)	0	0	0.180(8)	2	0.250(4)
O (int)	¼	¼	¼	0.15	0.197(9)

a = 5.48(3) Å, *b* = 5.52(9) Å, *c* = 12.63(4) Å, *α* = *β* = *γ* = 90°. Space group: *Fmmm*. Wavelength: $Cu_{k\alpha 1}$ = 1.540562Å. Accordance factor: R-Bragg factor = 5.54 %, R_F factor = 4.01 %. O_{int} occupancy has been fixed to 0.15 according to previous work[12].

A zoom on the (113), (020) and (200) reflections indexed with both phases is shown in Figure 2.5. The difference of the cell parameters is clear. The stoichiometric phase shows a stronger orthorhombic lattice distortion. Moreover, *c* parameter is a bit smaller for the oxidized phase (not shown on the figure).

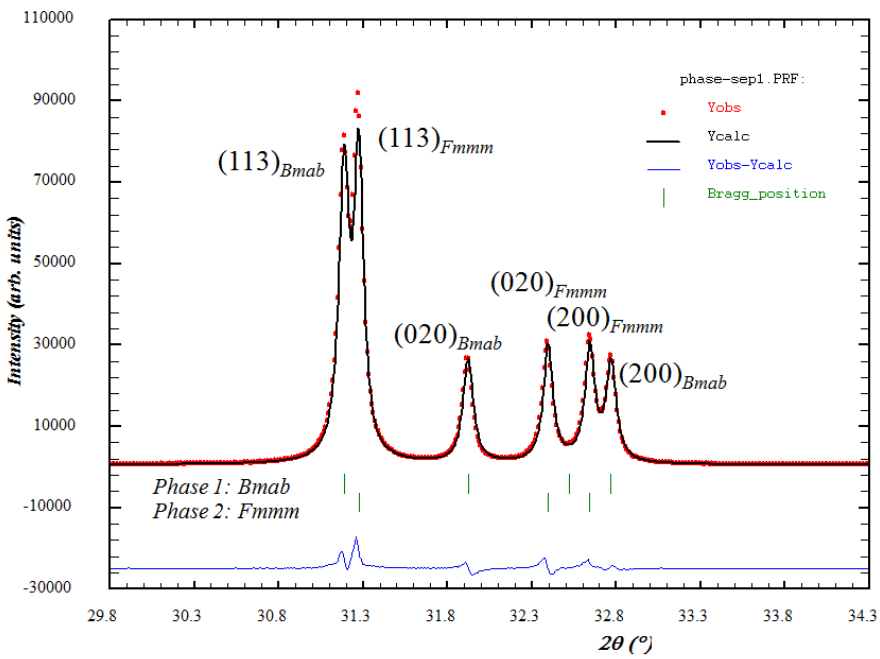

***Figure 2.5**: Zoom on some characteristic reflections refined with the structural model of table 2.2, showing the phase separation between Bmab and Fmmm phases.*

1.3.3. *Spontaneous oxidation of $La_2CoO_{4.00}$ under air*

Pure stoichiometric compound has been obtained by reduction treatment on the as-obtained products (*c.f.* section 1.1.3). Its experimental X-ray pattern could be successfully refined with a single phase model of *Bmab* space group (purely stoichiometric LTO phase, *c.f.* Table 2.2 phase 1). Figure 2.6 *a*) shows the typical portion of the X-ray powder diffraction pattern, zoomed on the characteristic reflections (113), (020) and (200), showing the single phase character of the product (in comparison with Figure 2.5); only the reflections belonging to the *Bmab* phase are present. But it appears that this phase is not stable under atmospheric conditions. Indeed, it has the tendency to self-oxidize partially already after few hours of simple exposition to air: the stoichiometric phase partially convert into *Fmmm* phase, yielding to coming back of phase separation. Spontaneous oxidation[9] of the stoichiometric polycrystalline sample has been measured *in situ* under simple exposition to air at RT. Figure 2.6 *b*) shows the evolution of these reflections with time, indicating emergence of the less orthorhombic phase of *Fmmm* space group, corresponding to the phase 2 of Table 2.2 (section 1.3.2).

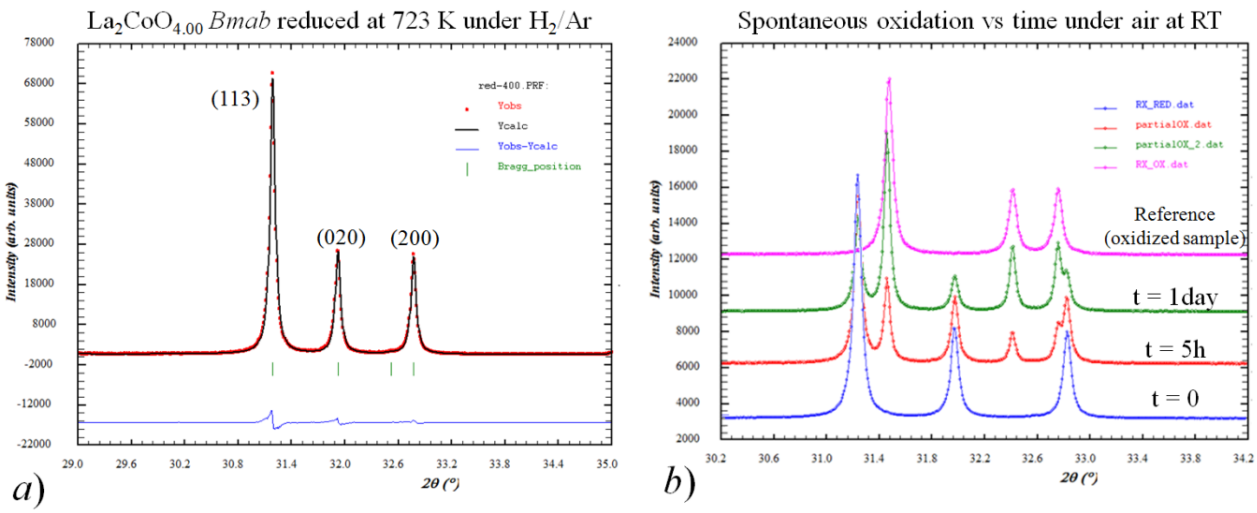

***Figure 2.6**: a) plot of X-ray powder diffraction pattern of purely stoichiometric $La_2CoO_{4.00}$, zoomed on few characteristic reflections; b) phase separation occurring in the stoichiometric compound with time, measured in situ under air, revealing spontaneous oxidation of the compound already after few hours with a discontinuous transformation from Bmab to Fmmm symmetry.*

The profile of pure *Fmmm* phase (on the top), obtained by oxidizing post-treatment, is presented as reference on the Figure. Although traces of *Bmab* phase still remains, even after one week, the amount of stoichiometric phase always decreases with time. Hypothetically the stoichiometric phase would completely transform into oxygen rich phase in infinite time. The results indicate that La_2CoO_4 does not undergo a continuous variation of cell parameters with

oxidation, but on the contrary, a miscibility gap divides the powder into two different phases of different oxygen contents, yielding discontinuous transformation from *Bmab* to *Fmmm*. It can be assumed that the shell of grains composing the powder (grain boundaries) gets richer in oxygen whereas the core remains stoichiometric. With time, oxygen rich phase propagates deeper in grains.

The spontaneous slow oxidation of La_2CoO_4 at room temperature by topotactic reaction is remarkable and invokes questions concerning *i*) the structural aspects of the reaction mechanism and *ii*) the oxygen ionic migration pathway across the three-dimensional lattice at low temperatures. The cobaltate compound is the only oxide of the $La_2MO_{4+\delta}$ family to show this high reactivity at RT. This phenomenon must also be taken into account for single crystals which have a tendency to self oxidize at the surface.

2. Synthesis of La_2CuO_4 T'-phase

2.1. Synthesis of polycrystalline samples from T-phase, followed *in situ* by thermogravimetry and *ex situ* by X-ray diffraction

Synthesizing La_2CuO_4 by usual solid state routine always stabilizes the T-type structure. However, it is possible to transform T-phase into T'-phase through an intermediate oxygen deficient state of pseudo-S-phase, as reported by Chou *et al.*[13]. Conceptually, the process consists of taking off oxygen atoms from the structure, creating vacancies and oxygen disorder, then re-introducing oxygen at relatively low temperature, yielding stabilization of T' instead of T-type structure. To achieve this conversion, two steps have been performed: *i*) first, reducing the starting T-La_2CuO_4 powder under H_2/He mixed atmosphere (1:20) for at 600 K with an isothermal step of 1 hour (temperature ramp number 1 on Figure 2.7); *i*) re-oxidizing the intermediate product under mixed atmosphere O_2/He (1:1) at 623 K with an isothermal step of 30 min (temperature ramp 2 on Figure 2.7). This procedure has been followed by thermogravimetry. The starting, intermediate and final products have been subject to X-ray diffraction experiment.

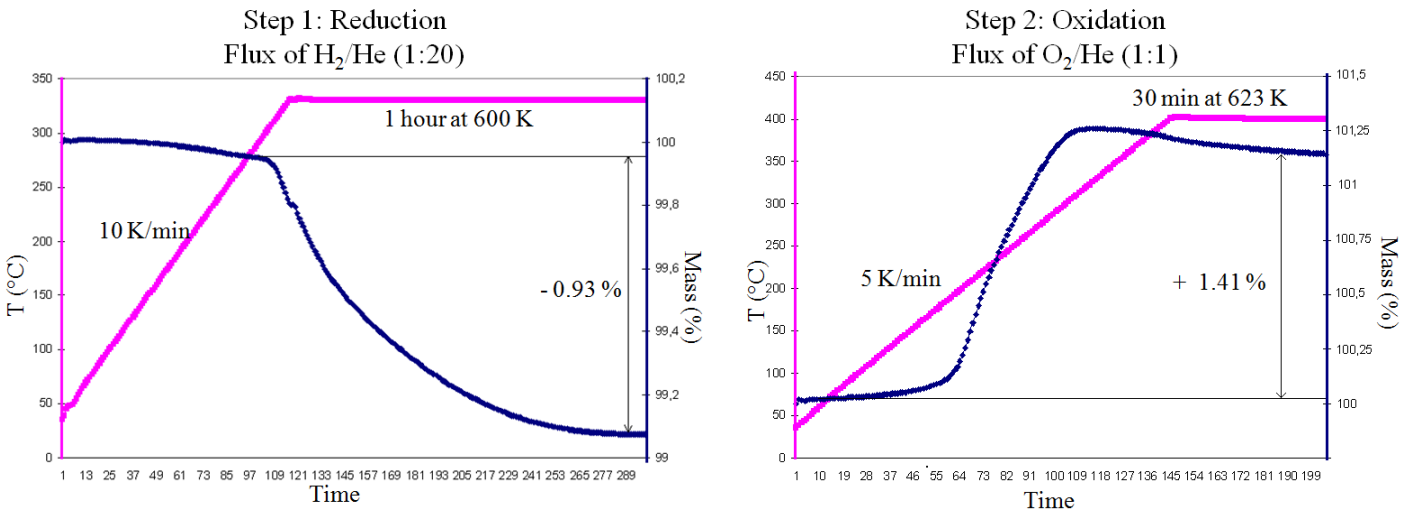

***Figure 2.7**: Thermogravimetric studies in two steps: i) reduction of T-La_2CuO_4 to form an intermediate oxygen deficient phase La_2CuO_{4-x}; i) re-oxidation of the intermediate phase and formation of T'-La_2CuO_4. The line in clear blue corresponds to temperature evolution and the line in dark blue corresponds to the loss of weight in %.*

The starting sample was pure polycrystalline T-La_2CuO_4 obtained by the experimental procedure described in the section *1.1.2*. The reducing step of the process yielded to a loss of 0.93 % of the original mass. Considering that departure of oxygen atoms from the sample is the only cause of weight loss, the stoichiometry can be assumed to change to La_2CuO_{4-x} with $x \sim 0.33$, according to the following chemical reaction:

$$La_2CuO_4 + x\,H_2 \rightarrow La_2CuO_{4-x} + x\,H_2O\uparrow$$

The experimental X-ray powder diffraction pattern of this intermediate state (Figure 2.8) shows a very strong background, the profiles of Bragg reflections are broad, reflecting the bad quality of the powder. The crystallinity must be very low. These data have been refined only with the Lebail method ($\chi^2 = 2.09$) with a single phase of monoclinic unit-cell corresponding to the following cell parameters: $a = 5.66(6)$ Å, $b = 5.69(7)$ Å, $c = 12.04(4)$ Å, $\alpha = \beta = 90°$ and $\gamma = 83°$. Tentatives of Rietveld refinements have been carried out, but the convergence could not have been reached. The X-ray data profile possesses similarities with a typical diagram of S-type structure (*c.f.* Chapter 1, section III.4.) but could not be refined with its corresponding structural model. Obviously, lacks of oxygen create vacancies, implying a structural disorder. The monoclinic character of the unit-cell suggests a strong distortion of the structure.

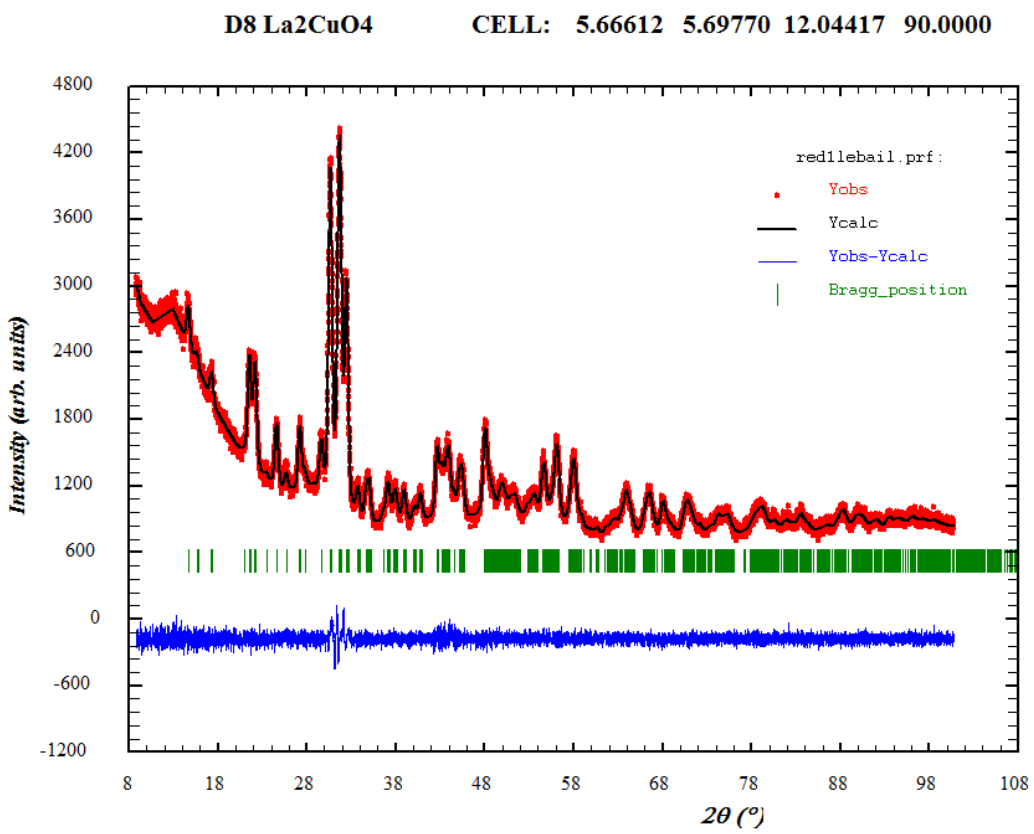

***Figure 2.8**: Plot of the Lebail refinement of the intermediate oxygen-poor $La_2CuO_{3.7}$. (χ^2 = 2.09)*

When re-oxidized, the intermediate oxygen deficient phase re-absorbs oxygen atoms, which re-orders the oxygen lattice. According to the experimental results of the thermogravimetric measurements, the gain in mass is of 1.41 %. As before, if we assume that only the uptake of oxygen by the sample from the atmosphere is responsible for mass changing, according to the following chemical reaction:

$$La_2CuO_{4-x} + \frac{x+\delta}{2} O_2 \rightarrow La_2CuO_{4+\delta}$$

the calculations result in a stoichiometry of $La_2CuO_{4.05}$. The X-ray powder diffraction profile clearly indicates the presence of a secondary phase in the final product. But when reflections of this impurity are excluded, the rest of the experimental profile can be refined with good agreement factors (Figure 2.9) with the structural model of the T'-phase (table 2.3), space group *I4/mmm*, corresponding to a unit-cell of following cell parameters: $a = b = 4.01(6)$ Å, $c = 12.50(1)$ Å. The impurity could not be identified.

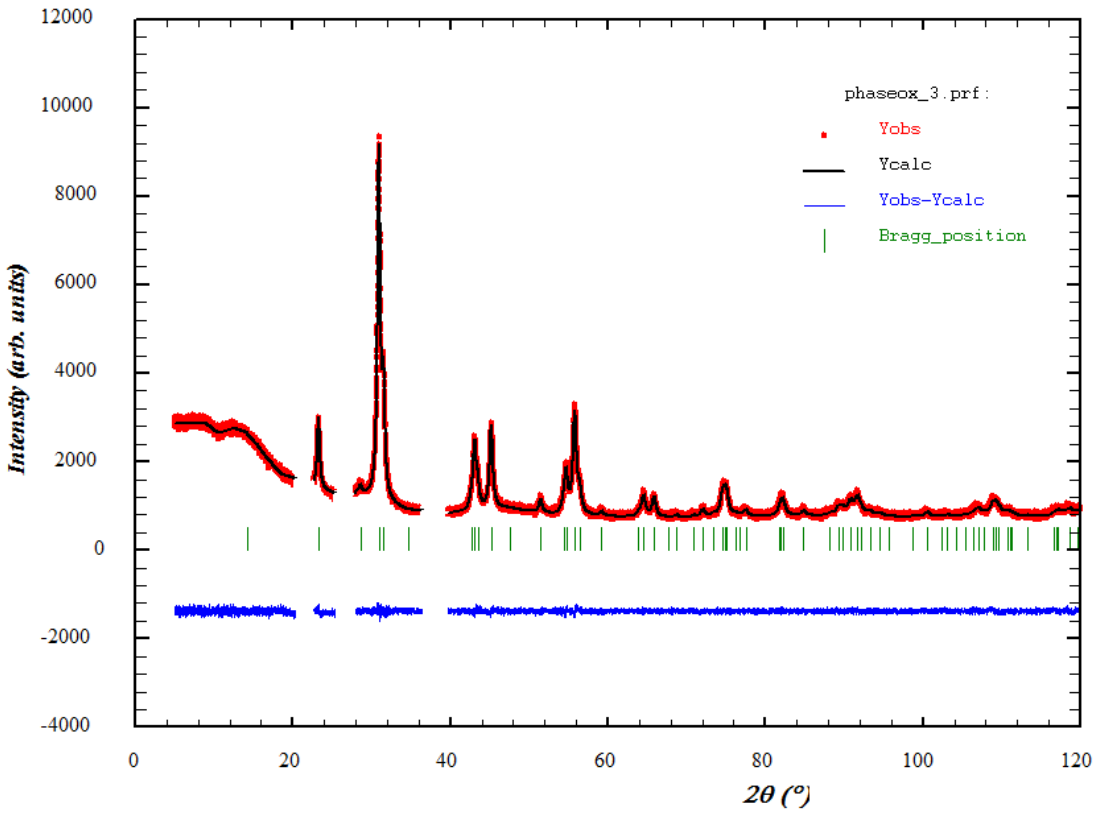

***Figure 2.9**: Plot of the Rietveld refinement of X-ray diffraction pattern of the final product after re-oxidation of pseudo S-phase. The resulting structural model is show on table 3 below. Different regions have been excluded for suppressing Bragg reflections of impurities. The resulting atomic structure corresponds to the T'-phase*

Table 2.3: Structural model of La_2CuO_4 resulting from the Rietveld refinement shown above.

Atom	*x/a*	*y/b*	*z/c*	*Occ*	*β iso*
La	0	0	0.351(4)	2	0.097(6)
Cu	0	0	0	1	0.087(6)
O (eq)	½	0	0	2	0.124(8)
O (int)	½	0	½	2	0.097(6)

$a = b = 4.01(6)$ Å, $c = 12.50(1)$ Å, $\alpha = \beta = \gamma = 90°$. Space group: *I4/mmm*. Wavelength: $Cu_{k\alpha 1}$ = 1.54056 Å. Accordance factor: R-Bragg factor = 2.98, R_F factor = 2.14.

The final powder is of higher quality than the intermediate phase, but it still remains rather bad: the background is lower, but reflections are still broad. The full width at half maximum (FWHM) resulting from the fit of the most intense reflection (103) take the value of 0.446(1)° as shown on Figure 2.10. It is a very high value in comparison with the starting sample of T-phase for which the FWHM is of 0.078(9)° (five times less).The transformation from T to T' structure for La_2CuO_4 by the red/ox process lowers the crystallinity and induces structural defects. However, on the phenomenological point of view, the structural phase transitions between the different polymorph states, which differ only by oxygen position in the unit-cell

of their structures, enhance the role of oxygen in the stability of these compounds. It also implies different oxygen sites of close energy, and high oxygen mobility (these aspects are discussed in chapter 5, section 1).

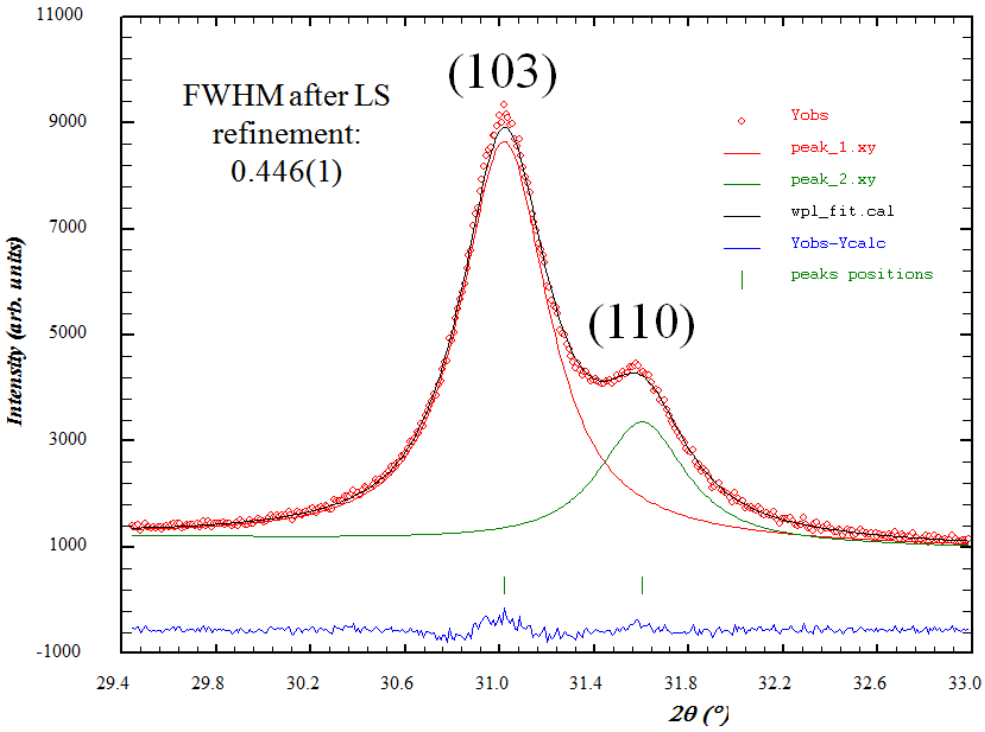

***Figure 2.10**: Fitting profile of the reflections of highest intensity; the resulting full width at half maximum takes the value of 0.446(1)°.*

2.2. Synthesis of single crystal samples by molten salt technique

Single crystal samples of La_2CuO_4 with T'-structure have been exclusively provided by Prof. R. Schöllhorn from the Walther Meissner Institute (BAdW, Garching, Germany). A collaboration has been agreed, and he kindly offered several batches of samples for structural investigations. The samples have been synthesized by molten salt technique which can be performed at rather low temperature in comparison with usual techniques. It has permitted to obtain microscopic single crystals. The procedure was the following: La_2O_3 & Cu in stoichiometric proportions were mixed, grounded and put in an alumina crucible together with an eutectic mixture of KOH/NaOH. The crucible was kept at 623 K under different gas flux for two weeks. The melt was then quenched to room temperature by removing the crucible from the furnace. It has to be specified that this technique is mainly used to synthesize polycrystalline samples which can be isolated by dissolving traces of hydroxides with distilled water. But here, very small single-crystals were found on the border of the crucible. If the

process is performed under air, crystals of T-phase are formed, but under Argon flux crystals of T'-phase can be obtained.

Nevertheless, this technique shows few disadvantages. First, it produces various unavoidable impurities (*e.g.* Cu and La oxides, La hydroxides). It also yield incorporation of Al^{3+}, Ni^{2+}, Na^{+}, K^{+}, or vacancies into the material (presumably on the metallic sites), coming from crucible and reactants. Moreover, the suitable conditions for successful reaction are difficult to attain (reactant quantities, reaction temperature, atmosphere around the melt, time of addition of reactants, etc.). Finally, the small size of the isolated single-crystals (as low as 50 µm) is constraining for further analysis. For instance, it disables neutron diffraction experiments. Despite these inconveniences, this technique has permitted to synthesize high quality pure single crystals of T'-La_2CuO_4 for the first time, allowing single crystal diffraction experiments.

2.3. Compositional characterizations of T' single crystal samples by SEM

The *as grown* T'-La_2CuO_4 samples consisted of small slats, typically from 50 to 200µm large and ~1-5µm thick. They were mostly interpenetrated to one another like sand roses. Experimental investigations have been carried out with a SEM (Scanning Electron Microscope) to characterize the chemical composition and to detect eventual traces of impurities. Samples have been visualized by BSE imaging (Back Scattered Electrons) and their chemical compositions have been checked by EDX (Energy Dispersive X-ray spectroscopy). Heavy elements (high atomic number) scatter electrons more strongly than light elements (low atomic number), and thus appear brighter in the image. BSE are used to detect contrast between areas with different chemical compositions. Figure 2.11 shows the BSE picture of a sample composed of several single crystals stuck together; the different shading reveals the non-homogeneity of the chemical composition.

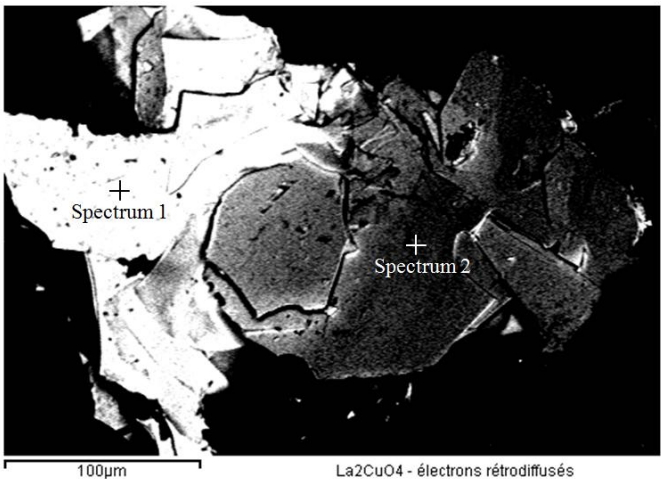

Spectrum 1

Element	% mass	% atomic
O	16.68	58.71
Cu	15.65	13.86
La	67.67	27.43

Spectrum 2

Element	% mass	% atomic
O	15.22	48.62
Al	6.07	11.49
Ni	1.17	1.15
Cu	23.05	18.54
Mo	1.02	0.54
La	53.47	19.67

***Figure 2.11**: Back scattered electron picture of sample composed of several single crystals stuck together. The non-homogeneity of the distribution of chemical element is indicated by the brightness.*

In fact it appears that, the darkish zone contains impurities whereas the clearest one is the pure La_2CuO_4 phase. It has revealed the partial and non-homogenous contamination of samples: traces of Ni and Al have been observed by EDX in some samples although pure La_2CuO_4 crystals were present in majority in the batch. The major impurities where identified as Ni^{2+} which stabilizes the La_2NiO_4 compound in T-phase. Nevertheless, several pure T'-La_2CuO_4 samples have been isolated. They have been used as a starting sample for structural analysis carried out with synchrotron X-ray diffraction experiments. The results are presented and discussed in the chapter 4 and 5.

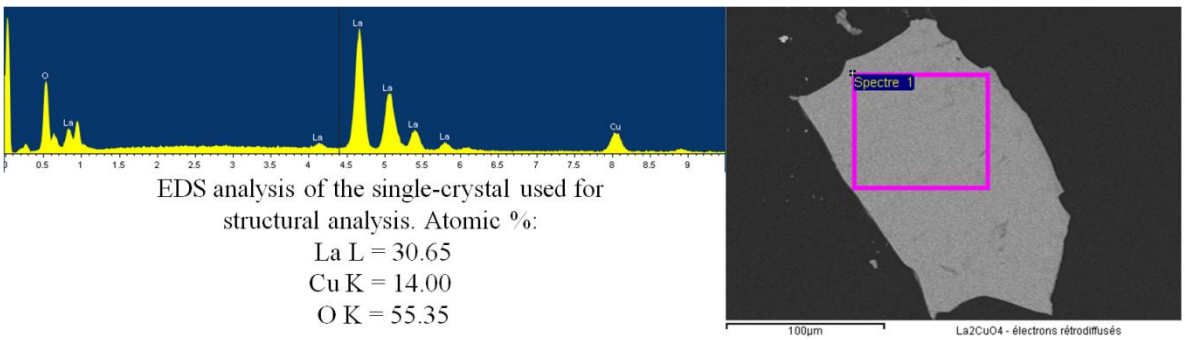

***Figure 2.12**: EDX Analysis of a single crystal of T'-La_2CuO_4*

3. Growth of $La_2CoO_{4+\delta}$ single crystal samples

3.1. Choice of adapted synthesis procedure

High quality single crystals of well defined stoichiometry are essential for investigating intrinsic properties of condensed phases. This is particularly true for the study of compounds owing anisotropic features ensuing from layered structures. Besides, samples for fundamental studies must be free of defects, grain boundaries and impurities, which have drastic impacts on the physical properties. Since all experimental results will depend on the quality and on the purity of the samples taking care of the synthesis is crucial, and is probably the most important step in the whole procedure. Growth of high quality single crystals is not an easy task and must be carefully considered in order to be successful. The process of crystallization involves the ordering of ions which take up regular positions at the liquid/solid interface. The initial stage is the nucleation and is followed by a continuous deposition on the crystallite faces. It can be described as a dynamic equilibrium between the fluid and the crystal. As explained hereafter, many parameters enter into account in the process, interfering together non-linearly, and thus resulting in a rather complex context. However, overcoming these difficulties is mandatory for achieving the desired experimental studies. For instance, neutron scattering experiments on single crystals necessitate large bulk samples due to the weak interaction between neutrons and matter.

Crystal growth of Ruddlesden-popper phases and derivatives has been carried out by several techniques and has been the object of well documented reviews[162,163,164,165]. Most of the first reported studies consist of slow, well-controlled cooling procedures, carried out on high temperature solutions (fluxes), which have generally led to millimetric size plate-shaped crystals, usually detached from clusters in which crystals of other phases are also present. However, single crystals grown by a flux method always show several drawbacks: *i*) contamination due to the chemical reaction between the melt and the crucible material, such as Al_2O_3 or gold, or due to the incorporation of materials present in the molten phase; *ii*) low-homogeneity of the *as grown* crystals since the composition of the liquid phase changes as the crystal grows; *iii*) and the major disadvantage: it provides only small crystals with typical thickness of the *c*-axis less than 0.1 mm for La_2MO_4 samples. Consequently, the flux technique should be avoided if possible for these compounds, other existing methods being preferred. Although the Czochralski method[166,167,168] (also called “pulling method”) is famous in the field of crystal growing to be a powerful technique for synthesizing large crystal samples of basic semiconductors, metal alloys and synthetic gemstones, it unfortunately does not provide the synthesis of phases which melt incongruently, *i.e.* from melts of different

composition than the solid phase; which is the case of La_2CoO_4 compound. Until now, the most common technique yielding synthesis of large single crystal bulks (centimetric size) of transition metal oxides and insulating compounds remains the floating zone (FZ) method with optical furnace apparatus[169,170,171,172,173]. Not only does this procedure provides suitable thermodynamical conditions stable enough for fast crystal growth of big samples, but it is also the first one that allows to grow compounds which melt incongruently thanks to the so-called Travelling Solvent Floating Zone technique (TSFZ)[174,175]. This *modus operandi* has been evidently chosen for the synthesis of the starting samples.

After hundreds of studies, many La_2CuO_4 and La_2NiO_4 single crystals have been synthesized by different groups of research, and nowadays synthesis procedures have been optimized for both. However, the experimental growth procedure for high quality La_2CoO_4 single crystals remains unspecified. According to literature, only three single crystal samples have been obtained until now. Among them, one was an oxygen deficient sample[89] and the two others had different extra oxygen contents[93,10], one was pure δ = 0.15 and the last one was multiphasic. The synthesis of the cobaltate compound remains complicated because of the same reasons mentioned for polycrystalline synthesis, *i.e.* high volatility of cobalt, formation of $LaCoO_3$ impurity, non-stoichiometric character of the oxygen content, etc. Besides, the phase diagram of La_2CoO_4 has been only poorly explored[176,177]. Owing to these obstacles, the first tries of growth remained unsuccessful and it appeared that, the panel of possibilities for growth conditions being too wide, the entire time dedicated for this thesis could even be insufficient for obtaining usable samples. In order to be productive, a fruitful collaboration has been established with Prof. Hosoya, from the Center for Crystal Science and Technology at the University of Yamanashi (Kofu, Japan), who already grew such crystals for one of the three studies cited above. After two stays in this institute and thanks to the helpful experience of Prof. Hosoya, high quality single crystal samples of $La_2CoO_{4+\delta}$ have been grown, permitting in one hand to develop an experimental procedure for synthesizing this compound, and on the other hand to perform further single crystal studies.

3.2. Image furnace

Different zone melting techniques have been developed, both applied to horizontal or vertical configurations[169,173]. The vertical floating zone method is the "cleanest" method where the molten zone is formed by contactless heating and held between two solid rods by its own surface tension. This crucible free method avoids any contamination material and is often

applied if the melts have high chemical activity or high-melting temperatures. Besides silicon, a broad variety of other substances such as metals, intermetallics, and oxide compounds are grown by the FZ method[178]. Indeed, large crystals of transition metal oxides, superconductors, colossal magnetoresistance materials and frustrated magnets can be obtained with this technique, which is indeed also famous for synthesizing single crystals of ruby quite easily[172]. The basic difference of most oxide compounds compared with metals is their low electrical conductivity. Moreover, oxides exhibit much smaller heat conductivities than metals and intermetallics. In the case of metals and semiconductors high frequency heating coils are often used to create the molten zone. Conversely, for insulating materials, infrared image furnaces are applied which enable a focus of the radiation by gold-coated ellipsoidal mirrors, into a narrow band around the material. Powerful lamp(s) located at the focal point of the mirror(s) generate(s) light which heat the substance placed at the common image point of the mirrors, up to temperatures high enough to melt polycrystalline oxides. Nowadays, temperatures of at least 3000°C are easily reached. Therefore, optical heating with diverse modifications of image furnaces has become a well-established method for FZ growth of oxides. Three types of optical floating zone furnace are commercially available, with one, two or four ellipsoid mirrors. They all employ halogen or Xenon arc lamps of different power as energy source. A double-mirror configuration has been used for the present study, being a good compromise between the single mirror model which has a limited power, and the four-mirror, one for which adjusting lamps positions for ideal focusing is extremely delicate..

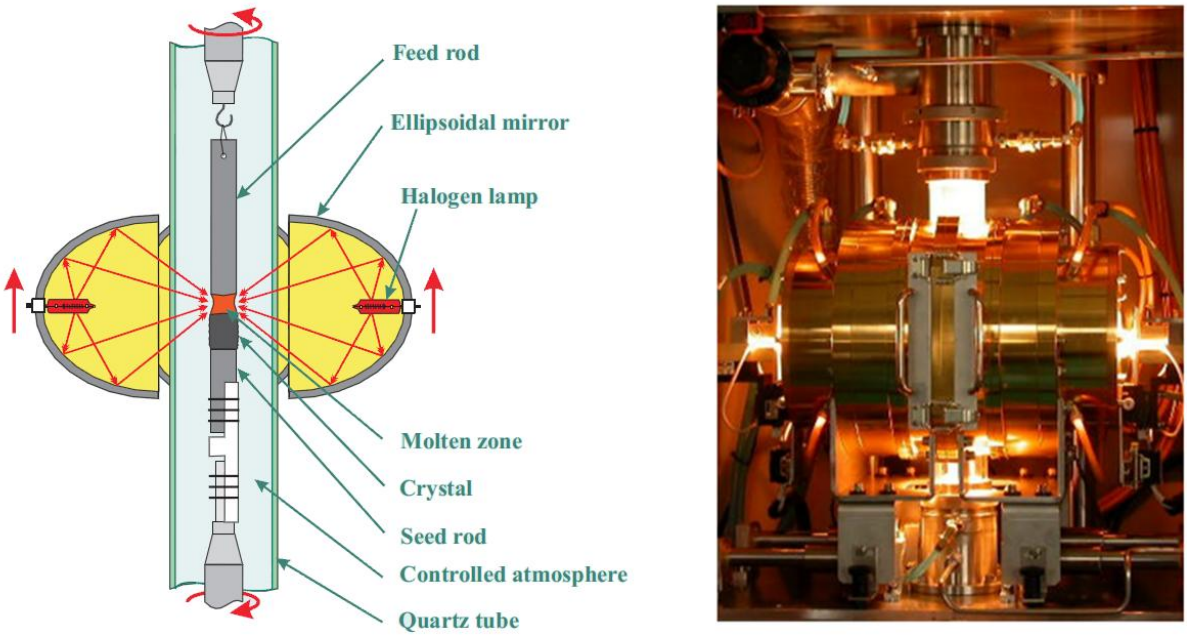

***Figure 2.13**: Scheme of optical furnace apparatus, accompanied with a picture of the inside of the furnace used in the present work.*

The growth process takes place inside the quartz tube (*c.f* Figure 2.13) which allows using inert, oxidizing or reducing atmospheres and pressure up to 5 bars. Movements of the mirrors and rotations of both rods (called “seed” and “feed” rods) can be controlled independently. The setup is equipped with an infrared camera giving a possibility of *in situ* observation permitting to control the growth process by eye. The melt’s temperature during growth can be precisely set by adjusting the power of the lamps, but it cannot be measured directly. Contactless measurement of the temperature by pyrometry is practically impossible as the light reflected from the floating zone competes with those emitted. Hence, stability of the molten zone is usually controlled by visual observation and manual adjustments of the lamps’ power.

The principle of crystal growing with image furnace is rather simple. The first step is to melt the starting material, usually named “solvent” for the growth of incongruent melt compositions, then to connect, *via* the liquid phase, the feed and seed solid rods made of polycrystalline powder pressed and pre-annealed (*c.f.* “rod preparation” section). The solvent is thus located in between the two rods which rotate in opposite directions. When the molten zone is approximately stable and when suitable conditions are reached, the zone can be moved through the cylindrical feed rod in order to precipitate the solid phase on the seed. This can be achieved either by moving the lamps upward, or by moving the whole system ‘rod-solvent-rod’ downward, depending on the type of apparatus. Thus, the melt undergoes solidification on the seed, and if the moving rate is adapted, together with thermodynamic conditions, a crystalline phase can be grown. Usually, in a first step, the seed will move much faster than the feed. Then gradually, a slim neck will form. This process is usually called “necking” (Figure 2.14).

Necking is critical to obtain large single crystals since it permits to support the formation of a single domain yielding a favorable initiator for growth. Then, gradually decreasing the speed of the seed rod permits to enlarge the diameter of the domain and thus to grow a large single crystal. If possible it is preferable to use a piece of single crystal as seed rod (it is usually the product of previous tries). This permits to start the growth directly on a single grain, providing a better nucleation.

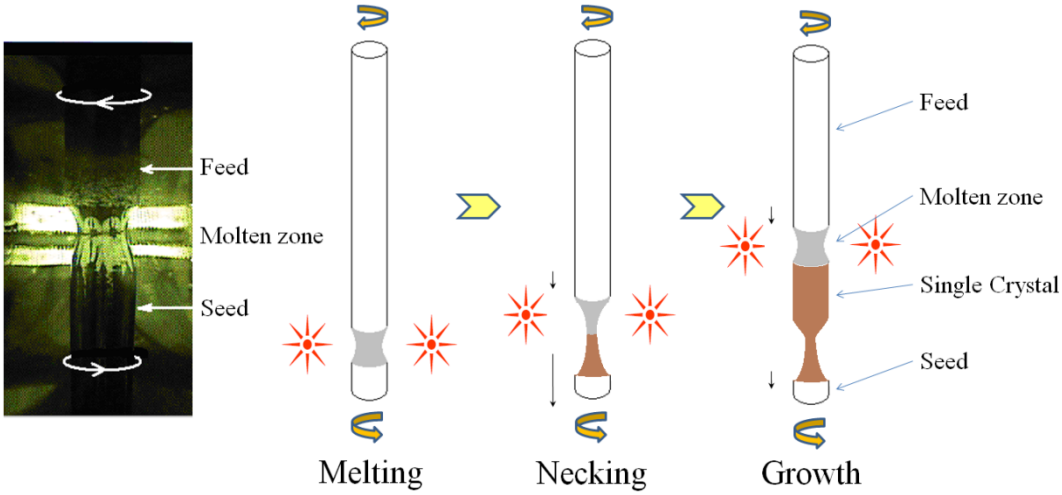

***Figure 2.14**: General process for single crystal growth with optical furnace; the necking permits to form a single grain which serves of substrate for the growth.*

Temperature gradient in the crystal remains a very important parameter and must be controlled with precaution. The stability of the floating zone is of outmost importance for the crystal growth processes, which does not only mean a constant height, but also a proper crystal–melt interface's shape, chemical composition, and homogeneity of the melt. These aspects are detailed in the "key process parameter" section.

3.3. Travelling Solvent Floating Zone technique for incongruent melting phases

Within the 'temperature versus composition' phase diagrams of binary compounds, the particular conditions for which the system possesses no degrees of freedom constitute the invariant points. They can be of different types and among them two particular ones, eutectic and peritectic points, correspond respectively to congruent and incongruent melting, designated by the numbers 1 and 2 on the Figure 2.15 below, which represents the idealized phase diagram of La_2O_3-CoO binary system.

If the wanted material can be molten without decomposition, *i.e.* monophasic (congruent melting point), the FZ method can be used without any specific solvent. In this case the compositions of both, liquid and solid phases, are identical and a single crystal can be obtained directly from the melt of stoichiometric polycrystalline compound. In the latter case, the whole system keeps the same composition when cooling down, which corresponds to the vertical lines (in blue) on the phase diagram. But the TSFZ method enables successful growth of materials which do not melt congruently, *i.e.* which cannot directly solidify from their own

melt. For instance, a phase separation occurs when La_2CoO_4 melts, before the complete liquid state (point marked by number 2 on Figure 2.15). Thus, if the liquid is stoichiometric, La_2O_3 and other phases will be stabilized when cooling down, preventing the formation of La_2CoO_4. In order to avoid this, a solution (flux) of different composition is used between the feed material and the seed crystal.

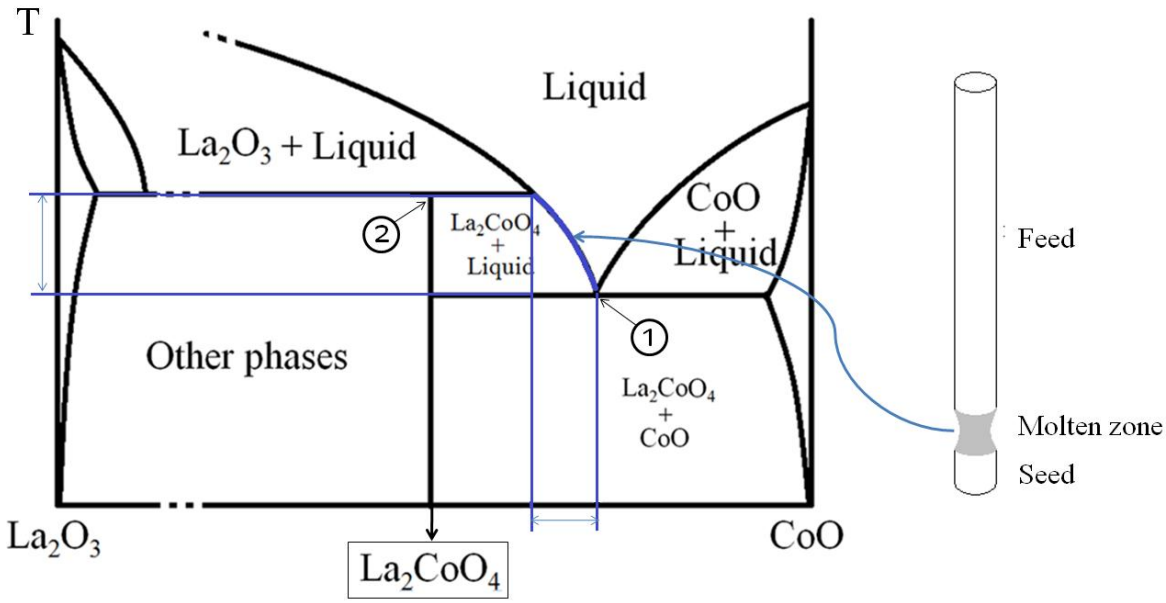

***Figure 2.15**: idealized qualitative binary phase diagram of La_2O_3-CoO binary system, the mark number 1 corresponds to congruent melting point and the number 2 to incongruent melting. The proportions of constituents and the temperature of the molten zone should be comprised in the ranges pointed by the blue lines.*

The processing temperature has to be kept well below the decomposition point of stoichiometric La_2CoO_4, and an excess of CoO (solvent) must be supported to the melt. During the process, the feed material is dissolved in the solution zone and diffuses to the seed/solution interface. When the solution (floating) zone is translated, solidification, in the form of single crystal, occurs at the seed/solvent interface and new feed material dissolves continuously at the feed/solvent interface. Ionic migration and exchanges between the solid and liquid phases occur constantly during the process, sustaining the composition of the melt.

Technically, the extra amount of Co in the molten zone can be introduced by two distinct ways: either continuously by “self adjusting flux” process or by direct pre-enrichment of the molten part. The self adjusting flux consists in pre-doping the feed rod with an excess of CoO powder, supplying the solvent during the growth.

The different steps of the technique are summarized in Figure 2.16 and can be listed as follows:

- Melting the extremity of the feed rod and connecting the two rods (step 1)
- Moving the zone upward trough the feed in order to supply extra Co to the melt. The composition of the melt changes and the temperature should be simultaneously decreased. Solidification of α phase. (step 2)
- The last step consists in stabilizing the molten zone at the lower temperature possible/at the lowest possible temperature (would be better). Solidification of La_2CoO_4 (step 3).

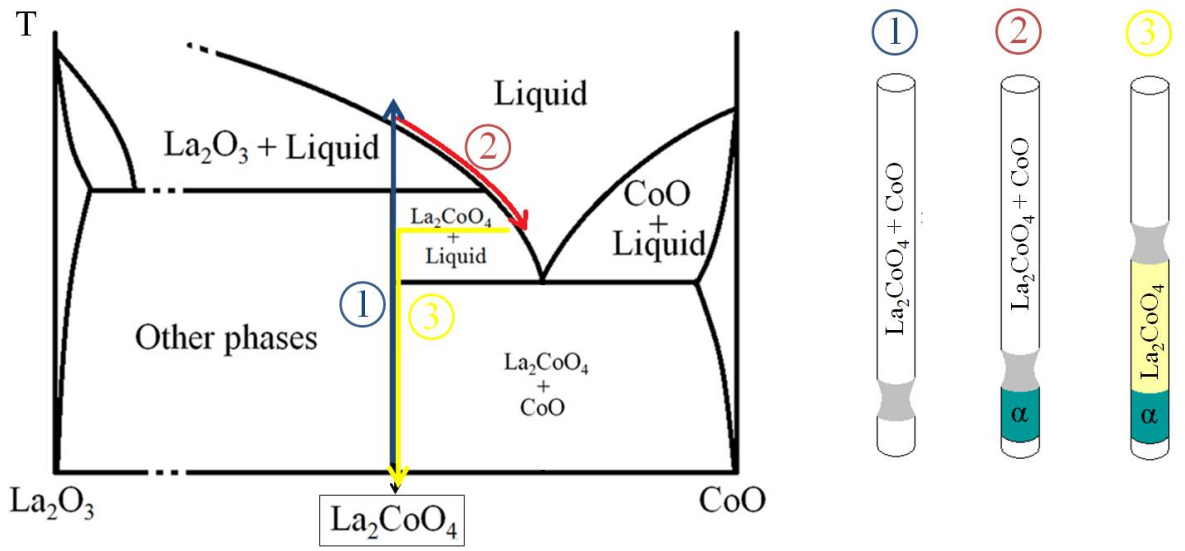

***Figure 2.16**: Self-adjusting flux technique for TSFZ method. 1) the molten zone is created from the stoichiometric composition; 2) the extra Co present in the feed gradually enter the melt while the zone moves upward, an impure phase is solidified on the seed; 3) composition of the melt self-adjusts to the concentration yielding solidification of the incongruent phase.*

Nevertheless, this technique has the disadvantage to involve the creation of an unwanted phase, named α on the Figure, appearing before reaching the appropriate region of the phase diagram. And this primary phase can generate new grains that are not favorable for the growth of high quality single crystals, and usually prevents it since they are not good initiators for crystallization of the wanted phase. In order to get rid of such inconveniences, the melt can be directly pre-enriched with solvent (CoO) prior to the process in order to start immediately with the correct concentration and temperature. For this, it suffices to prepare a third rod composed of stoichiometric La_2CoO_4 mixed with an appropriate extra amount of Cobalt oxide, then to cut a thin slice of it (few millimeters) and finally to place it at the interface

between the feed and seed rods (the quantitative details for successful growth of high quality La_2CoO_4 single crystals are given in section 3.5). Therefore, the initial molten zone would have the specific composition for direct stabilization of La_2CoO_4, *i.e.* on the border in blue on the phase diagram shown on Figure 2.15, between the "liquid" area and the "La_2CoO_4 + liquid" area. With this method, the melt is initially placed at the good point of the phase diagram, the incongruent melting phase is solidified from the first moment of the crystal growth, and thus no primary phase precipitation occurs. So, if the temperature is kept constant during process, if the composition of the melt remains stable, and if precipitation of the material leaves the liquid at a constant point of the phase diagram, the crystallization of a single phase with the appropriate conditions can be obtained. Thus, during the growth, solvent composition is maintained unchanged because the solute exhausted by the crystallization is continuously migrating with the molten zone, which is why it is called the "travelling solvent" technique.

3.4. Key process parameters

Synthesis of single crystals with high structural perfection by FZ/TSFZ techniques implies a deep understanding of all the physical processes occurring in the molten zone and at the interfaces with the rods. The quality of the crystals strongly depends on the stability of the molten zone which is extremely delicate and needs careful attention. Since thermodynamical conditions always oscillate, even slightly, the system must be under constant surveillance during the whole process. The growth can suddenly collapse for many reasons. Convection patterns arise in the melt and strongly affect the solid-liquid interface curvature, as well as the segregation and corresponding elements distribution in the growing crystal. Those phenomena play a significant role in the crystal perfection. Most of the effects have been already simulated with mathematical models and confirmed experimentally for various materials and geometrical configurations[179,180]. In spite of the general theory for all the processes occurring in the molten zone and near the solidified interface, crystal growth of every individual compounds requires more experience and knowledge of the crystal grower. This is based on general principles, rather than an exact mathematical simulation and process automation.

Experimental details corresponding to the growth of $La_2CoO_{4+\delta}$ single crystals are given in the next section, here, only the qualitative aspects of general cases are developed.

3.4.1. High quality feed rod

The feed rod is made of polycrystalline powder pressed and annealed prior to be used in optical furnace. For a successful crystal growth, the rod should obviously be dense, uniform, and have the right composition. Uniformity of the rod, *i.e.* nearly constant diameter and density are critical to keep the molten zone stable. Homogeneousity must be high and chemical composition accurately respected, otherwise impurities will form within the crystal bulk. In addition to the fact that it affects the crystal's purity, it can lead to dramatic consequences. For instance, in the case of La_2MO_4, a slight excess of La_2O_3 is already sufficient to completely disintegrate the crystal when cooled down to RT after a few hours of exposition to air. Indeed, formation of lanthanum hydroxide implies the increasing of the volume which breaks the final product.

During the crystal growth, some components with low melting point in the molten zone might penetrate along the cavities or grain boundaries of the feed. This penetration can be attributed to the capillary phenomenon through these cavities among the fine particles constituting the feed rod. A fraction of the solvent penetrates throughout the feed up to the cooler part of the rod until it reaches a height where the temperature is lower, yielding solidification. The penetration of the solvent into the rod slowly modifies the composition of the molten zone, which destabilizes the system. Usually, this change will not terminate the growth unless the penetration is so serious that ring-like ditches appear, due to the formation of other phases on the feed. These ditches usually have a disc-like structure as shown below:

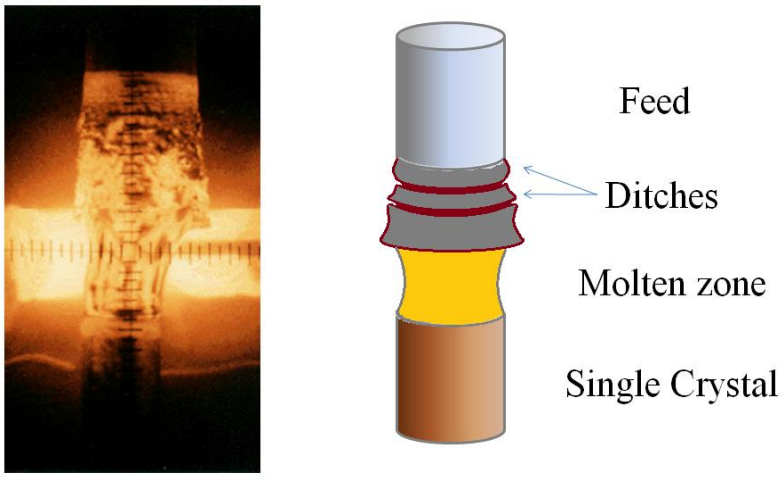

***Figure 2.17**: Penetration of solvent into the feed rod, responsible of ditches.*

Ditches would suck the solvent into the feed rods, thus preventing the smooth traveling of the molten zone and amplifying the composition mismatch. In the worst case, the feed rod breaks at the position of a ring. The penetration can be controlled by using a well-sintered feed rod

and by decreasing the temperature gradient of the molten zone as low as possible. Lowering the melting temperature and thus increasing the density of the feed can be achieved by introducing an extra amount of solvent in the feed, like for the self adjusting flux technique[181].

3.4.2. Solvent ratio

The self-adjustment can yield the precipitation of extra components as inclusions into the grown crystal or as a residue on the crystal surface. But, preparing the starting materials of the molten zone in such way that it has initially the proper solvent concentration, can shorten the time to reach a stable growth, and avoid impurities. The major problem is to find the correct ratio of solvent that the melt should contain. The composition and amount of solvent determines the starting power of lamps for crystal growth. Nevertheless, the quality of the *as grown* crystals is closely related to the quantity of solvent. With too much solvent the crystal can be grown smoothly at a relatively low power, but with poor quality. With too little solvent a high power is necessary and the solvent needs more time to self-adjust to the proper composition. In the worst case, the proper composition is never reached before the end of the crystal growth. This amount varies a little depending on the diameter of the rod, the density of both the feed and seed[182].

3.4.3. Sharpness of the temperature gradient

As shown in Figure 2.18, a steeper temperature gradient reduces the penetration, which leads to a clear boundary between the molten zone and the feed rod. This parameter is extremely important, not only for chemical compositions with low melting point or serious penetration, but also for volatile compounds which tend to evaporate before entering the melt, creating an imbalance of stoichiometry. Moreover, a sharp temperature gradient can greatly lift the supersaturation level and thus enhance the driving force for the growth.

For the floating zone technique with optical heating the temperature gradients in the sample are mainly determined by the optical geometries of the furnace, lamp features and sample characteristics, such as optical and thermal coefficients of the solid and liquid states. Temperature fields are also determined by the reflectance, transmittance and emmitance of the material in relation to the radiation spectrum and to thermal conductivities, dimensions, convection flows and to the latent heat of melting/solidification transition. The sharpness of

the temperature gradient in generally improved by covering part of the quartz tube with Aluminum foil or by covering part of the ellipsoidal mirror with Indian ink.

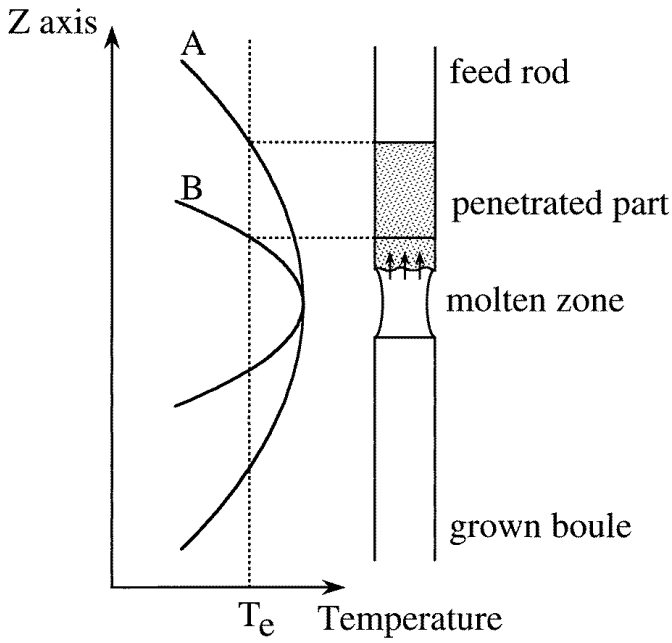

Figure 2.18: *A steeper temperature gradient reduces the penetration of solvent in the feed rod*[183].

Among all the parameters driving the temperature field, the size and the position of the lamps are probably the most important criteria. A small defocusing of the lamp with respect to the focal point of the ellipsoid (~1 mm) strongly changes the light distribution and the corresponding temperature profile in the sample. Hence, for a successful crystal growth, the position of the lamps, which regulates focusing, must be systematically checked and corrected prior to experimental procedure. Not only the size of the filament inside the bulb of the lamp, but also their orientation with respect to the system, have an impact on the steepness of the molten zone. Indeed filaments are longitudinal which results to an anisotropic temperature gradient, as shown on figure 2.19.

Clearly, the second solution presented on the down part on the Figure 2.19 is the best one for reducing the temperature distribution along *z, i.e.* toward the direction of the rods[184]. The lamps should be installed in such way that filaments are oriented along *y*-axis for the steepest temperature gradient. The smaller the filament is, the steeper the temperature distribution will be. Various types of lamps of different power are commercially available; the choice of an appropriate one must be done wisely, in accordance to the characteristics of the material to grow.

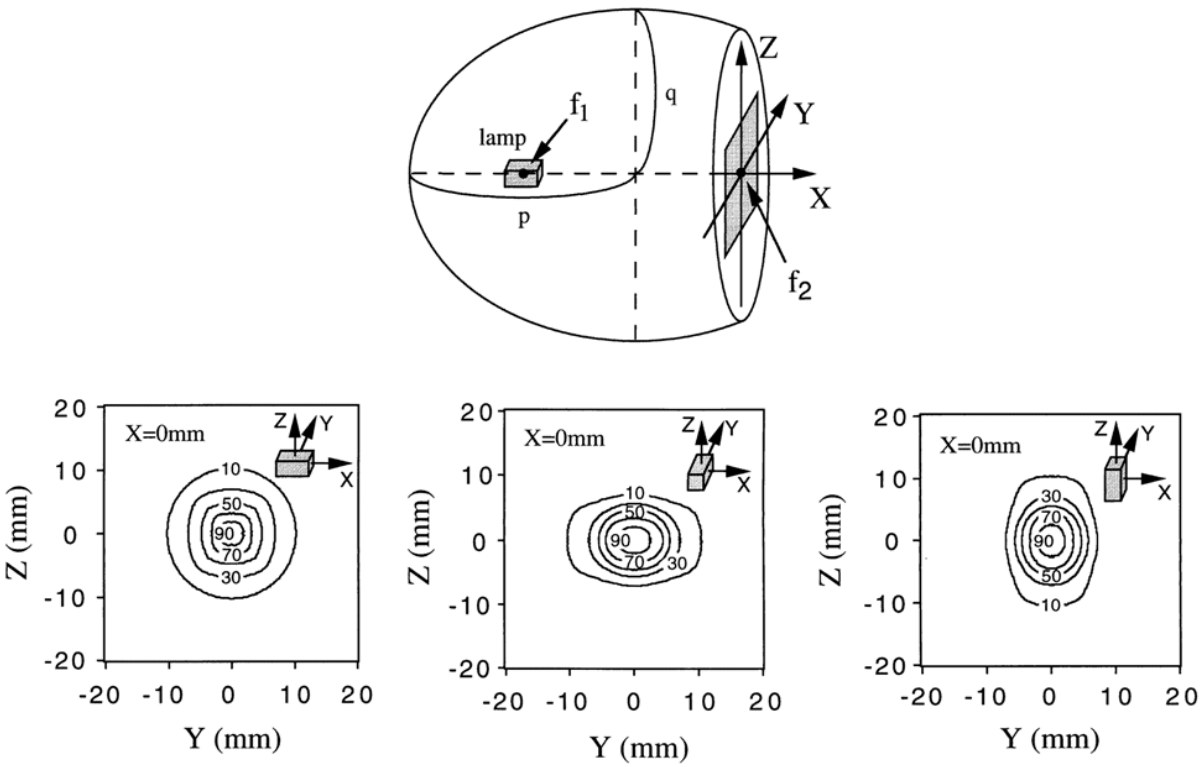

Figure 2.19*: Isothermal curves of temperature gradient around the molten zone depending on the orientation of the filament of the lamp*[183].

3.4.4. Growth rate and power of lamps

The growth rate, *i.e.* the speed at which the molten zone moves through the feed, and the power of the lamps, driving the temperature, are interdependent. Equilibrium must be attained in order to adjust the stability of the growth. All the techniques implying solidification from molten phases have a common limitation: melt supercooling, which destroys the morphological stability and leads to cellular and dendrite structures in the final product. TSFZ method needs a particularly slow travel rate of the zone, typically of few millimeters per hour. Due to the high concentration of the solvent in the molten zone, the growth rate should be much smaller than in the case of congruent melting materials in FZ technique. Indeed, for incongruent melting the compositional difference between rods and melt causes a solute diffusion at the feed/melt interface. The driving force for this diffusion is supersaturation, which is proportional to the temperature gradient at the solid-liquid interface. The diffusion process takes place very slowly, thus limiting the growth implying a slow motion of the molten zone toward the feed. Otherwise, constitutional supercooling occurs at the solidification interface; secondary phase precipitations and generation of new grains arise.

Both the growth rate and the power level must be kept as constant as possible[185]. From the phase diagram, one can see that any change of power change, *i.e.* temperature change, directly alters the composition of the liquid phase. Reaching equilibrium needs time and the molten zone has the tendency to self-adjust and to slowly evolve. During the stabilization, the two solid/liquid interfaces can expand inside the melt, and after some time, even enter in contact if temperature is too low. As a result, the feed rod, which is hung by a simple wire, will shake and deviate from the aligned configuration. Hence, the feed will be partially out of focus, its temperature will lower, which will amplify the solidification. If the power is not slightly increased on time, the melt will rapidly drop and rods will be disconnected. Conversely, if the power is too high, the melt will not be viscous enough and its surface tension will not hold the liquid anymore, resulting/leading once more to a drop… once more in a drop and following issues. It is possible to reconnect the rods afterwards, but the whole process has to be re-started from the beginning (*i.e.* melting, necking, growing, *c.f.* Figure 2.20).

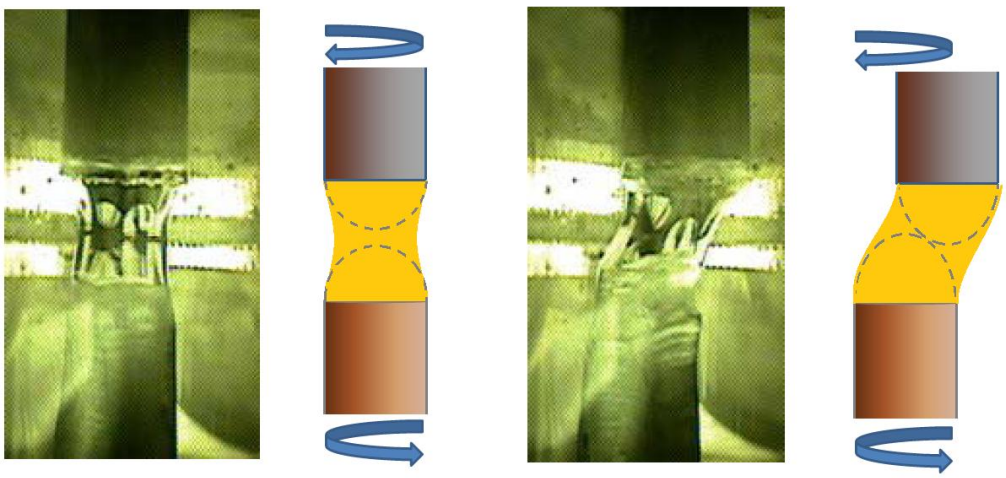

Figure 2.20*: Left: ideal configuration, Right: de-focusing of the feed induced by contact between seed and feed*

3.4.5. Molten zone shape and dynamics

The floating zone is not a stagnant drop of melt. Several types of free and forced convections may occur in the molten zone[186], affecting significantly the shape of solid-liquid interfaces as well as the zone length. Fluid motion influences strongly the stability of the crystallization process, solute and temperature. Various papers have been devoted to the theoretical and numerical simulation as well as experimental studies[187,188] of these phenomena aiming to elucidate the best conditions for an optimal crystal growth process. The theoretical convection

patterns of the fluid inside the molten zone are shown on Figure 2.21, for static and rotating rods. Rods counter-rotation is essential to homogenize the molten zone.

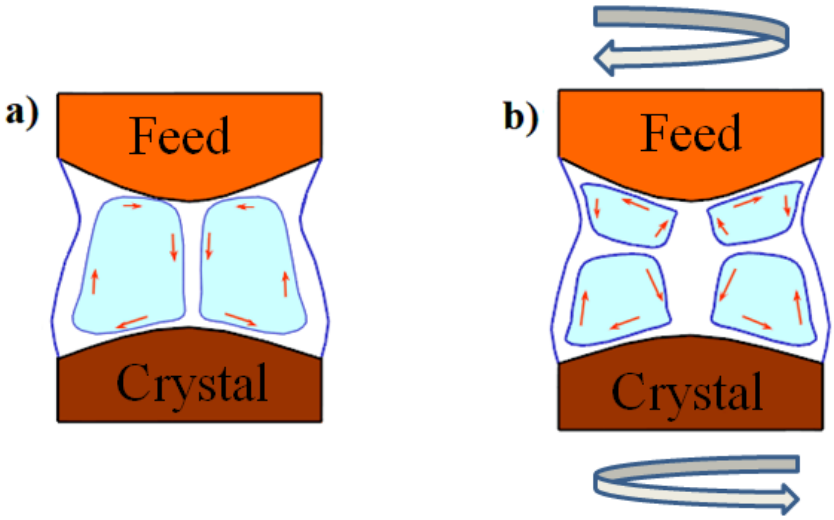

Figure 2.21*: The schemes of convectional flows in the molten zone: (a) natural convection, (b) forced convection driven by crystal and feed rotation*[187,189,190].

Experimental investigations of the mass and heat transfer induced by fluid motion are very complicated due to the high temperature and to the high chemical activity of most melts. Moreover these parameter strongly depend on the chemical composition. This is why crystal growing is so complex: each case is particular and requires a complete description for the optimization of the growth.

The outer molten zone shape is the only visible characteristic of the FZ growth process. Its curvatures correspond unambiguously to the bending of the solid-liquid interfaces. Finding the relations is a key to control the growing stability and the subsequent perfection of the obtained crystals. For instance, a too thin molten zone will induce a decrease of the solvent concentration in the melt which tends to create impurities. Conversely, a too thick molten zone will increase the amount of solvent in the melt which will modify the stoichiometry of the final product. The following scheme illustrates these phenomena.

The ideal case corresponds to a straight molten zone, increasing its stability by favoring the constancy of solvent concentration.

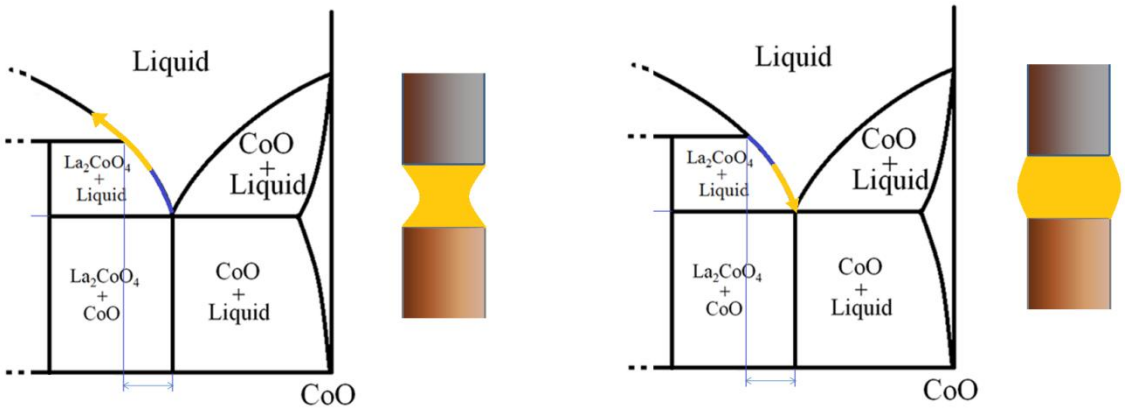

***Figure 2.22**: Influence of thickness of the molten zone on the solvent concentration.*

However, it has to be accepted that a part of luck comes into play for a successful single crystal growth; it can be very complicated to find the appropriate conditions for stable molten zone due to the non-linear character of the whole system. Controlling all parameters is not an easy task, and several tentative are usually needed for it. The list of parameters entering in game is non-exhaustive, and some effects cannot be handled. For instance, the shape and stability of the molten zone is also strongly influenced by the crystal growth direction, which can deviate from the linear trend. So many criteria drive the growth together that, usually, several tries are necessary in order to understand and control the synthesis of a specific compound.

3.4.6. Gas flowing

Since the system is enclosed into a cylindrical quartz tube, the atmosphere in which the growth proceeds can be modulated. Different inert or active gases can be flowing in the tube during growth, and additionally, their partial pressures are individually controllable. However, the thickness of the tube should be proportional to the highest possible pressure in order to avoid any crack or even explosion during the process. Debit of various gases are usually controlled independently by different manometers. Often, oxidizing or reducing gases are mixed with a dominant inert gas (usually Argon), depending on the system. Since the molten zone is in constant interaction with its gaseous environment, composition of the atmosphere determines the type of phase which is stabilized at the melt/seed interface, and especially oxygen content for oxides. Internal pressure inside the quartz tube establishes the temperature until it reaches a level where the molten zone stands and does not drop. Indeed, the melt is hold by its own surface tension, as explained before, and the difference of pressure between

the inside and the outside of the melt, plays a significant role in the stability of the surface. The more elevated the pressure is, the higher the temperature can be.

3.5. Detailed procedure for growth of high quality single crystals of La_2CoO_4

The growth of La_2CoO_4 single crystal samples is particularly delicate. A fine tuning of the setup, prior to process, is absolutely necessary for reaching the proper growth conditions. First of all, starting materials of extremely high purity are mandatory to avoid any impurity resulting from slight unbalance in the chemical composition. The growth must be strictly carried out under Argon flux since any trace of oxygen in the atmosphere remains a source of contamination. Besides, the molten zone has to be highly enriched in CoO as solvent (50% molar mass) in order to avoid solidification of secondary phases on the seed/melt interface (the composition of the melt is symbolized by the yellow spot on figure 2.23). In addition to this, measures must be taken against Cobalt evaporation (red arrow on the figure), which is probably the most problematic issue, since it destabilizes strongly the molten zone if it is not counterbalanced. So, it appeared that not only the melting zone but also the feed rod had to be enriched in Cobalt (3% molar mass). It has to be underlined that the excess of Co in the feed was not put for self-adjusting the melt's composition, which has already been doped with solvent, but for supplying an equivalent amount of cobalt to the one which evaporates (blue and red arrows on the figure). Hence, when the melt moves toward the feed rod, extra quantity of Co can be constantly provided to the melt during the process.

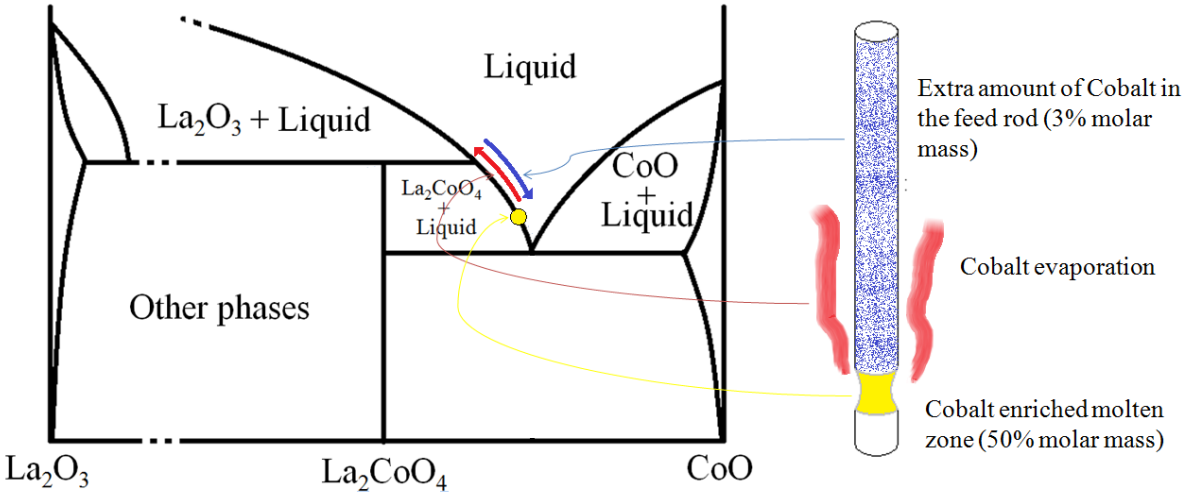

***Figure 2.23**: Adaptation of the system for stabilizing the incongruent molten zone by counter balancing evaporation of cobalt. The yellow point on the phase diagram symbolizes the composition of the melt, the red arrow show the effect of cobalt evaporation on the melt composition and the blue arrow shows how extra amount of cobalt in the feed rod permit to stabilize the system.*

Nevertheless, it came into sight that optimizing cobalt concentrations was not even sufficient to solve the problem of cobalt evaporation; in fact, it must be associated with a very steep temperature gradient. Indeed, the temperature distribution in the region of the molten zone provided by usual lamps is too broad in the case of La_2CoO_4; it provokes, in one hand, the penetration of solvent in the feed, and on the other hand, the fast evaporation of the extra Co from the feed before it enters the melt. Therefore, if the temperature profile is not sharp enough, enriching the feed with extra Cobalt is useless since it evaporates before compensating the loss of the melt, and the system collapses anyway. Moreover, the concentration of solvent in the melt is high, implying a great compositional difference in comparison with rods. Thus solvent can easily penetrate into the feed and ionic migrations at the solid/liquid interfaces are rather prominent. That is why a very slow growth rate is compulsory. Several tries have been necessary to find the good conditions and thus to develop a reproducible experimental procedure.

3.5.1. Preparation of rods

For preparing the feed, seed and solvent rods, powders have been prepared as described in the section concerning polycrystalline synthesis (subchapter 2.1). It has to be underlined that the preparation of the starting material for rods is crucial and must not be neglected; powders have to be carefully weighted, and purity has to be checked after each step of the procedure. Contrary to the seed which consisted only of stoichiometric La_2CoO_4 powder, the feed has been enriched by 3% of the molar mass of Co and the solvent has been enriched by 50% of the molar mass of Co (which is a rather high amount). The obtained powders have been put into thin rubber tubes and compressed, under hydrostatic pressure of 400 MPa, into rods with diameter of ~5 mm and length of ~100 mm. Finally, the rods used as feed and seed have been sintered at 1200°C for 24 hours in helium atmosphere, whereas no post treatment have been applied on the rods used as solvent, permitting to melt it more easily.

3.5.2. Special settings of the system for a very steep temperature gradient

The crystal growth apparatus was equipped with two ellipsoidal mirrors and, therefore, two halogen lamps have been installed as heat source with a power of 600 W each for reaching the appropriate temperature yielding melting. The model of lamps has been selected carefully for its extremely small size of filaments in order to decrease the temperature gradient around the molten zone, which is a very important parameter in the case of La_2CoO_4, as explained

before. Figure 2.24 shows a pictorial view of the specific lamps used for the successful growth.

Figure 2.24*: Picture of the type of lamp used for the successful growth of* $La_2CoO_{4+\delta}$.

However, since these lamps were not made for such use, special devices have been designed *ad hoc* for adapting the lamps to the furnace: two pieces of Copper, separated by insulating Teflon, have been used to prolong anodes and cathodes, permitting to adjust the lamps' positions at the focal points of the mirrors. Naturally, filaments have been oriented in accordance to the sharpest temperature distribution along the rods, as explained on the Figure 2.20. Thanks to these modifications, the temperature distribution around the molten zone has been well sharpened, permitting to decrease the solvent penetration in the feed, to considerably reduce the cobalt evaporation from the upper rod, and thus to stabilize the molten zone.

3.5.3. Setup and stabilization of the molten zone

The first step of the procedure consists in setting up the system 'feed-melt-seed' properly in the furnace, and then the molten zone can be stabilized. Since a third rod has been prepared for the melt in order to start directly with some solvent in the molten zone, the following *modus operandi* has been employed:

- Step 1: the feed rod is fixed at the lower shaft of the furnace and a slice of ~3 mm, previously cut from the rod of solvent phase is just put on top of it.
- Step 2: after adjusting the slice at the focal point of the mirrors, rotation of the shaft can be activated together with the power of lamps which is slowly increased until the

slice starts to melt. The purpose of this step is to attach the solvent phase to the feed, but without melting the feed.

- Step 3: the temperature is cooled down to RT and the furnace is shut off. Thus the melt is solidified but keeps the shape of a drop. The feed-melt system is then suspended at the upper shaft of the furnace while the seed can be fixed at the lower shaft. Then the furnace can be switched on again.

- Step 4: each shaft is counter-rotated at a rate of 12 rpm; the solvent phase has to be melted again and then the rods can be connected.

- Step 5: a growth rate of 1 mm/h is applied, and argon gas (1 atm) is flushed in the quartz tube. The temperature can then be adjusted, and kept as low as possible.

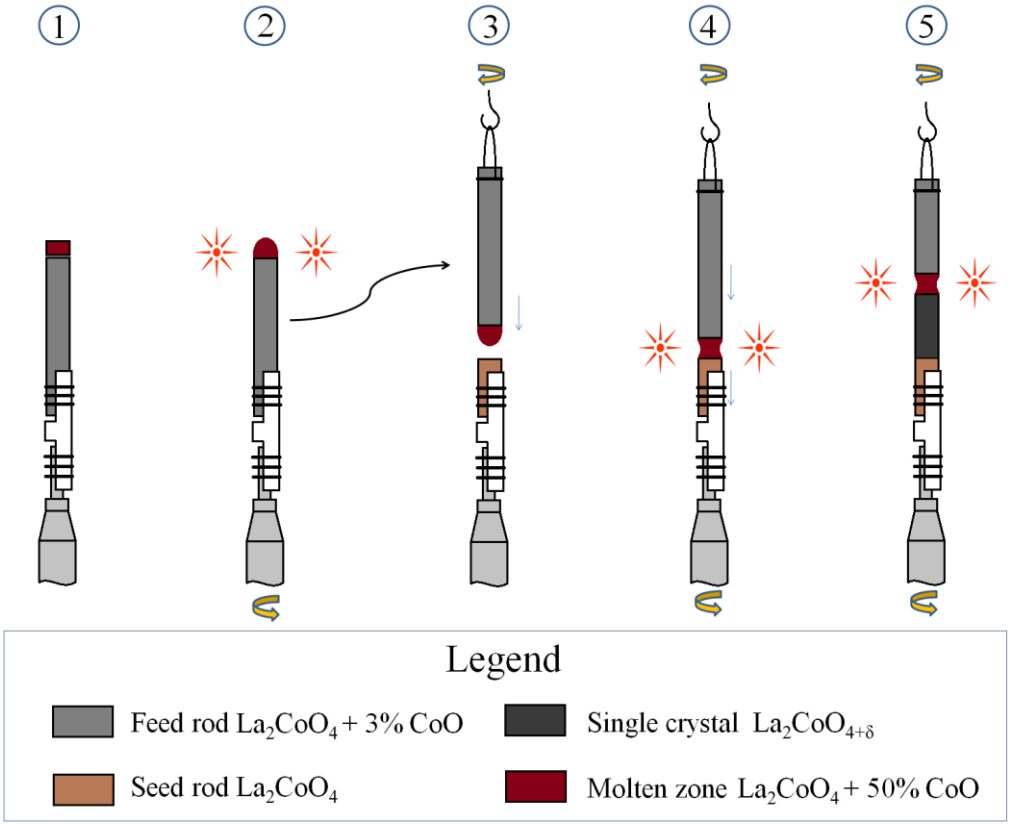

***Figure 2.25**: Successive steps for growth of $La_2CoO_{4+\delta}$ single crystal*

The fourth step is rather subtle; connecting the rods with the melt is easy to fail. The interface liquid/gas must stay as straight as possible in order to keep the composition of the melt constant; it has to be controlled by hand (using up/down motors independently for lower and upper shafts). The fifth step is the longest one; it usually lasts four days. During this time, every parameter has to stay as constant as possible, and the operator has to keep a constant eye on the process. Temperature can be gradually adjusted during the first day of the

operation. Stabilization of the molten zone was extremely difficult to reach, and the growth usually ended by a drop of the melt. This was due to a continuous thin deposition of solvent on the surface of the crystal grown, as shown on Figure 2.26. It resulted in a slight but continuous loss of solvent which finally destabilized the molten zone after some time.

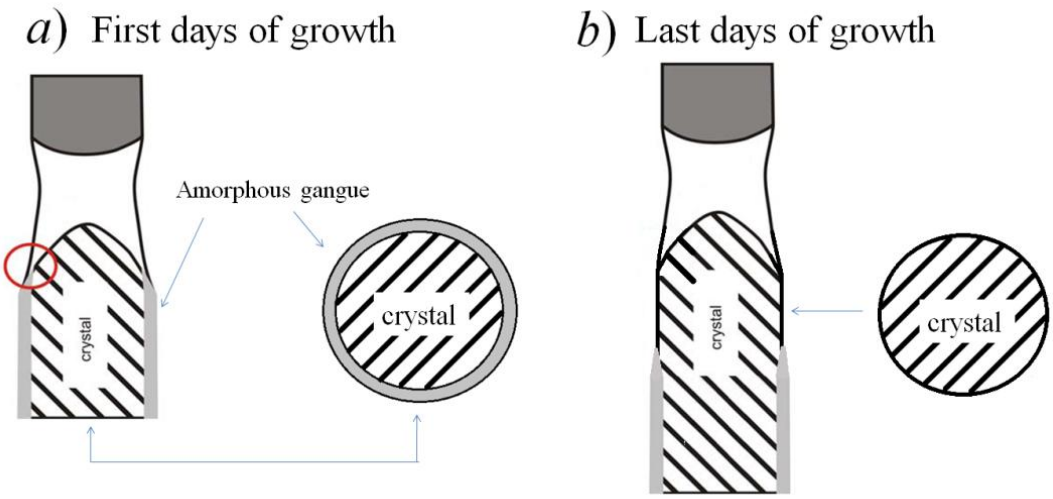

***Figure 2.26**: a) During first days of growth an amorphous gangue surrounds the crystal piece; b) in best cases, the gangue could be eliminated during the last days of growth, allowing to obtaining pure single crystal portions.*

The latter effect could not be avoided but only reduced with time and finally completely eliminated after at least 40 hours of growth, by constant adjustment of the temperature. Consequently, only the last parts of the whole final crystallized ingots were really pure and thus exploitable for further studies.

***Figure 2.27**: Three pieces of as grown single crystals, cut from final bulk products.*

3.5.4. *Qualitative characterizations and orientation of as grown crystals*

A piece of the *as grown* $La_2CoO_{4+\delta}$ single crystal has been finely powderized in mortar. X-ray powder diffraction experiments have then been carried out with a Bruker AXS D8 Advance diffractometer in Bragg-Brentano geometry, equipped with a LynxEye detector for suppressing the background caused by fluorescence of Cobalt. Figure 2.28 shows the plot (WinPLOTR[191]) of the Rietveld refinement of the experimental profile, performed with FULLPROF software[160,161]. The agreement factors are good: Bragg R-factor = 3.56 % and R_F factor = 1.84 %, when data are refined with *Fmmm* space group. The first important result is the high purity of the sample, no secondary phases were found, thus no phase separation occurred; all reflections could be fitted with one single phase. The second significant outcomes are the proportions of the unit-cell (a = 5.48(8) Å, b = 5.52(9) Å and c = 12.64(8) Å) and the space group *Fmmm*, which correspond to a non-stoichiometric oxygen content according to the polycrystalline results (section 2.1.3), and it is furthermore in accordance with the literature[47,12]. However, X-rays do not allow to precisely determine the oxygen content of the interstitial site; the extra oxygen content has been evaluated to be δ = 0.15 for refinements since this value has often been reported[47,12] to be the extra oxygen content of the as-prepared $La_2CoO_{4+\delta}$.

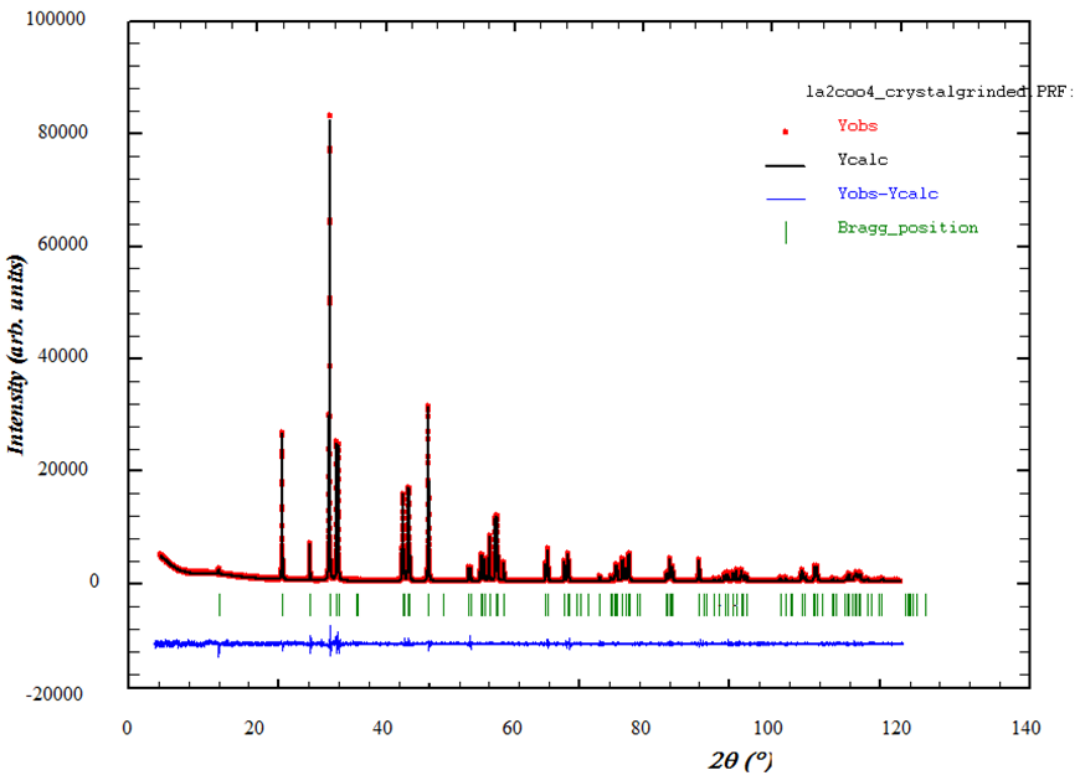

***Figure 2.28**: Rietveld refinement of X-ray diffraction pattern of a part of as grown crystal ground in fine powder (Cu kα_1, Bruker AXS D8 Advance diffractometer, Rennes).*

Table 2.4: Structural model resulting from Rietveld refinements carried out on the experimental X-ray profile of a part of crystal ground into fine powder.

Atom	*x/a*	*y/b*	*z/c*	*Occ*	*β iso*
La	0	0	0.3613(3)	2	0.193(9)
Co	0	0	0	1	0.157(6)
O (eq)	¼	¼	0	2	0.193(3)
O (ap)	0	0	0.187(5)	2	0.236(1)
O (int)	¼	¼	¼	0.15	0.178(6)

a = 5.48(1) Å, b = 5.52(5) Å, c = 12.63(8) Å, $\alpha = \beta = \gamma = 90°$. Space group: *Fmmm*. Wavelength: $Cu_{k\alpha 1}$ = 1.54056Å. Accordance factor: R-Bragg factor = 3.56 %, R_F factor = 1.84 %. O_{int} occupancy has been fixed to 0.15 according to previous work[12].

A more precise value of the oxygen content in the sample has been measured experimentally with thermogravimetric hydrogen reduction (NETZSCH Jupiter STA 449C system combined with mass spectrometer ThermoStar Pfeiffer Vacuum). The chemical reaction for hydrogen reduction can be written as follows:

$$La_2CoO_{4+\delta} + H_2 \rightarrow La_2O_3 + Co_{(metal)} + (1+\delta)\ H_2O\uparrow$$

Temperature was increased from RT to 1273 K with a heating rate of 10 $Kmin^{-1}$. The gas flow was a mixture of helium (protective gas) with 5% of hydrogen. The reduction process started around 534 K until ~750 K and the resulting weight of the decomposed sample remained constant for the rest of the measurement. After subtracting the baseline (which is the contribution of the apparatus in the raw experimental signal), the total loss of weight, attributed to the oxygen departure, was measured to be 3.97(1) % of the starting sample mass. According to the chemical reaction written above, calculations result in an oxygen content value of $\delta = 0.14 \pm 0.02$.

Orientation of single crystals has been carried out by back-scattered X-ray Laue diffraction method, which is usually used to determine point groups of crystalline structures. However it is also a rather convenient technique for crystal orientation. The sample has been fixed on a goniometer and placed in front of the X-ray beam partially scattered back to a screen made of two CCD cameras (Photonic Science). Generally between 2 and 4 minutes of expositions were sufficient to acquire a signal exploitable when the sample/detector distance was ~3 cm. Different softwares exist for data treatments of Laue patterns; here "OrientExpress"[192] has been used to determine directions of unit-cell vectors, $\vec{a}$, $\vec{b}$ and $\vec{c}$ of the *as grown* crystals. First the crystal has been positioned randomly. The software generates several theoretical Laue patterns depending on the various input values given by the operator. Then the good

solution can be selected, by superimposing experimental and theoretical patterns and comparing them by eye. A detailed procedure for finding crystal orientations with this software has been well described elsewhere[193,194]. Figure 2.30 shows one Laue diffraction pattern taken with a crystal oriented randomly (*a*), and its respective superposition with good solution (*b*). The two other pictures (*c* and *d*) show the Laue diffraction pattern for crystal oriented with $\vec{c}$ and $\vec{a}$ collinear to incident X-ray beam.

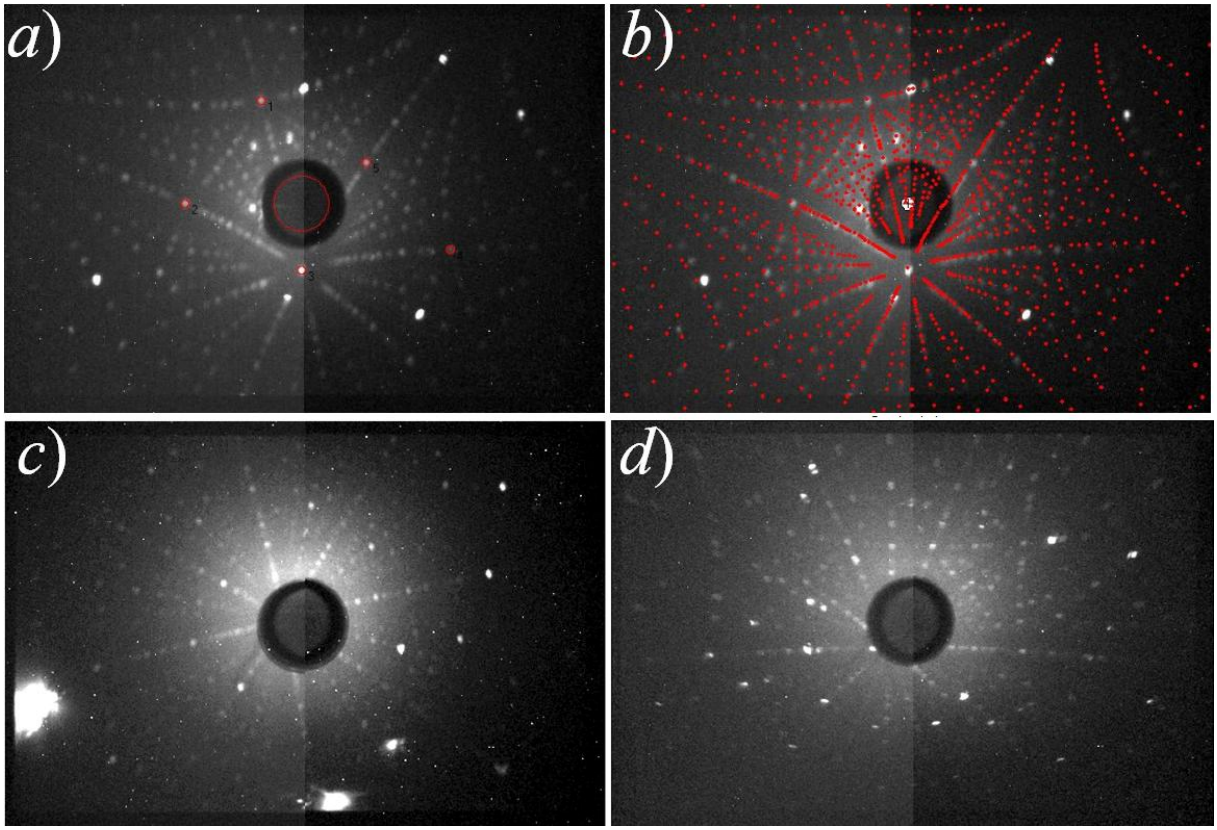

Figure 2.29*: X-ray Laue diffraction pattern of a) randomly oriented crystal; b) superposition of experimental picture and theoretical model generated by OrientExpress software; c) crystal oriented with c-axis collinear to the incident beam; d) crystal oriented with a-axis collinear to the incident beam.*

The "star" shape on the picture shown in Figure 2.29 *c)* is characteristic of the $La_2MO_{4+\delta}$ crystals oriented with *c*-axis collinear to the incident beam. Indeed the fourfold axis induces this symmetry by rotation of 90° (even if at RT the space group is *Bmab*, the orthorhombicity is rather small and the fourfold axis of the HTT phase, *i.e. I4/mmm*, is not much deformed and still visible). With experience, it becomes easier to orient these types of crystals since the *c*-axis is generally perpendicular to the direction of the growth; so, the *c*-direction can be found easily with only few scans. However *a*- and *b*-axis are more difficult to find, the Laue patterns corresponding to their colinearity with incident beam (see *d)* on Figure 2.29) is not as recognizable as the one of *c*-axis. But they can be found with the help of theoretical

simulations. Generally, the growth direction of La_2CuO_4 single crystals follows the [110]-axis of the LTO unit-cell (equivalent to [100]-axis of the HTT unit-cell), *i.e.* a_{LTO} and b_{LTO} making an angle of 45° with the growth direction; but it is not the case for the *as grown* $La_2CoO_{4+\delta}$. Indeed, experimental results indicate that *a*-axis astonishingly makes an angle of 30° with the growth direction, whereas this angle is of 60° for the *b*-axis. Consequently, the growth direction of the crystals is [120]-axis of the LTO unit-cell (equivalent to [130]-axis of the HTT unit-cell).

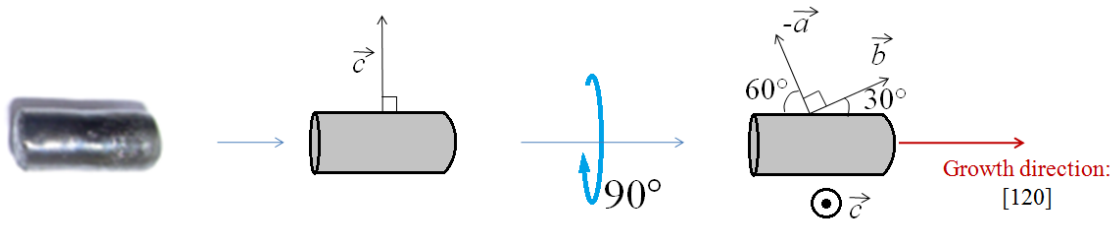

Figure 2.30*: Orientation of as grown single crystals and determination of growth direction.*

All the La_2CoO_4 *as grown* samples have been found to possess the same orientation of unit-cell vectors with respect to the growth direction.

For technical reasons, it is convenient to orient the samples prior to single crystal diffraction experiments in order to know how to fix them on the sample holders and furthermore, it permits to save precious time during beamtimes granted on the instruments of large scale facilities.

Chapter 3

Strategy of experimental analyses adapted to the study of twinned $La_2MO_{4+\delta}$ crystals with modulated structures

1. Twinning in $La_2MO_{4+\delta}$ single crystals

1.1. Generalities on twinning

Ideally, the perovskite structure corresponds to a cubic unit-cell of space group $Pm\bar{3}m$. However, as explained in the first chapter, the real atomic structure is determined by the ionic radius of the chemical components or by their interatomic bond length. Above a certain value of the Goldschmidt factor, strains become too intense and the structure transits to lower symmetry, *e.g.* tetragonal, orthorhombic, etc. This kind of phase transition is very common for oxides and usually occurs as function of the temperature. It can be due to two distinct phenomena: either shifts of cations from their original position in the unit-cell, or tilts of rigid octahedra, etc. Lowering the symmetry implies the loss of one or more symmetry elements, which gives higher degree of freedom for certain crystallographic sites of the unit-cell. As a result, atomic shifts or polyhedra tilts can occur in different directions, resulting in different possible orientations of subsequent unit-cells. Contrary to powders which are composed of a high amount of crystallites oriented randomly, single crystals are oriented in space, *i.e.* the directions of $\vec{a}$, $\vec{b}$ and $\vec{c}$ vectors are ideally invariable in the three-dimensional space. However, phase transitions with modification of symmetry can create the problem of twinning in crystals, *i.e.* two or more orientations of the unit-cell inside the bulk. They are intergrown (macro- or microscopically) in such way that the lattice of the individual orientations are linked by specific symmetry operation.

The *twin law* gives the geometrical relationship between the *twin components*, also called *twin domains* or even *twin individuals*[195]. The twin law specifies a *twin operation* which brings one twin component into the same orientation than the other(s). The corresponding symmetry element is called *twin element* which is precisely the element of symmetry lost after the

transition. In other words, the element of symmetry lost is the unit-cell, with regards to the higher symmetry before transition, is then applied between the twin domains after transition. There are several kinds of twin laws: *reflection twins*, *rotation twins* and *inversion twins*. In some cases, one twin can be equally well described by more than one twin law. The surface between twins can be well-define, *e.g.* for reflection twins it is usually a plane parallel to the twin plane, but it can also be non planar with irregular shape for other kinds of twin law. These borders are regularly called *twin interface*, *composition surface*, or *twin boundary*. If more than two twin components are twinned together according to the same law, the twin is called *repeated twins* or *multiple twins*. Twinning can appear according to diverse manners: *growth twins*, *mechanical twins* and *transformation twins* can be differentiated with respect to their formation process: *i*) Growths twins obviously happen during natural crystal growing and usually product few large twin domains. For instance, the staurolite (monoclinic) is famous to form crosses; twin with 60° between individuals (*"croix de St André"*) is more frequently observed than the one with an angle of 90° ("*croix grecque*").

Figure 3.1*: Different examples of growth twins a) Staurolite, « croix grecque », b) twinned gypsum, c) twinned pyrite.*

ii) Mechanical twins are due to external stresses and can be described in terms of shear of the structure. Finally, *iii*) transformation twins occur for structural phase transitions, and usually result in high amount of small twin domains in the bulk, also called *microscopic twinning*. They are usually intergrown making believe, as first impression that the twin components could have grown simultaneously, but they ensue from phase transitions, as for the example of perovskites given above.

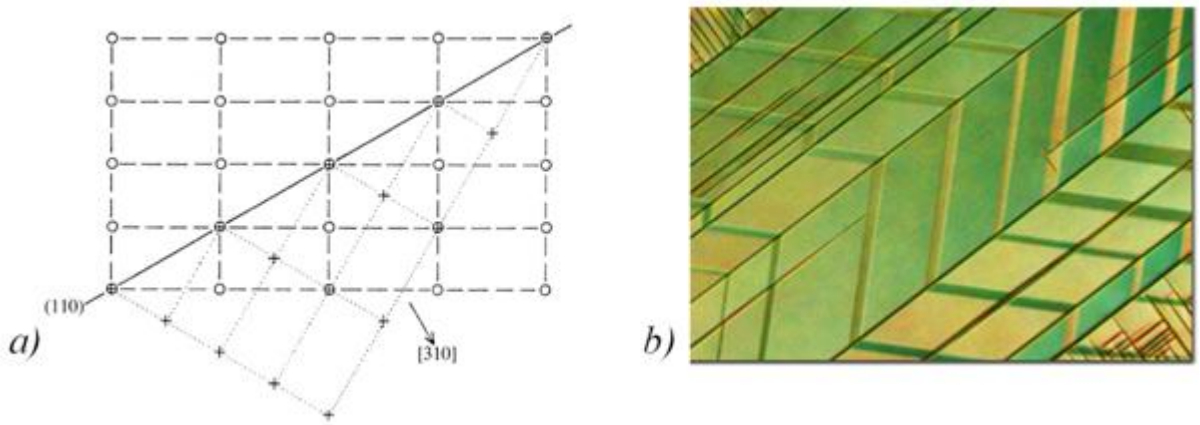

Figure 3.2*: a) Projection of the twin components of an orthorhombic twinned crystal, the twin law can be interpreted either as reflection twin with the plane (110) or as rotation twin around the [310] axis (ref: international tables vol. c, chap 1.3); b) experimental image of microscopic twinning in La-Al system viewed by microscope with polarized light.*

Classification of twinning is based on the effects observable on the reciprocal lattice of the crystal[196]:

- Holohedral twinning: in this case the twin element belongs to the point group; consequently the calculation of the structure is not affected.
- Merohedral twinning: the twin element belongs to the crystal system but not to the point group. Different orientations of the crystal coincide exactly and consequently some reciprocal lattice points overlap perfectly.
- Partial merohedral twinning: this is the case when there is a fortuitous relationship between cell-parameters of the twin components, which result in an overlapping of reciprocal lattice spots for some particular planes.
- Pseudo-merohedral twinning: corresponds to rather rare cases for which cell parameters are very close to higher symmetries. It results in partial overlapping of some reflections.
- Non-merohedral twinning: In this case the reciprocal lattice points of the twin components are not overlapped and it is possible to integrate their intensities separately. This is the most common case.

Twinning is constraining for the resolution of the atomic structure since it can induce pseudo-symmetries. Indeed, when some reflections are overlapped, integrated intensities can correspond to one or both individuals, and the resulting structural model will be skewed. That

is why twinning law must be found prior to structural refinements, and if possible, twin domains should be integrated individually.

1.2.Twinning law for the basic unit-cell of $La_2MO_{4+\delta}$ system

The twinning effect, classical in these types of oxide, ensues from the cooling process of the synthesis when the crystal sample undergoes the phase transition from high temperature tetragonal unit cell (HTT phase) to low temperature orthorhombic (LTO phase) induced by a cooperative tilt of the MO_6 octahedra occurring when the lattice relaxes to release internal strains (*c.f.* Chapter 1, section 2.1.1). Thus, the type of twinning in La_2MO_4 is transformation twins and the domains are microscopically intergrown. Two or four domains can appear in the bulk, owing different orientations of the $\vec{a}$-$\vec{b}$ plane but sharing the *c* axis. Two symmetry elements can be lost below the transition: the $(110)_{LTO}$ and $(-110)_{LTO}$ diagonal mirror planes which constitute the twin element(s) of the twin law. The loss of each mirror plane generates one set of two twins, *i.e.* if only one of them is lost, two individual twins appear, and if both are lost, four individual twins arrive on the scene (multiple twins)[139,197]. After the transition, the diagonal mirrors no longer belong to neither the point group nor to the crystal system. Consequently, the twinning is non-merohedral; but due to the very small orthorhombicity and the resulting partial overlapping of superlattice reflections, it is of pseudo-merohedral type.

On the phenomenological point of view, orthorhombicity of the LTO phase is induced by a cooperative tilt of MO_6 octahedra. To reach this state when cooling, the tetragonal structure can be distorted by two different ways: octahedra can rotate either along $[110]_{HTT}$ or $[-110]_{HTT}$ directions since they are equivalent by symmetry at high temperature by the fourfold symmetry axis. As the crystal passes through the T/O transition, none of the tetragonal basal plane axes is privileged to become the shortest orthorhombic axis[198,199]. Keeping the same crystallographic basis of the LTO unit-cell, the structural modifications provoked by the orthorhombic distortion leads to the *Abma* space group when displacements of octahedra are parallel to the *a*-axis (rotation around $[010]_{LTO}$ axis and $a_{LTO} > b_{LTO}$), and to *Bmab* if the corresponding displacement is parallel to the *b*-axis (rotation around $[100]_{LTO}$ and $b_{LTO} > a_{LTO}$). Indeed, the cooperativity of tilt between octahedra cannot be kept in the whole volume of the large single crystals. In other words, the transition occurs simultaneously at different locations of the crystal lattice, the direction of tilts cannot propagate fast enough to form a single domain. Consequently, twin domains are formed, owing different orientation of $\vec{a}$-$\vec{b}$ plane. They are separated by clear twin boundaries, usually forming stripes. The twin

individuals are symmetric by the twin element(s), *i.e.* the $(110)_{LTO}$ and $(-110)_{LTO}$ mirror planes, which are collinear to $\vec{a}_{HTT}$ and $\vec{b}_{HTT}$. As mentioned above, the loss of only one mirror plane leads to one set of two twin domains (*Abma* and *Bmab*), and losing the two mirror planes results in the apparition of two sets of two twin domains (four in total: $Abma_1$, $Bmab_1$ and $Abma_2$, $Bmab_2$) as shown on Figure 3.3. Connected to the transition, the fourfold tetragonal axis (parallel to *c*-axis) is reduced to a twofold, but it is precisely this fourfold rotation which relates the mirror planes and therefore the two sets of twins. Consequently, when four twin domains are present in the bulk, the reciprocal lattice is symmetrical by rotation of 90° along *c*-axis. Thus, the reciprocal pattern consisting of superimposition of each twin lattice can be averaged in a unique tetragonal unit-cell (*F4/mmm* space group).

The small difference between the values of *a*- and *b*-parameters combined with the twinning effects induce a split of some Bragg reflections as follows:

- For the case of only one set of two twin individuals, the Bragg reflections split in two peaks, they can be well separated or partially overlapped depending on 2Θ; except for the (-*hh*0) and (*h*-*h*0) reflections which are perfectly overlapped when the (110) mirror plane is lost (or (*hh*0) and (-*h*-*h*0) reflections if the (-110) mirror plane vanishes).
- For the case of two sets of two twin domains, the Bragg reflections split in four peaks, excepted for the (±*h*±*h*0) reflections which split in three peaks (two of the four are exactly overlapped).

In fact, the reciprocal pattern for two sets of twins individuals can be viewed as a superimposition of two patterns of one set, rotated by 90° from one to the other, *i.e.* symmetric by fourfold axis lost from HTT phase. The angular separation between reflections depends on the orthorhombicity and can be defined as follows[49]:

$$\Delta = \arctan\left(\frac{a}{b}\right) - \arctan\left(\frac{b}{a}\right) \qquad equation\ 3$$

The angular separation for (*h*00) and (0*k*0) reflections is Δ, while it is 2Δ for (*hh*0). For crystals oriented with the *c*-axis perpendicular to the diffraction plane of the diffractometer, this relation between Δ and cell parameters allows to measure directly, and with high accuracy, any variation of the orthorhombicity with only one ω-scan of one (*hh*0) reflection, *i.e.* a simple rotation around the *c*-axis when the crystal samples is oriented with *c*-axis

perpendicular to the diffraction plane. Δ is independent to both miller indexes and wavelength.

For the stoichiometric compound $La_2CoO_{4.00}$, each twin individual can be described with the distinct space groups *Bmab* and *Abma* as it permits, for practical reasons, to index all reflections with the same Miller indexes for all twin individuals. However, integration of intensity separately for each twin domain is more complicated due to the partial overlapping. So, all Bragg reflections can be indexed with a single structural model, with tetragonal lattice, for which the twin domains are not differentiated and their respective (*hkl*) intensities are integrated together for a single reflection. This simplifies a lot data reduction process, but it averages the atomic structure of all domains into one primitive pseudo-lattice[43,144,200].

The twinning in oxygen-rich phases is similar to the one of stoichiometric compounds. However the space groups are different. In $La_2CoO_{4+\delta}$, the disorder in the arrangement of octahedra created by interstitial oxygen atoms modifies the symmetry; the basic unit-cell is averaged and the space group is *Fmmm* (*c.f.* Chapter 1, section 2.2.3). The unit-cell remains orthorhombic but the characteristic reflections of the *Bmab* space group are extinct; in addition the orthorhombicity is smaller than for $\delta = 0$. Hence, when the space group of the domains is *Fmmm*, the symmetry averaged on the whole reciprocal pattern corresponds to the space group *F4/mmm* for the tetragonal pseudo unit-cell. The situation becomes more complex when the twinned structures are also modulated, *cf.* section 2.

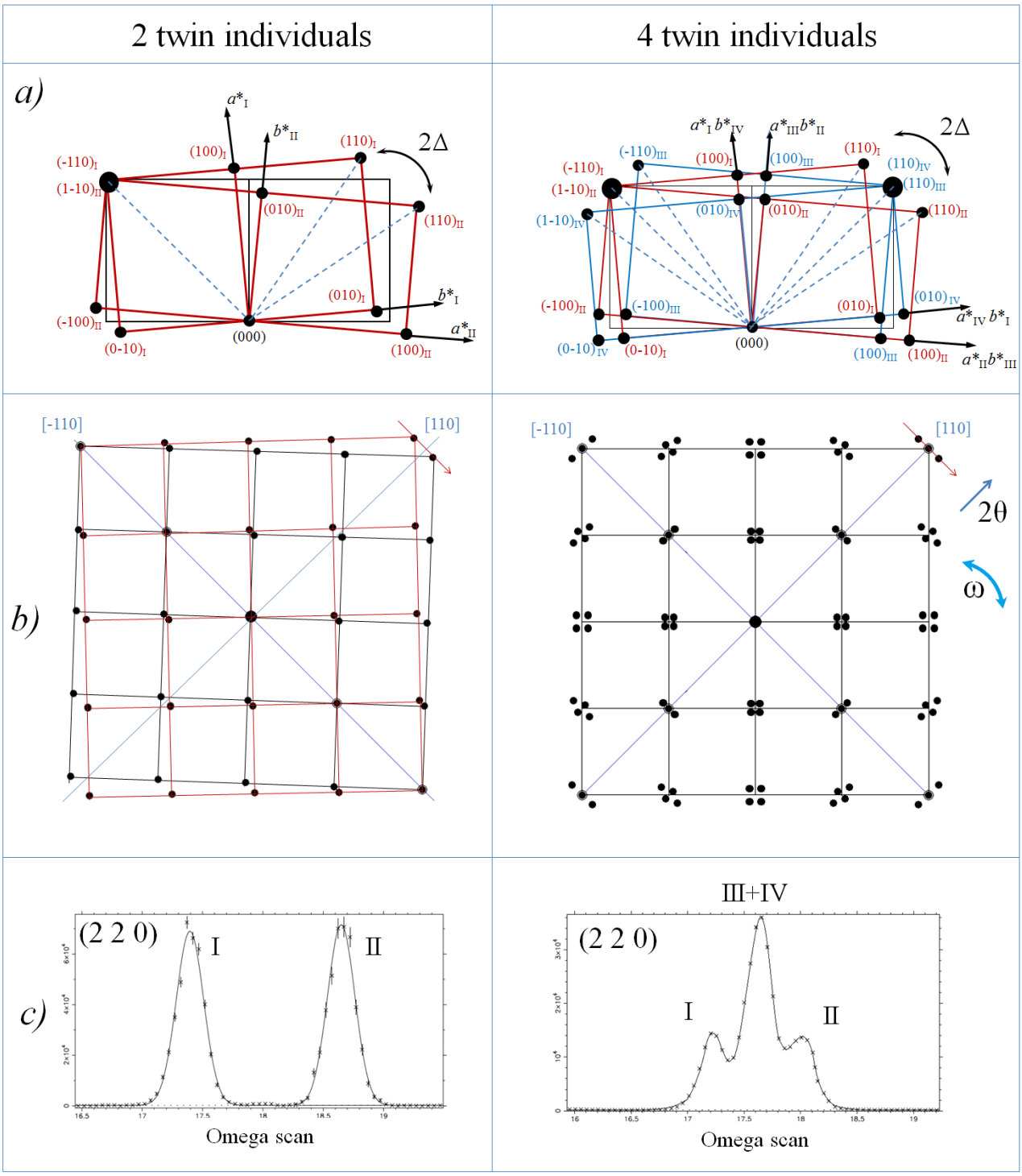

***Figure 3.3**: Scheme of twinning in $La_2MO_{4+\delta}$ single crystals, with the loss of either [110] or both [110] and [-110] mirror planes, resulting respectively in 2 or 4 twins individuals. a) Twin law in reciprocal space view perpendicular to $\vec{c}$* which is the axis shared by the two twin components; b) Ideal projection of the Bragg reflections until the 3rd order on the $\vec{a}$*-$\vec{b}$* plane corresponding to ω-2Θ plane when c-axis is perpendicular to the diffraction plane of the diffractometer, arrows in red, show the x-axis of the following scans: c) Experimental neutron ω-scan of the (220) Bragg reflection, for an equal volume repartition of twin domains, the integrated intensity of each peak gives directly the ratio of twin volumes (TriCS@SINQ).*

1.3.Implications of pseudo symmetry

The majority of the samples we studied by diffraction were twinned either once or twice; crystals of $La_2MO_{4+\delta}$ made of only one domain being extremely rare. Due to the partial and intermittent overlapping of most reflections, integrating intensities accurately and separately for each individual domain is very difficult. The proportions of overlapping are irregular: it depends on d_{hkl}. Consequently, the pseudo symmetry, space group *F4/mmm*, has been first used for data acquisition and treatment, *i.e.* the twin components have been re-grouped in a single structural model. The reciprocal lattice corresponding to the *F4/mmm* unit-cell (of same proportions as the *Bmab*, with $a = \sqrt{2} \times a_{HTT}$ and $c = c_{HTT}$) is in fact equivalent to the one of the HTT unit-cell; indeed it can be indexed with the smaller unit-cell of *I4/mmm* space group. However, the *F*-centered unit-cell has been systematically used for the sake of clarity, in order to be consistent with the real *Fmmm* orthorhombic unit-cell. During neutron diffraction experiments, averaged cell parameters have been obtained after centering generally about 10 reflections of strongest intensity: (*hh*0), (*hhl*) or (00*l*) type. The *a*- and *b*- parameters were taken equal, and their averaged value are $a_{F4/mmm} = (a_{Fmmm} + b_{Fmmm})/2$. Measuring reciprocal pattern of twinned crystal by diffraction is performed with the averaged cell parameters in order to center the scans on the centroid of the reflections split. So, the reflections of same (*hkl*) for each individual twin are integrated together. The most important experimental parameters are thus the opening of the point detector and the width of the scan, which have to be optimized because of the broadness of split reflections. The total intensity for one reflection can be written as follows for *n* twin domains:

$$I_{tot} = \sum_n \alpha_n \mathrm{I}(hkl)_n \qquad \text{With} \quad \sum_n \alpha_n = 1 \qquad\qquad equation\ 4$$

With the average tetragonal space group *F4/mmm*, the integrated intensity (I_{tot}) is the sum of the intensities ($\mathrm{I}(hkl)_n$) of each twin component multiplied by their respective volumic ratios (α_n). Ideally, the volumes of each twin component are equal, and in this case $\alpha = 1/n$ for each twin individual. However, even in this ideal situation, the profile of the peak depends on the type of reflection. For instance, the two ω-scans of the (220) reflection for 2 and 4 twin individuals of the same volume shown on Figure 3.3, clearly depict this fact: some reflections are totally split but others are partially overlapped. In the case of four twin components, the (*hh*0) reflections are made of three peaks; the two on the sides correspond to two different domains whereas the one in the middle is the exact superimposition of the intensities of two domains. Consequently the middle peak is twice more intense than the two others when the domains are of same volume. The average cell parameters can be refined with the position of

the middle peak, whereas the real orthorhombicity can be calculated from the angular separation between the peaks on the sides thanks to equation 3.

2. Introduction to crystals with modulated structures

2.1. Generalities

Periodicity in three dimensions is a basic concept for defining crystals. The subsequent Bragg reflections forming the corresponding three-dimensional reciprocal lattice can be observed by diffraction and allows to determining the symmetries of the structures ensuing from atomic ordering. However, more and more long-range-ordered condensed-matter phases observed in nature cannot be described with such direct and reciprocal three-dimensional lattices, and they differ from "normal" crystals in very subtle ways. As detailed further, the concept of crystal can be extended in such manner that it includes the so called *modulated* phases as well. As a result, crystallographic concepts are still valid and relevant for such compounds, and thus, instead of limiting the validity of the crystallographic notions, this development show how rich the depiction of atomic ordering can be. The first indications on the fact that crystals with complex internal structures have abnormal periodicity, appeared at the end of the 19th century from the morphological studies of minerals for which some faces could not be indexed with rational indexes. Then, at the beginning of the 20th century, it was shown that these peculiar faces corresponded to additional reflections in the X-ray diffraction pattern. These firstly named "*Gittergeister*" (lattice ghosts) have then been called '*satellites'* after studies concerning aluminum-copper alloy[195]. Then, periodic (and static) displacement waves were found to be at the origin of satellites through the creation of long-range ordering, and these modulations have been extended from atomic to magnetic ordering plus to other types of ordered structures.

A structural modulation can be considered to be a periodic deformation of a *basic structure* having basic space group symmetry[201]. The modulation which gives rise to satellites can have two different origins, and can even be a combination of them: *i*) a *displacive* (or *positional*) modulation consists in a periodic displacement of atoms from their original position in the basic structural model, forming wave-like distortions, *ii*) an *occupational* modulation for which some atomic position of the basic structure are occupied with a periodic probability function. Often, an occupational modulation is combined with positional modulation of the surrounding atomic sites. If the periodicity of the modulation belongs to the periodicity of the

basic structure, the modulation is *commensurate*, and if not it is *incommensurate*. In other words, if the ratio between the period of the modulation and the one of the basic structure is: *i*) equal to a rational number, the structure is commensurately modulated, and *ii*) equal to a irrational number, the structure is incommensurately modulated. This description is generally based on the observation of the reciprocal lattice, composed of two kinds of reflections: the *main reflections* (or *basic reflections*) forming a lattice which corresponds to the basic unit-cell, and the *superlattice reflections* generally of weaker intensity, also called satellites, which are generated by long range ordering, *i.e.* by the modulation waves. The intensity of superlattice reflections depends on the nature of super-ordering: for instance, while the order of magnitude is ~1% of the intensity of the main reflections for atomic modulation, it is only of 1.10^{-4} % of it for charge and spin modulation.

Commensurate superstructures can be considered as a particular case of the more general incommensurate modulation. Indeed, commensurability implies that the modulation can be taken into account and fully described by a larger three dimensional unit-cell, with a volume of N times the basic one (N integer), still having usual space group, although different from the average one. In this case, the new cell parameters of the supercell ($\vec{a}_s$, $\vec{b}_s$ and $\vec{c}_s$) can be written from the parameters of the basic unit-cell ($\vec{a}_b$, $\vec{b}_b$ and $\vec{c}_b$) as follows:

$$\vec{a}_s = n_1\vec{a}_b \qquad \vec{b}_s = n_2\vec{b}_b \qquad \vec{c}_s = n_3\vec{c}_b \qquad \text{with} \quad N = n_1 \times n_2 \times n_3$$

and the corresponding volume of the new unit-cell becomes:

$$V_m = N\, V_b$$

Conversely, incommensurate modulation does not obey the classical requirements for crystals; *e.g.* no general space group can be assigned to the symmetry of their atomic structure although their long-range order is as perfect as the one we find in ordinary crystals. The diffraction pattern is also made of sharp and well separated spots but the whole reciprocal pattern does not form an identifiable Bravais lattice. In order to introduce the basic concept of higher dimensional crystallography for incommensurate phases, it is possible to start from the general expression of the vector $\vec{H}$ giving the position of Bragg peaks in the reciprocal space:

$$\vec{H} = \sum_{i=1}^{n} h_i\, \vec{a}_i^* \qquad \textit{equation } 5$$

Here n represents the number of dimensions; in the case of a "normal" crystal n = 3 which corresponds to the three spatial dimensions $\vec{a}_1^*$, $\vec{a}_2^*$ and $\vec{a}_3^*$ are denoted by $\vec{a}^*$, $\vec{b}^*$ and $\vec{c}^*$ while the indexes h_1 h_2 and h_3 correspond to the Miller indexes h k l. But, for instance, in the case of a one-dimensionally modulated crystal, corresponding to a periodic plane wave deformation of the basic structure, n = 4. Conventionally, $\vec{a}_1^*$, $\vec{a}_2^*$ and $\vec{a}_3^*$ are kept as $\vec{a}^*$, $\vec{b}^*$ and $\vec{c}^*$, generating main reflections, and $\vec{a}_4^* = \vec{q}$ is the wavevector of the modulation generating the satellites. The corresponding indexes h k l and m are integers, they can either be positive or negative. Modulated structures can have more than one wavevector, *i.e.* their dimension n can be equal to 5, 6 or more; hence, the positions of peaks in the reciprocal space can be generalized as:

$$\vec{H} = h\vec{a}^* + k\vec{b}^* + l\vec{c}^* + \sum_d m_d\,\vec{q}_d \qquad \textit{equation } 6$$

The integer d represents the number of extra dimensions. The main reflections can be indexed with only h k and l as in the normal case (*i.e.* $m_d = 0$), but not the satellites for which $m_d \neq 0$. Generally, intensities of the satellites strongly decrease when m increases; therefore, usually only satellites of low order are observable. The propagation vector(s) $\vec{q}_d$ of the modulation is/are expressed with respect to the basis $\vec{a}^*$ $\vec{b}^*$ $\vec{c}^*$ as following:

$$\overrightarrow{q_d} = \alpha_d\,\vec{a}^* + \beta_d\,\vec{b}^* + \gamma_d\,\vec{c}^* \qquad \textit{equation } 7$$

If at least one of the three coefficients α β or γ of a vector q_d is irrational, the modulation is incommensurate, whereas if all are rational numbers, it exists at least one integer N for which the product $N \times \vec{q}$ matches with the reciprocal lattice spanned by $\vec{a}^*$ $\vec{b}^*$ and $\vec{c}^*$; in this case the structure is commensurately modulated and satellites are called *superstructure reflections*. In this case, satellites of different orders are superimposed and give the impression that very high orders are observable. The case of commensurate modulation can be treated without propagation vector, as explain above, by considering a *supercell* in three dimensions owing a volume N times larger than the basic unit-cell. Though, the superstructure reflections can still be indexed with a commensurate propagation vector with α β γ rational coefficients. It is sometimes more convenient to adopt the latter choice for compounds showing structural transitions between incommensurate to commensurate modulation, in order to keep a coherent description of the structure through the different states. Generally, the nomenclature used to specify modulated lattices is "(3+d) (in)commensurate structure", permitting to easily

differentiate the number of extra dimensions brought by the propagation vector(s) and the type of modulation.

The superlattice reflections can be indexed by applying $\vec{q}_d$ on the main reflections as shown on the following example where a reciprocal space projection of the modulation plane of a P-orthorhombic lattice is shown, modulated incommensurately by an arbitrary propagation vector lying in the $\vec{a}$*-$\vec{b}$* plane (γ = 0). For the sake of clarity only the satellites of first order have been presented ($|m_d| \leq 1$).

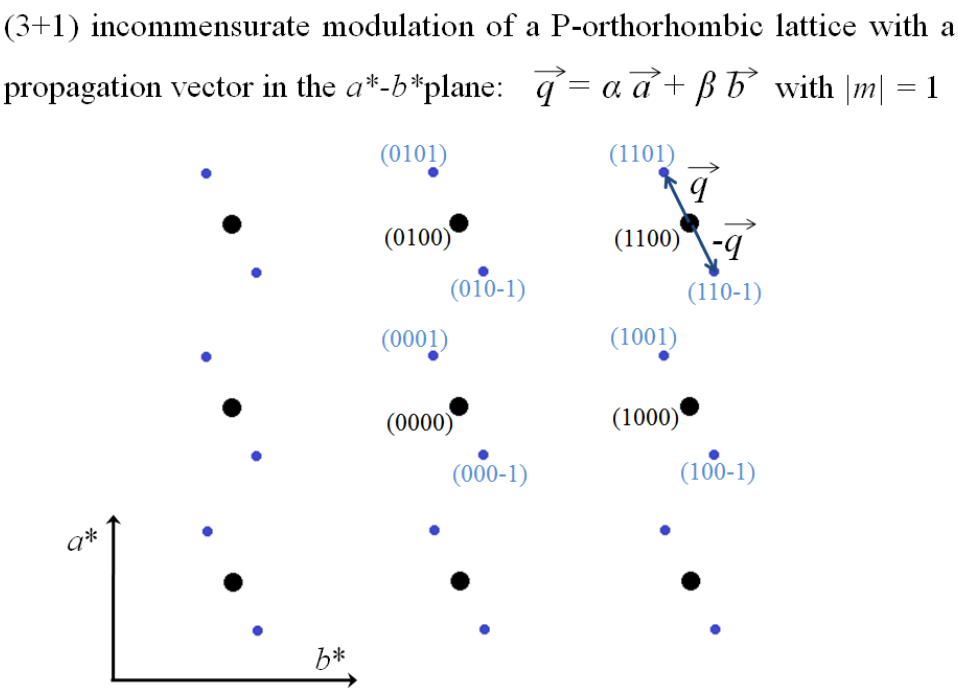

***Figure 3.4**: Theoretical example of indexation of superlattice reflections shown on the projection of the $\vec{a}$*-$\vec{b}$* reciprocal lattice plane.*

There are different ways of expressing the long range order of incommensurate phases in terms of symmetry. The easiest choice is to consider that the measuring process limits the precision of the irrational coefficients α β and γ, which can thus be approximated to rational values, in order to fit with the closest commensurate modulation. But this procedure has two main disadvantages: *i*) good approximations often imply very large unit-cells, involving a huge number of parameters and complicated extinction rules; *ii*) the resulting space group strongly depends on the approximated values of α β and γ, showing the irrelevance of space group determination. However, these difficulties can be avoided through the use of adapted *superspace groups*[195] which have been developed by enlarging the class of symmetry transformations from Euclidean spaces of three dimensions to Euclidean spaces of *n*

dimensions. It permits to leave not only the basic structure but also the modulation invariant by symmetry. The (3+1) incommensurate superspace groups are listed in section 9.8.3.5 of the volume C of the International Tables of Crystallography[195], (3+*d*) superspace groups with *d* = 2 and 3 have also been listed elsewhere.

Determining superspace groups for modulated structures is rather arduous due to the high amount of solutions brought by extra dimensions (756 solutions for (3+1) modulation, 3355 for (3+2) and 11764 for (3+3)) and also due to the difficulty to find the good solution for the propagation vector within the reciprocal lattice which appears disordered. The superspace group determination procedure can be separated into several distinct steps:

- Finding the point group of the basic reciprocal lattice that transforms each main reflection into a reflection of same intensity.
- Choosing a basis and a propagation vector from the centering extinctions to index all satellites.
- Finding the space group of the basic structure from the main reflections only. The basic structure is averaged, generally involving split atomic positions.
- Identifying the (3+*d*) Bravais lattice type (in superspace also centering give rise to extinctions). The Bravais class of the superspace group depends strongly on the coefficients α_d, β_d, γ_d, of the propagation vectors $\vec{q}_d$. It can be different from the one of the basic structure.
- Finding the arithmetic crystal class (point group) compatible with the Bravais class, with the coefficient of the propagation vector: $\alpha\ \beta\ \gamma$. They are all given in the table 9.8.3.3 of the volume C of the International Tables of Crystallography[195].
- Determining the (3+*d*) superspace group compatible with the experimental extinctions.
- Confronting the solution ensuing from the latter steps with the restrictions imposed by the displacive-type and/or occupational-type modulation waves.

Often, several propositions can fit to experimental data, either due to a lack of resolution or to a not high enough quality of samples. Measuring properly the superlattice reflections of low intensities requires both very good single crystal samples and highly efficient diffraction methods.

As a remark, it must be underlined that commensurate and incommensurate modulated structures are frequently accompanied by a typical diffuse scattering, demanding an extensive experimental and theoretical study in order to arrive at a satisfactory explanation. A reliable structure determination becomes very difficult in cases where the interpretation of diffuse scattering has not been incorporated. The solution of problems of this kind needs careful thermodynamical consideration as to whether a plausible explanation of the structural data can be given. It is useful to start the interpretation of diffuse scattering by checking the diffraction pattern with respect to the dimensionality of the disorder concerned. Since each disordered direction in the crystal demands a violation of the corresponding Laue condition, diffuse streaks in reciprocal space correspond to one-dimensional disorder. This kind of order is typical for layer structures, but it is frequently observed in cases where several sequences of layers do not differ in the interactions of next-nearest neighbors.

2.2.Complexity induced by the coexistence of twinning and structural modulation

As explained in section 1, single crystals can be twinned, involving distinct individual orientations of the unit-cell in space, symmetric by the twin element. The presence of supplementary reflections within the basic reciprocal lattice due to twinning is not limited to basic reflections but also concerns the superlattice. Extra satellites are created by additional orientations at supplementary positions, and must be assigned together with their respective main reflections to their corresponding to their twin domain. It significantly complicates the determination of propagation vectors from the raw experimental diffraction pattern which thus corresponds to the superimposition of several modulated lattices, generating a high amount of superlattice reflections. Hence, the resulting apparent disorder of the diffracted pattern made of peaks which can be partially overlapped or not, is very confusing. Therefore, finding modulation vectors appears to be delicate and must be done very carefully, step by step, by considering separately all the effects entering in game, *e.g.* symmetry considerations, the number of twin individuals, as well as the restricted possibilities linked to the chemistry of the crystal. The following Figure depicts the effects of the particular twinning law of $La_2MO_{4+\delta}$ single crystals applied on the (3+1) incommensurately modulated P-orthorhombic lattice given as example in the Figure of the previous section.

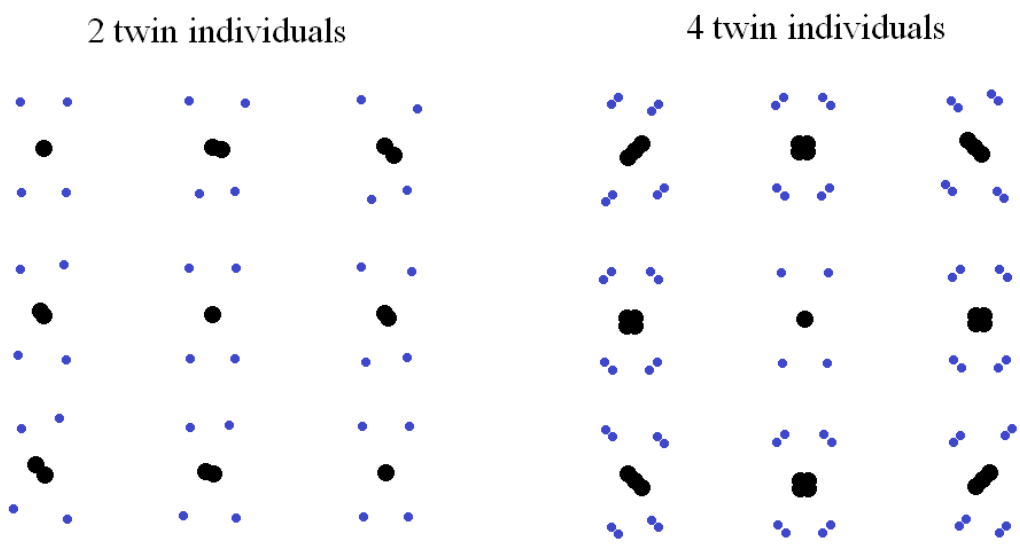

***Figure 3.5**: Twinning law of $La_2MO_{4+\delta}$ single crystals applied on the (3+1) incommensurately modulated P-orthorhombic lattice given as example in the Figure 3.4.*

Modulated structures are usually low-temperature phases of some periodic structures which are not modulated at higher temperatures. The symmetry of the high-temperature phase is preserved as the symmetry of the basic structure, but loss of mirror planes or rotational symmetry cannot be excluded, resulting in twinned crystal. Twinning can be merohedral for main reflections, but non-merohedral for satellites. This results in the multiplication of satellites but not basic reflections, yielding confusion for the determination of propagation vectors. Equivalences between satellites must be carefully checked in order to clarify the number of twin domains.

3. Choice of adapted method for characterizing modulated structures

Basically, all diffraction methods are suitable for exploring structural modulation *via* superlattice reflections in reciprocal spaces of ordered phases; however the different techniques and apparatus show advantages or disadvantages depending on the aim of the measurement and on the composition of the sample. In the complex context described in the previous section, and because modulation remains unknown in $La_2CoO_{4+\delta}$, the first step mandatory for solving the real structure of these compounds consists in visualizing the reciprocal space in order to determinate the positions and intensities of superlattice reflections. Nowadays, the experimental techniques used for standard diffraction experiments allow a much deeper insight into crystal structures than in the past. Using CCD cameras

(Charge Coupled Device) permits to scan a large portion of the reciprocal space, by diffraction, in a reasonably short time. Thus the problem on how to collect sufficient number of systematically weak reflections such as satellites is considerably reduced because it can be done without orientation matrix. This opens the possibility to study difficult modulated structures at very reasonable resolution and redundancy. Diffraction experiments with point-detectors are more valuable once the positions of the satellites are known, and make a very good complementary technique, in a second step.

The method usually adopted to characterize structural modulation in oxides remains, in great majority, electron diffraction. The efficiency of this technique does not need to be proven; a large amount of results ensuing from this experimental technique allowed solving complex modulated structures. The short coherence length of electrons permits to carry out experiments on powder samples by focusing the beam on single crystallites composing powders (nanometer sized regions of interaction). It is very convenient since it provides reciprocal space planes even without single crystal samples, and furthermore they can be obtained simply with one single data acquisition by two-dimensional detectors. Indeed the wavelengths associated to energetic electron beams used for diffraction is much smaller than the wavelengths of X-rays (the order of magnitude is of $\lambda \sim 1$ pm for electrons, while $\lambda \sim 100$ pm for X-rays). Hence, the Ewald sphere of electrons being much bigger than the one of X-rays, it allows to place all the reflections of a particular reciprocal plane together in diffraction condition (*c.f.* Figure 3.5). Moreover, the interaction of electrons with matter is much stronger (10^6-10^7 times higher) than X-rays due to the fact that electrons are scattered by the positive potential inside the electron cloud (Coulomb interaction), while X-rays interact with the whole electron cloud around the nuclei. Hence, the diffracted electron beams have a high intensity and thus require short exposure times for detection, *i.e.* in the order of only a few seconds per scan. ED patterns can thus be directly observed on the viewing screen of the electron microscope. Therefore, orienting a crystal along a special direction can be easily achieved by tilting the sample holder while observing changes of the ED pattern simultaneously.

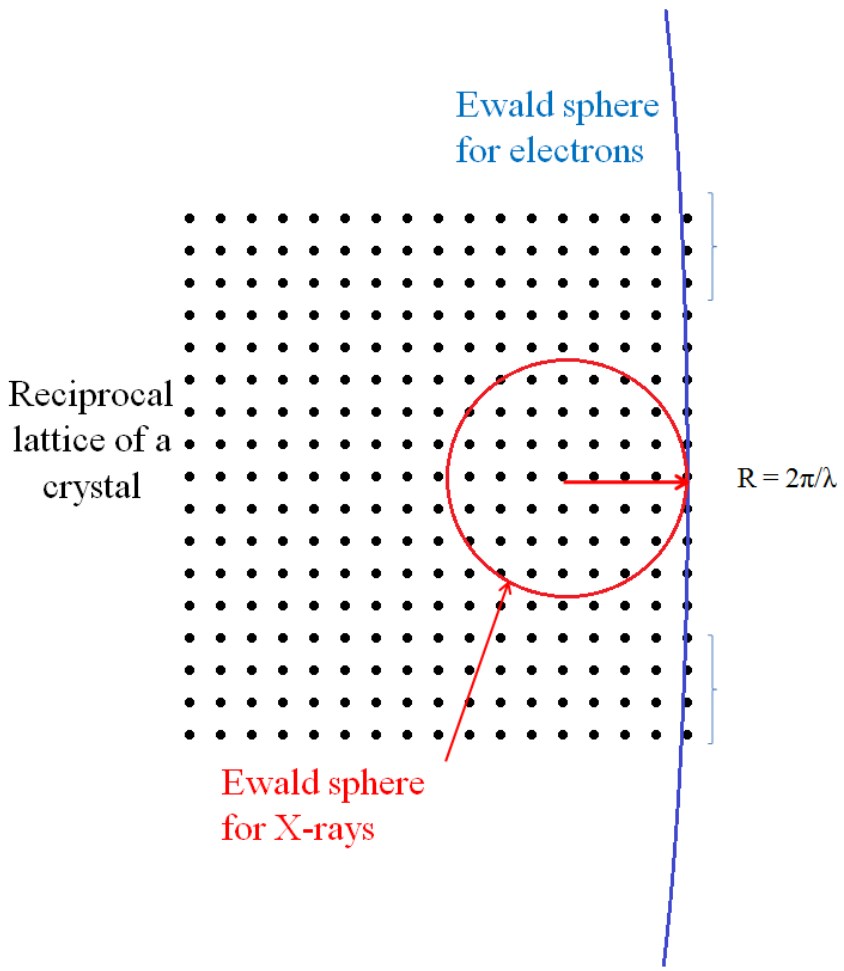

Figure 3.5*: Schematic representation of the comparison between the size of the Ewald sphere of typical electron and X-ray beams, relatively to a reciprocal space of a crystal of condensed phase. The two braces show that a small deviation of the Ewald sphere of electron from the reciprocal direction still persists at high angles.*

Despite all these advantages, electron diffraction is limited, and more particularly in our case. As shown on the figure above, even if the Ewald sphere of electrons possesses a huge radius in comparison to X-rays, its curvature still induces a distortion at high angles (pointed out by the blue braces on the figure), which usually prevents observing satellites of low intensity far from the center of the plane. Thus, this technique favors the detection of low angle regions, which is in contradiction with the expectations of this work, *i.e.* measuring as high angle as possible for better separation of split reflections in order to attribute each reflection to its individual twin. Indeed, as explained in section 1, the small orthorhombicity of $La_2CoO_{4+\delta}$ induces the overlapping of diffracted peaks at low angles whereas they are more clearly split for higher angles. Measuring only small angles constitutes a strong handicap precluding the

differentiation of satellites depending on their respective twin components. It is true that, theoretically, the nanometer-sized interacting region between electron and matter might be small enough to be focused on single domains, but experimentally it is not so simple, and generally, all electron diffraction studies reported in literature about parent compounds consist of twinned diffraction patterns. In addition to this, the strong interaction between electrons and crystal lattice gives an important role to multiple scattering, and consequently intensities of reflections are much influenced by this effect. This makes structure determination from electron diffraction more difficult and less reliable than the one from X-ray diffraction data.

In fact, the real disadvantages coming with electron diffraction for exploring the reciprocal space of $La_2CoO_{4+\delta}$ comes from: *i*) the problem of distortion at high angles explained above, *ii*) problems related to the reactivity of the compound itself. Electron beams have dramatic effects on the stability of this compound. Indeed, two main peculiarities of electron diffraction make this experimental technique inadequate for studying the structural modulation caused by interstitial oxygen ordering in twinned $La_2CoO_{4+\delta}$ single crystals. Firstly, except for very few specific apparatus, electron diffraction must be carried out under high vacuum; which strongly and very easily takes extra oxygen atoms out of the oxygen-rich samples, yielding a total vanishing of super-ordering and a transition to basic LTO phase. Secondly, the zone of interaction between electrons and matter is heated to rather high temperatures, which causes the same effects as before: it completely disturbs the metastable states of $La_2CoO_{4+\delta}$ samples, their oxygen content, their structural modulation, forbidding again to investigating long range ordering. The disappearance of satellites, when exposing the sample under electron beam, has been reported several times for $La_2NiO_{4+\delta}$[141,127]. It is true that the isostructural compounds, namely $La_2CuO_{4+\delta}$ and $La_2NiO_{4+\delta}$, have been studied a lot by electron diffraction, yielding to fruitful results (presented and referenced in the first chapter); however, these studies did not generally permit to differentiate twins although they allowed to visualizing the raw reciprocal space, and no definitive structural model could be refined from these data. Another fact which can also be underlined is the higher reactivity of Cobaltate compound, in comparison with Cu and Ni (spontaneous oxidation etc…), which makes the Cobaltate even more unstable than the two latter under intense conditions. Even if a modulated diffraction pattern of La_2CoO_4 could be possibly obtained from electron beam, a doubt would still remain concerning the validity of the subsequent results under atmospheric conditions.

That is why electron diffraction has been eliminated as a possible method for visualizing reciprocal-planes, this technique being too perturbing for $La_2CoO_{4+\delta}$. On the contrary, X-ray diffraction method is non-destructive, it does not necessitate vacuum conditions during the

operation, and thus allows collecting reciprocal patterns of samples remaining in suitable and stable thermodynamic conditions throughout experiments. Moreover, X-ray diffraction provides accurate structural refinements. Although slices of reciprocal space cannot be directly obtained by X-ray diffraction techniques due to the small radius of the corresponding Ewald sphere (*c.f.* Figure 3.5), it remains possible to reconstruct pictures of experimental space planes by means of post-acquisition data treatments. Indeed, because reflections of the same [*uvw*] direction are not in condition for diffraction at the same time, several scans have to be made for different positions of the lattice. Therefore, the whole diffraction patterns of single crystals is collected step by step by sample rotation (in φ angle), and acquiring intensities diffracted with a two dimensional detector (*e.g.* CCD cameras or image plate detectors). Then, slices of experimental reciprocal space can be reconstructed pixel by pixel *via* adapted softwares. Nevertheless, this procedure is time consuming in comparison with electron diffraction technique, but shows several advantages in the case of $La_2CoO_{4+\delta}$. It permits to obtain very well defined reciprocal maps up to high angles, allowing to differentiating reflections of each twin components. Moreover it allows to carry out reliable structural refinements, and especially with synchrotron X-ray beam.

Nevertheless, neutron diffraction is more adapted to the present studies for structural refinements. The coherent neutron scattering length of oxygen (~5.803 fm) is of the same magnitude than the one of La (~8.24 fm) and Co (~2.49 fm). It provides a good sensitivity to oxygen, in comparison with X-rays whose scattering length is proportional to atomic numbers. In addition, neutrons interact with nuclei of atoms which are quasi punctual; the Fourier transform of a punctual object being widely spread in the reciprocal space, neutrons are still strongly scattered at high angles in opposition to the one of X-rays which interact with the broad electronic cloud and thus are weakly diffused for high $\sin\Theta/\lambda$ values. However, two-dimensional detectors for neutrons are still not as well developed as the one for X-rays, and furthermore, such experiment would need a disproportionate time because of the weak interaction between neutrons and matter. Nevertheless, neutron single crystal diffraction with point-detectors is a powerful tool once satellite positions in reciprocal space are determined, and also simply for the study of the basic structure which also provides fruitful results; thus such experiments has been carried out complementary to X-ray diffraction experiments.

4. Reconstruction of reciprocal space planes and intensity integration from single crystal X-ray diffraction experiments.

4.1.X-ray diffraction apparatus

Initial characterizations of single crystals samples have been performed with a *KappaCCD* X-ray diffractometer (Bruker Nonius). The wavelength of the generator was the kα_1 emission line of Molybdenum (λ = 0.7092 Å). The X-ray area-detector consisted of a CCD camera. This type of detectors permits to reduce the time of acquisition, in comparison with usual point-detectors, several reflections being collected simultaneously. Moreover, gain in intensity is achieved through reducing the distance sample/detector concomitantly with a better collimation. In return, integration of intensities is more complicated. It is furthermore constraining in the case of complex systems, like twinned crystals for instance. The two-dimensional area which delimits the zone of integration for one reflection spot (in ω and 2Θ) is called "integration box"; its shape and size depend on the software used for data treatments. The software *EvalCCD*[203] commercialized with the *KappaCCD* diffractometer, allows calculating an optimized integration box by Fourier transformation of the physical shape of the crystal. It also refines unit-cell parameters and mosaicity in addition to intensity integration. The software *EvalCCD*[203] has been developed especially for challenging circumstances, such as the cases of crystals with non-spherical shapes, anisotropic mosaicity, overlapping of neighbor reflections for twin lattices, or satellite reflections for modulated structures. Its main advantage is the optional possibility to generate theoretical reciprocal planes of modulated structures that can be compared with experimental data by superimposition. This is a very practical tool, giving first hints concerning the symmetries of the diffraction pattern by try/error procedure.

Although reciprocal space planes could be successfully obtained with the latter apparatus, its resolution was not accurate enough for succeeding in separating the sets of reflections of each twin component. Moreover, harmonics of the incident X-ray beam (λ/2, λ/3 …) were polluting the data, creating artifact reflections. And finally, absorption effects were hardly differentiable from extinction effects, yielding a supplementary error in the experimental intensities. The wavelength of X-ray beam must be below the K-absorption edge of Lanthanum, *i.e.* below ~ 0.32 Å, in order to avoid absorption effects. Overcoming these obstacles could be done through performing similar experiments with synchrotron X-rays, instead of usual X-rays, on ID11 beamline at the European Synchrotron Radiation Facility (ESRF). ID11 is a multipurpose beamline concentrating on diffraction experiments in the area

of materials science. This beamline has been designed to exploit micro- and nano-focus X-ray beams. The X-ray synchrotron source is highly brilliant (5.10^{19} ph $s^{-1}mrad^{-2}mm^{-2}$) with a high flux (2.5^{16}ph s^{-1}) and the small wavelengths reachable (until λ = 0.17723 Å) allows to avoid absorption effect, which simplifies data treatments. Harmonic wavelengths of the source were systematically filtered. The system was equipped with a FReLoN detector[204] (Fast Read out Low Noise), a low noise CCD camera that combines high dynamic range, high read out speed, accuracy and improved duty cycles in single image. This camera has been developed by the Instrument Support Group at ESRF for experiments that require data acquisition on a time scale of milliseconds or a few tens of milliseconds. It has been reported[204] that the FReLoN can be applied equally to the investigation of rapid changes in long range order (via diffraction) and local order (via energy dispersive extended X-ray absorption fine structure) and in situations of X-ray hardness and flux beyond the capacity of other detectors. Consequently, the time of acquisition was strongly reduced (~1/2 h for a full data collection ID11 in comparison with ~20 hours on the *KappaCCD*) and the quality of the experimental data could be significantly optimized (very weak background, high resolution, accurate intensities…). Moreover, a heat blower has been mounted on the system, allowing to follow structural phase transitions with temperature.

The results ensuing from diffraction with *KappaCCD* will neither be shown nor discussed. This instrument was very useful and permitted to test many samples and appropriate experimental conditions. But the quality of data was not comparable with the one obtained from synchrotron X-ray diffraction. That is why, only the results from experiments performed on ID11 beamline are presented in this thesis.

4.2.Key process parameters and data treatments

Different essential parameters have to be adjusted during diffraction experiments. The step in rotation angle ($\Delta\varphi$) should be small enough for detecting all reflections; ideally one reflection should appear on three consecutive images for precise integration of intensity. The step $\Delta\varphi$ used was typically of 0.3°. The time of exposure t_{exp} for each scan should be chosen carefully depending on the purpose of the experiments. Each sample was systematically measured twice, one data set optimized for satellite detection and a second one for structural refinements. For determining positions of satellites, long exposure time was selected for accurate intensity; however it provokes saturation of main reflections. For structural refinements, t_{exp} was optimized to satisfy the two following conditions: *i*) no saturation of

main reflections, *ii*) higher possible intensity of satellites. Due to the very high flux of ID11 beamline, only 0.3 seconds of exposure were typically necessary per image. The last decisive parameter is the distance sample/detector. Small distances allow attaining high angles while long distances provide a better separation of split reflections. For $La_2CoO_{4+\delta}$ samples, the intermediate distance of 230 mm was chosen as the best solution, after several tries. For La_2CuO_4 samples which are not modulated, the distance sample/detector was reduced to 130 mm.

Raw experimental data resulting from ID11 experiments consist of two-dimensional images in bruker format. They can be directly treated *via SMART* and *SAINT* softwares for peak indexing and intensity integration respectively, but those applications do not provide reciprocal space reconstructions. Hence, raw data have always been converted to a format adapted to *CrysAlis* program. The latter combines several convenient functions. It permits to refine the orientation matrix and instrument parameters, to reconstruct reciprocal planes pixel by pixel, to index all reflections even for twinned and modulated lattices and finally to integrate their intensities. For satisfactory structural refinements, intensities of all Bragg reflections should be properly integrated, which is particularly delicate. Overlap of reflections often prevents this goal to be reached. Lack of accurate intensities hampers the application of computational methods of structure analysis, and thus it deteriorates the structure model resulting from refinements.

An acceptable list of (*hkl*)-intensities for single twin domains remains hard to sort from experimental data. It implies that *i*) the volumic ratio of each twin must be carefully calculated from intensities, *ii*) all (*hkl*) reflections have to be associated to their respective domain(s) and *iii*) all reflections are classified whether they are split into two, three or four peaks. It permits to calculate, for each reflection, the ratio of the global intensity corresponding to the same single-domain. Then, it ideally results in a list of (*hkl*)-intensity for each domain. But in addition to the complexity of twin separation, problems also arise with the integration of intensities. Main reflections are much broader than satellites, and consequently the area integrated must be optimized for each kind of peak. If the so-called “integration box” is adapted to the size of the main reflections, several satellites will be integrated together. On the contrary, if it is adapted to the size of satellites, main reflections will be cut. After testing different softwares designed for such tasks, the step of integration has been chosen to be carried out with the software *CrysAlis* which allows adapting the size of integration boxes on each peak.

Several softwares have been developed for the treatment of experimental diffraction intensities and structural refinements by Least-Square method. Among them, the Software *JANA2006*[205] has been used since it is adapted for solving modulated structures[206]. Moreover, it also provides Fourier calculations which have been also useful. The subsequent electronic densities have been visualized by the software *VESTA*[207]. Figures of atomic structures and 3D visualizations of polyhedra have been made through Diamond 2.1b[208] software.

5. Single crystal neutron diffraction experiments and Maximum Entropy Method.

5.1.Neutron diffraction apparatus

The thermal neutron single crystal diffractometer TriCS[209] is installed at the Swiss spallation neutron source (SINQ[210]) at the Paul Scherrer Institute (PSI, Villigen, Switzerland). TriCS is designed for investigations of commensurate and incommensurate crystal and magnetic structures as well as phase transitions driven by temperature, magnetic field or pressure. The flux is up to 1.02×10^6 n/cm^2/sec. Two wavelengths are available; the smallest one, corresponding to the (311) reflection of the Ge-monochromator, λ = 1.178 Å, has been systematically used for the experiments. It is consistent with scattering angular limits of $0^o < 2\Theta < 115^o$, $(\sin\Theta/\lambda)_{max} = 0.715$ Å^{-1}.

Prior to experiments, the crystal sample is adjusted into the geometrical center of the Eulerian cradle by optical alignment. In a second step, Bragg reflections are searched with neutrons. In the general case, the orientation of the unit-cell is not known and the search can be done by performing random scans in ω and φ at fixed positions of χ and 2Θ using the point-detector (one single He^3-tube). Pre-alignment on other instruments fastens this procedure. In our case, single crystal samples have been systematically oriented beforehand through X-ray Laue diffraction measurements (*c.f* section 3.5.4, chapter 2) so they could be directly oriented with *c*-axis perpendicular to the diffraction plane. This is the optimal orientation since it allows to measure orthorhombicity from a single ω-scan on a (*hhl*) reflection. Knowing at least two reflections and the unit cell of the crystal, the *UB* matrix (orientation matrix of the crystal with respect to the cradle) can be roughly determined. The program *INDEX* helps to find the (*hkl*) indexes. The *UB* matrix is then improved by centering 10 to 20 reflections and by refining cell parameters. The collection of scattered intensity can then be launched automatically from an input file including all preferences for the acquisition. In case of

modulated structures, superlattice reflections can be collected as well, but the modulation vector has to be previously determined since the point detector-should be set at the proper position and the crystal in condition of diffraction. In any case, neutron diffraction on basic reflections is still powerful for investigating average structures, yielding mandatory results for understanding the disorder. Indeed, data collection of modulated structures is delicate, as well as subsequent data analysis. Many precautions must be taken for the interpretation of the results. Much valuable information can be obtained from average structure investigations.

In 4-circle mode, the system can be equipped with cryostats or cryofurnaces allowing to studying phase transitions driven by temperature.

5.2.Maximum entropy method (MEM)

This calculation method, coming from the research in astronomy, has been used in crystallography since the beginning of the 1990's[211]. Applying the maximum entropy method for the reconstruction of the nuclear density from neutron diffraction data permits to emphasize the real positions of oxygen atoms in the lattice. One advantage using the MEM in particular for partially disordered structures is that the reconstructed scattering density is not associated to an atom with its proper thermal ellipsoids but to the most probable scattering density distribution. This is equivalent to an anharmonic description of all the constituents which is model free, the only constraint being the symmetry imposed by the space group. The second advantage results from the quality of the density distribution concerning the background, which is usually close to zero and allows the visualization of details, which are inconclusive with standard Fourier techniques. This concerns above all the description of the extra oxygen atoms. The third advantage using MEM is that partially phased data sets can be used, *e.g.*, excluding prior information on the interstitial or apical oxygen atoms. As the phases of the structure factor are well determined by the rest of the structure, the phase problem does not really exist in our case. Here, the phases (0 or π) have been systematically found through least square refinements with good agreement factors, and listed together with their corresponding experimental intensities and (*hkl*) indexes.

MEM is based on thermodynamic theories. When applied in crystallography on experimental diffraction data, it provides calculation of the most probable three-dimensional distribution of electronic density (for X-rays) or nuclear density (for neutrons). Different algorithms are available for MEM; among them, the famous Sakata-Sato algorithm has been chosen for this

thesis. Its principle is the following. The direct unit-cell is gridded in three dimensions into N pixels of the same size. The guidelines concerning the choice of the number of pixels along each axis of the unit-cell depends exclusively on the size of the cell and on the space group. It is preferable to choose values not only leading to judicious pixel size but also yielding symmetry elements to be located at the intersections of grid lines. To each pixel is attributed the two following variables: ρ, the normalized density calculated from the model, and τ, the density derived from prior information (F(000), homogeneity or not of the density, space group restrictions…). The density ρ is obtained from the entropy S:

$$S = -\sum_{N} \rho \ \ln \frac{\rho}{\tau} \qquad equation\ 8$$

S is maximized by imposing the following constrains for convergence:

- for each pixel: $\rho > 0$
- $C_N = \sum_N \rho = 1$
- $C_M = \sum_M \frac{|F_o - F_c|^2}{\sigma^2} = M$ (M = total number of reflections with known phase)

The structure factor F_C is given as:

$$F_C = T \sum_{i}^{N} \rho_i \exp\left(2\pi \mathrm{i}\ h_j r_i\right) \qquad equation\ 9$$

For neutrons, T is the summation of all the coherent scattering lengths b_{coh} for one unit-cell; For X-rays it corresponds to the total number of electrons in the cell. The theoretical structure factor F_C is calculated for each reflection h_j and for every pixel of the gridded unit-cell r_i. The density ρ cannot be calculated analytically. Several approximation methods can be used depending on each particular case. In this work the 0th order single-pixel approximation method was systematically used. Then, ρ can be expressed as:

$$\rho = \frac{\tau}{Z} \exp\left(-\lambda \ \frac{\partial C_M}{\partial \tau}\right) \qquad equation\ 10$$

with

$$Z = \sum_{N} \tau \exp\left(-\lambda \ \frac{\partial C_M}{\partial \rho_n}\right) \qquad equation\ 11$$

Maximum entropy distribution is reached through n iterations, as following:

$$\rho_{n+1} = \frac{\rho_n}{Z} \exp\left(-\lambda \frac{\partial C_M}{\partial \rho_n}\right) \qquad equation\ 12$$

The Lagrangian multiplier λ is constantly adjusted during iterations as follows:

$$\lambda_{n+1} = \lambda_n + t\lambda_0 \qquad equation\ 13$$

Initial parameters λ_0 and t have to be estimated by the operator and are both set prior to calculations. The choice of this combination of parameters is crucial for reaching the convergence, which is, in general, rather arduous. With a too small value for λ_0, the convergence will be slow and may not reach $C_N = 1$. Conversely, with a too big λ_0, the convergence will never be attained. Choosing $t \neq 0$ permits to adjust λ to each iteration, which considerably favors the convergence of the calculation process. For the 0th order single-pixel approximation method, a sufficiently small value has to be chosen for λ_0, which leads to an increase in the total number of iterations but which works well in nearly every cases.

The agreement factors R_F and R_{wF} are indicators of the reliability of MEM analysis. They are defined similarly to the agreement factors linked to usual structural least square refinements of diffraction data, as follows:

$$R_F = \frac{\sum_M |F_c - F_O|}{\sum_M |F_O|} \quad and \quad R_{wF} = \sqrt{\frac{\sum_M |F_c - F_O|^2}{\sum_M |F_O|^2}} \qquad equations\ 14$$

Different programs have been designed to treat experimental diffraction data *via* MEM. Among them, two softwares have been used: '*BayMEM*', working directly with the output files of *JANA2006* and the so-called "super-fast program" *PRIMA*[212] (PRactice Iterative MEM Analysis). The latter has been preferentially chosen. Indeed, *PRIMA* is an improvement of the initial program *MEED*[211]; but whereas the latter, it has been written in Fortran 90 and it operates on Windows 2000/XP. The time of calculation has been considerably reduced providing fast data treatments. *PRIMA* is included in the software package called *VENUS*[213] (Visualization of Electron/NUclear densities and Structures), which also contains the application *VESTA*[214] (Visualization for Electronic and STructural Analysis), providing visualization of 3D electron/nuclear density profiles directly from the output files generated by *PRIMA*. The application *VEND*[213] (Visualization of Electronic/Nuclear Densities) of *VENUS* package has been used in parallel for the visualization of two dimensional projections of densities.

Chapter 4

Crystal structures of stoichiometric La_2CuO_4 T and T', and oxygen rich $La_2CoO_{4+\delta}$ phases with δ = 0.14, 0.19, 0.25, at ambient temperature

1. Introduction

In this chapter, the atomic structures of stoichiometric La_2CuO_4 compounds and oxygen-rich $La_2CoO_{4+\delta}$ phases, stable at room temperature (RT) will be presented in details. A good knowledge of the phases at RT will allow a better comprehension of the phase transitions with temperature and δ, presented in chapter 5.

Investigating stoichiometric phases is an inevitable step. The comprehension of the O_{int}-free structure is necessary before investigating the effects of oxygen intercalation which precisely consist in deformations of this basic lattice. The stoichiometric cobaltate La_2CoO_4 has been very well characterized by R. Le Toquin through single crystal X-ray and neutron diffraction experiments[8]. Therefore, studies of the stoichiometric phase have not been repeated on the cobaltate compound but have rather been focused on La_2CuO_4. The latter cuprate has been enormously studied but the recent discovery of polymorphism for the La_2CuO_4 system put new inquiries forward concerning the crystal chemistry. This compound is able to adopt both, the T-type structure (isostructural to La_2CoO_4) and the T'-type one (isostructural to Nd_2CuO_4), at ambient temperature depending on the synthesis procedure. The fact that we obtained and analyzed single crystal samples of T'-La_2CuO_4 for the first time permitted further structural investigations yielding to new results.

For non-stoichiometric compounds of T-type phase, insertion of interstitial oxygen ($\delta > 0$) induces the deformation of the interlayer tetrahedral sites when occupied by extra oxygen atoms. If δ is relatively small ($\delta < 0.1$), the subsequent modification of the tilts of octahedra cannot spread in three-dimensions. The structure is thus partially disordered[8]. But it is conceivable that above a certain critical value of δ, long-range orders emerge from propagation of tilts concomitantly with the ordering of interstitial oxygen atoms. In $La_2NiO_{4+\delta}$ extra oxygen ordering has been shown to be associated with charge localization on the transition metal ions, inducing simultaneous charge ordering[151,152,215,216]. In comparison with

Cu and Ni compounds, the cobaltate allows a higher amount of extra oxygen (δ_{max} = 0.25) due to the stability of the +III oxidation state of cobalt[47,12]. The mixed valence state of Co induced by extra oxygen intercalation reduces the size of the Cobalt's coordination sphere, resulting in disparities in the Co-O interatomic bond lengths. This makes $La_2CoO_{4+\delta}$ a very good candidate for investigating the effects of oxygen intercalation on the structure and properties of this type of compounds. However, for high values of δ, only the average structures have already been described; although superlattice reflections have been clearly observed, they have not been included in the structural descriptions available in literature because of the complexity induced by the combination of twinning and modulation. Hypothetical oxygen ordering has been proposed, but solving the real structural arrangement of oxygen-rich compounds remains a challenge. Nevertheless, the work of R. Le Toquin has remarkably emphasized the comprehension of $La_2CoO_{4+\delta}$, and has permitted to state solid basis for further investigations. The state of the art concerning $La_2CoO_{4+\delta}$ is summarized in chapter 1, and more details are given about the stoichiometric compound in the following section.

In the present work, a strong accent has been put on the study of structural modulation in oxygen-rich $La_2CoO_{4+\delta}$ in order to complete the structural studies previously carried out on this oxide. The procedure employed to solve the structures is described in details in order to give references for allowing further investigations on this compound, or on others, with this kind of experimental data. The $La_2CoO_{4+\delta}$ compound adopts distinct structures at RT as function of δ. Starting samples of $La_2CoO_{4+\delta}$ have been taken out from the *as grown* single crystal rods, scratched with a razor blade. After testing various thermal treatments in the range of RT-800K, three prototype crystal phases with modulated structures stable under atmospheric conditions could have been distinguished and isolated at RT: *i*) the *as grown* phase itself δ = 0.14, *ii*) the phase obtained after simple annealing under air δ = 0.19, and *iii*) the phase obtained after annealing under oxygen-rich atmosphere δ = 0.25. The temperature of annealing is not significant but is correlated to the time of the process: the lower the temperature is, the longer the annealing should be. A second type of $La_2CoO_{4.25}$ sample, previously obtained *via* electrochemistry in KOH electrolyte by R. Le Toquin, has also been studied for comparison. Among these phases stable at RT, the structure of the *as grown* $La_2CoO_{4.14}$ has been investigated by neutron diffraction.

Samples appropriate for ID11 beamline have been selected as function of their shapes, which must be as isotropic as possible, and as function of their sizes that should be comprised between 100 and 150 µm. They have been systematically analyzed with the *KappaCCD* diffractometer (Bruker Nonius, λ = 0.7092 Å) prior to synchrotron measurements, in order to

choose the best samples with fewer amounts of twin components and of best quality (crystallinity, sharpness of reflections, no impurities, satellites until high angles…). During experiments, samples have been systematically placed in quartz capillaries (Ø 0.2 mm). They have been let randomly oriented, and they were not glued for avoiding any contamination, unwanted chemical reaction, or even strains in case of important volume changing.

2. Stoichiometric La_2MO_4 compounds at RT: single crystal structures of basic T and T'-phases.

2.1. Stoichiometric phase for M = Co and Cu, combination of static and dynamic displacements

The stoichiometric T-phase of La_2MO_4 (M = Co, Ni, Cu) compounds has been extensively studied for several decades; many descriptions of those phases are available in peer reviews (cf. chapter 1, section 1.3 and section 2). However few words will be given specifically about La_2CoO_4 and La_2CuO_4 in order to state the foundations of the present work. As explained in the introduction, investigating the structural modulation of oxygen-rich samples necessitate a good knowledge of the basic structures. At RT, $La_2CuO_{4.00}$ and $La_2CoO_{4.00}$ synthesized by usual solid state routine are isostructural, space group *Bmab*, but their respective cell-parameters differ. While *c*-axis of the stoichiometric cobaltate is of 12.65 Å, it takes the value of 13.15 Å for the cuprate due to the strong Jahn-Teller effect brought by Cu as central atoms in CuO_6 octahedra. The interatomic distance M-O between apical oxygen and transition metal is of 2.41 Å in La_2CuO_4 and of 2.30 Å in La_2CoO_4. Previous neutron diffraction results on twinned single crystals of these compounds show that angular separation 2Δ (equation 3) of (*hhl*) reflections is of 3° for La_2CoO_4, while it is of 1.5° for La_2CuO_4. The strong orthorhombicity of La_2CoO_4 implies tough internal strains in this compound. Octahedra tilt in the $[010]_{Bmab}$ direction. The corresponding angle of tilt is of 3° in La_2CuO_4 and of 7° in La_2CoO_4. In brief, the structure of stoichiometric La_2CoO_4 at RT is strongly distorted in comparison with La_2CuO_4.

The Goldschmidt tolerance factor *t* (equation 1) calculated from the structural model of La_2CoO_4 is very low (0.86); and that might be the reason why $La_2CoO_{4.00}$ compound is so unstable under atmospheric conditions. It tends to decrease internal strains by uptaking oxygen atoms from air into interstitial sites yielding elongations of La-O_{ap} bond distances and stretching of Co-O_{ap} ones. In the stoichiometric compounds the interstitial site (empty of

atoms, *occ* = 0) is strongly asymmetrical, two distances O_{int}-O_{ap} exist in the *Bmab* symmetry: for instance in the cobaltate, the distances between interstitial site and closest apical oxygen atoms is of 1.96 Å, and it is of 2.26 Å for the two others apical oxygen atoms. Consequently, the centroid of the tetrahedral site is shifted from the interstitial position (¼ ¼ ¼). Hence, insertion of extra oxygen atoms within the layers involves the opening of tetrahedral sites by the tilt of MO_6 octahedra in opposite directions.

Comparatively to the results concerning T'-La_2CuO_4 (next section), synchrotron X-ray diffraction has been carried out on the T-phase of $La_2CuO_{4.00}$. Data collection has been performed with $\Delta\varphi$ = 0.3° for a total coverage of 270°; and t_{exp} = 0.3 seconds per image. The resulting 934 pictures were handled with *CrysAlis* yielding the reconstruction of experimental diffraction patterns in two dimensions. Figure 4.1 shows the resulting (*hk*1) reciprocal space map, with $\vec{c}$* normal to the plane, of a twinned La_2CuO_4 single crystal sample synthesized in a previous work[217]. The resulting diffraction pattern is typical of stoichiometric LTO compounds, *Bmab* symmetry, twinned into two domains (twin element: (-110) mirror plane).

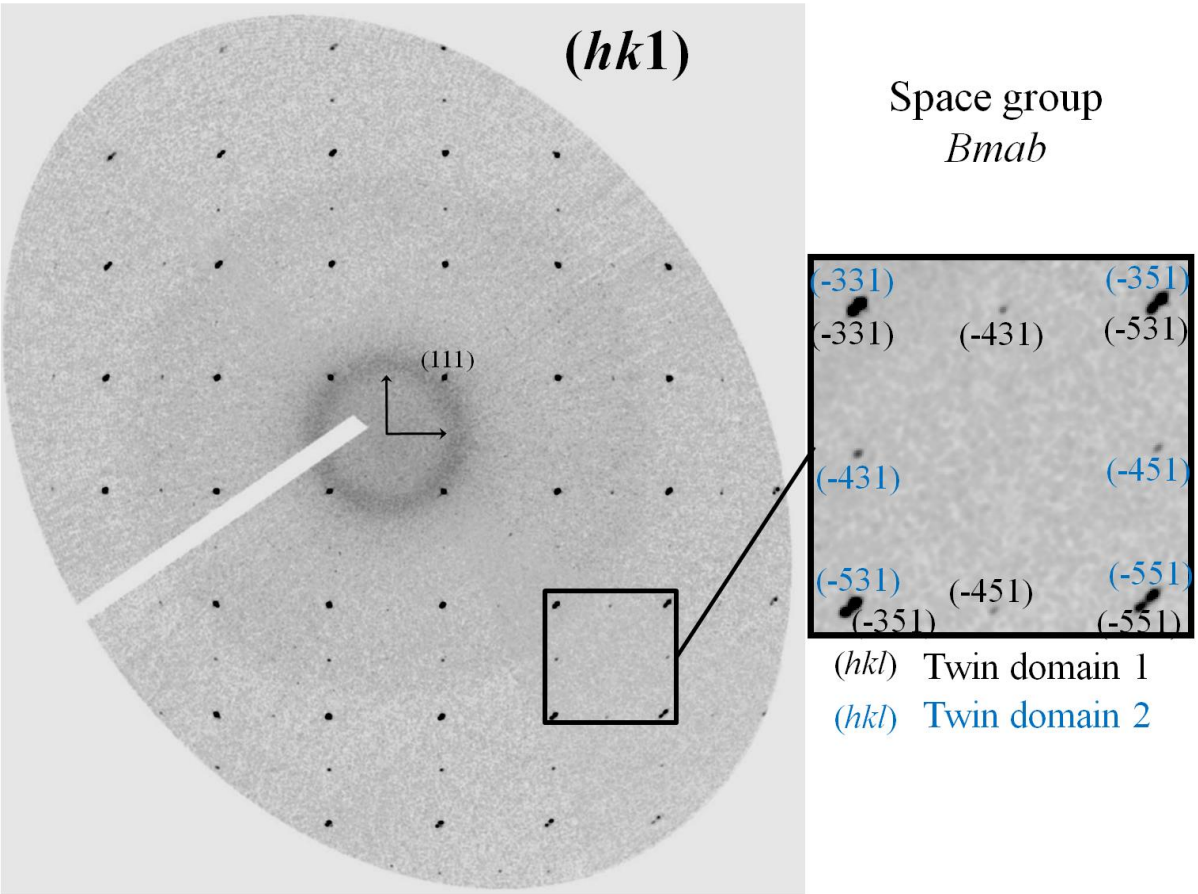

***Figure 4.1**: Experimental reciprocal space plane reconstructed from synchrotron X-ray diffraction data (ID11@ESRF), of orthorhombic T-La_2CuO_4 at RT , space group Bmab. Bragg reflections can be indexed with two twin individuals.*

The reflections of lower intensities, allowed by *Bmab* space group, are related to the specific structural distortion of the stoichiometric LTO phase. Indexation of all these low-intensity reflections can be done according to the twinning law for two individual orientations of the unit-cell in the crystal (section 1, chapter 3), as shown on figure 4.1.

Intensities have been successfully integrated separately for the two individual twins through *CrysAlis* program, with good agreement factors, R_{int} = 4.2 %. The diffraction pattern of once twinned LTO-phase remains simple enough to allow a twin separation on account of the twinning law. The structural model of a single domain resulting from least-square refinements carried out with *JANA2006* is shown on the part *a)* of table 4.1. On part *b*), are presented the anisotropic displacement factors reported by H. Kwei *et.al*[103] resulting from pulsed-neutron diffraction experiments that are thus more precise for oxygen coefficients. The two models are in good agreement: the displacement factors follow the same tendencies. The CuO_6 octahedra are all, and exclusively, tilted in $[0\pm10]_{LTO}$ direction in each twin domain, symmetric by the diagonal mirror plane (110).

Table 4.1:

a) Structural model of T- La_2CuO_4 single domain refined with JANA2006 from synchrotron X-ray diffraction data.

Atom	*x/a*	*y/b*	*z/c*	*Occ*	U_{11}	U_{22}	U_{33}	*Ueq*
La	0	0.9933(5)	0.3614(7)	2	14.2(2)	13.9(2)	11.2(1)	13.1(2)
Co	0	0	0	1	11.1(2)	9.2(2)	18.3(1)	12.8(2)
O (eq)	¼	¼	0.992(1)	2	12.(2)	11.(1)	15.(9)	13.(4)
O (ap)	0	0.036(4)	0.182(2)	2	15.(1)	27.(1)	14.(9)	18.(4)

Cell parameters: a = 5.35(3) Å b = 5.40(9) Å and c = 13.14(6) Å, $\alpha = \beta = \gamma = 90°$. 2Δ = 1.19°, V = 380.42(1) $Å^3$. Space group *Bmab*, R_{int} = 4.2 %, 389 observed reflections. Wavelength of X-rays: 0.2072 Å. Agreement factors: R_F = 3.97 %, R_{WF} = 3.82 %. *Uij* are given in 10^{-3} $Å^2$.

b) Anisotropic displacement factors of La_2CuO_4 at RT reported by H. Kwei et.al[103]*, resulting from pulsed-neutron diffraction experiments (HIPD@LANSCE, Los Alamos).*

Atom	U_{11}	U_{22}	U_{33}	U_{12}	U_{13}
La	8.2(3)	6.00(26)	4.74(19)	0	1.1(3)
Co	5.3(4)	2.4(4)	9.2(4)	0	1.5(5)
O (eq)	5.8(4)	4.5(3)	12.4(5)	-2.69(16)	0
O (ap)	14.1(5)	22.1(4)	6.74(28)	0	-9.(5)

Space group Bmab, Uij given in 10^{-3} $Å^2$.

Even if the structure was refined in both cases with the *Bmab* space group, *i.e.* taking the static tilting of octahedra into account, the in-plane atomic displacement factors of apical oxygen atoms remain high in comparison with the other atoms. This characteristic is of first importance, since in addition to static distortions of octahedra, it demonstrates the occurrence of dynamic motion of apical oxygen atoms in addition to their static displacements. This fact

is in accordance with several previous studies[103,86,87,218], based on single crystal neutron elastic and inelastic scattering results, concerning the vibrational properties and lattice dynamics of La_2CuO_4 that have revealed soft-phonon modes at RT involving cooperative dynamic switching of rigid CuO_6 octahedra along the [100]-axis. More recently, phonon frequencies and lattice relaxation have been calculated for $La_2CuO_{4+\delta}$ from first principles within density functional theory (DFT), highlighting the prominent role of phonon modes and lattice instabilities in the oxygen diffusion process[219]. Concerning the stoichiometric $La_2CuO_{4.00}$, *i.e.* without O_{int}, the mode of lowest energy corresponds to octahedra tilting (Figure 4.2) at the *X*-point of the primitive Brillouin zone. A similar experimental observation has also been reported for La_2NiO_4[85].

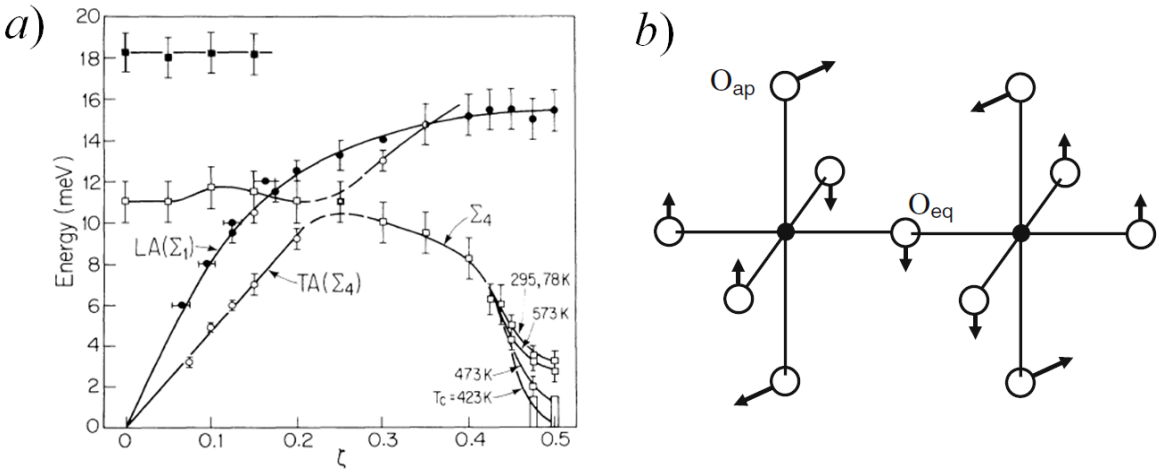

***Figure 4.2**: a) Phonon dispersion curve in La_2CuO_4 resulting from inelastic neutron scattering experiments reported by R. J. Birgeneau et.al[86] in 1987, showing a different position of the tail at the X-point of the TA phonon branch depending on temperature. b) Representation atomic displacements involved by this lowest soft mode calculated by DFT at the X point of the Brillouin zone, for stoichiometric La_2CuO_4, reported by Villesuzanne et.al[219] in 2010, similar to what has been found in La_2NiO_4 by Pintschovius et.al[85] in 1989.*

All unstable optical modes calculated for $La_2CuO_{4.00}$, except the two rotational modes around -12.4 meV, involve large O_{ap} displacements along the [100] or [010] axes, in particular for the bending modes found at -12.1 and -11.3 meV and more precisely for the tilting mode at -10.3 meV. In addition, supplementary modes, associating appropriate in-plane lanthanum displacements, involve the breathing of the La_2O_2 windows connecting interstitial sites. Besides CuO_6 tilting modes, the La_2O_2 windows breathing modes of low energy might be correlated to, and even amplify, oxygen mobility along the [100] or [010] axes in $La_2CuO_{4+\delta}$. Implication of soft-phonons and lattice instabilities on oxygen diffusion properties of $La_2MO_{4+\delta}$ will be further discussed in chapter 5.

2.2.Single crystal structure of T'-La_2CuO_4, only static contribution

The typical sizes of T'-La_2CuO_4 single crystal samples synthesized by the molten salt technique are in the order of magnitude of 100 µm, which prevents neutron diffraction studies. However, samples could have been investigated by synchrotron X-ray diffraction experiments (with λ = 0.2072 Å, $\Delta\varphi$ = 0.2° and t_{exp} = 0.3 s/image). The representative (*hk*1) reciprocal plane reconstructed from experimental data is shown in Figure 4.3.

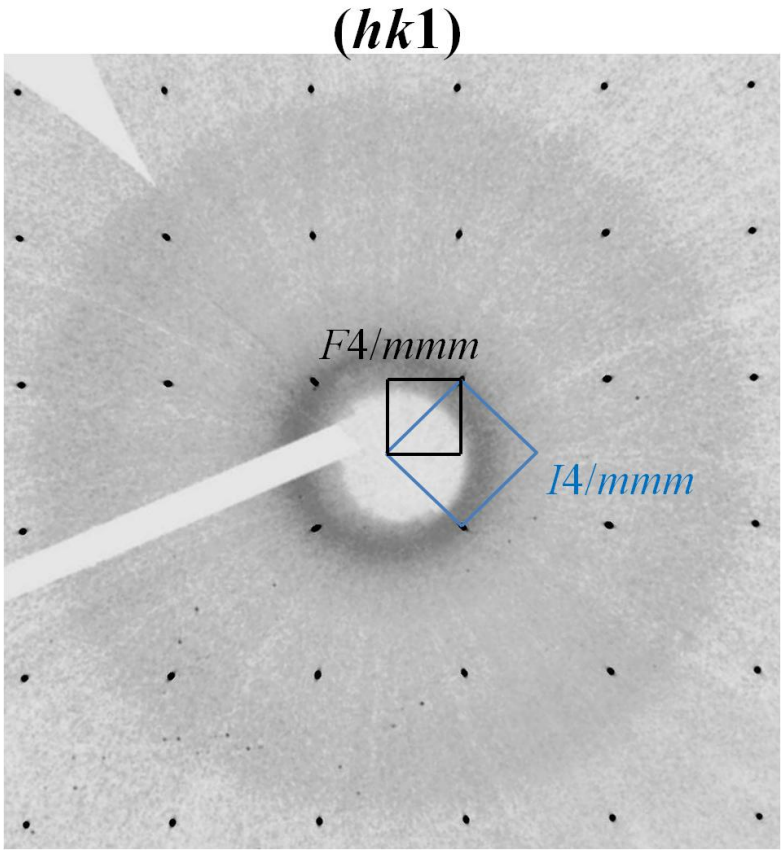

Figure 4.3*: (hk1) Experimental reciprocal space plane reconstructed from synchrotron X-ray diffraction data (ID11@ESRF), of tetragonal T'-La_2CuO_4 at RT.*

The reciprocal space of this phase corresponds to tetragonal symmetry, it is empty of reflections characteristic of *Bmab* space group. The diffraction pattern can thus be indexed through the tetragonal unit-cell model, space group *I4/mmm*, which is equivalent to the *F4/mmm* space group of the unit-cell of same proportions than LTO phase (*c*-axis is identical for the two cells). Relations between unit-cell vectors are the following $V_I = V_F/2$ and $a_I = \frac{1}{\sqrt{2}} \times a_F$. Both reciprocal unit-cells are shown on the figure for clarity. Because of the fourfold axis collinear to $\vec{c}^*$, twinning does not occur in T'-La_2CuO_4; hence, results are consistent with single phase sample. At first sight, this diffraction pattern could be easily confused with the

one of HTT phase of same space group, and qualitatively of similar reciprocal space. However, the experimental cell-parameters are the following: $a = b = 4.02(3)$ Å and $c = 12.53(4)$ Å corresponding to unit-cell volume of V = 202.85(6) Å^3. These values are consistent with T'-type atomic structure[13,16] and allow to differentiate clearly T'- and T-type phases. One other practical way yielding to an easy distinction between diffraction patterns of T- and T'-phase, is to look at (*hk*2) reciprocal plane. The latter is empty of reflections for T', whereas intensity peaks are observable on this plane for the T-phase. Indeed, for T'-phase the structure factor is equal to 0 when $|l| = 2$, yielding extinction of the corresponding reflections.

Intensities have been integrated and averaged with equivalences related to the *I4/mmm* space group, the resulting internal agreement factor was R_{int} = 1.4 %. Hence, data are of good quality and the space group matches very well with the experimental results. Structural refinements resulted in the model presented in table 4.2. The corresponding 3D electron density repartition in the unit-cell, calculated by MEM (*cf.* chapter 3, section5.2) is shown on figure 4.4, together with the subsequent structural model. At the convergence, agreement factors of least square refinements are R = 2.07 %, R_w = 1.61 %., and the ρ_{min}/ρ_{max} values of Fourier difference maps are -0.89/1.04 electron/Å^3.

Table 4.2: *Structural model of T'-La_2CuO_4 single crystal refined with JANA2006 from synchrotron X-ray diffraction data.*

Atom	*x/a*	*y/b*	*z/c*	*Occ*	U_{11}	U_{22}	U_{33}	U_{eq}
La	0	0	0.35261(1)	2	7.9(1)	7.9(1)	9.41(2)	8.4(1)
Cu	0	0	0	1	5.1(1)	5.1(1)	10.4(3)	6.8(2)
O (eq)	½	0	0	2	7.(2)	7.(2)	12.(1)	8.(8)
O (int)	½	0	¼	2	6.(4)	6.(4)	9.(1)	7.(3)

Cell parameters: $a = b = 4.02(3)$ Å and $c = 12.53(4)$ Å, $\alpha = \beta = \gamma = 90°$, V = 202.85(6) Å^3 Space group *I4/mmm*, R_{int} = 1.4 % on 271 observed reflections. Wavelength of X-rays: 0.2072 Å. Agreement factors: R_F = 2.07 %, R_{WF} = 1.61 %. *Uij* are given in 10^{-3} Å^2.

Anisotropic displacement factors, refined independently for each site, are all very small in comparison with the ones of the usual T-phase, as portrayed on Figure 4.4 where ellipsoids are proportional to the refined anisotropic displacement factors (they are shown with the same scale of amplitude for both phases). Conversely to the T-phase, the T'-La_2CuO_4 crystal lattice does not exhibit proofs of dynamic fluctuations. Instead, atoms appear to be well localized and thus not submitted to large amplitude lattice vibrations. The total absence of oxygen on apical site replaced by full occupation of interstitial site seems to reduce considerably internal strains and lattice instabilities, stabilizing the atomic structure and yielding to very well defined, localized and static atomic positions. The Goldschmidt tolerance factor calculated from the structural model shown above, is of t = 0.84 (equation 1) corresponding to a

tolerance factor of *tf* = 0.97 (equation 2). Both are consistent with very low internal strains. Hence, the T'-phase does not necessitate extra-oxygen to relax. The atomic structure is stable and oxygen stoichiometry is "locked". Therefore, the uptaking of oxygen does not occur in T'-phase. The totally different reactivity of T and T'-phases with regard to oxygen mobility and bulk diffusion must be correlated to the presence or not of low energy lattice dynamics, under the form of soft phonon modes.

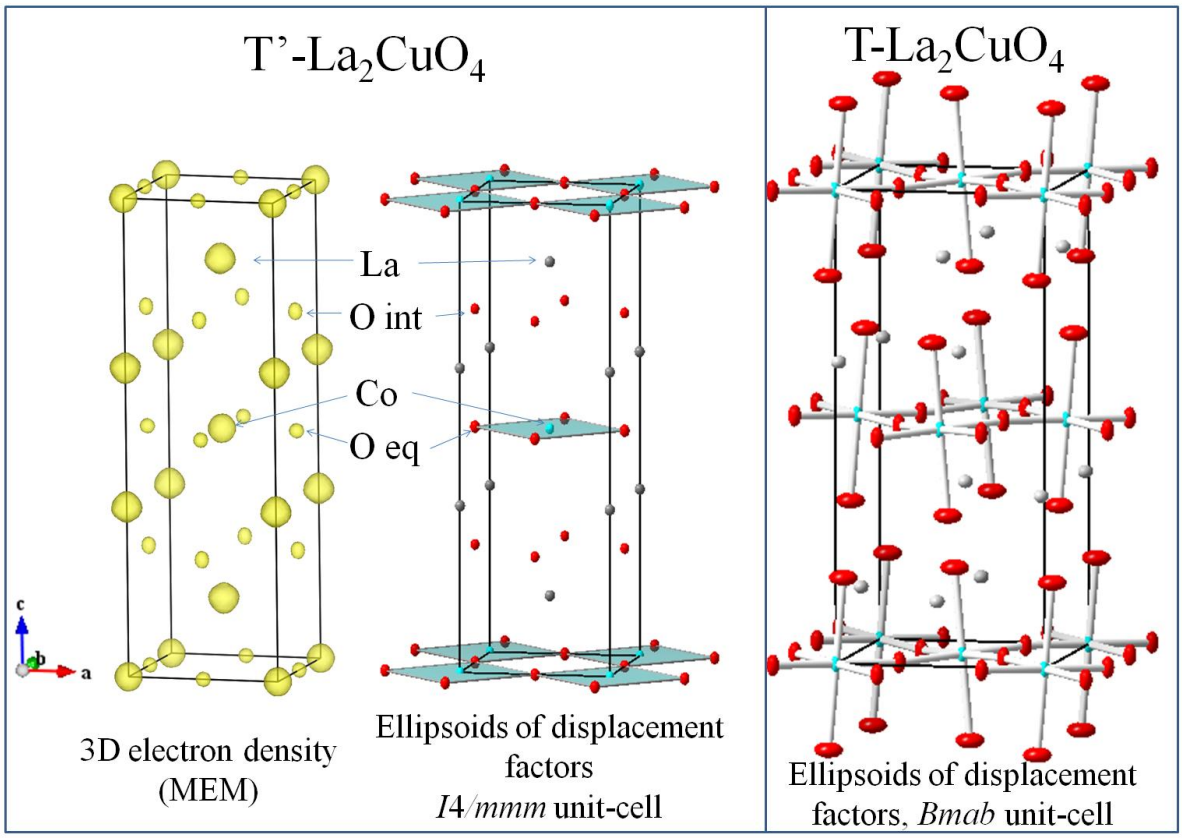

***Figure 4.4**: 3D electron density in the I4/mmm unit-cell calculated by MEM after least square refinements of synchrotron X-ray diffraction data (ID11@ESRF), together with the pictorial view of atomic displacement factors ellipsoids for T'-La_2CuO_4, and for T-La_2CuO_4 (refined in Bmab cell) for comparison.*

3. *As grown* $La_2CoO_{4.14}$ single crystal

The *as grown* $La_2CoO_{4.14}$ compound has a (3+2) incommensurately modulated structure derived from the ideal T-phase. It is the most complex state that has been found for this oxide until now. However understanding the modulation of this phase is a good starting point for the study of other stable states at RT since it can be seen as the most general case. The basic unit-cell serves as a basis for indexing superlattice reflections, and that is why the structural characterization will be split into two steps. First only main reflections will be considered,

describing the average atomic structure in the unit-cell of same proportions than the one of stoichiometric compound. In a second step, satellites will be taken into account for the depiction of the structural modulation and symmetries at longer range.

Single crystal synchrotron X-ray diffraction experiments, λ = 0.2072 Å, at RT on as grown $La_2CoO_{4.14}$ samples have been performed successively with an exposure time t_{exp} of 0.2 (for refinements) and 0.4 seconds per image (for satellite detection) with angular coverage of 280° with a step $\Delta\varphi$ = 0.2°, resulting in 1400 images per acquisition (~30 min/acquisition). Reciprocal maps have been reconstructed pixel by pixel with one *UB* matrix based on main reflections. Figure 4.5 shows the typical (*hk*1) experimental reciprocal space map, with $\vec{c}^*$ normal to the plane, as a comparison with the other phases. This plane results from analysis of a dataset collected with t_{exp} = 0.4 s/image, optimized for the detection of superlattice reflections, which are thus very well visible. Main reflections of strong intensities correspond to the *F*-centered basic cell while others are satellites, generated by symmetries at longer range.

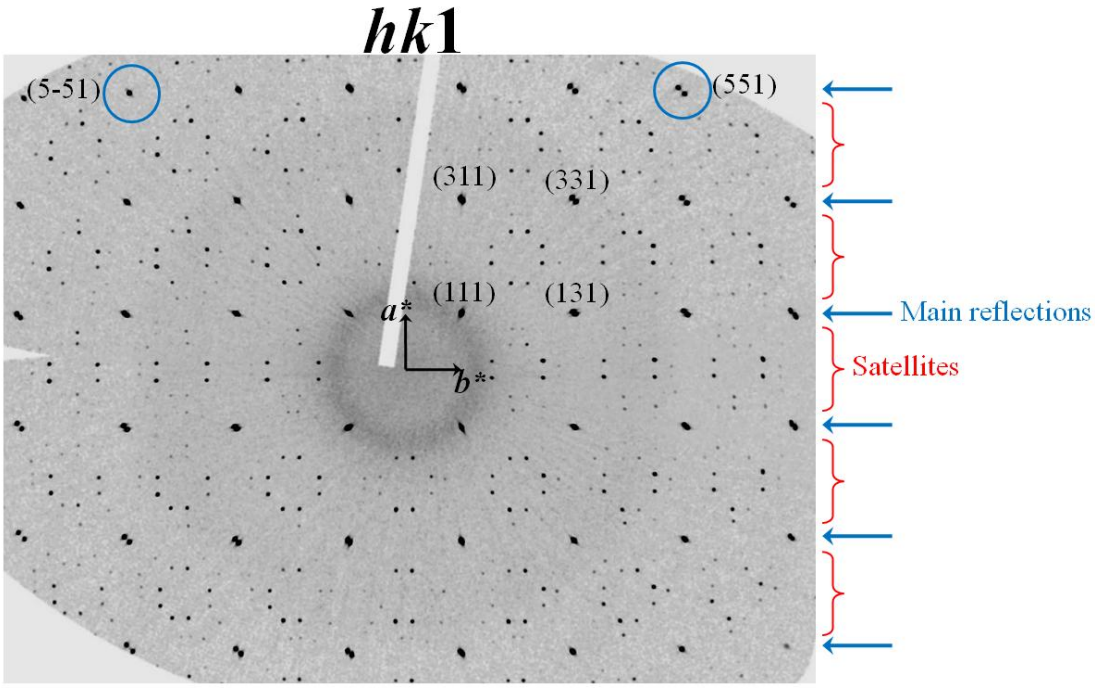

***Figure 4.5**: experimental (hk1) reciprocal space plane of $La_2CoO_{4.14}$ reconstructed from synchrotron X-ray diffraction data (ID11@ESRF), were main reflections and satellites are visible.*

In complement to X-ray studies, neutron diffraction experiments have been carried out on a crystal piece of 3x3x5 mm^3, yielding complementary results concerning the average structure

through the reconstructions of nuclear densities in the basic unit-cell by maximum entropy calculations (*cf.* chapter 3, section 5.2 for details about MEM).

3.1.Average basic structure, anisotropic displacements of all atoms

Within the experimental reciprocal pattern, the extinction conditions for main reflections are: $h + k = 2n$, $h + l = 2n$ and $k + l = 2n$. The Bragg reflections characteristic of the stoichiometric phase with *Bmab* space group, *i.e.* corresponding to the coherent tilt toward the $[010]_{LTO}$ direction, are absent. For instance, the intense (054) peak is extinct, and it is true for all superstructure reflections of this type allowed by *Bmab* space group, but forbidden by the *F*-centered symmetry. Consequently, octahedra can be considered as locally disordered in the basic unit-cell, which is coherent with the presence of interstitial oxygen.

The reciprocal lattice of the basic orthorhombic unit-cell can be indexed with *Fmmm* space group according to equivalencies between main reflections. However, two twin individuals are present in the sample. It has never been possible to find one *as grown* sample made of a single domain, owing to the microscopic nature of twinning in these crystals. Therefore, due to the superimposition of the two sets of *Fmmm* twin lattices, symmetric by the (110) mirror plane, the main reflections can be indexed all together with a pseudo-tetragonal unit-cell, space group *F*4*/mmm*, summing up both twin components in one average tetragonal structure (analogous to HTT-phase). The cell parameters of the average tetragonal unit-cell were refined as $a = b = 5.500(2)$ Å and $c = 12.642(4)$ Å, which is in accordance with the experimental value of extra oxygen content $\delta = 0.14$ Å (*cf.* Figure 1.15 chapter 1) and with the results of thermogravimetric measurements (chapter 2).

As explained in the section 1 of chapter 3, considering the average symmetry of the crystal structure involves that a part of the main reflections are split. As visible on Figure 4.5, the Bragg reflections (*hhl*) and (-*h*-*hl*) are well separated into two peaks at high angles whereas they are overlapped at lower angles. Conversely (-*hhl*) and (*h*-*hl*) reflections are systematically single peaks; the reflections of each twin being exactly overlapped (see the blue circles on Figure 4.5). Cell parameters of a single twin individual's orthorhombic unit-cell have been calculated from an orientation matrix based on some diffraction peaks belonging exclusively to a single domain. The resulting values are $a = 5.473(3)$ Å, $b = 5.527(2)$ Å and $c = 12.647(5)$ Å. The angular separation between the peaks of split reflections, namely 2Δ, is proportional to the orthorhombicity and can be calculated directly from the

values of *a* and *b* (*cf.* equation 3). It results in 2Δ = 1.122°, which is in good agreement with the experimental values of: *i*) 2Δ = 1.13° measured directly on the X-ray diffraction pattern, and *ii*) 2Δ = 1.12° measured with the 4-circles neutron diffractometer. The volumic proportion of each individual domain in the total volume of the crystal sample has been estimated by calculating the ratio between the integrated intensities of peaks forming split reflections (*hhl*). After averaging this ratio, calculated for 10 different reflections completely split into well separated peaks; the resulting volumic repartition for each twin domain is of 60-40% of the total crystal volume. Neutron diffraction experiments have been performed on a much bigger sample, which was twice twinned (four domains).

Table 4.3: *Average structural model of as grown $La_2CoO_{4.14}$ single crystal refined with main reflections only.*

a) Results from synchrotron X-ray diffraction experiment (ID11@ESRF).

Atom	*x/a*	*y/b*	*z/c*	*Occ*	U_{11}	U_{22}	U_{33}	U_{12}	U_{eq}
La	0	0	0.36094(7)	2	21.2(5)	21.2(5)	18.1(1)	-	20.1(6)
Co	0	0	0	1	15.6(4)	15.6(4)	29.5(6)	-	20.2(3)
O (eq)	¼	¼	0	2	19.(3)	19.(3)	47.(8)	(-2)	28.(3)
O (ap)	0	0	0.178(1)	2	47.(0)	47.(0)	19.(7)	-	37.(6)
O (int)	¼	¼	¼	0.14	2(7.2)	-	-	-	2(7.2)

Average cell parameters: $a = b$ = 5.500(2) Å and c = 12.642(4) Å, $\alpha = \beta = \gamma$ = 90°. Angular separation of (*hhl*) reflections 2Δ = 1.13°.Average structure refined in *F*4/*mmm* on 452 independent reflections. R_{int} = 5.1 %.Wavelength of X-rays: 0.2072 Å. Agreement factors: R_F = 5.78 %, R_{WF} = 4.97 %. *Uij* are given in 10^{-3} Å^2.

b) Results from neutron diffraction experiment (TriCS@PSI).

Atom	*x/a*	*y/b*	*z/c*	*Occ*	U_{11}	U_{22}	U_{33}	U_{12}	U_{eq}
La	0	0	0.36091(6)	2	17.4(8)	17.4(8)	10.3(1)	-	15.0(5)
Co	0	0	0	1	11.2(8)	11.2(8)	17.2(1)	-	13.2(3)
O (eq)	¼	¼	0	2	15.1(5)	15.1(5)	36.1(3)	-1.(7)	22.1(6)
O (ap)	0	0	0.1733(3)	1.31(2)	18.4(7)	18.4(7)	11.9(5)	-	16.2(6)
O (ap2)	0.095(3)	0.095(3)	0.1836(2)	0.75(6)	33.(1)	-	-	-	33.(1)
O (int)	¼	¼	¼	0.135(4)	27.(3)	27.(3)	3.(4)	-	19.(4)

Average cell parameters: $a = b$ = 5.508(4) Å and c = 12.649(7) Å, $\alpha = \beta = \gamma$ = 90°. 2Δ = 1.12°. Average tilt angle of CoO_6 octahedra: 17.7°. Average structure refined in *F*4/*mmm* on 113 independent reflections. R_{int} = 3.1 %. Wavelength of neutrons: 1.178 Å. Agreement factors: R_F = 2.54 %, R_{WF} = 1.98 %. *Uij* are given in 10^{-3} Å^2. U_{iso} for O(ap2).

Synchrotron X-ray diffraction data yielded to reliable refinements of the average structure, especially for results of La and Co atoms (more X-ray sensitive than Oxygen). The positions of the latter atoms in the unit-cell complied with theoretical expectations. Occupation of interstitial site was fixed for refinements of X-ray data but was refined with good precision with neutron diffraction data (part *b* of table 4.3). The value of interstitial oxygen occupation resulting from refinements δ = 0.135(4) is in agreement with the previous characterizations

(*cf.* section 1.3.2 chapter 2). Atomic displacement factors of this site are rather high in comparison with other sites; furthermore, the corresponding anisotropic ellipsoid is smeared out in *a*-*b* plane ($U_{11} = U_{22} = 0.027(3)$ while $U_{33} = 0.003(4)$).

The apical site was refined with a split model for which total occupancy of O_{ap} is shared between two distinct sites as follows: ~62% of O_{ap} occupy the (0, 0, *z*) position in the unit-cell corresponding to non-tilted octahedra, and ~38% are on an adjacent (*x*, *x*, *z*) site, corresponding to tilt of octahedra of 17.7° from the *c*-axis. Coordinates and occupations refined for the split apical site should not be taken as definitive values but rather as a tendency. It demonstrates that, even if the basic lattice is *F*-centered, octahedra are not systematically aligned toward *c*-axis.

The Maximum Entropy Method (MEM, *cf.* chapter 3, section 5.2) has been applied on the neutron diffraction data and provides finer results. Experimental reflections were phased on the account of previous least-square refinements presented in table 4.3*b*. Nuclear densities were reconstructed with a pixel size of 1.10^{-3} Å^3, the initial Lagrangian λ_0 was set to $\lambda_0 = 0.02$ and the adjustment coefficient *t* to *t* = 0.2. When constrains of convergence were satisfied, agreement factors resulted in $R_F = 1.87$ % and $R_{wF} = 1.51$ %. Figure 4.6 shows the subsequent configuration of 3D nuclear density profile of the average structure, accompanied with two different projections on the $\vec{a}$-$\vec{c}$ plane for clarity. In order to avoid any confusion brought by the presence of too much sites, the smaller *I*4/*mmm* unit-cell is shown. This cell is absolutely equivalent to the *F*4/*mmm* (*cf.* Figure 4.3), with $a_I = \frac{1}{\sqrt{2}} \times a_F = 3.89$ Å. Maximum entropy analyses confirm and even enhance the anisotropic character of the nuclear densities. Furthermore, it exhibits much more details regarding the preferred directions of atomic displacements. For instance, La site appears to be broad and nearly semi-spherical shaped, suggesting positional modulation for this atom. In addition to this, Co site is patently elongated toward *c*-direction.

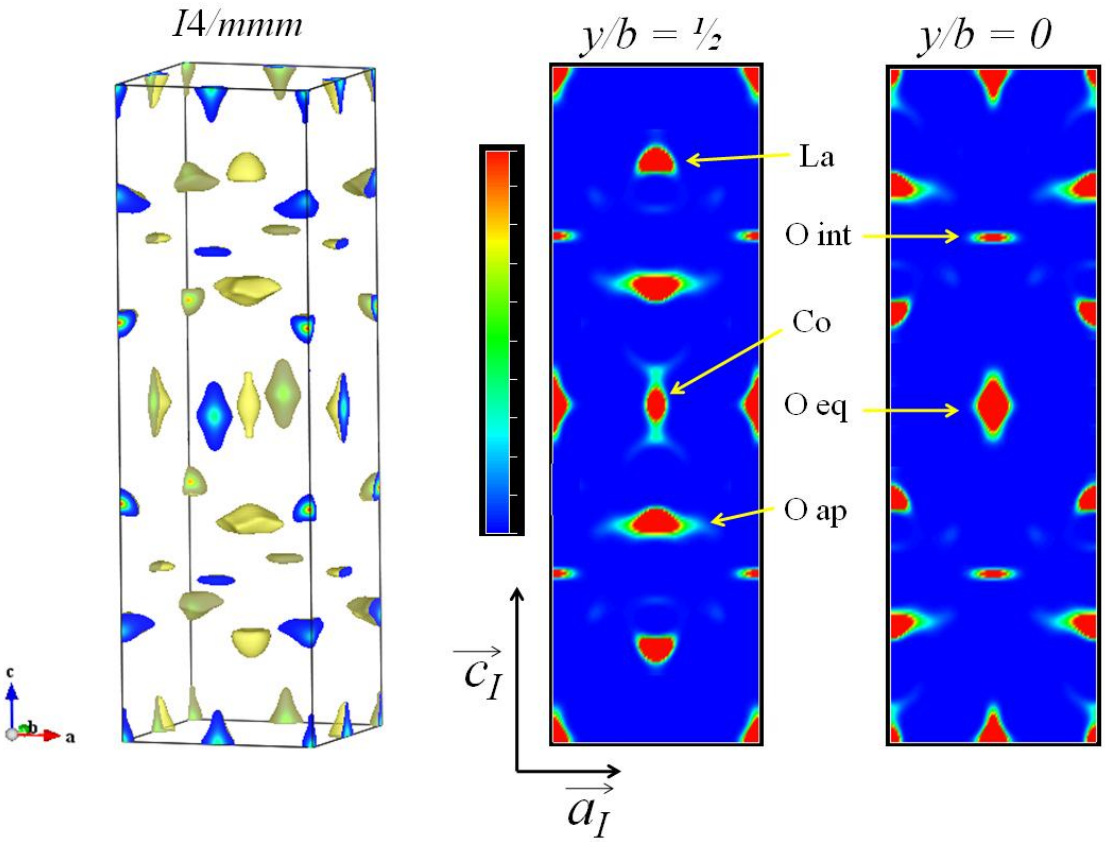

***Figure 4.6**: Nuclear densities in $La_2CoO_{4.14}$ resulting from maximum entropy method applied on experimental neutron diffraction data (TriCS@PSI).*

Figure 4.7*a* displays a zoom on the 3D profile of the isosurface densities of CoO_6 octahedra (they are all identical in the average structure) surrounded by 8 interstitial sites, which are statistically occupied (δ = 0.135 corresponds to a bit more than one interstitial for four *I4/mmm* unit-cells, *i.e.* one interstitial site occupied over 16). Nuclear densities of interstitial sites appear rather broad and smeared out in the $\vec{a}$-$\vec{b}$ plane. Conversely, the nuclear density of the site occupied by equatorial oxygen (O_{eq}) follows the tendency of Co site to elongate toward the *c*-axis. This is consistent with rigid tilts of octahedra which imply not only a shift of O_{ap} but also such a displacement of O_{eq}. Finally, the apical site clearly shows the most anisotropic 3D density profile. A zoom of it is presented on the right side of the figure, together with the 2D projection on the $\vec{a}$-$\vec{b}$ plane of apical site's nuclear density integrated in the range of $0.66 \leq z/c \leq 0.69$. Contour lines are drawn for $0.5\ \% < \rho < 50.5\ \%$ of ρ_{max} with a step of 2.5 %.

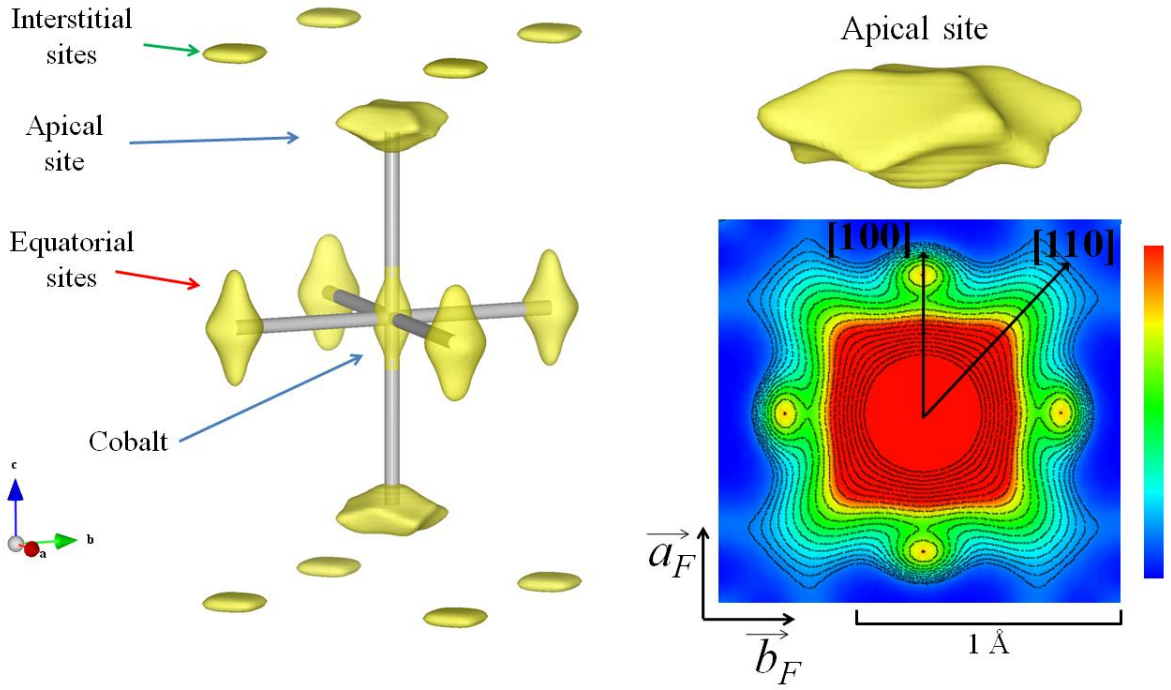

***Figure 4.7**: a) Nuclear density of CoO_6 octahedra and interstitial sites calculated by MEM on neutron diffraction data (TriCS@PSI), b) strongly anisotropic apical site in 3D, and below, the 2D projection on the a-b plane of the density within $0.66 \leq z/c \leq 0.69$ corresponding to apical site.*

The nuclear density around the apical site is broad and strongly anisotropic. Its shape suggests two main preferred orientations for atomic displacements. Apical oxygen atoms tend to shift not only toward the $[\pm100]_F$ (and $[0\pm10]_F$) axes, which are the directions of the tilts for the stoichiometric phase, but also toward the $[\pm1\pm10]_F$ axes which are consistent with the opening of tetrahedral interstitial sites for extra-oxygen atoms. These diagonal directions of tilt with respect to the *F*-centered unit-cell have also been shown on the parent compound $La_2NiO_{4.125}$ by C. Frayret in her Ph. D thesis[220] through DFT simulations. She has evidenced the tilts of NiO_6 octahedra toward $[\pm1\pm10]_F$ directions occurring alternatively in the NiO_2 planes when $\delta = 0.125$. These calculations confirmed what has been previously reported earlier by Tranquada *et.al*[142] from single crystal neutron diffraction results. But, contrary to what has been found for the nickelate, here for the cobaltate, both types of tilts are observable. Recently, maximum entropy reconstructions have also been reported by Villesuzanne *et.al*[219] about $La_2CuO_{4.07}$ obtained *via* electrochemistry in aqueous electrolyte (KOH), showing the same tendency to tilt in two distinct orientations, similarly to what is found here for $La_2CoO_{4.14}$. In this sense, the cobaltate looks more like the cuprate in terms of octahedra arrangements. In addition, both cuprate and cobaltate stay orthorhombic for $\delta > 0$, while the nickelate turns into tetragonal.

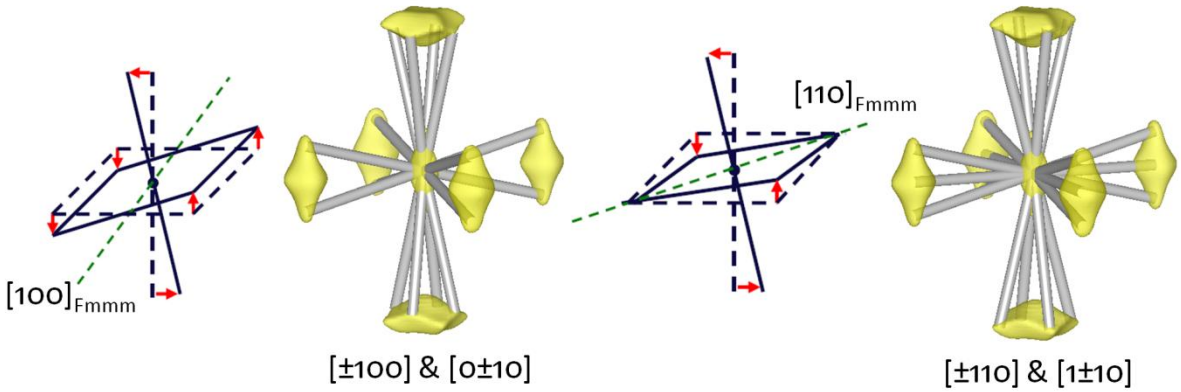

***Figure 4.8**: Schematic representation of the two types of MO_6 tilting in $La_2MO_{4+\delta}$ by C. Frayret[220] compared to our MEM results. Left: Type of tilt in the stoichiometric phase, but also present in oxygen-rich $La_2CuO_{4.07}$[219] and here for $La_2CoO_{4.14}$. Right: Type of tilt occurring for the oxygen-rich compounds with M = Co, Ni, Cu and δ = 0.14, 0.125 and 0.07 respectively.*

Figure 4.8 compares the two types of tilts depicted by C. Frayret[220], and the nuclear densities we obtained by maximum entropy calculations for the cobaltate. Since the MEM reconstructions correspond to the average tetragonal unit-cell, all the possible directions of tilt are symmetrical by the fourfold axis collinear to $\vec{c}$*.

Besides static tilting, the apical site still exhibits a prominent broadness significant of local disorder. Neither potential intermediate orientation nor anisotropic and dynamic vibrations of the lattice should be excluded. It is not straightforward to attribute such anisotropy of atomic displacements either to static or dynamic disorder effects. Indeed, as mentioned earlier for the stoichiometric La_2CuO_4 compound, in addition to structural modulation, phonons take place at RT in this family of oxide. The presence of interstitial oxygen has been shown to activate not only dynamic tilting of MO_6 octahedra, but also significantly La/O_{ap} displacements along [110]-type directions and even at low energies[219]. Both allow the apical oxygen atoms to displace towards the interstitial vacancy sites in a facile way. This kind of vibration is a potential enhancing factor for push-pull migration mechanism[221] at moderate temperatures. However, the relatively intense incommensurate satellites on the experimental diffraction pattern confirm the presence of static displacements. Nevertheless, combination of static and dynamic effects is perfectly conceivable, like for the stoichiometric La_2CuO_4 at RT (*cf.* section 2.1 of the present chapter).

Together with La atoms, apical oxygen atoms are in the first coordination sphere of the interstitial site. They are thus the first affected by the presence of extra oxygen and *vice versa*, and that is obviously why their respective nuclear densities appear to be the broadest. Static

atomic displacements of La and O_{ap} sites, which are fully occupied, suggest positional modulation, whereas occupational modulation is relevant for interstitial site.

3.2.First modulation vector $\vec{q}_1$ in $\vec{a}$*-$\vec{b}$* plane, attribution of satellites, second twinning effect

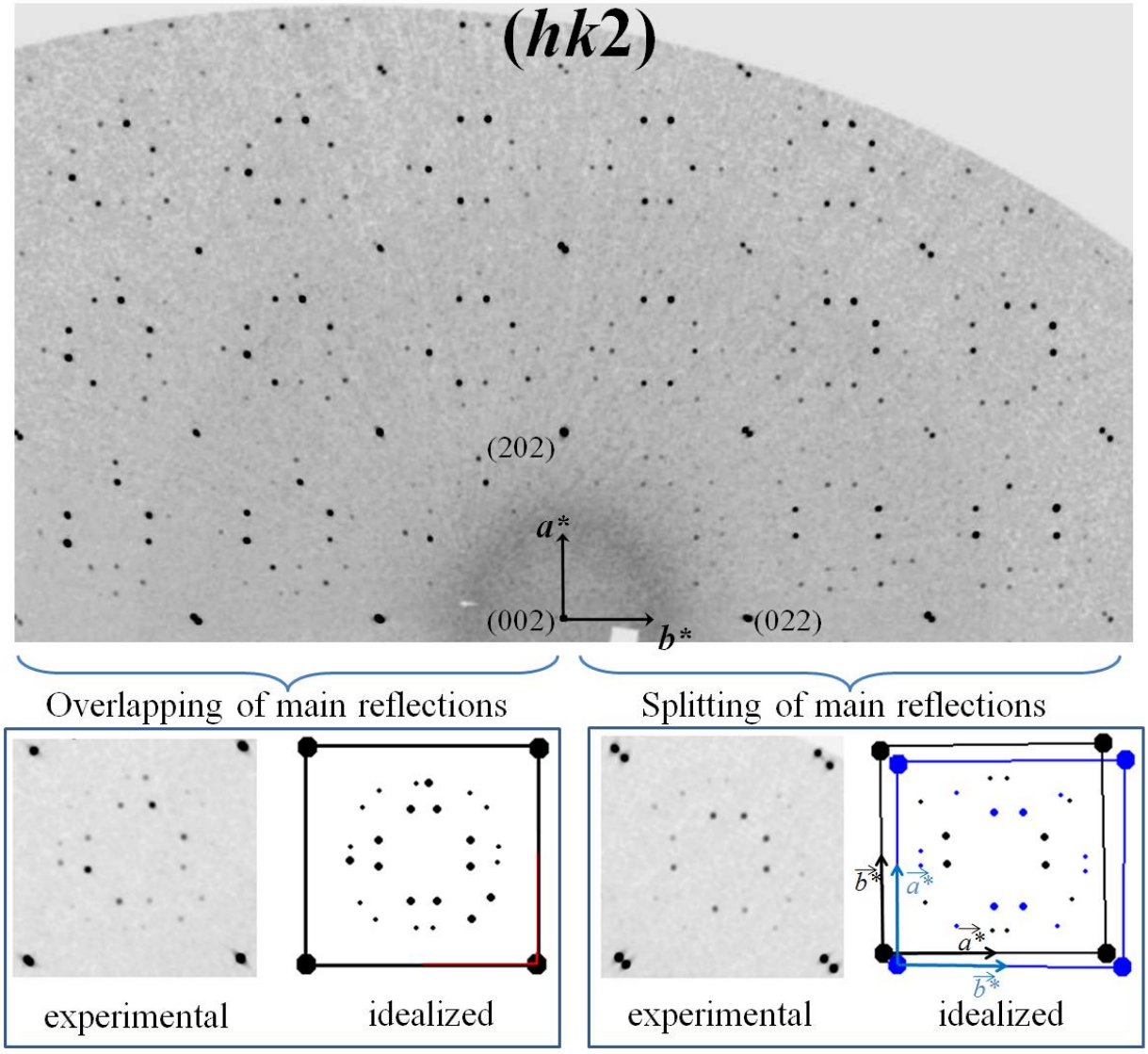

***Figure 4.9**: Up: Experimental (hk2) reciprocal space map of the as grown $La_2CoO_{4.14}$ single crystal reconstructed from synchrotron X-ray diffraction data (ID11@ESRF). Down: comparison of the idealized patterns of the left and right side, permitting to differentiate the two domains.*

The experimental pattern has been firstly explored by 2D reciprocal space map reconstructions with $\vec{c}$* normal to the planes. Several planes have been reconstructed for $0 \leq |l| \leq 10$, with l integer. They correspond to the $\vec{a}$*-$\vec{b}$* planes of different orders n. Besides

main reflections, an incredibly large amount of satellites with irrational Miller indexes are observable on each of these maps until high sinΘ/λ values, implying periodicity at long distances in direct space. It is consistent with a structural modulation in the $\vec{a}$-$\vec{b}$ plane, which corresponds to the planes of layers composing the structure. The experimental reciprocal maps are invariant by twofold rotation axis collinear to $\vec{c}$*; consequently only their upper part will be presented on the figures. Among them, the (*hk*2) plane, shown on Figure 4.9, is the plane for which main reflections are the less intense, but conversely satellites are the most discernible.

The crystal sample is made of two domains. Similarly to main reflections, satellites have to be attributed either to the first or to the second twin component: half of the satellites belong to domain 1 and the other half to domain 2. Contrary to main reflections, satellites are not overlapped, due to the incommensurate character of the modulation. Recognizing which superlattice reflection belongs to which twin component is not an easy task and requires a fine observation of the experimental data. As depicted on Figure 4.9, the reconstructed (*hk*2) reciprocal plane can be conventionally separated into two distinct parts: *i*) the left side where main reflections are single peaks and satellites form a rather symmetric pattern; *ii*) the right side where main reflections are split, where satellites appear to be at less symmetrical positions. The lower part of the figure displays the experimental and idealized patterns characteristic of each side of the plane. Assigning superlattice reflections to their respective twin domain can be achieved by comparing the positions of satellites according to the positions of the main reflections. Since each satellite is generated by the propagation vector applied on one particular main reflection, the satellites coming from the split ones (right side) appear to be at a different position than the one coming from the overlapped one (left side). But in fact, they "follow" the shift of their corresponding main reflections as shown below:

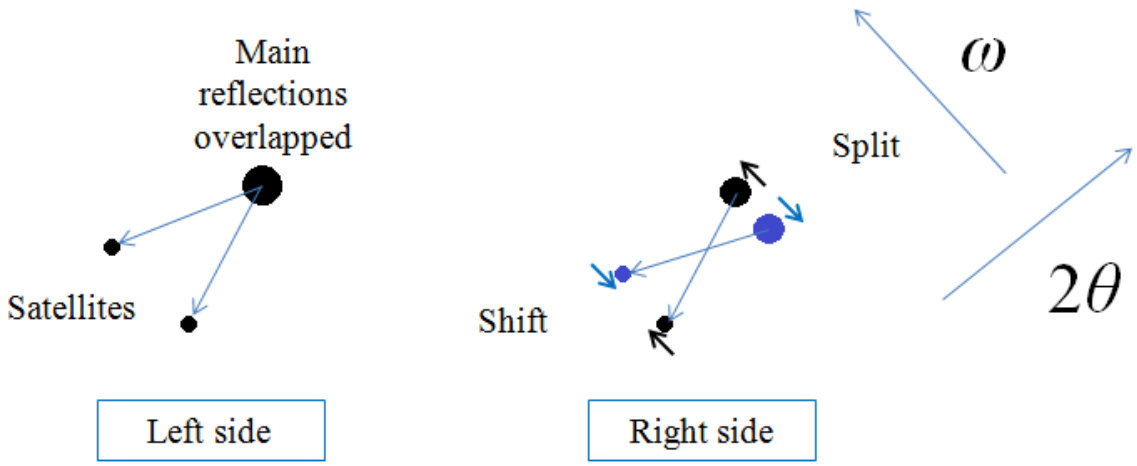

So, depending on the directions of deviation (right side of the map) from symmetric positions (left side of the map), concomitantly with symmetry operations of the twinning law, each satellite can be ascribed to its respective main reflection and thus, to its specific twin domain. Hence, the idealized reciprocal pattern can be constructed for one single twin, as shown on Figure 4.10*a*.

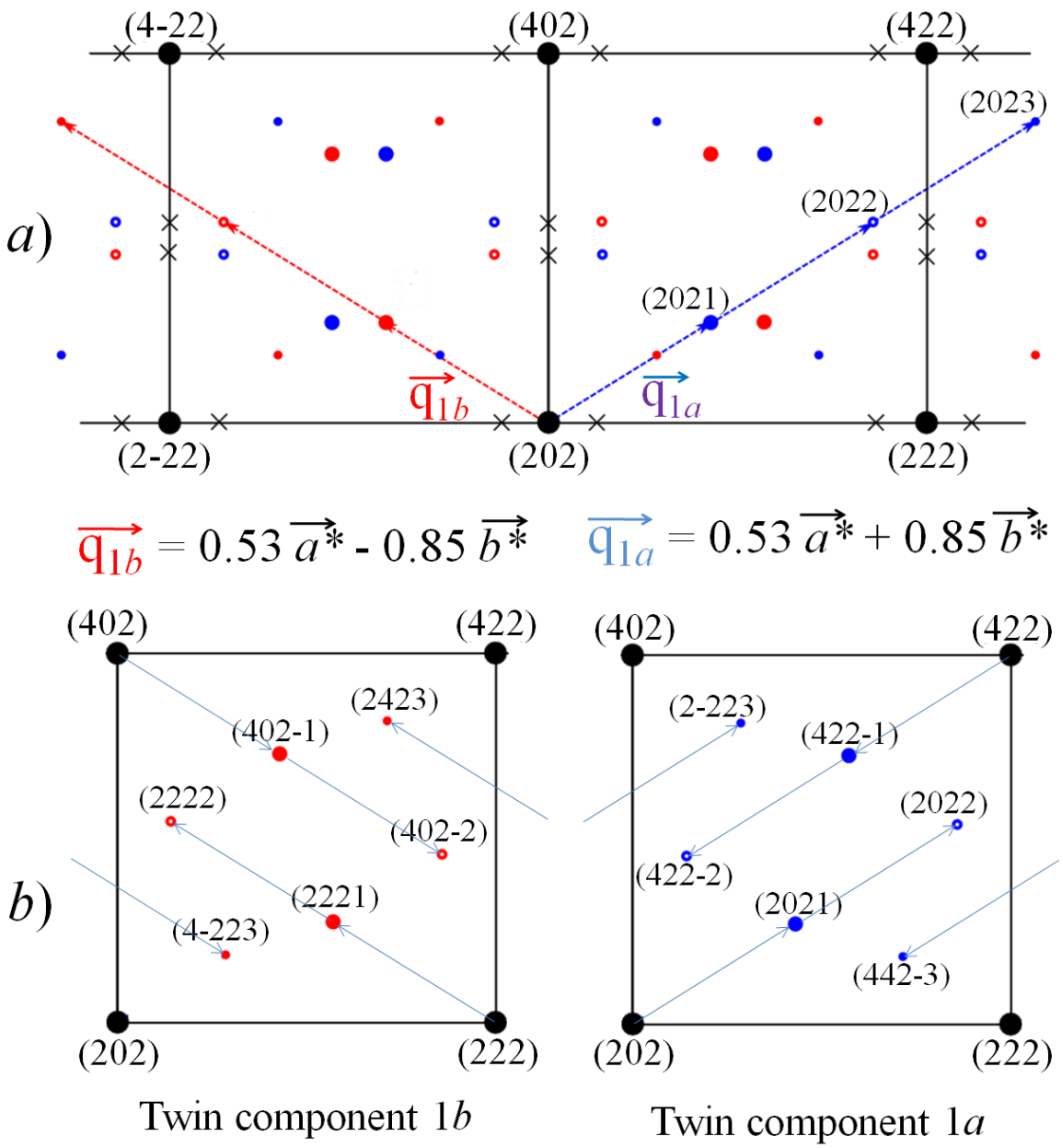

***Figure 4.10**: a) Idealized (hk2) reciprocal pattern for a single pseudo-merohedral twin individual. Satellites can be indexed through two incommensurate propagation vectors. Black spots are main reflections, big colored spots correspond to satellites of 1st order (m = 1), empty circles to 2nd order (m = 2) and small full circles to the 3rd order (m = 3). Blue circles are indexed by $\vec{q}_{1a}$ and the red ones by $\vec{q}_{1b}$. Crosses show the systematic absence of the sum of $\vec{q}_{1a} + \vec{q}_{1b}$. b) Indexation of all the satellites depending on the twin component.*

For a single twin individual, two incommensurate propagation vectors are necessary for indexing all satellite reflections: $\vec{q}_{1a}$ = (α_1, β_1) in blue on the figure and $\vec{q}_{1b}$ = (α_1, -β_1) in red, with α_1 = 0.85 and β_1 = 0.53. The corresponding modulation period in direct space is of ~5.5 Å. Superlattice reflections are visible until the 3rd order, indicating that the modulation is not purely sinusoidal (presence of harmonics). However, the reflections whose positions correspond to the vector sum $\vec{q}_{1a}$ + $\vec{q}_{1b}$ (marked X on Figure 4.10*a*) are systematically absent on the experimental pattern. According to theoretical considerations[222] related to incommensurate crystallography, they strongly suggest that the two vectors do not modulate simultaneously the same domain of the crystal bulk. The orthorhombic nature of the basic unit-cell allows two equivalent directions of propagation in the $\vec{a}$-$\vec{b}$ plane for an oblique incommensurate modulation vector. Each domain of the basic structure is in fact twinned in his turn into two individual domains (4 in total). The twinning class is of partial merohedral type: main reflections are perfectly overlapped but satellites are systematically separated. Therefore, the second twinning is only observable through satellites, but not *via* basic reflections. The twin element is the mirror plane perpendicular to $\vec{b}$*, *i.e.* this symmetry element is lost in the average structure and is applied between the twin lattices. The loss of that mirror plane lowers the basic space group to *F*2/*m*, which is also centrosymmetric. Experimental intensities of superlattice reflections confirm this space group and validate the presence of four domains in total. For instance, when taking into account only one pseudo merohedric domain of the basic structure (domain 1), the satellites (*hklm*) and (*h-klm*) symmetric by the (100) mirror plane are not equivalent; the ratio between their respective intensities systematically results in the same proportion: 65-35 ± 5 % which corresponds to the twin's volumic fraction of domain 1*a* and 1*b* (this value is averaged on a set of 20 pairs of satellites). However the reflections ($hklm_1$), (-h-klm_1), remain equivalent by the twofold rotation axes (ΔI_{obs} = 2.5 %), as well as ($hklm_1$) and (hk-lm_1) by the mirror plane normal to *c*-axis (ΔI_{obs} = 3.2 %).

Therefore, vectors $\vec{q}_{1a}$ and $\vec{q}_{1b}$ shown on Figure 4.10*a* are invariant by the second twin element ((100) mirror plane). In fact, only a single propagation vector $\vec{q}_1$ (α_1, β_1) modulates the structure in the $\vec{a}$-$\vec{b}$ plane, but in four distinct twin individuals. Figure 4.11 summarizes all of them, depending on their respective modulation vectors and volumic fractions.

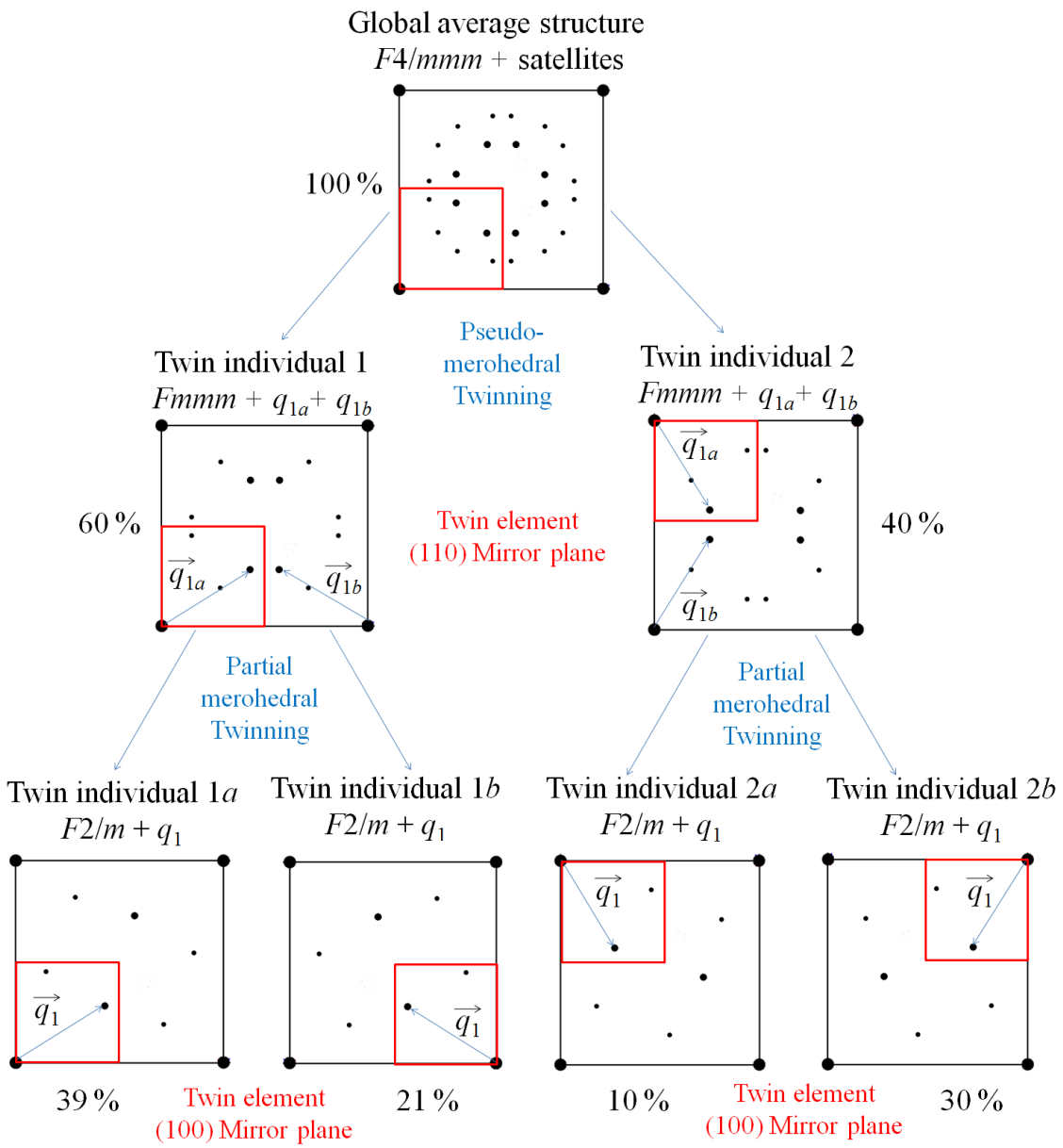

***Figure 4.11**: Scheme summarizing the different modulated twin individuals in as grown $La_2CoO_{4.14}$. Volumic fractions are given in percentage of the total volume. Red squares denote the basic unit-cells.*

3.3.Second modulation vector $\vec{q}_2$ with a supplementary component along $\vec{c}$*

The reciprocal space maps with $\vec{a}$* or $\vec{b}$* normal to the plane, *e.g.* corresponding to (0*kl*) and (*h*0*l*)-type planes, have also been reconstructed. For *h* or *k* integers, the resulting planes exhibit only main reflections, due to the incommensurable character of $\vec{q}_1$. However, strong one-dimensional diffuse scattering is observable between the reflections (*h*06) and (*h*08) as shown below:

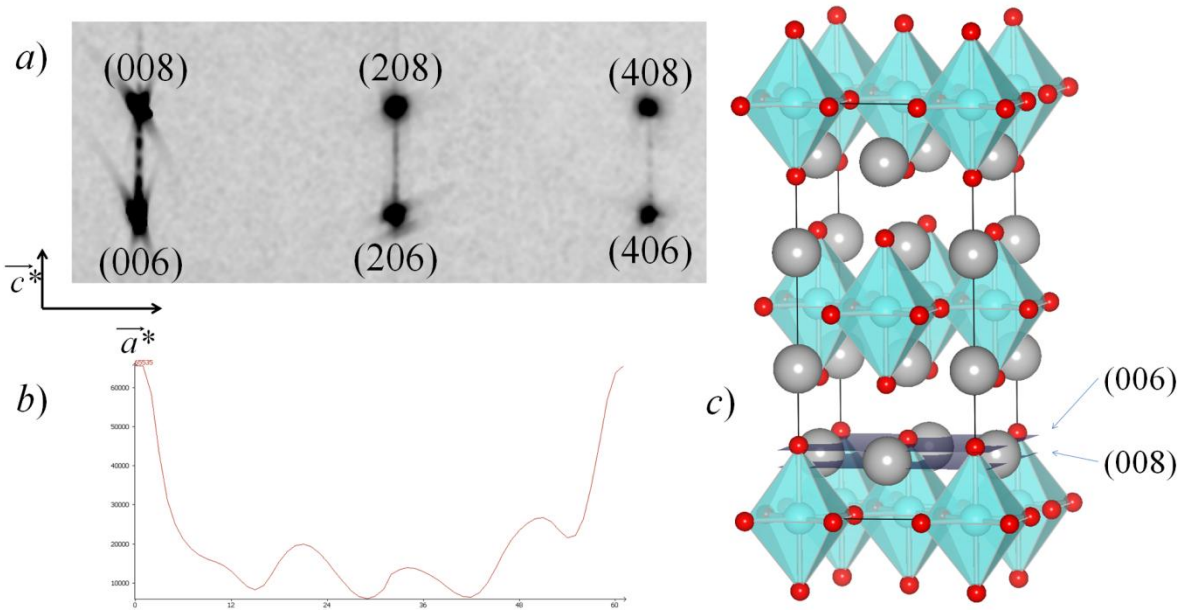

***Figure 4.12**: a) diffuse scattering observed on (h0l)reciprocal map of $La_2CoO_{4.14}$, b) linear profile of the diffuse scattering between (006) and (008), c) visualization in real space of the (006) and (008) lattice planes*

The diffuse scattering shows several distinct maxima between (006) and (008), supplementary peaks might be covered by the tails of main reflections, and thus it is difficult to discriminate precisely the number of maxima. Figure 4.12 also shows the (006) and (008) planes in direct space on the 3D visualization of the basic unit-cell. Those lattice planes cut the cell at a rather critical location since they sandwich the La site between them. So, this one dimensional diffuse scattering suggests disorder on the La site in the $\vec{a}$-$\vec{b}$ plane, indicating that positional modulation of La is not perfectly ordered. The diffuse scattering will be subject to more attention in chapter 5.

Series of maps with $\vec{a}*$ normal to the planes comprised between h = 0 to h = 1 have also been reconstructed, *i.e.* from (0*kl*) to (1*kl*), with a step of Δh = 0.02, in order to "catch" incommensurate reflections with component along $\vec{c}*$ ($\gamma \neq 0$). Different resulting planes revealed satellites with γ = ½, for instance with h = 0.88 as shown below on Figure 4.13:

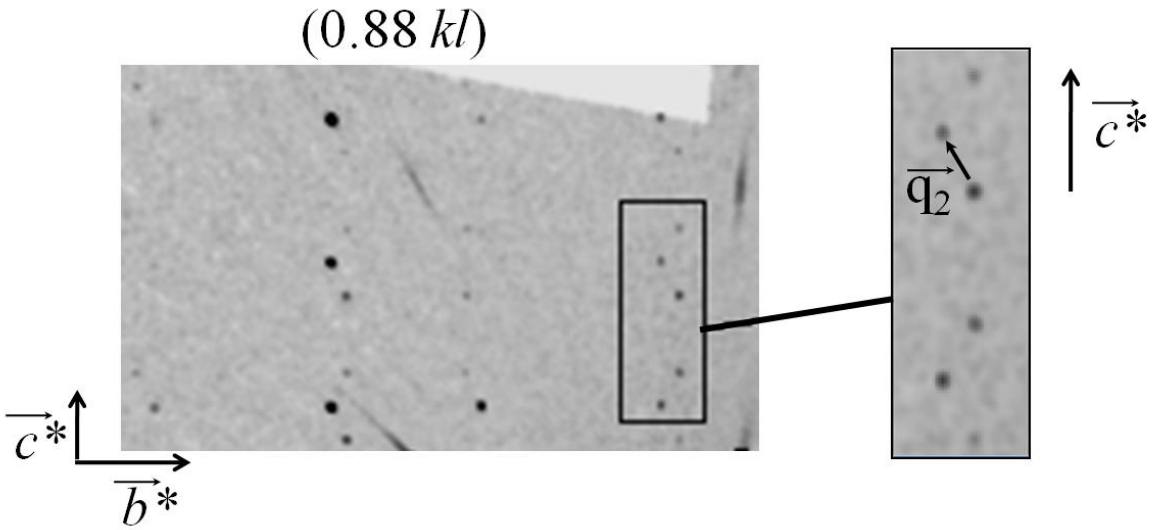

Figure 4.13*: Reciprocal space map reconstructed from synchrotron X-ray diffraction data (ID11@ESRF), with $\vec{c}$* in the plane, h = 0.88, showing satellites with $\gamma \neq 0$.*

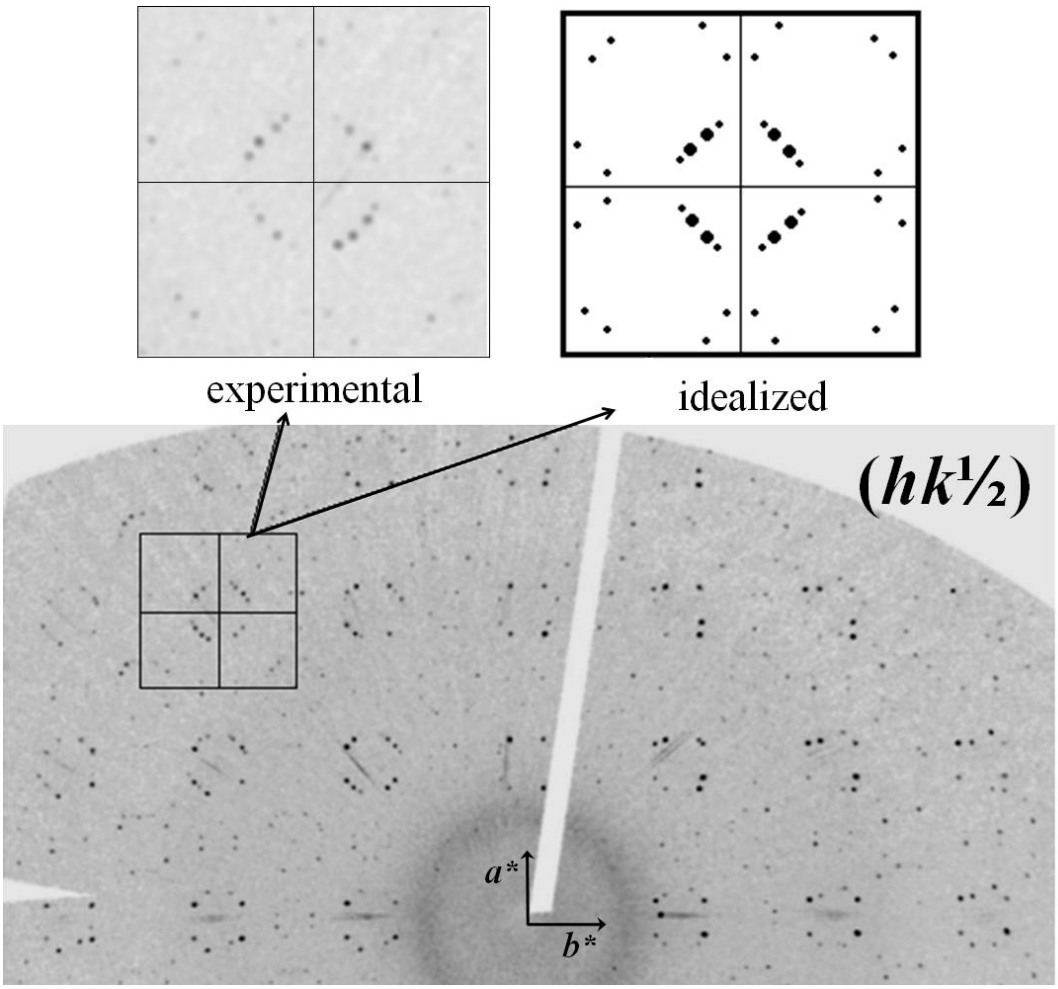

Figure 4.14*: (hk½) reciprocal plane of $La_2CoO_{4.14}$ at RT reconstructed from synchrotron X-ray diffraction data (ID11@ESRF), containing only superlattice reflections. Experimental and idealized pattern are shown above.*

Figure 4.14 shows the (hk½) reciprocal space plane of $La_2CoO_{4.14}$ at RT, representative of the family of planes with $l = n + ½$ (n integer). In this plane basic reflections are forbidden and as a consequence, all the reflections are satellites with irrational Miller indexes. A zoom on a characteristic part of the plane is shown together with the idealized positions of satellites, determined after careful observation of experimental data. The vector $\vec{q}_1$ used to index satellites for $l = n$ do not have a component toward $\vec{c}^*$ ($\gamma_1 = 0$). No solution has been found permitting to index all satellites with a single modulation vector ($\alpha\beta\gamma$). Therefore, it has been chosen to introduce a second propagation vector, $\vec{q}_2$, for indexing satellites with $l = ½$. Since this solution matches very well with experimental data, the results are detailed below.

The reflections of the plane with $l = n + ½$ can be indexed with a global vector $\vec{H} = h\,\vec{a}^* + k\,\vec{b}^* + l\,\vec{c}^* + m_1\,\vec{q}_1 + m_2\,\vec{q}_2$. The second modulation vector, $\vec{q}_2 = (\alpha_2, \beta_2, \gamma_2)$, is incommensurate in the $\vec{a}^*$-$\vec{b}^*$ plane, $|\alpha_2| = 0.27$, $|\beta_2| = 0.23$, but has a rational component along $\vec{c}^*$, $|\gamma_2| = ½$. These values are consistent with a modulation period of approximately 26.48 Å in direct space. Satellites with $-1 \leq m_2 \leq 1$ are observable on all planes with $l = n + ½$. Consequently, two types of reflections are visible on the (hk½) plane: *i*) satellites ensuing from main reflections of (hk0) plane, with $m_2 = 1$; *ii*) satellites ensuing from main reflections of the (hk1) plane with $m_2 = -1$, as depicted below on Figure 4.15:

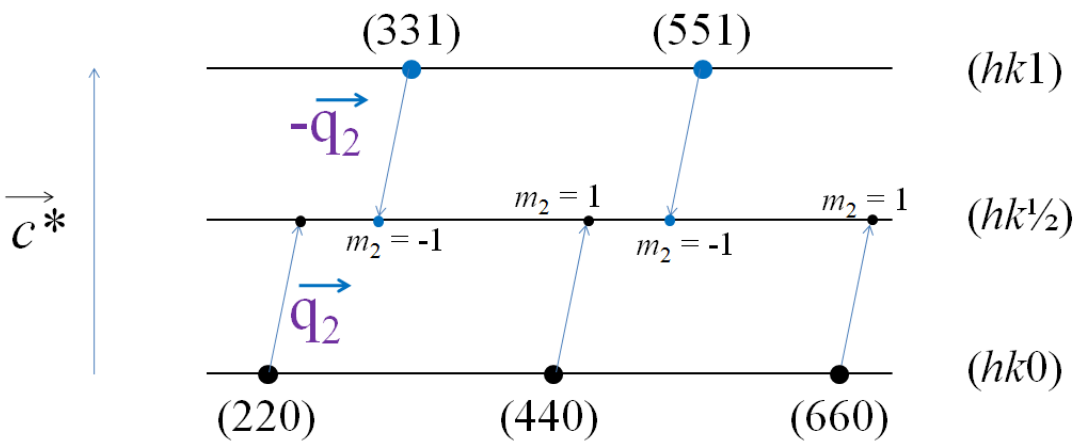

***Figure 4.15**: Schematic representation of the reciprocal space toward $\vec{c}^*$, explaining the presence of satellites with $m_2 = 1$ and $m_2 = -1$ on the (hk½) plane of $La_2CoO_{4.14}$ at RT.*

Upon assigning each peak to its corresponding pseudo-merohedral twin domain, 1 or 2, on the basis of the twinning law and on the positions of satellites on the right side of the plane, it is possible to draw the idealized reciprocal plane (hk½) of a single pseudo-merohedral domain, as shown in Figure 4.16. The commensurate component $\gamma_2 = ½$ of vector $\vec{q}_2$ is not represented on the figure; only its irrational indexes are taken into account.

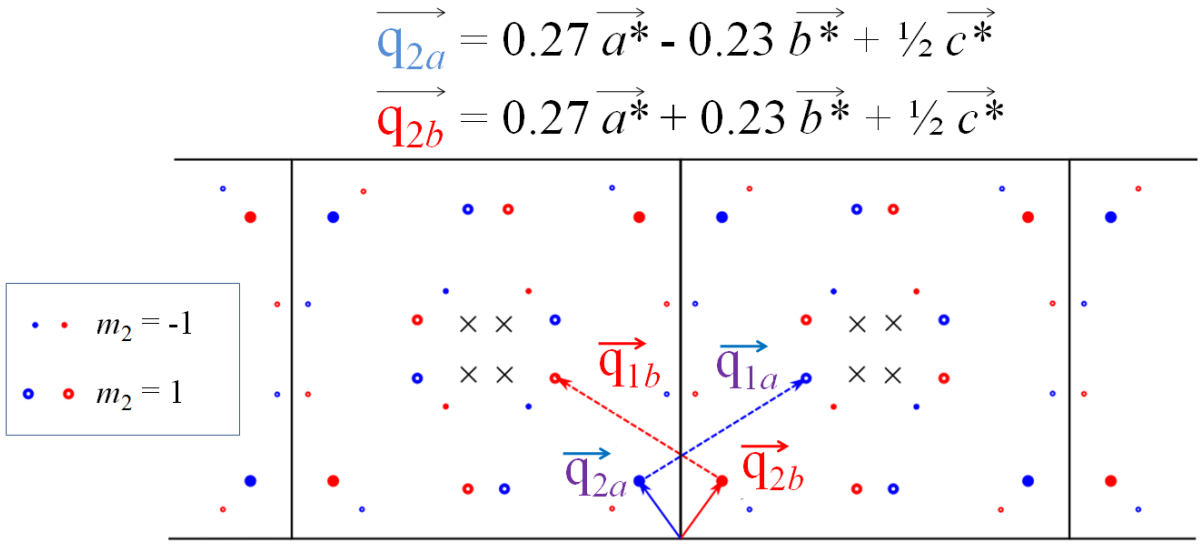

***Figure 4.16**: Idealized (hk½) reciprocal pattern of $La_2CoO_{4.14}$ at RT for a single pseudo-merohedral twin individual.*

The difference of intensity between satellites generated by (*hk*1)-type main reflections (m_2 = -1) and by (*hk*0)-type ones (m_2 = 1) (small and large spots respectively on the figure), is proportional to the ratio of intensity between the main reflections themselves. For instance the structure factor of the basic reflection (111) is 135.15 whereas it is 483.64 for the reflection (220). That is why, on (*hk*½) plane, intensity of satellites m_2 = 1 is stronger than the one of satellites m_2 = -1. Moreover, the pattern of small intensity (m_2 = -1) is symmetrical by translation to the one of higher intensity (m_2 = 1) with the translational vector [110], *i.e.* the planar translation between main reflections of (*hk*0) plane and main reflections of (*hk*1) plane.

As for the (*hk*2) plane, the reciprocal pattern of (*hk*½) plane is indexable with two vectors $\vec{q}_{2a}$ and $\vec{q}_{2b}$, which correspond in fact to respectively twin domain 1*a* and twin domain 1*b*. Vectors $\vec{q}_{2a}$ and $\vec{q}_{2b}$ are symmetrically invariant by the (100) mirror plane which is the twin element of the merohedral twinning between the domains. Moreover, satellites resulting from the vector additions $\vec{q}_{2a} + \vec{q}_{1a}$ and $\vec{q}_{2b} + \vec{q}_{1b}$ (empty circles on the figure) are observable whereas the reflections coming from $\vec{q}_{2a} + \vec{q}_{1b}$ and $\vec{q}_{2b} + \vec{q}_{1a}$ (represented by crosses on the figure) are systematically absent. Furthermore, the ratio of intensities calculated for the satellites generated by $\vec{q}_2$ and symmetric by the twin element, agrees with the volumic proportions of each twin individual found for $\vec{q}_1$. Therefore, for one single individual (out of four), the angle between $\vec{q}_1$ and $\vec{q}_2$ vectors is of 90° within the experimental resolution. For instance, for domain 1*a*, $\vec{q}_1$ = (0.53, 0.85, 0) then $\vec{q}_2$ = (0.27, -0.23, ½), *cf.* Figure 4.17. Consequently, all satellites of the whole experimental reciprocal space can be indexed with 4

orthorhombic domains, basic space group $F2/m$, modulated incommensurately in two-dimensions by $\vec{q}_1$ and $\vec{q}_2$, with $0 \leq |m_1| \leq 3$ and $0 \leq |m_2| \leq 1$.

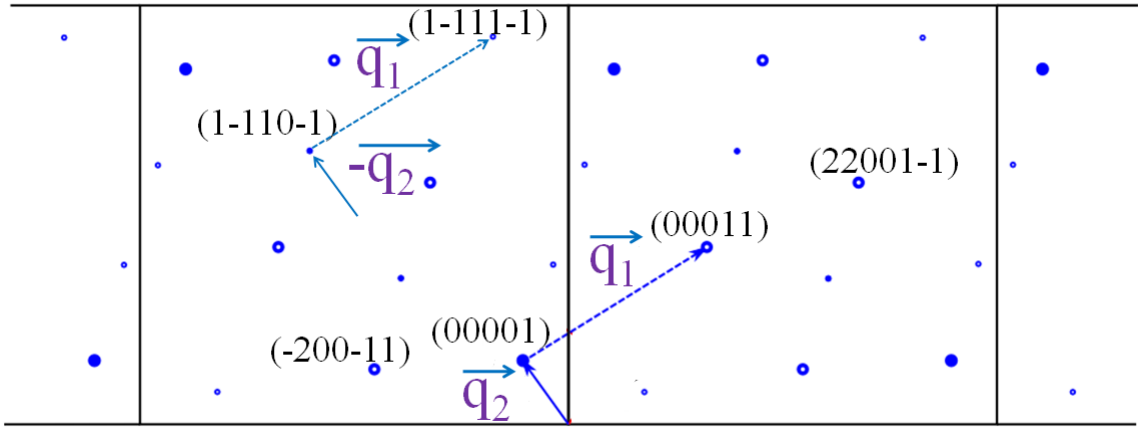

***Figure 4.17**: Indexation of satellites on the idealized (hk½) reciprocal plane for a single individual of $La_2CoO_{4.14}$ at RT.*

3.4.Conclusions about the real structure of $La_2CoO_{4.14}$

A superspace group approach is necessary to take into account long range ordering and subsequent symmetries of the modulated structure. On the basis of the F-centered unit-cell modulated by the propagation vectors $\vec{q}_1$ (α_1, β_1, 0) and $\vec{q}_2$ (α_2, β_2, ½), and according to systematic extinctions, the general reflection conditions are the following: ($hklm_1m_2$): $h + k = 2n$, $h + l = 2n$, $k + l = 2n$; and ($hk0m_10$): $m_1 = 2n$. According to these conditions, we can propose the superspace group labeled $F2/m(\alpha_2\beta_2½)00(\alpha_1\beta_10)0s$. It is a non-conventional (3+2) superspace group derived from the conventional[223] $P2/m(\alpha_1\beta_1½)00(\alpha_2\beta_20)0s$. Indeed, the oblique character of $\vec{q}_1$ and $\vec{q}_2$ with respect to the basic lattice formed by ($\vec{a}$*, $\vec{b}$*, $\vec{c}$*), directly implies that the conventional Bravais lattice of the modulated structure is monoclinic[195]. The latter is based on a different unit-cell with a'= (0, -2, 0), b'= (½, ½, 0) and c'= (0, 0, 1). But the superspace group based on the F-centered unit-cell is totally legitimate and can be kept for modeling the modulation; it is even more convenient since it is based on the common orthorhombic unit-cell.

Integration of the ($hklm_1m_2$) experimental intensities for a single domain was arduous due to coexistence of four twins, resulting from two twinning laws, modulated by two incommensurate propagation vectors each. Separation of the raw experimental diffraction pattern into distinct sets of reflections for single individual was extremely complex. No

satisfactory structural model could be obtained from refinements. But qualitatively, planar wave deformation of the atomic structure related to $\vec{q}_1$ is coherent with long-range ordering of interstitial oxygen inside interstitial layers. According to MEM results, the occupational modulation of O_{int} is correlated to the positional modulation of the rest of the structure which is distorted in comparison with the basic unit-cell model. Not only octahedra are tilted but also La and Co atoms are coherently misaligned from their average positions. This is emphasized not only by the MEM reconstructions but also by the intensities of satellites which would not be so strong if only oxygen atoms would be modulated. The existence of $\vec{q}_2$ with γ = ½ is consistent with doubling of the *c*-axis. Hence, the real unit-cell includes in fact four consecutive interstitial layers toward *c*-axis, instead of two for the basic one. This scheme is repeated each 25.28 Å along *c*-axis, but translated in the plane because of α_2 and β_2 (the real module of $\vec{q}_2$ in direct space is 26.48 Å). The angle of 90° between $\vec{q}_1$ and $\vec{q}_2$ reflects orthogonality of modulation waves in superspace. This might not be hazardous but rather linked to symmetry impositions. Finally, it is noteworthy that the irrational components of the modulation vectors $\vec{q}_1$ (α_1 = 0.53, β_1 =0.85, γ_2 = 0) and $\vec{q}_2$ (α_2 = 0.27, β_2 = 0.23, γ_2 = ½) can be seen to be related with interstitial oxygen occupancy (δ = 0.14) as following: $\alpha_1 \approx 4\delta$, $\beta_1 \approx 1 - \delta$, and $\alpha_2 \approx 2\delta$, $\beta_2 \approx ½ – 2\delta$. The value equal to 2δ is also the concentration of holes (Co^{3+}). This finding is not surprising since the incommensurability of charge order modulation (g_{CO}) in parent compounds have been previously found to be roughly a function of the concentration of the core hole (x); for instance in $La_2NiO_{4.125}$ $g_{CO} \approx (2x, 0, 1)$, in $Pr_{1.67}Sr_{0.33}NiO_4$ g_{CO} =(0, 2x, 2/3), and (0, 2x, 1)[200].

Further considerations about the real structure of this phase will be developed in chapter 5; results obtained from investigations of phase transitions with temperature and oxygen content provide supplementary deductions about the real atomic ordering in the incommensurately modulated $La_2CoO_{4.14}$ compound.

4. Atomic structure of oxygen rich $La_2CoO_{4.25}$ at RT

Oxygen rich $La_2CoO_{4.25}$ samples have been obtained by two distinct post-synthesis treatments, by:

i) electrochemical oxidation in KOH electrolyte (cf. Ph. D thesis of R. Le Toquin[8]), and

ii) thermal treatment under high oxygen partial pressure (6 hours at 773 K under mixed atmosphere of argon and oxygen 1:1, followed by slow cooling, 0.5 K/min).

Both kinds of samples have been subject to synchrotron X-ray diffraction (ID11@ESRF), λ = 0.2072 Å, with an exposure time t_{exp} of 0.2 (for refinements) and 0.4 seconds per image (for satellite detection), covering 280° with a step of $\Delta\varphi$ = 0.2°. Both types of sample show similar commensurate modulation in $\vec{a}$-$\vec{b}$ plane, even though their ordering along the *c*-axis differs. While the sample obtained by electrochemistry clearly shows commensurate quadrupling of *c*-axis, the samples obtained by thermal method show instead a very strong one-dimensional diffuse scattering toward this direction, implying disorder between the layers. Indeed, thermal treatments are more brutal for crystal samples than electrochemistry which is a soft chemistry technique and thus yields to more homogeneous metastable states. Furthermore, it probably provides higher concentrations of extra oxygen. Only few hours are sufficient to reach $La_2CoO_{4.25}$ stoichiometry with thermal treatment whereas up to one week is necessary with electrochemistry (with respect to an identical sample size of 1.10^2 µm). Consequently, oxidation with the latter procedure is gentler, allows a better structural stabilization and thus generates samples with better crystallinity and interlayer ordering.

However, on the phenomenological aspect, both techniques are significant concerning the crystal chemistry. The topotactic oxidation of $La_2CoO_{4+\delta}$ until such high extra oxygen content as δ = 0.25, corresponding to one interstitial oxygen atom per *F*-centered unit-cell of the crystal, implies strong lattice distortions without collapsing the basic structure. Moreover, for this value of δ, half of Cobalt ions have a degree of oxidation of Co^{3+} in low spin state while the other half are of Co^{2+} in high spin state. The questions of charge separation and spin states are still ambiguous, but what is sure is that mixed valence state for cobalt plays a prominent role in the reactivity of $La_2CoO_{4.25}$ crystal.

4.1.Basic structure explored by synchrotron diffraction

$La_2CoO_{4.25}$ crystal samples are usually twinned into four individual orientations. The scheme representing the corresponding split of main reflections in reciprocal space is shown in chapter 2, Figure 2.34. The raw diffraction pattern of these twinned crystals consists of superimposition of the four individual reciprocal lattices. The observed diffraction maxima can thus correspond to Bragg reflections of a single domain, or several domains together in the same peak, depending on their positions in the reciprocal space. So, first of all, the

average *F*4/*mmm* unit-cell is considered; cell parameters $a = b = 5.49(7)$ Å and $c = 12.53(4)$ Å with V = 377.65(5) Å^3. The *c*-axis is rather small in comparison with other phases of $La_2CoO_{4+\delta}$, but it is in agreement with oxygen stoichiometry of $\delta = 0.25$ (cf. Figure 1.15). It is rather astonishing to observe such decrease of the *c*-parameter's value for high extra oxygen content δ. One could think that, identically to $La_2CuO_{4+\delta}$ and $La_2NiO_{4+\delta}$, insertion of interstitial oxygen would enlarge the volume of the basic unit-cell toward *c*-axis by the elongation of interatomic bond distances between layers by steric effect. But on the contrary, the *c*-parameter is shrunk, which differentiates the cobaltate compound from other oxides of the same family. Insertion of extra oxygen between layers reduces internal strains yielding to the stabilization of the crystal structure by strong octahedra tilting. Moreover, the conversion of Co^{2+} into Co^{3+} reduces the size of the Co-O bond lengths. Least-square refinements converged with good agreement factors to the structural model presented in table 4.4. A Split position was used for apical site. Their respective occupancies were the last parameters refined during data analysis; and their values must be used with precaution since they result from X-ray diffraction data. However, they corroborate the tendency of octahedra to be in majority tilted by O_{ap} shift in [110] direction; and to be exact, also to the other orientations symmetrical by the fourfold axis collinear to $\vec{c}*$ (here only average structure is considered). The second position of apical oxygen corresponds to a tilt angle of 14.8°, which is rather big. But this value is an average. Occupancy of interstitial site was fixed during the refinements.

Table 4.4: *Structural model of as grown $La_2CoO_{4.25}$ single crystal refined only with main reflections.* Results from synchrotron X-ray diffraction experiment (ID11@ESRF) refined with *JANA2006*.

Atom	*x/a*	*y/b*	*z/c*	*Occ*	U_{11}	U_{22}	U_{33}	U_{12}	U_{eq}
La	0	0	0.3588(7)	2	19.1(3)	19.1(3)	13.1(6)	-	17.1(4)
Co	0	0	0	1	13.(1)	13.(1)	27.(1)	-	22(3)
O (eq)	¼	¼	0	2	21.(3)	21.(3)	32.(9)	(-3)	24.(7)
O (ap1)	0	0	0.174(7)	0.3(4)	58.(7)	58.(7)	17.(9)	-	45.(7)
O (ap2)	0.071(1)	0.071(1)	0.166(3)	1.6(4)	2(7)	-	-	-	2(7)
O (int)	¼	¼	¼	0.25	2(3)	-	-	-	2(3)

Average cell parameters: $a = b = 5.49(3)$ Å and $c = 12.53(4)$ Å, $\alpha = \beta = \gamma = 90°$. V = 377.65(5) Å^3, $2\Delta = 0.29°$.Average structure refined in *F*4/*mmm* on 476 independent main reflections. $R_{int} = 4.6$ %. Wavelength of X-rays: 0.2072 Å. Agreement factors: $R_F = 4.05$ %, $R_{WF} = 3.88$ %. *Uij* are given in 10^{-3} Å^2. U_{iso} for O(ap2) and O(int).

Orthorhombicity of the $\vec{a}$-$\vec{b}$ plane is rather small for $La_2CoO_{4.25}$; experimental value of 2Δ is of 0.29° when measured directly on reconstructed reciprocal maps. Values of *a*- and *b*-axis could have been estimated from orientation matrix based on main reflections belonging to a single domain: $a_b = 5.49(1)$ Å and $b_b = 5.50(4)$ Å (index *b* for 'basic' cell parameters, space

group *Fmmm*), corresponding to $2\Delta = 0.27°$, according to equation 3 (chapter 3), which is not far from the experimental value.

4.2.Modulation in the $\vec{a}$*-$\vec{b}$* plane

4.2.1. Determination of the supercell

The two-dimensional reciprocal space maps, with $\vec{c}$* normal to the planes, have been reconstructed from synchrotron X-ray diffraction data for $-11 \leq l \leq 11$ ($l = n$, with n integer). Figure 4.18*a* shows the experimental (*hk*1) reciprocal plane on which the splitting of the main reflections is barely distinguishable due to saturation combined with the low orthorhombicity. This experimental plane results from measurement with long exposure time (0.4 seconds), saturating main reflections but stressing superlattice reflections which are thus strong enough to be clearly observable.

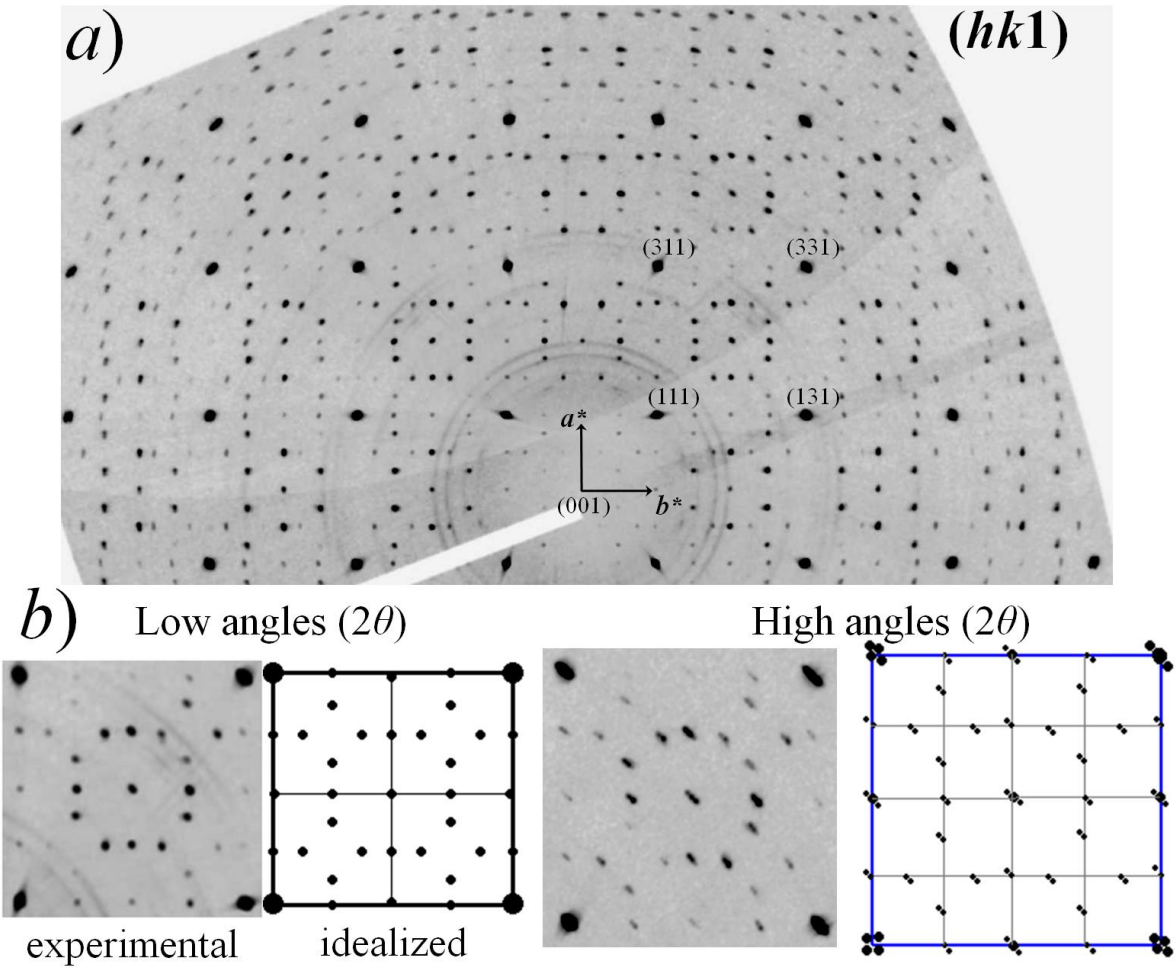

***Figure 4.18**: Experimental (hk1) reciprocal space map of $La_2CoO_{4.25}$ reconstructed from synchrotron X-ray diffraction data (ID11@ESRF), showing four twin components of commensurately modulated structure.*

Contrary to the *as grown* sample, the satellites are located in commensurate positions (rational indexes), they are *superstructure reflections*. Consequently not only main reflections but also superstructure reflections are split at high sinΘ/λ because of the four pseudo-merohedrally twinned domains. Satellites reflections are made either of two or three individual peaks, depending if they are common respectively with two or four domains. Attribution of each superstructure reflection to each individual twin has been carried out through the procedure previously described in section 3.2; and it results in the reciprocal lattice shown in Figure 4.19.

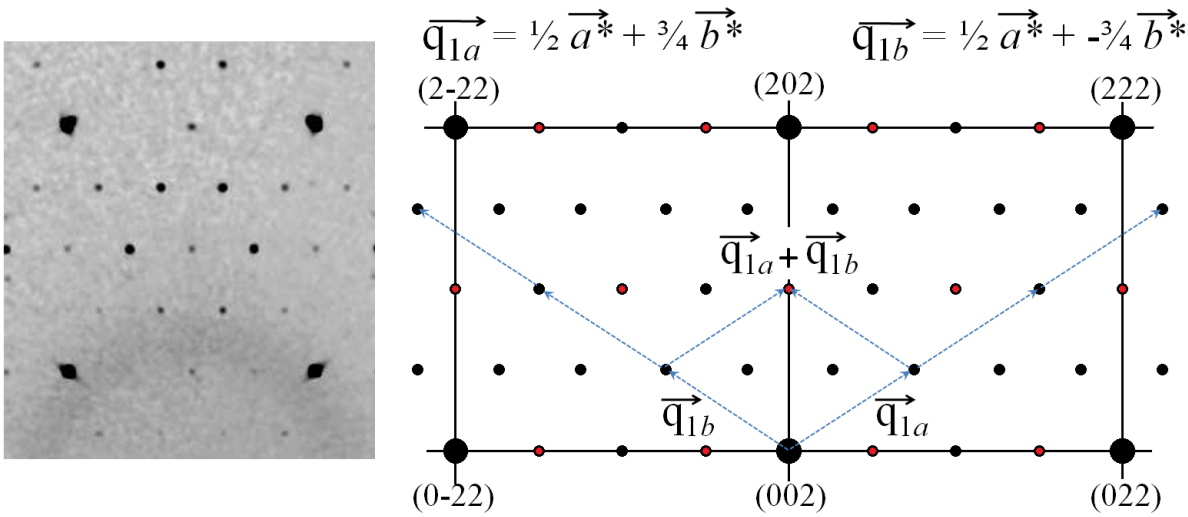

***Figure 4.19**: Zoom on the (hk1) experimental space map of a single domain sample, confirming the position of satellites for one individual. The resulting F-centered lattice can be indexed with two commensurate propagation vectors.*

One crystal sample made of a single domain has been extracted by chance. Its experimental reciprocal lattice confirms the attribution of superlattice reflections ensuing from twinned sample analysis. A zoom on a characteristic part of the (*hk*1) reciprocal map of the untwinned $La_2CoO_{4.25}$ sample is shown on the left part of Figure 4.19. Satellites can be indexed with two propagation vectors $\vec{q}_{1a} = (\alpha_1, \beta_1)$ and $\vec{q}_{1b} = (\alpha_1, -\beta_1)$ with $\alpha_1 = ½$, $\beta_1 = ¾$. In opposition to the *as grown* crystal, here, for $\delta = 0.25$, satellites are systematically present at the positions corresponding to the vector sum $\vec{q}_{1a} + \vec{q}_{1b}$. The two vectors modulate the same domain and the commensurate modulation can be considered as a superstructure with a three dimensional unit-cell of higher volume and of usual space group. Indexing the whole experimental diffraction pattern can be successfully achieved *via* two different superstructural models:

i) Considering a direct multiplication of the basic vectors: $\vec{a}_s* = ½\ \vec{a}_b*$, $\vec{b}_s* = ¼\ \vec{b}_b*$ and $\vec{c}_s* = \vec{c}_b*$, resulting in a *C*-centered orthorhombic unit-cell with a volume 8 times the volume of the *Fmmm* basic unit-cell in direct space, or

ii) Choosing a primitive monoclinic unit cell with $\vec{a}_s* = ½\ \vec{a}_b* + ¼\ \vec{b}_b*$, $\vec{b}_s = ½\ \vec{b}_b*$ and $\vec{c}_s* = \vec{c}_b*$, 4 times bigger than the basic one in direct space.

The indexation of the diffraction pattern with the two latter commensurate supercells is shown in Figure 4.20.

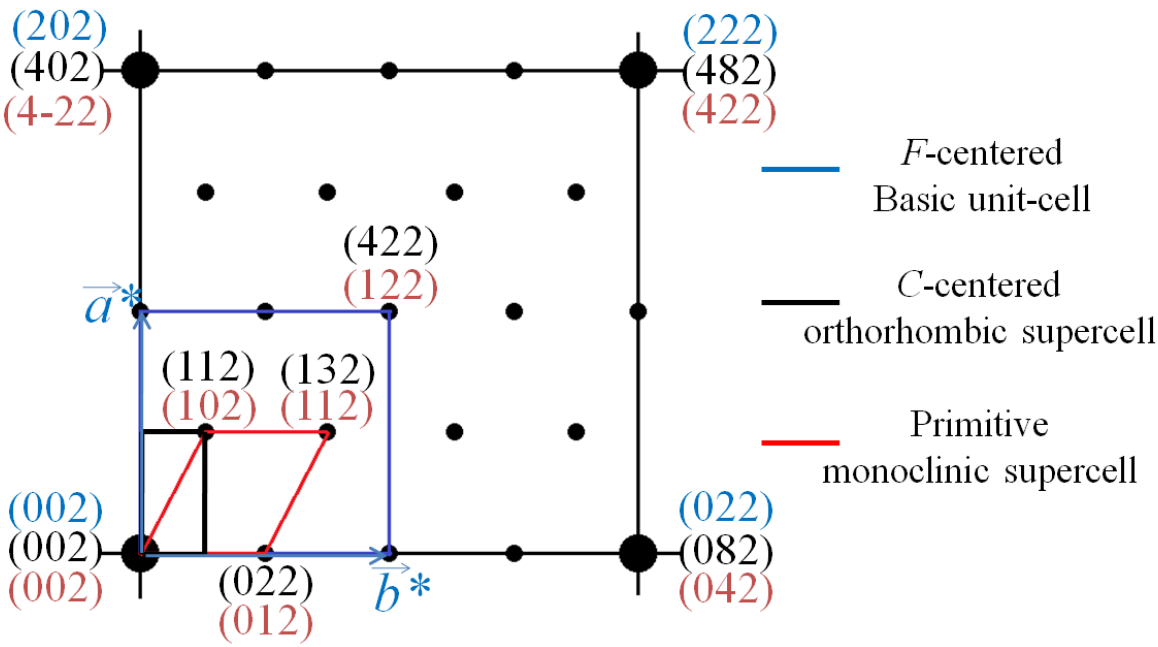

Figure 4.20*: Indexation of the reciprocal lattice shown for the F-centered basic unit cell, volume V (blue), for the C-centered orthorhombic supercell V' = 8V (black), and for the primitive monoclinic supercell V''= 4V (red).*

According to systematic extinctions found in the experimental diffraction pattern, the reflection conditions are:

- For the orthorhombic *C*-centered supercell ($½\ \vec{a}_b*$, $¼\ \vec{b}_b*$, $\vec{c}_b*$) (black on the figure): (*hkl*): $h + k = 2n$ (*C*-centering); (0*kl*): $k = 2n$; (*h*0*l*): $h = 2n$; (*hk*0): $h, k = 2n$ (glide plane parallel to *c-axis*); (*h*00): $h = 2n$; (0*k*0): $k = 2n$, those conditions match only with the space group *Cmme* (former space group *Cmma*)[201].

- For the indexation with the primitive monoclinic supercell (½ $\vec{a}_b$* - ¼ $\vec{b}_b$*, ½ $\vec{b}_b$*, $\vec{c}_b$*) (red on the figure): (*hk*0): *h* = 2*n*; (*h*00): *h* = 2*n*. It is consistent with the space group *P*112/*a* (*c* unique)[201].

4.2.2. Structural refinements

The integration of experimental intensities has been carried out through *CrysAlis* software, with the two superstructural models on the same set of experimental reflections. For the *Cmme* supercell, the resulting internal agreement factor R_{int} = 4.3 %, and for the *P*2/*a* supercell, R_{int} = 2.1 %, which are both acceptable values. The *C*-centered orthorhombic supercell seems to be more convenient: it simply implies direct multiplications of basic vectors (2 x 4 x 1) and its lattice is of higher symmetry. However, the primitive monoclinic superlattice is a better choice for refinements; its unit-cell volume is twice less important than the orthorhombic supercell and thus involves less parameter to refine. Indeed no reliable convergence could be reached for structural refinements based on the *C*-centered supercell, whereas it was successful with the monoclinic supercell model *a* = 11.05(8) Å, *b* = 12.26(9) Å and *c* = 12.53(1) Å, γ = 116.7(9)°, V = 1517.73(4) Å^3 (in direct space $\vec{a}$ = 2$\vec{a}_b$, $\vec{b}$ = 2$\vec{b}_b$-$\vec{a}_b$ and $\vec{c}$ = $\vec{c}_b$). Refinements have been carried out with *JANA2006* software on 2152 independent reflections. $\sigma(I)$ values have been averaged by *maxima* method. First, positions of La and Co atoms in the unit-cell have been determined with the *superflip* mode, and then refined *via* least-square method. Afterwards, oxygen positions were determined by the positions of maxima of electron density observed on the Fourier-difference maps calculated from the previous structural model (no oxygen yet). Figure 4.21 shows examples of resulting maps with *c*-axis normal to the plane, for different *z/c* slabs (F_{max}/F_{min} = 20/-5 and isosurfaces cut at 6/-2).

The interstitial atoms are clearly visible on the Fourier difference maps with 0.22 < *z/c* < 0.27 and 0.72 < *z/c* < 0.77. They are all equivalent by symmetry to one single independent position in the unit-cell, with full occupation (*cf.* O_{int} site 4*g* in Appendix A). The whole resulting model, taking oxygen atoms into account this time, has been refined; after convergence agreement factors resulted in R = 3.77 %, R_w = 3.59 %, and for final Fourier difference maps, ρ_{min}/ρ_{max} = -1.01/1.18 electrons/Å^3. The atomic parameters of the resulting structural model are given in Appendix A. All sites have full occupancy (*occ* = 1); their respective Wickoff symbol are given. Anisotropic displacement factors have been refined for La and Co atoms whereas isotropic displacement factors have been used for O atoms.

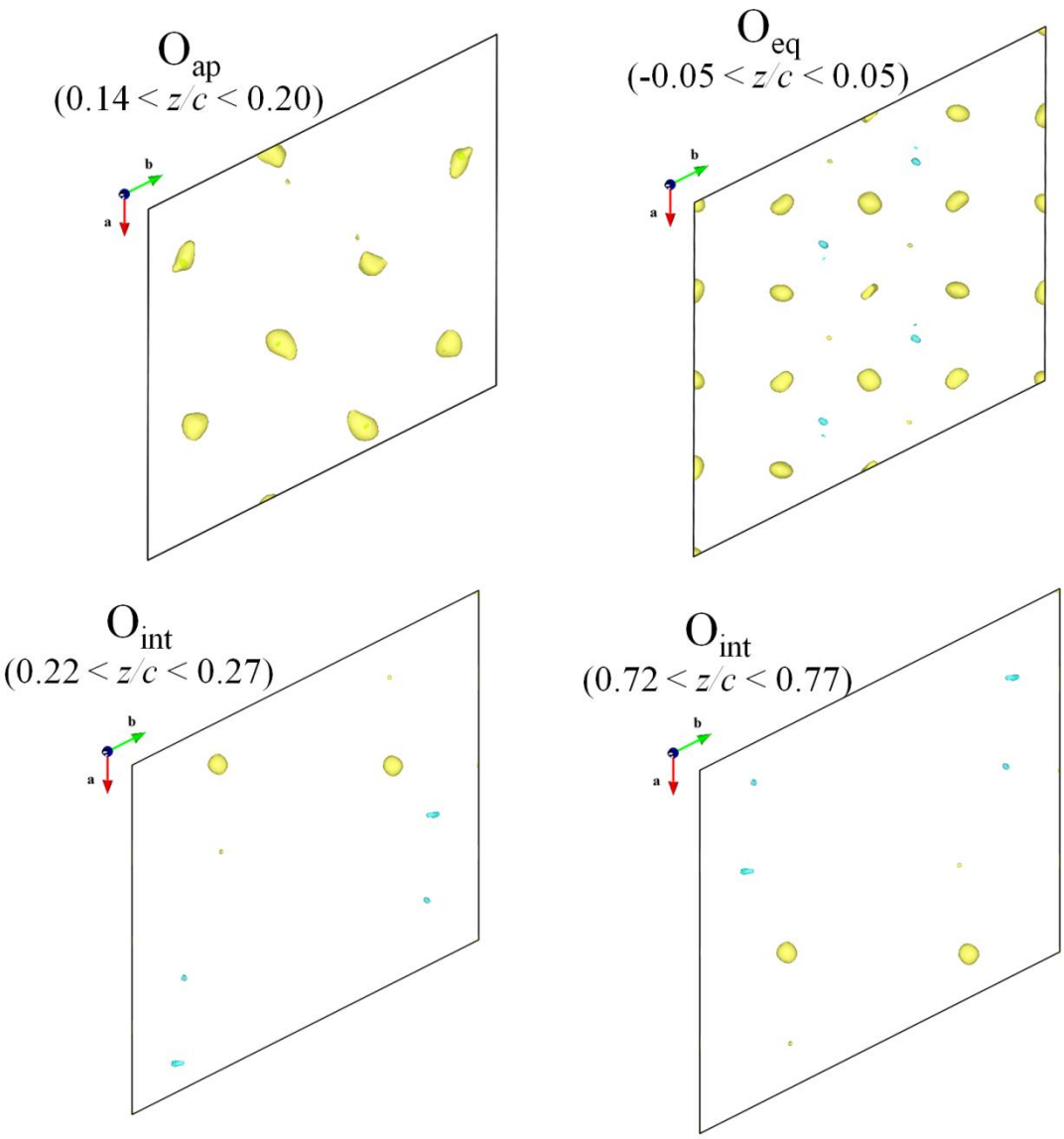

***Figure 4.21**: Fourier difference maps of $La_2CoO_{4.25}$ resulting from structural refinements with La and Co atoms only, showing the 3D profiles of the remaining electronic densities. It permits to determine the positions of oxygen atoms in the unit cell.*

Conversely to the basic space group *Fmmm*, the one of the monoclinic supercell: *P*2/*a* (*c* unique), provides non-split apical positions for tilted octahedra (8 independent positions). All CoO_6 octahedra of the same layer possess a common axis of rotation in the plane. But, axes of rotation alternate periodically between two orthogonal directions consecutively with the neighbor layers along *c*-axis: $[\pm110]_F$ for one layer and $[1\pm10]_F$ for the next one. Figure 4.22*a* shows the atomic positions refined for cobalt and oxygen atoms in the monoclinic supercell viewed from the two directions of rotation. La atoms have been removed for the sake of clarity (their electronic densities are shown separately with the one of Co atoms in Figure 4.23). The specific axis of rotation of each layer is well visible on Figure 4.22. It is, in this

sense, a different configuration that what was found for the oxygen-rich $La_2NiO_{4.125}$ compound by C. Frayret[220] who has shown that for the nickelate, the orthogonal directions of octahedra rotations alternate in the plane itself, leading to $P4_2/ncm$ space group. But here octahedra of same layer share a common rotation axis.

Furthermore, the refined positions of apical sites are coherent with the opening of the tetrahedral interstitial site which is occupied: it systematically goes in the sense of elongation for O_{ap}-O_{int} bond distances (2.61 Å in average). On the contrary, distances between apical oxygen and empty interstitial sites are reduced (1.95 Å in average). The four interstitial oxygen atoms in the monoclinic supercell, labeled by numbers on the part *a)* of Figure 4.22, are also shown on the part *b* for better distinction. The interstitial site determined from Fourier difference maps is compatible with the two supersymmetries, *i.e.* not only the *P*2/*a* cell but also the *Cmma* supercell. R. Le Toquin has reported many interesting results concerning the $La_2CoO_{4.25}$ in the manuscript of his Ph. D[8]. But since his reciprocal planes reconstructions resulted from usual X-ray diffraction with *KappaCCD* diffractometer, superstructure analyses and subsequent intensity integration was very arduous. Nevertheless, he managed to find the *C*-centered supercell (he suggested *Cmmm* instead of *Cmma*) and proposed a possible ordering of interstitial oxygen, not far to what is shown here, but yet different.

Here, according to the results and interpretations, interstitial oxygen ordering is very clear. The part *b*) of Figure 4.22 clearly shows the specific alternation of tilts, forming a non-perfect zig-zag scheme, systematically opening the interstitial sites occupied by extra oxygen atoms. While octahedra surrounding interstitial atoms are rather strongly tilted in opposite directions, the ones which are not in the first coordination sphere of O_{int} are less misaligned. If we believe that refinements are good enough for such fine interpretation, atomic displacement waves can be distinguished in the rows of apical oxygen atoms along diagonal directions marked by the red arrows on the figure. It is coherent with planar displacive modulation waves for O_{ap} correlated to occupational modulation of O_{int}. Angles of tilts have been calculated for each individual position refined for O_{ap} atoms, and are shown in Appendix A, together with the related Co-O_{ap} interatomic distances. In the table, apical atoms are listed from the smaller tilt to the bigger, the tilt angle continuously increases from 1.07° for $O_{ap}(1)$ up to 20.24° for $O_{ap}(8)$; intermediate tilts are associated to other O_{ap} atoms, with specific angle for each. In average, the interatomic distance between O_{ap} and Co is of ~ 2.24 Å, which is low in comparison to the other phases and explains the small value of *c*-parameter. O_{int}-O_{ap} distances are also given; they increase together with the tilt angle. The whole crystal structure

is distorted by long range ordering of O_{int}, and this is true for all types of atoms, *i.e.* not only oxygen but lanthanum and cobalt atoms too.

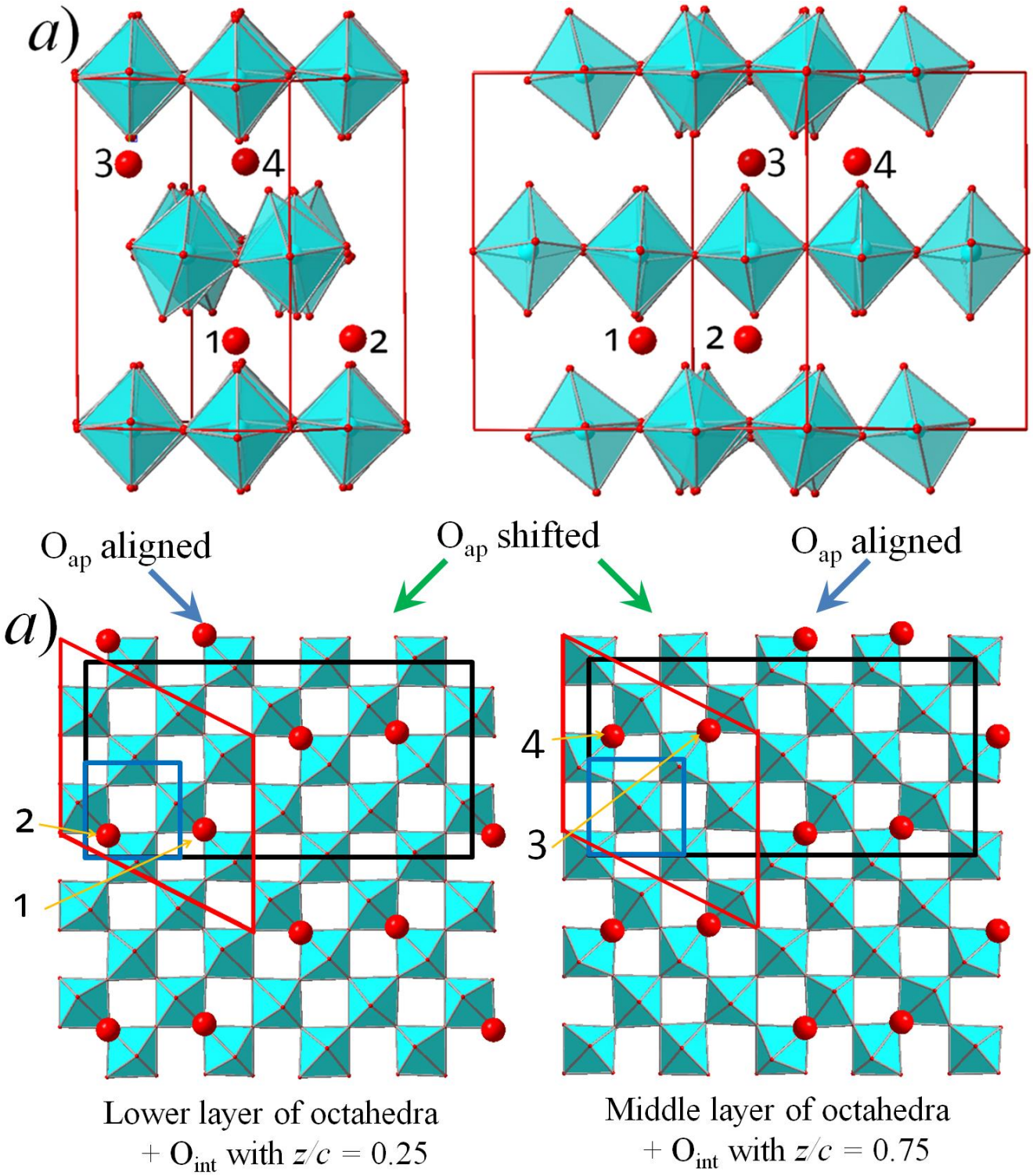

***Figure 4.22**: a) Arrangement of CoO_6 octahedra in the monoclinic supercell of $La_2CoO_{4.25}$ viewed from the two orthogonal directions of rotations of octahedra, depending on the layer. b) View with c-axis normal to the plane of the two kinds of layers of octahedra accompanied with the positions of long-range ordered interstitial oxygen atoms with z/c = 0.25 and 0.75. Interstitial oxygen atoms labeled by numbers on part 'a' are also shown on part 'b' for better distinction.*

Selective displacive modulation of La and Co

After convergence of structural refinements, electronic densities in the direct unit-cell have been calculated by Fourier transform of observed reflections this time. The subsequent 3D-profile of the electronic repartition is shown in Figure 4.23 for a triple unit-cell, providing a better view of atomic rows. Densities corresponding to oxygen sites have been cut in order to visualize only La and Co positions (F_{max} = 297, isosurfaces cut at 100). On the figure, the structure is oriented in such way that rows of atoms in the $\vec{a}$-$\vec{b}$ plane are shown on the bias, rendering optimized view of positional shifts. At first sight, one can see that atoms with z/c < 0.25 are only slightly subjected to positional modulation; Co atoms with z/c ~ 0 are even very well aligned. Conversely, the La and Co atoms with 0.25 < z/c < 0.75, stressed by the blue brace on the figure, display stronger displacements from their respective average sites. They are shifted toward the *c*-axis, which is in accordance with the in-plane modulation. La atoms seem to follow a crenel function while rows of Co atoms with z/c ~ 0.5 form waves.

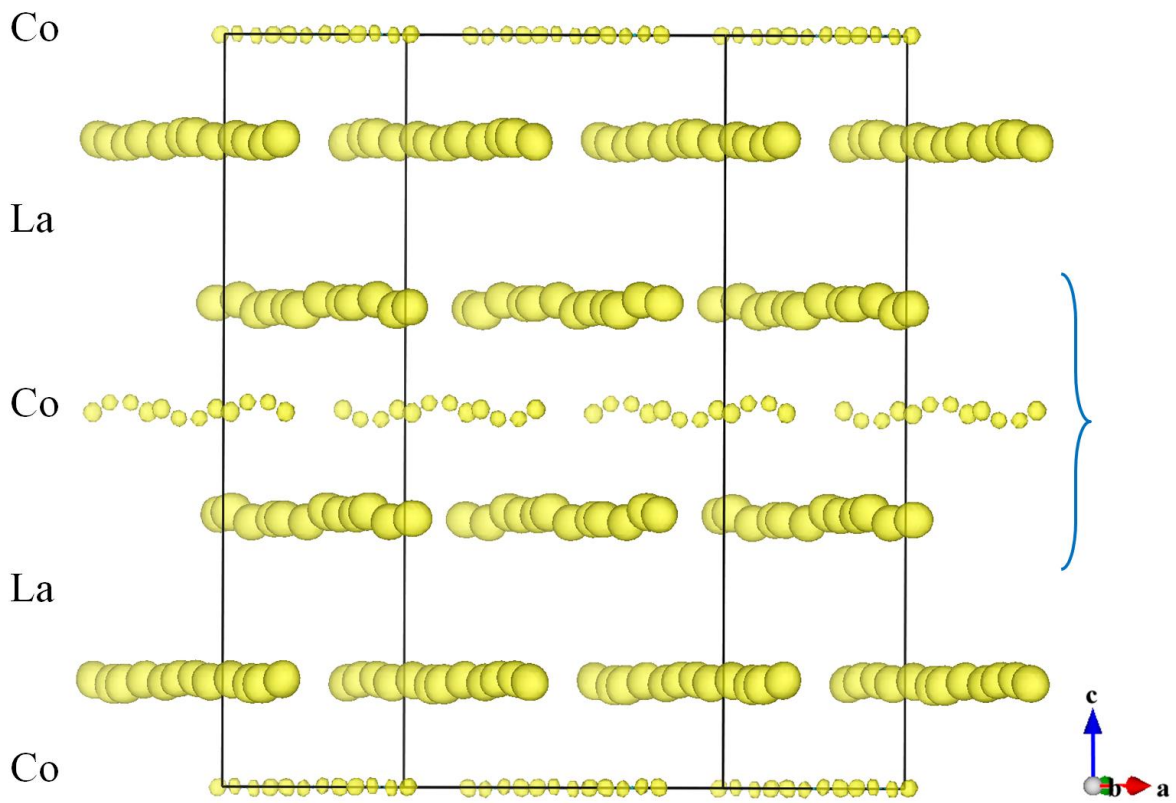

***Figure 4.23**: 3D profile of electronic density repartition calculated by Fourier (obs) transform after convergence of least square refinements. Oxygen atoms have been cut in order to stress positions of Co and La atoms in particular. The unit-cell is oriented in such way that it permits to view the rows of Co and La atoms in the structure. Electronic densities of three consecutive unit-cells are shown for a better view of atomic rows.*

Remark

The high quality of synchrotron data was determinant in the course of refining the atomic structure of $La_2CoO_{4.25}$. Neutron diffraction would naturally provide more precise information about oxygen atoms, notably concerning their displacements. But big single crystal samples, necessary for such experiments, are generally twinned into four domains, which drastically complicate the data treatment as explained in section 4.2 of chapter 3. In addition to this, with neutrons, data collection itself is arduous because of point-detectors. Indeed, positions of split reflections are hard to center, and meaningful intensities can be easily mislaid if the *UB* matrix set for the data collection is not perfectly adjusted to the lattice, which is particularly tricky for such twinned and modulated structures. The single domain character of the present sample, together with the use of area-detector for data acquisition, was crucial for solving the superstructure. Only microscopic single-domain samples can be expected, unless untwinning centimetric-sized crystal of $La_2CoO_{4.25}$ would be possible. Such post-synthesis processes have already been developed and are efficient for other types of oxides. It consists in applying electric/magnetic field to oriented samples under mechanical pressure applied anisotropically on specific external faces of the crystal. However this procedure works only on ferroelectric/magnetic samples, which is not the case here.

4.2.Order/disorder along $\vec{c}$* in $La_2CoO_{4.25}$

In the previous section only the in-plane modulation was considered. However, for an inclusive description of the real structure, ordering perpendicular to the $\vec{a}$-$\vec{b}$ plane, *e.g.* normal to layers, must also be taken into account. As explained before, samples of $La_2CoO_{4.25}$ prepared by thermal treatments are not modulated along $\vec{c}$*, but instead, show 1D-diffuse scattering toward this direction. This is related to disorder, consistent with random in-plane translation of the unit-cell between consecutive layers. Long-range ordering remains identical inside the layers but the distribution of O_{int} is arbitrary in the direction perpendicular to layers. The existence of such samples shows how strong the flexibility of the basic structure is. Indeed it demonstrates that the crystal lattice is able to adapt itself to relatively extreme situations, simultaneously keeping its coherency and crystal structure even for partially disordered phases.

In opposition to thermally treated samples, the ones obtained by electrochemistry are commensurately modulated along $\vec{c}$*. Sharp and intense commensurate superlattice reflections are observable toward this axis. For these samples symmetries exist between different layers, long-range order emerged perpendicularly to the $\vec{a}$-$\vec{b}$ plane. The presence of

well defined commensurate modulation in the $La_2CoO_{4.25}$ samples obtained by electrochemistry, but only diffuse scattering for the sample obtained thermally can be due to a slight difference of extra oxygen content δ. Since a very small amount of extra oxygen can be at the origin of important structural modifications, a difference of $\Delta\delta \sim 0.01$ would probably be enough for inducing/to induce different arrangements in the direction normal to the $\vec{a}$-$\vec{b}$ planes. It is possible that such high oxygen contents as $\delta = 0.25$ can only be reached by using soft-chemistry techniques which are famous to allow obtaining metastable states, while the thermal treatments are more brutal for single crystals. Consequently, even if the in-plane modulation is perfectly similar for the two kinds of samples, the ones resulting from annealing at 773 K under oxygen pressure could have an oxygen content value a bit inferior to 0.25. Figure 4.24 shows different zooms on particular reciprocal maps reconstructed for the sample obtained *via* oxidation at RT in aqueous KOH electrolyte. Characteristic cuts of experimental reciprocal space containing $\vec{c}$* in the plane are shown, and the manner these maps cut the (*hk*1) is depicted by colored lines labeled by numbers.

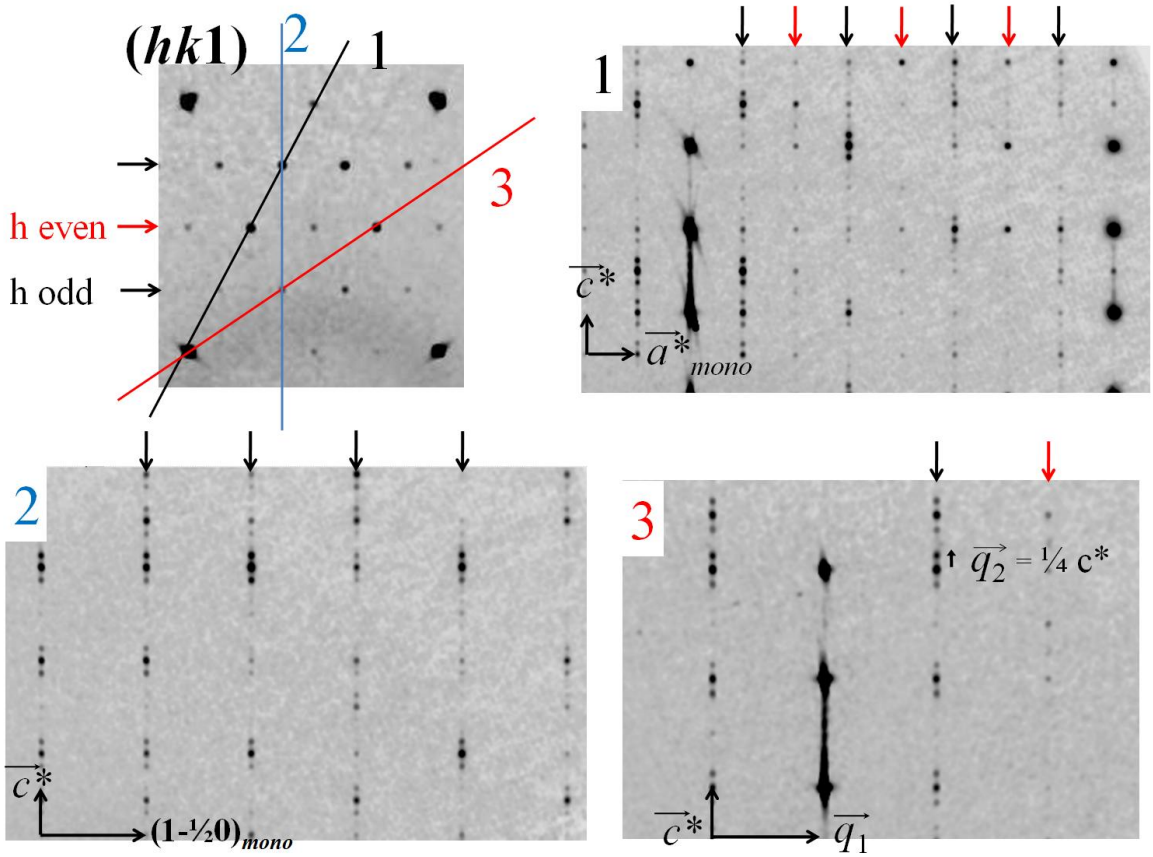

***Figure 4.24**: Experimental reciprocal space planes of $La_2CoO_{4.25}$ electrochemically oxidized sample modulated along $\vec{c}$* reconstructed from synchrotron X-ray diffraction data (ID11@ESRF). The manner the three planes containing $\vec{c}$* cut the (hk1) plane is indicated up left. Black arrows shows lines of reflections along $\vec{c}$* with h odd while red arrows correspond to h even.*

First of all, like for the *as grown* $La_2CoO_{4.14}$ phase, linear diffuse scattering takes place between the main reflections (*hh*6) and (*hh*8). Hence, disorder must be significant on the La site. Commensurate superlattice reflections visible on the maps containing $\vec{c}^*$ can be indexed with a propagation vector $\vec{q}_2$ = ¼ $\vec{c}^*$, *i.e.* quadrupling of the basic *c*-axis, with $|m_2| = 1$. After indexation of superstructure reflections with $\vec{q}_2$ based on the commensurate monoclinic supercell, space group *P*2/*a*, adopted as the best solution in the last section, special reflection condition on satellites are the following ($hklm_2$): $h + m_2 = 2n$, revealing centering in superspace. The maps show an alternation of the satellites depending on the parity of *h* (black arrows for *h* odd and red ones for *h* even); different planes are presented on the figure to confirm the extinction rule. Due to the presence of only first order satellites, a commensurate approach *via* usual space group is not very well adapted: it involves too much extinction. For instance, when considering a new *c*-axis for the monoclinic supercell, which equals four times the basic one, yielding to the indexation of all the commensurate satellites, all reflections (*hkl*) with $l = 2n + 4$ will be extinct. This fact has been validated by reconstructions of the corresponding planes, which are totally empty of reflections. Moreover, subsequent reflection conditions unfortunately do not fit with a conventional space group for monoclinic supercell with quadruple *c*-axis. Instead, transformations to inconvenient unit-cells are necessary. That is why it is preferable to keep the formalism of modulation vector, even if commensurate, with superspace group approach for defining symmetries along the *c*-axis, *i.e.* $P2/a(00\gamma)s0$ with γ = ¼. No reliable refinements based on this superspace group can be presented here because too many parameters are involved in the refinements. Indeed, it would necessitate modulation wave functions with at least six parameters for each independent atomic position of the monoclinic supercell (33 in total); and this, only if 1st order harmonics are considered, which generally does not allow an accurate structural description.

However, qualitative conclusions can be drawn from experimental reciprocal maps together with the results of in-plane modulation. It is legitimate to attribute the commensurate modulation along $\vec{c}^*$ to translational symmetries existing between alternating sequence of identical layers described by the monoclinic supercell. In other words one can consider that: *i*) the atomic structure of each layer, stacked toward the *c*-axis, corresponds to the monoclinic supercell *P*2/*a* described in the previous section, *ii*) two consecutive identical layers are not perfectly aligned along the *c*-axis; instead, each one is shifted with respect to the other *via* in-plane translational vector $\vec{v} = (p\ q\ 0)$, *iii*) four consecutive layers constitute a unit-block of ~50.12 Å thick which is repeated all along the *c*-axis, forming the whole crystal structure. According to these hypotheses, the last criterion which has to be determined for a total

depiction of the real atomic structure is the translational vector $\vec{v}$. According to all the results and conclusions presented until now concerning $La_2CoO_{4.25}$, and particularly on the base of the specific ordering found for O_{int}, the best hypothesis that we propose concerning ordering in *c*-direction is that the translational vector between two consecutive layers is $\vec{v}$ = -½ $\vec{a}_{mono}$ + ¼ $\vec{b}_{mono}$. This is consistent with the vector (0, 1, 0) in the basis of the *F*-centered unit-cell. Figure 4.25 illustrates the latter vector (black) in the $\vec{a}$-$\vec{b}$ plane, showing that after four consecutive shifts, the original position is recovered, which agrees with the quadrupling of the *c*-axis. This also works for the other interstitial layer of the monoclinic unit-cell (with *z*/*c* = 0.75). Since the whole basic structure is modulated as function of positions of the interstitial oxygen atoms, finding translational symmetries between the layers amounts to finding translations between O_{int} themselves. Another obvious solution for the translational vector would simply be $\vec{v}$ = -¼ $\vec{b}_{mono}$ (in blue on the figure) but this vector involves presence of oxygen atoms on interstitial sites (red crosses on the figure) whose surrounding apical atoms cannot open the tetrahedral site due to symmetry constrains; this potential solution can thus be excluded.

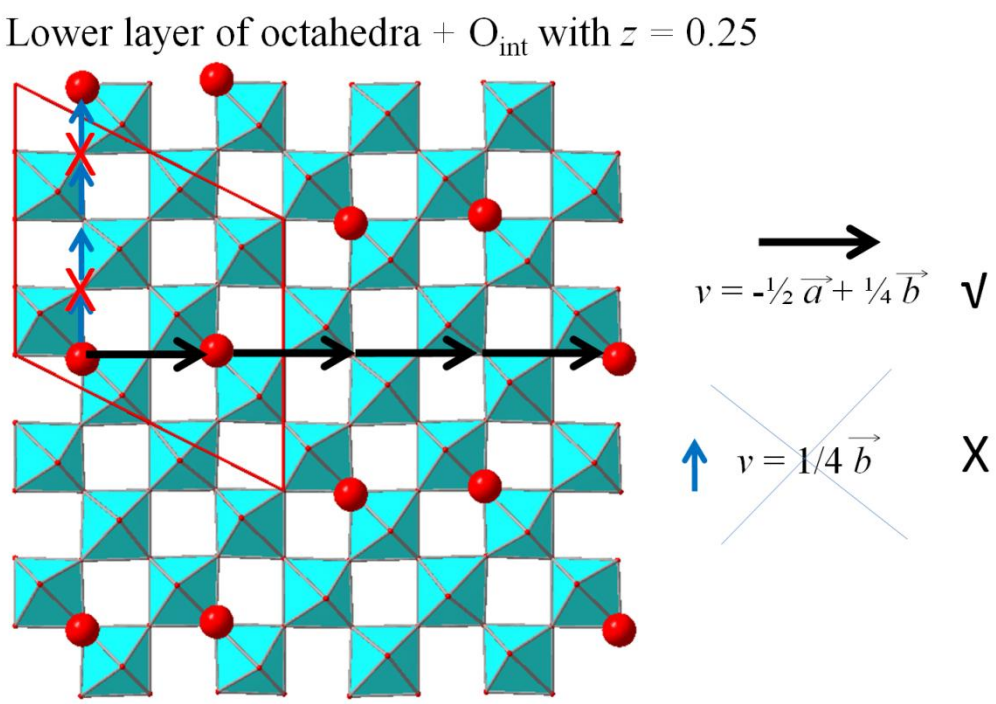

***Figure 4.25**: Probable translation vector depicting shift of interstitial oxygen atoms between two consecutive unit-cells along $\vec{c}$.*

5. Atomic structure of the intermediate oxygen-rich $La_2CoO_{4.19}$ at RT

The $La_2CoO_{4.19}$ compound has been obtained after thermal treatment on the *as grown* samples (δ = 0.14), *i.e.* six hours at 773K under air followed by slow cooling (0.5 K/min), no special gas flows have been applied during the process. The section 2.2 of chapter 5 describes the structural evolution, undergone by the *as grown* samples during this treatment, which is much more complex than expected. Here we consider the final state only. Oxygen content has been determined by thermogravimetry. Although $La_2CoO_{4.19}$ compound can be viewed as an intermediate state between the two phases presented beforehand (δ = 0.14) and (δ = 0.25), it is introduced in last for clarity. In order to avoid complexities and confusions, structural modulation analysis of this compound should be, indeed, globally presented and not separately into modulation in $\vec{a}$-$\vec{b}$ plane first and then modulation toward the *c*-axis, which was the strategy chosen before. A global and commensurate approach is necessary. The knowledge of the structure of the phase with δ = 0.25 gives important hints for its comprehension. According to the oxygen content of δ = 0.19, there are 0.75 interstitial oxygen atoms per basic *F*-centered unit-cell, *i.e.* 3 O_{int} for 4 unit-cells.

One sample of good quality has been chosen among several others, after a few tests using the *KappaCCD* diffractometer (*cf.* section 4.1, chapter 3). The diffraction pattern of this single crystal of 130 µm has been collected by synchrotron X-ray diffraction (ID11@ESRF), λ = 0.2072 Å, with an exposure time t_{exp} of 0.2 and 0.4 seconds per image on 280° with a step $\Delta\varphi$ = 0.2°.

5.1. Basic structure

Most of the time, samples of $La_2CoO_{4.19}$ obtained after thermal treatments were twinned into four individuals, even when using very low cooling ramps. The cell parameters refined for the tetragonal average cell are $a = b$ = 5.47(4) Å and c = 12.59(7) Å, with angular separation of (*hhl*) reflections of 2Δ = 0.72°. Refinements carried out using *JANA2006* with main reflections only, space group *F*4/*mmm* R_{int} = 4.1 %, result in the structural model shown in Table 4.6. The cell parameters resulting from the orientation matrix based on single domain's reflections give the following orthorhombic basic parameters of a_b = 5.45(8) Å and b_b = 5.49(2) Å c_b = 12.59(7) Å. The value of 2Δ = 0.71° calculated from the latter parameters are in accordance with the experimental one. Both orthorhombicity and *c*-parameter have intermediate values between the ones of δ = 0.14 and δ = 0.25 phases. They are in good

agreement with the stoichiometry of δ =0.19, according to fig 1.15 of chapter 1, and also regarding to the results of R. Le Toquin[8]. A split model was used for O_{ap}, consistent with averaged value of tilt angle equal to 10.28° for the (*x*, *x*, *z*) site.

Table 4.6: *Structural model of as grown $La_2CoO_{4.19}$ single crystal refined with main reflections only. Results from synchrotron X-ray diffraction experiment (ID11@ESRF).*

Atom	*x/a*	*y/b*	*z/c*	*Occ*	U_{11}	U_{22}	U_{33}	U_{12}	U_{eq}
La	0	0	0.3597(1)	2	16.1(2)	16.1(2)	14.8(3)	-	15.(3)
Co	0	0	0	1	15.(7)	15.(7)	21.(9)	-	17.(7)
O (eq)	¼	¼	0	2	31.(1)	31.(1)	32.(4)	-5.(7)	31.(7)
O (ap1)	0	0	0.175(4)	0.5(7)	51.(3)	51.(3)	25.(4)	-	42.(3)
O (ap2)	0.050(2)	0.050(2)	0.169(4)	1.3(9)	2(9)	-	-	-	2(9)
O (int)	¼	¼	¼	0.25	3(6)	-	-	-	3(6)

Average cell parameters: $a = b = 5.47(4)$ Å and $c = 12.59(7)$ Å, $\alpha = \beta = \gamma = 90°$. V = 376.70(4) Å $2\Delta = 0.72°$Average structure refined in *F*4/*mmm* on 512 independent main reflections. R_{int} = 4.1 %.Wavelength of X-rays: 0.2072 Å. Agreement factors: R_F = 5.75 %, R_{WF} = 4.96 %. *Uij* are given in 10^{-3} Å^2.

5.2.Commensurate modulation in three dimensions, symmetry of supercell.

As explained beforehand, structural modulation in $\vec{a}$-$\vec{b}$ plane and toward $\vec{c}$ will be treated together for the $La_2CoO_{4.19}$ phase. This is due to the fact that satellites with component toward $\vec{c}$* are observable for $m > 1$, and commensurate approach using quadruple *c*-axis turns out to be relevant in this case. Furthermore, as we will see, interstitial oxygen ordering in this phase cannot be depicted by a model where identical layers are stacked along the *c*-axis; *i.e.* ordering of O_{int} differs from one layer to the other. At first sight, the superstructure of $La_2CoO_{4.19}$ seems to be rather close to the one of $La_2CoO_{4.25}$. They share similar in-plane propagation vectors, and thus their unit-cell parameters are almost identical. However extinctions and intensities of reflections are different and thus the atomic structure is completely dissimilar.

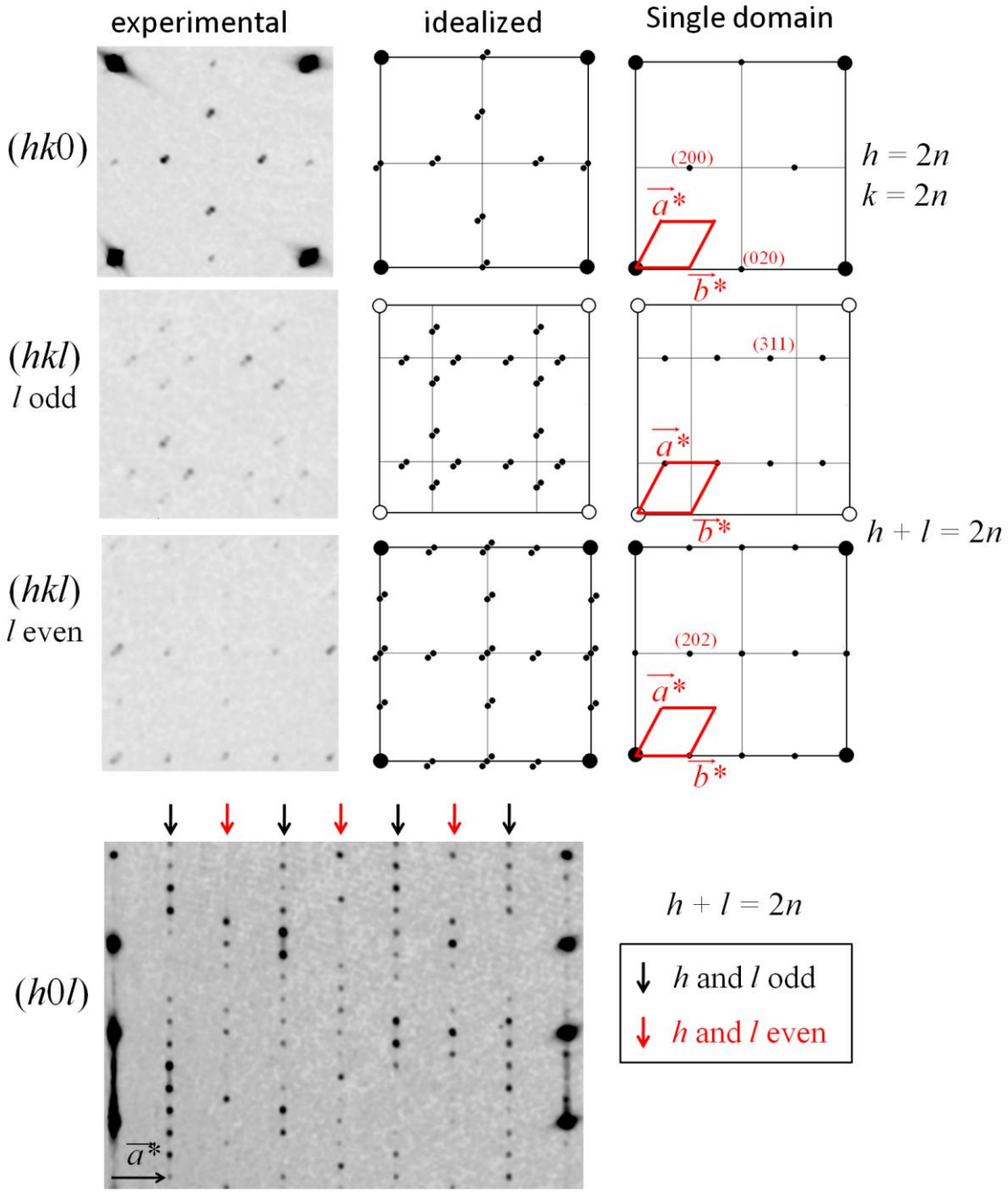

***Figure 4.26**: Zoom on few typical experimental reciprocal space planes of $La_2CoO_{4.19}$ reconstructed from synchrotron X-ray diffraction data (ID11@ESRF), together with their corresponding idealized pattern for 4 individuals and single twin individual. Reflection conditions for the monoclinic supercell can be deduced from these planes.*

Satellites doubly split correspond to two domains while satellites triply split correspond to the four domains. The idealized patterns presented on Figure 4.26 have been built after a fine observation of the whole experimental reciprocal space, not only from the experimental planes shown on the left. Shifts of superlattice reflections have been carefully studied and

permitted to separate the raw diffraction pattern into the 4 reciprocal lattices belonging respectively to each individual twin. Idealized diffraction pattern for the same single domain is shown on the right side of the figure for each plane. What first comes out of these results is that the reciprocal supercell parameters are $\overrightarrow{a^*}$ = ½ $\overrightarrow{a_b^*}$ + ¼ $\overrightarrow{b_b^*}$, $\overrightarrow{b^*}$ = 2 $\overrightarrow{b_b^*}$, $\overrightarrow{c^*}$ = 4 $\overrightarrow{c_b^*}$, *i.e.* the same *a*- and *b*-axes than for δ = 0.25 but with 4*c* this time. Consequently, in real space, $a = 2a_b$ = 10.94(8) Å, $b = 2b_b$-a_b = 12.26(9) Å, $c = 4c_b$ = 50.38(8) Å, γ = 116.6(4)° and V = 6047.20(2) Å^3 which is 16 times the volume of the basic *F*-centered unit-cell. According to the oxygen content which imposes 3 extra oxygen atoms per 4 basic unit-cells, there are 12 O_{int} for 16 *Fmmm* unit-cells. This volume for the supercell agrees with the commensurability of the modulation which requires an integer number of O_{int} per supercell. When indexing the experimental diffraction pattern on the base of the monoclinic supercell given above, reflection conditions are: (*hkl*) (*h*0*l*) (0*kl*): $h + l = 2n$, (*hk*0): $h, k = 2n$, (00*l*): $l = 2n$. This unambiguously corresponds to the conventional space group *B*2/*n* (*c* unique) which depicts the real symmetry of the crystal structure in the commensurate monoclinic supercell.

5.3.Structural refinements

One sample twinned in just two domains could have been measured and structural refinements have been tempted with the subsequent experimental data. The volumic repartition of each twin in the crystal was of ~78-22%; consequently, satellites have been easily differentiated and they confirmed the positions previously found for a single domain. Experimental intensities, indexed by the *B*2/*n* supercell, have been integrated for a single twin orientation by twin separation through *CrysAlis* program. The internal agreement factor resulted in R_{int} = 3.20 %. This is an acceptable value, even surprisingly good for such untwinned data of modulated structure. The volume of the unit-cell being huge, numerous atomic positions had to be refined, involving many parameters. Hence, results of refinements must be cautiously interpreted. However, the large amount of observed reflections remains an advantage (it is usually admitted that refinements are acceptable if the number of reflections is at least 10 times higher than the number of parameters refined, here 372 parameters refined in total, on 4594 observed reflections). The *modus operandi* for structural refinements was very similar to the one employed for $La_2CoO_{4.25}$. Nevertheless, it is more delicate since the supercell of $La_2CoO_{4.19}$ contains much more individual atomic positions since this time quadrupling of *c*-axis is taken into account.

First of all, positions of heavier atoms La and Co have been clearly determined through *superflip* calculations. Those positions and their corresponding atomic displacement factors have then been refined by least square method, up to R = 7.38 % and R_w = 7.97 %. Fourier-difference maps were calculated from this structural model, permitting to locate the positions of apical and equatorial oxygen atoms in the supercell from the remaining maxima of electron densities. Figure 4.27 shows, for instance, two Fourier-difference maps where maxima corresponding to apical and equatorial oxygen atoms are well visible (F_{max} = 14, isosurfaces are cut at 6).

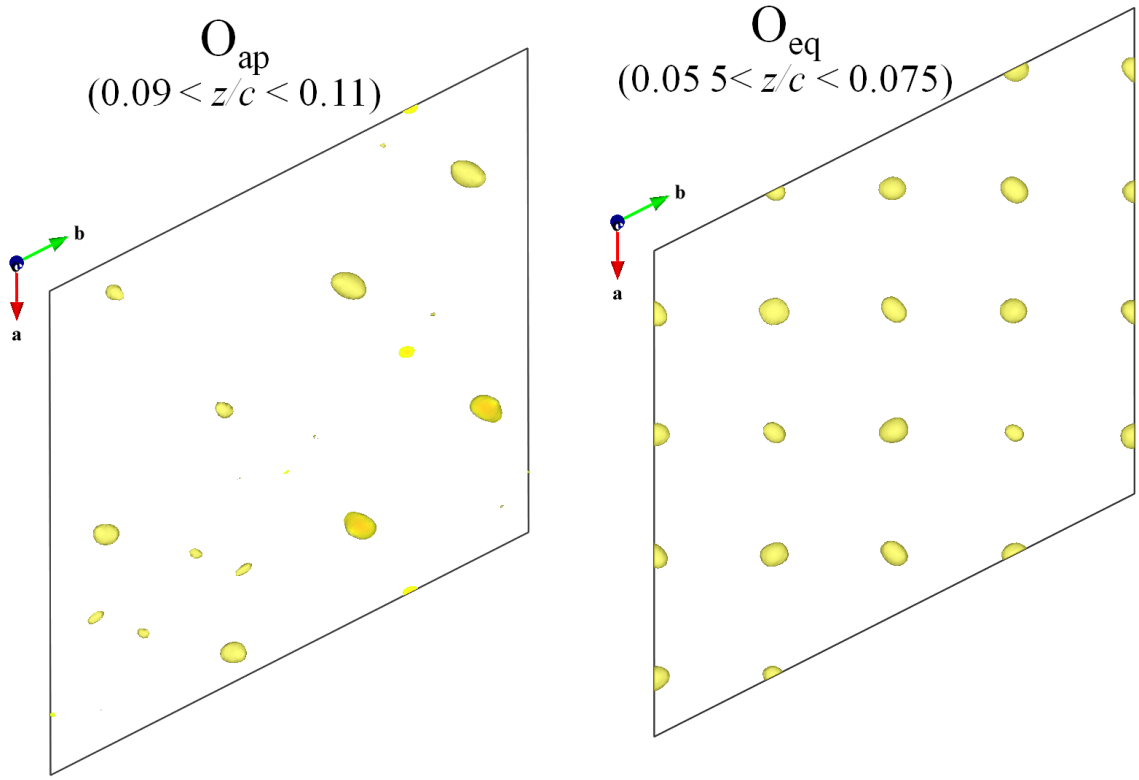

***Figure 4.27**: Examples of Fourier-difference maps calculated with structural model taking into account heavier atoms only, namely La and Co, permitting to determine the positions of equatorial and apical oxygen atoms in the monoclinic supercell.*

This time, interstitial positions were difficult to identify. They have been established according to *i*) the tilts of the octahedra found after the refinements, *ii*) Fourier-difference maps, and *iii*) symmetry/multiplicity of each possible site with regards to *B*2/*n* space group. Once those conditions gathered, very few possibilities were potentially relevant, only 3 combinations of possible positions in all. After testing all of them, one solution was preferred and adopted since it was the only one matching with both the oxygen content of δ = 0.19 and the apical oxygen positions. Moreover, only this solution results in a reasonable distribution

of the interstitial atoms, *i.e.* the most widely spread in the lattice. The other solutions implied illogical atomic positions for interstitial atoms. The whole resulting model has then been refined step by step until reaching a convergence with satisfactory agreement factors, R = 5.27 % and R_w = 5.12 %, with ρ_{min}/ρ_{max} = -1.8/2.03 for final Fourier-difference maps. Those values, even if acceptable, are not as accurate as the ones obtained for the other $La_2CoO_{4+\delta}$ phases; it is due to the large amount of independent atomic positions in one unit cell together with the fact that most of them are occupied by oxygen atoms (63 positions in total = 16 La + 8 Co + 20 O_{eq} + 16 O_{ap} + 3 O_{int}). Atomic displacement factors have been refined with anisotropic coefficient for La and Co atoms while isotropic coefficients have been used for oxygen atoms. All site of the model has full occupancy, even O_{int} sites. It has to be underlined that the following conclusions about superstructure and interstitial oxygen ordering are hypothetical, they should not be seen as definitive but rather with a critical eye, as a possibility but not as a fact. Even if many precautions have been taken for measurements and data treatments, errors or artifacts can appear by mischance. However, since the structural model ensuing from these analyses appears to be coherent, it is briefly discussed hereafter.

The results of our refinements (atomic positions and anisotropic displacements factors) are given in Appendix B, and the corresponding 3D visualization of atomic positions in the unit cell is depicted in Figure 4.28, in which La atoms have been removed to better distinct octahedra. The supercell *B*2/*n* is shown together with the four lower layers of CoO_6 octahedra, each one accompanied with their respective interstitial oxygen atoms lying above. The other layers, *i.e.* the four upper ones, are symmetrical by inversion center. The 12 interstitial atoms in the unit cell are generated by symmetry from 3 sites of multiplicity 4 (Wickoff symbol *e*) with full occupation. Their ordering is different from the one found for $La_2CoO_{4.25}$ in the sense that, this time, interstitial atoms are not aligned toward the direction of the tilts of the octahedra. Thus, in the case of $La_2CoO_{4.19}$, octahedra of the same layer are not tilted toward a common orientation, due to the specific ordering of oxygen atoms with $z/c = n/8$ (n integer). For instance, on the layers labeled number 2 and 4 on figure 4.28, the two interstitial oxygen atoms involve two orthogonal directions of tilt for their surrounding octahedra, which belong to the same layer, like for $La_2NiO_{4.125}$ results reported by C. Frayret[220]. Hence, whereas for δ = 0.25, here there are not diagonal rows of apical oxygen aligned, and separately rows forming zig-zag. The crystal structure when δ = 0.19 can be regarded as less ordered because zig-zag of O_{ap} are observed for both directions $[\pm110]_F$ and $[1\pm10]_F$ in the same layer.

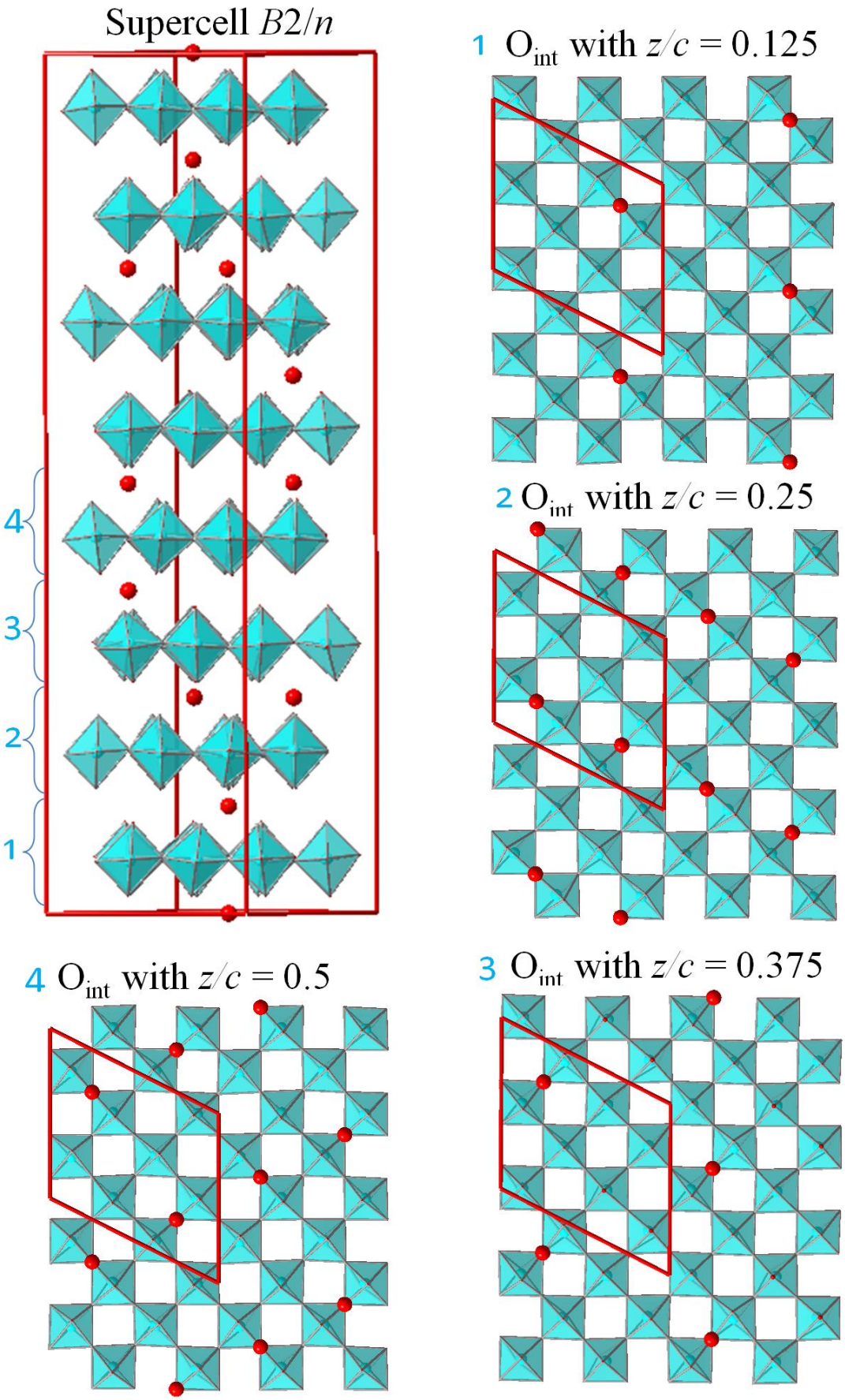

Figure 4.28: Visualization of the monoclinic supercell, space group B2/n, of $La_2CoO_{4.19}$. Four layers, labeled by numbers are shown with $\vec{c}$ normal to the plane.

As shown on the figure, ordering differs between interlayers. Moreover, two consecutive interlayers along *c*-axis do not contain the same amount of extra oxygen atoms with a ratio of (1:2). For instance, the layers labeled by odd numbers on the figure possess one O_{int} in the interlayer while there are two O_{int} for layers labeled by even numbers. This alternation of extra oxygen concentration between consecutive layers is comparable to stages found in $La_2NiO_{4.125}$ by Tranquada *et.al*[142]. However, here for $La_2CoO_{4.19}$, all interstitial layers contain extra-oxygen atoms. Nevertheless, disparities persist between interlayers. And this is confirmed by the positions of La atoms visualized by 3D electronic density profile calculated from Fourier-transform on observed reflections, presented in Figure 4.29. It shows how the rows of La atoms close to the interstitial layers with z/c ~ 0.25 (layer number 2, rich in O_{int}) are submitted to a strong positional modulation in comparison with rows of La atoms surrounding the interlayer with z/c = 0.125 (layer number1, poor in O_{int}), which are rather well aligned. It is conceivable that the more interstitial oxygen atoms there are in an interlayer, the more the local environment will be distorted.

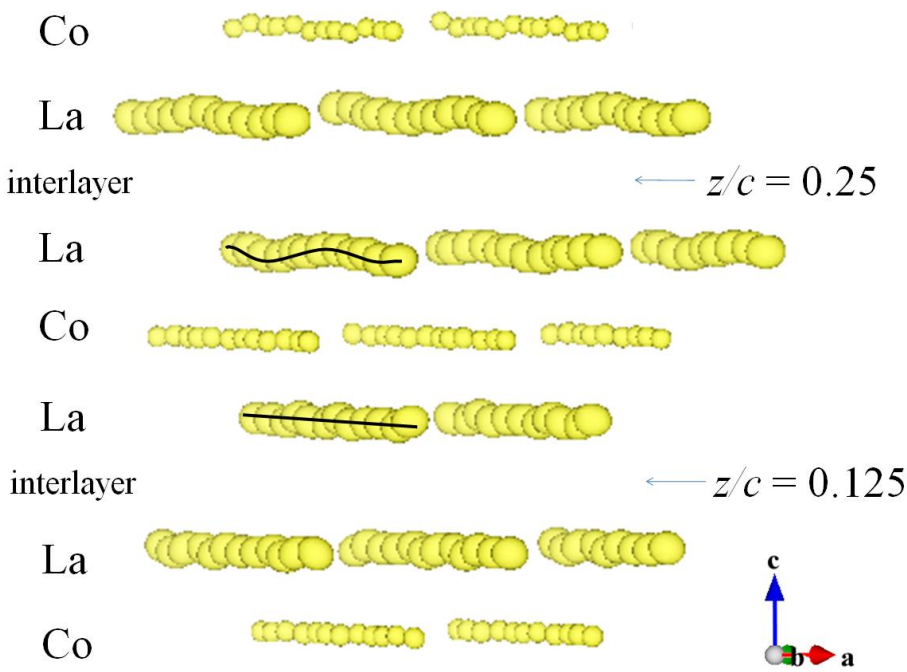

***Figure 4.29**: 3D profile showing isosurfaces of electronic density repartition calculated by Fourier (obs) after final convergence of least-square refinements. Densities corresponding to rows of La and Co atoms are visible. Electronic densities of three consecutive unit-cells along b are shown for a better view of the atomic rows. Rows of La atoms surrounding the interlayer with z/c = 0.25 are more distorted than the ones with z/c = 0.125, symbolized by the black lines.*

***Table 4.8**: Summary of structural characteristics for each oxygen-rich phase of $La_2CoO_{4+\delta}$ with modulated structure stable at RT*

$La_2CoO_{4+\delta}$	Average cell *F4/mmm*				Modulation					
δ	*a* (Å)	c (Å)	V (Å^3)	2*Δ* (°)	Type	$\vec{a}^*$-$\vec{b}^*$ plane	Toward $\vec{c}^*$	Supercell (Å)	V(Å^3)	Symmetry
0.14	5.508(4)	12.64(9)	383.74(6)	1.12	(3+2) INC	0.53 $\vec{a}^*$ + 0.85 $\vec{b}^*$	0.27 $\vec{a}^*$ - 0.23 $\vec{b}^*$ + ½ $\vec{c}^*$ (only 1st order)	X	X	Monoclinic $F2/m(\alpha_2\beta_2½)00(\alpha_1\beta_1 0)0s$ $\alpha_1 = 0.53$, $\beta_1 = 0.85$ $\alpha_2 = 0.27$, $\beta_2 = -0.23$
0.19	5.47(4)	12.59(7)	377.46(5)	0.72	3D COM	½ $\vec{a}^*$ + ¾ $\vec{b}^*$ ½ $\vec{a}^*$ - ¾ $\vec{b}^*$	¼ $\vec{c}^*$	a' = 10.94(8) Å b' = 12.26(9) Å c' = 50.38(8) Å γ = 116.7(9)°	6047.20(2)	Monoclinic $B2/n$
0.25	5.49(3)	12.53(4)	378.18(8)	0.29	(3+1) COM	½ $\vec{a}^*$ + ¾ $\vec{b}^*$ ½ $\vec{a}^*$ - ¾ $\vec{b}^*$	¼ $\vec{c}^*$ (only 1st order)	a' = 11.05(8) Å b' = 12.26(9) Å c' = 12.53(1) Å γ = 116.6(4)°	1517.73(4)	Monoclinic $P2/a(00\gamma)s0$ γ = ¼

Chapter 5

Phase transitions with temperature: Irreversible transformation of T' to T La_2CuO_4, Thermal evolution of $La_2CoO_{4+\delta}$ accompanied with variation of δ

The phase transitions driven by temperature occurring for the stoichiometric La_2MO_4 system with T-type structure have been subject to intense studies allowing to differentiate the thermal evolution of the three compounds with M = Co, Ni, Cu (*cf.* chapter 1). Besides the low-temperature phase transitions yielding to LTT or even to LTLO phases depending on the octahedra arrangements, the compounds are also submitted to structural transformations on heating. Indeed, above RT, a transition to the ideal HTT phase occurs, attributed to the activation of soft-phonon modes consisting of dynamic tilting of octahedra, happening at different temperatures and depending on the transition metal M (*cf.* section 2.1.1, chapter 1). However, the phase diagram of the T'-phase of La_2CuO_4, isostructural to Nd_2CuO_4, has not been explored in details. Only powder diffraction studies[13] have been reported until now and no correlations have been done between the atomic structure and the absence of oxygen diffusion properties for the T'-type compounds. Here we present the temperature dependence of single crystal samples of T'-La_2CuO_4, showing transition to T-phase at high temperature, and allowing supplementary deductions with regard to atomic migration between interstitial and apical site, which has been reported to be the diffusion pathway undertaken by oxygen atoms at high temperature in those type of materials[83,224,82].

Concerning the oxygen-rich $La_2MO_{4+\delta}$ compounds, the situation is different. For instance, the phase diagram of $La_2NiO_{4+\delta}$ as function of T and δ, built by J.M. Tranquada *et al.*[142] (Figure 1.20), involves several distinct states with complex atomic super-orderings. In this chapter, new results concerning the temperature dependence of $La_2CoO_{4+\delta}$ are reported showing how its phase diagram (T vs. δ) exhibits several modulated phases, implying phase transitions of displacive type. The phase transitions are, in some cases, not only driven by the temperature but also by the content of oxygen δ. Indeed, similarly to the spontaneous topotactic oxidation occurring for the stoichiometric La_2CoO_4 at RT (up to $\delta \sim 0.15$), the oxygen content of

$La_2CoO_{4+\delta}$ varies spontaneously with temperature. It appears that gain or loss of extra oxygen in the crystal lattice from the atmosphere is activated at specific temperatures depending on the crystal structure, *i.e.* on extra-oxygen concentration. This exceptional reactivity allowed exploring the effects, brought by variations of oxygen concentration on the atomic arrangements, through structural characterizations and thermogravimetric experiments.

1. Transitions between T' and T-phase by La_2CuO_4, migration pathway between interstitial site and apical site.

1.1. Motivations of the studies

All the RE_2CuO_4 compounds, of various Rare Earth (*RE*) elements, synthesized by solid state routine at high temperature (up to 1400 K) stabilize in the T'-type structure at RT, except for the Lanthanum compound which adopts the K_2NiF_4-type structure also called T-phase, with a small distortion at RT (LTO phase). The latter LTO-phase has been admitted for long time to be the only stable state for the cuprate compound. This different atomic stacking in comparison with the other rare earths was attributed to the larger ionic radius of La, responsible of the different atomic arrangement (cf. chapter 1, section 1.3.3). However, more recently, La_2CuO_4 samples of T'-type could have been obtained through different synthesis procedures involving lower temperatures of process (~700 K, *cf.* chapter 2, section 2). The coexistence of these two polymorph states for La_2CuO_4 at RT is remarkable and asks several questions about the respective stability of each state. For instance: which one is the more stable? Or maybe which one is the more metastable? What are the criteria defining the states of stabilization? What is the origin of polymorphism?

The atomic structure of T and T'-type phases appear to be rather close: only one atomic position differs. While for the stoichiometric T-phase interstitial sites are empty and apical sites have full occupation, it is the contrary in the T'-phase, interstitial sites have full occupation and apical sites are empty. Consequently, while the T-phase consists of planar array of corner-shared CuO_6 octahedra, the T'-phase can be portrayed as planar array of corner-shared CuO_4 square-planes. These two phases of same space group, *I4/mmm*, but different volume of unit-cell, can be considered as the two prototype phases. In between, the oxygen-enriched $La_2CuO_{4+\delta}$ compounds can be viewed as an intermediate situation for which apical sites are full and interstitial sites are partially occupied. The figure 5.1 depicts this fact. One astonishing aspect is that insertion of extra oxygen can be only and strictly achieved in T-

phase, while the T'-type structure is not reactive at all with regards to oxygen; insertion of extra oxygen remaining impossible in the T'-phase[16]. Only reduced states, as oxygen-deficient pseudo S-phase, are attainable (see chapter 2, section 2.1). This major difference between the two polymorph states is of first importance for understanding the oxygen diffusion mechanism in the T-phase.

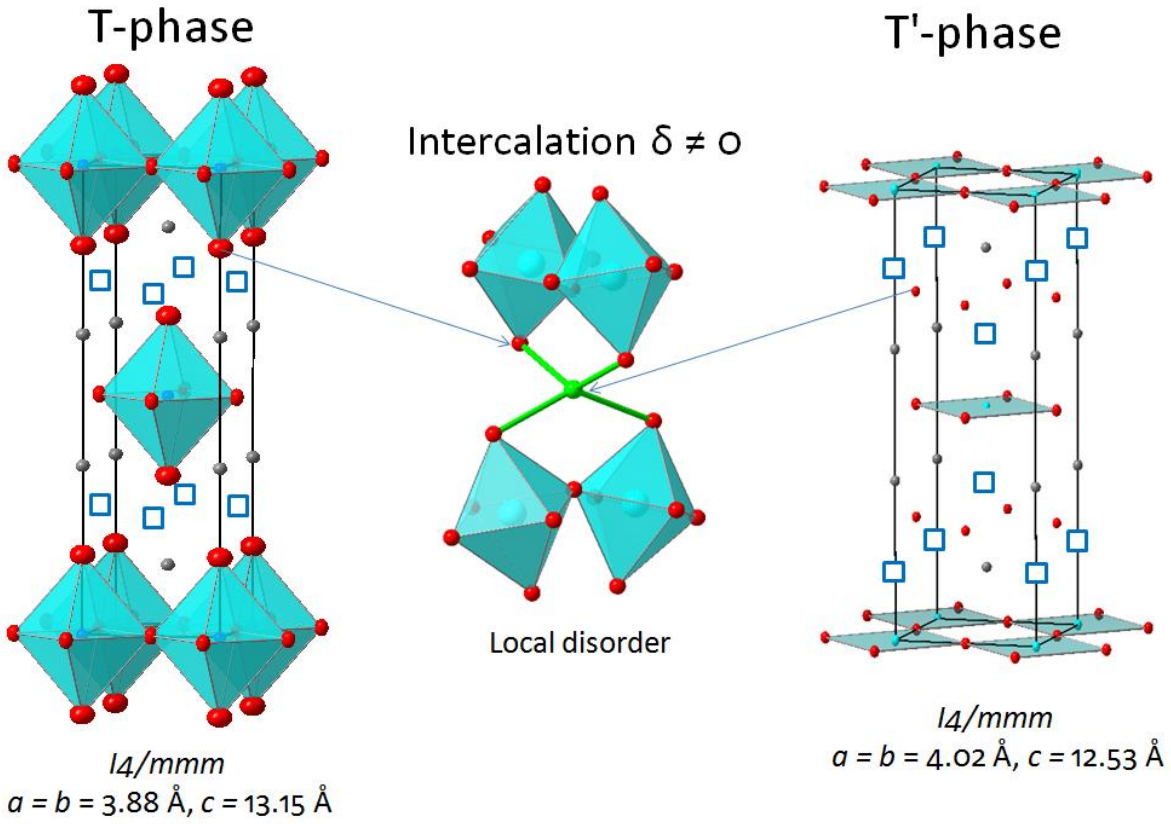

***Figure 5.1**: Basic structures of T and T-La_2CuO_4 compounds, showing the intermediate character of the oxygen-rich phases with $\delta \neq 0$.*

Very recently, several non-exhaustive studies have been reported about different compounds of the Ruddlesden-popper family, notably about $La_2NiO_{4+\delta}$[83,84], $Pr_2NiO_{4+\delta}$[225], $La_2CoO_{4+\delta}$[224], having the T-type structure and being oxygen conductors, all of them evidencing a strong correlation between apical and interstitial site in the diffusion process. The studies cited above show, principally by DTF (density Functional Theory) and MD (Molecular Dynamics) simulations, the occurrence of mutual ionic exchanges between apical and interstitial sites, yielding anisotropic diffusion pathway in those compounds (although those results have been obtained by calculations based on the average cell only). Therefore, the interstitial oxygen atoms do not diffuse linearly in the interlayers by direct hopping between interstitial sites, but their migration in the crystal bulk involves the participation of apical sites in the diffusion

process. Furthermore, the migration between apical and interstitial sites appears to be the only active pathway yielding oxygen diffusion[224], the direct hopping between adjacent interstitial sites demanding much energy. Consequently, the availability of La_2CuO_4 under the two prototype forms, either with apical or interstitial site fully occupied, allows to study the transformation from one to the other and thus to investigates the diffusion pathway experimentally.

1.2. Reconstructive phase transition from T' to T-phase

Single-crystals of T'-La_2CuO_4 could have been synthesized for the first time *via* the molten salt technique (cf. chapter 2, section 2.2) by Prof. Schöllhorn from Walther Meissner Institute (BAdW, Garching, Germany). He kindly offered us two batches of highly pure single crystal samples that have been grown separately with different parameters of synthesis (different durations, different debits of argon in the system, different concentrations of reactants) but at the same temperature of process: 673 K. After several pre-testing carried out with a *KappaCCD* X-ray diffractometer (Bruker Nonius, λ = 0.7092 Å), one high-quality single crystal sample of pure T'-phase has been selected from each batch and they have both been used to investigate the thermal stability of T'-La_2CuO_4 by synchrotron X-ray diffraction experiments (ID11@ESRF). Although the two samples undergo a reconstructive phase transition to La_2CuO_4 T-phase at high temperature, they exhibited different thermal behavior on many aspects. Therefore, the experimental results are presented for each sample separately. Then, they are compared and discussed in a third part, yielding a global overview of the phenomena entering the game and providing conclusions about oxygen migration between interstitial and apical sites.

1.2.1. First sample: complete destruction of the T'-type single crystal into polycrystalline T-phase around 1000 K.

Experimental procedure

For the first sample, the experimental parameters of diffraction measurements were set as following: distance sample-detector 120 mm, λ = 0.17723 Å, $\Delta\varphi$ = 0.3° and t_{exp} = 0.3 s/image. The samples' temperature was controlled in real time by a heat blower, and increased with a rate of 1K/min between each isothermal steps for data collection. The acquisition of the diffraction data have been carried out under air each 100 K from RT to 773 K and then with a

step of 25 K until 1073 K. It is worth noting that a technical hitch occurred during the night with a probable overshooting of the temperature, while measurements were running automatically, the temperature was blocked during 6 hours at 673 K. The experiment has been continued from this point. Although the temperature of 673 K is far below the temperature of transition we observed, this hitch even had consequences on the results. But phenomenologically this experiment remains interesting. That is why, the results are discussed hereafter. The reciprocal space planes have been reconstructed for each temperature, and the (*hkl*) intensities have been integrated with *CrysAlis*. Structural refinements have been carried out with *CRYSTALS2000*[226].

Appearance of secondary phases and transition to polycrystalline T-phase

According to the diffraction data, the single crystal sample at RT is highly pure T'-phase, and the sharpness of reflection spots denotes the high crystallinity. After a peak search with low threshold *via CrysAlis* interface, 99.97 % of the detected peaks could be indexed with the *UB* matrix corresponding to tetragonal *I4/mmm* unit-cell of parameters a = 4.011(16) Å, c = 12.511(50) Å. Then, on heating the crystal sample remains stable until phase separations occur in the range of 573-773 K yielding emergence of two secondary phases before a transformation into polycrystalline T-phase between 800 and 1000 K. The transformations undergone by the sample can be separated in different steps which refer successively to the Figure 5.2 and 5.3:

i) The (0*kl*) reciprocal space map reconstructed from the data collected at 573 K exhibit new diffraction spots forming a sublattice toward *c*-axis in supplement to the reflections of the T'-phase. The *d* value in angstroms for the periodic sublattice toward $\vec{c}^*$ is of 13.17 Å, which is the value of *c*-parameter for the T-phase. Therefore, it appears that already at 573 K, a small portion of the T'-La_2CuO_4 has transited to a secondary phase grown epitaxially. Indeed, the (*hk*0) plane does not exhibit additional reflections, only peaks belonging to the T'-lattice. Hence, it seems that both domains share their $\vec{a}$-$\vec{b}$ plane while their *c*-axis differs. If correct, this interpretation would evidence a new hybrid tetragonal phase in half way between T and T'-type, with a = 4.035(3) Å and c ~ 13.17 Å, and thus of large volume. Unfortunately, the integration of the intensity diffracted by the sublattice was of very bad quality and no satisfactory refinements could be achieved. Moreover, the fact that the reflections of both phases are overlapped in the $\vec{a}$-$\vec{b}$ plane is also constraining. Therefore the real atomic structure of the hybrid phase could not be found. Several options can be suggested, as for instance a T*-type like structure (cf. chapter 1, section 1.3.4). Although the cell parameters

are not in accordance with the usual dimensions of the latter type of lattice (generally, a ~ 3.9 Å and c ~12.6 Å), the T*-like structure remains flexible in terms of volume, depending on the chemical composition. Few traces of aluminum and nickel have been detected for some samples (cf. chapter 2, section 2.3) and they might be responsible of the partial transformation into hybrid phase. But this assertion remains extremely hypothetical.

ii) At 673 K, a second sublattice arises made of broad diffracted spots, appearing not only toward $\vec{c}$*-direction but this time also in the $\vec{a}$-$\vec{b}$ plane. This sublattice could be indexed with a body-centered cubic unit-cell of cell parameter a = 11.374(5) Å. As before, no satisfactory integration and refinement were successful; however, as we will see, the structural refinements at higher temperature show that it corresponds to the C-M_2O_3-type phase of La_2O_3 compound. It appears that formation of the latter is proportional to the disappearance of the hybrid tetragonal phase appeared at 573K. The proof is given by the technical hitch that has fixed the samples temperature at 673 K during 6 hours (with probable overshooting), while data collection was continuing to run. After this duration, we can see on the figure that all intensity of the first tetragonal sublattice disappeared (blue arrows), while reflections of the cubic sublattice get stronger in intensity (black arrows). Hence, the hybrid tetragonal phase appearing at 573 K turns out to be unstable at higher temperatures and would transform into cubic La_2O_3, although loss of transition metal (Cu or impurities) is remarkably weird. One additional astonishing point is that the two crystal phases have same orientation of cell parameters even if the proportions of the cells are completely different. We could not distinguish if the grains were intergrown microscopically or if there was two macroscopic domains connected only by one single interboundary.

iii) At 800 K, a part of the diffraction spots belonging to the T'-lattice disappears and is replaced by some diffuse streaks with a circular shape, centered on (000). The sample starts to disintegrate and fragment into various individual grains. The reconstructive transition into polycrystalline compound begins.

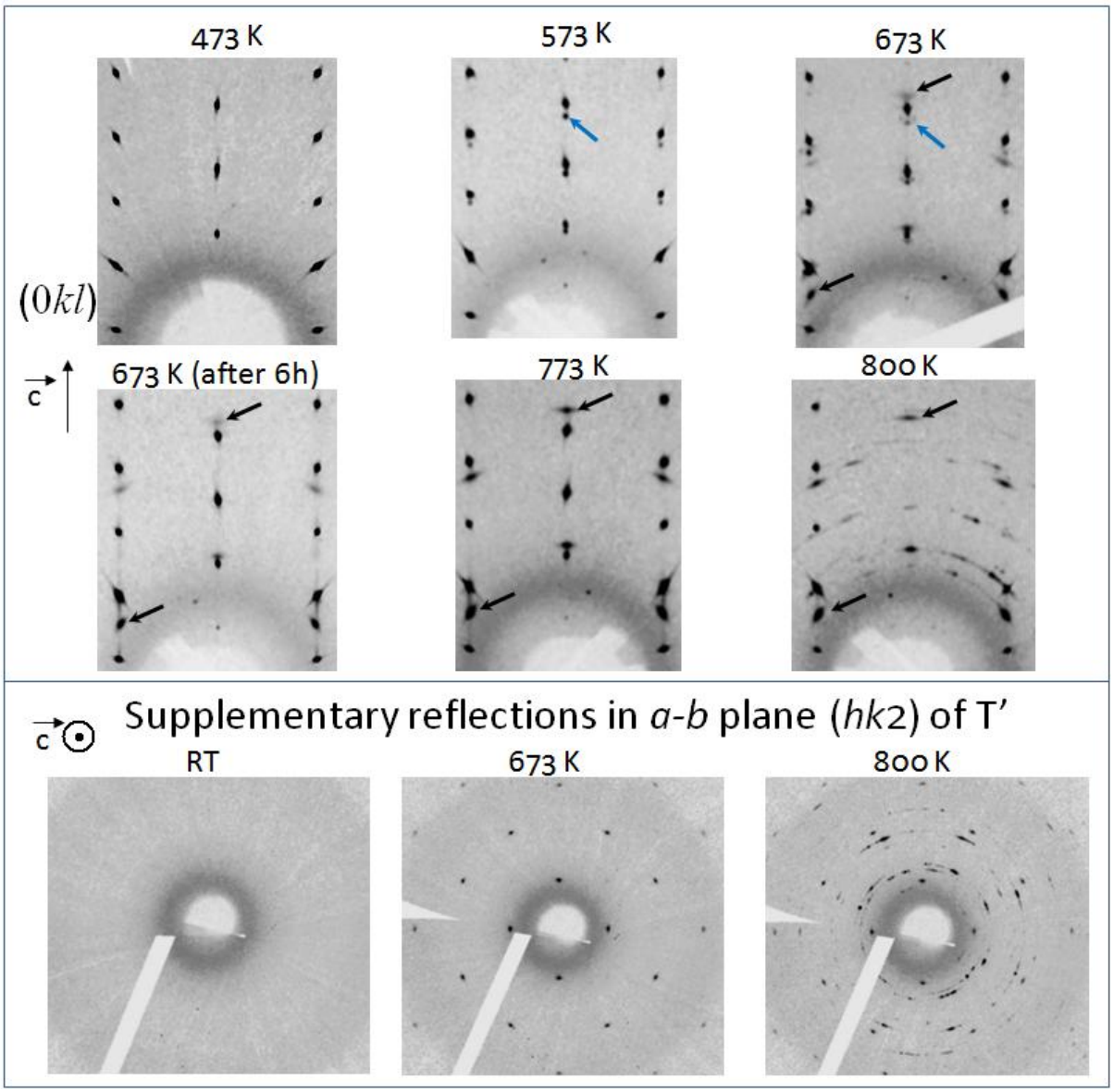

***Figure 5.2**: Reciprocal space planes of T'-La_2CuO_4 starting sample reconstructed at various temperatures from synchrotron X-ray diffraction data (ID11@ESRF).*

iv) In the range of temperature between 800 and 1000 K the T'-La_2CuO_4 phase undergoes a transition to T-type structure involving a complete fragmentation of the monodomain into multiple individual grains, yielding concentric circles of diffused intensity on the bidimensional diffraction pattern, characteristic of polycrystalline compounds. Nevertheless, few circles are still structured at low angles and exhibit maxima of intensity, representative of preferred grains' orientations. The Figure 5.3 displays the experimental 2D-pattern collected at 1073 K by the area detector, together with the powder diffraction patterns resulting from circular intensity integration carried out with *FIT2D* software at 1073 K and at RT. The subsequent data have been refined by Rietveld method through the program *FULLPROF*[160]. At high temperature, the T-La_2CuO_4 phase, space group *F*4/*mmm*, is prominent, but the

impurity remains is small quantity, *i.e.* the cubic La_2O_3. At RT, the La_2CuO_4 polycrystalline compound transits to LTO phase, space group *Bmab*. Hence: the transition from T' to T-phase is clearly irreversible.

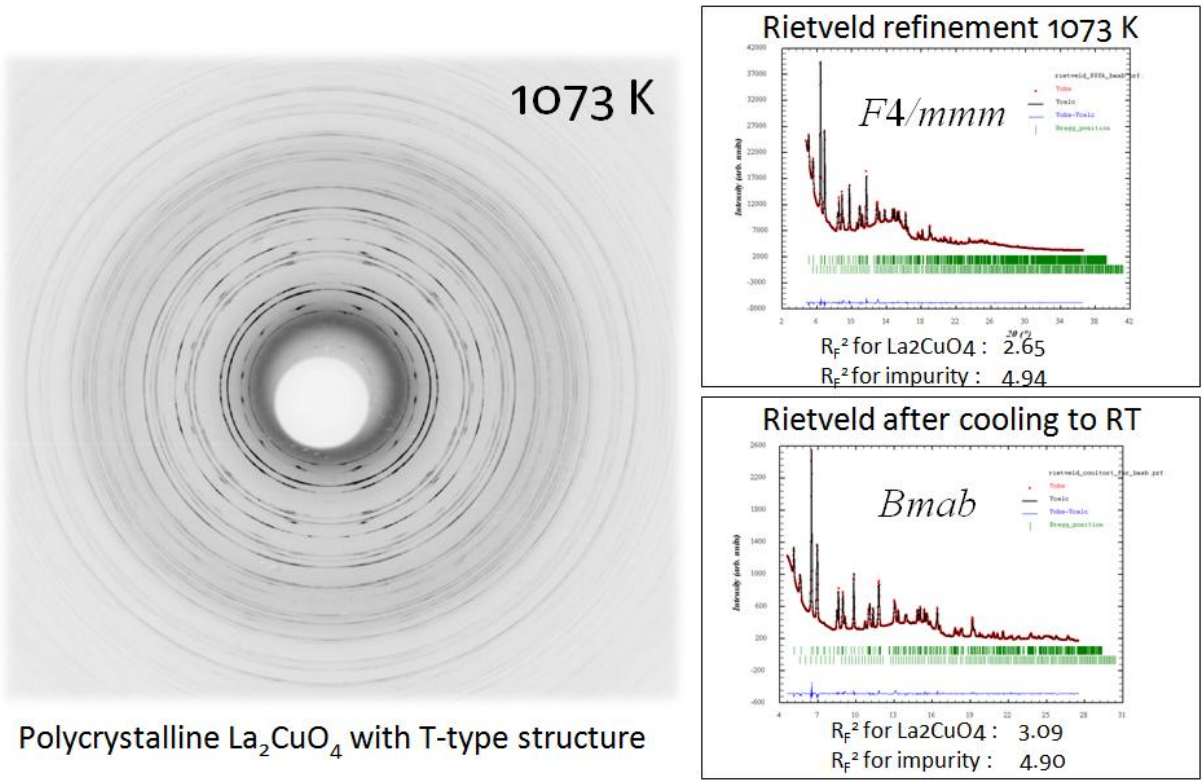

***Figure 5.3**: Polycrystalline diffraction pattern of T-La_2CuO_4 collected by synchrotron X-ray diffraction (λ = 0.17723 Å, ID11@ESRF) at 1073 K and integrated circularly by FIT2D, allowing Rietveld powder refinements at high temperature, and then cooled back to RT.*

Temperature dependence of cell parameters

Figure 5.4 displays the temperature dependence of the ratio *c/a* and of the volume of the cell, both depicting the lattice transformations. These values have been calculated from the refined cell-parameters and the error bar is not bigger than the size of the markers on the chart. Both profiles exhibit a drastic changing at the transition. While the volume of the cell increases linearly (8.1×10^{-3} $Å^3K^{-1}$) in the range of temperature between RT and 973 K, it suddenly decreases of 7 % at the transition. On the contrary, the ratio *c/a* shows a slight slope down between 800 and 973 K before abrupt increase of 10 % at the transition. Hence, the crystal lattice undergoes very strong modifications at the transition induced by densification from 6.506 gcm^{-3} for T'-phase at 973 K to 6.897 gcm^{-3} for T-phase at 1073 K ($\Delta\rho$ = 0.391 gcm^{-3}). Together with elongation of *c*-axis and stretching of *a*-axis, these drastic alterations give rise to formation of different grains in the bulk. What is more unexpected is that the shape of the

crystal has been maintained after transformation into polycrystal, which means that an intergrowth effect has kept the coherency of bulk.

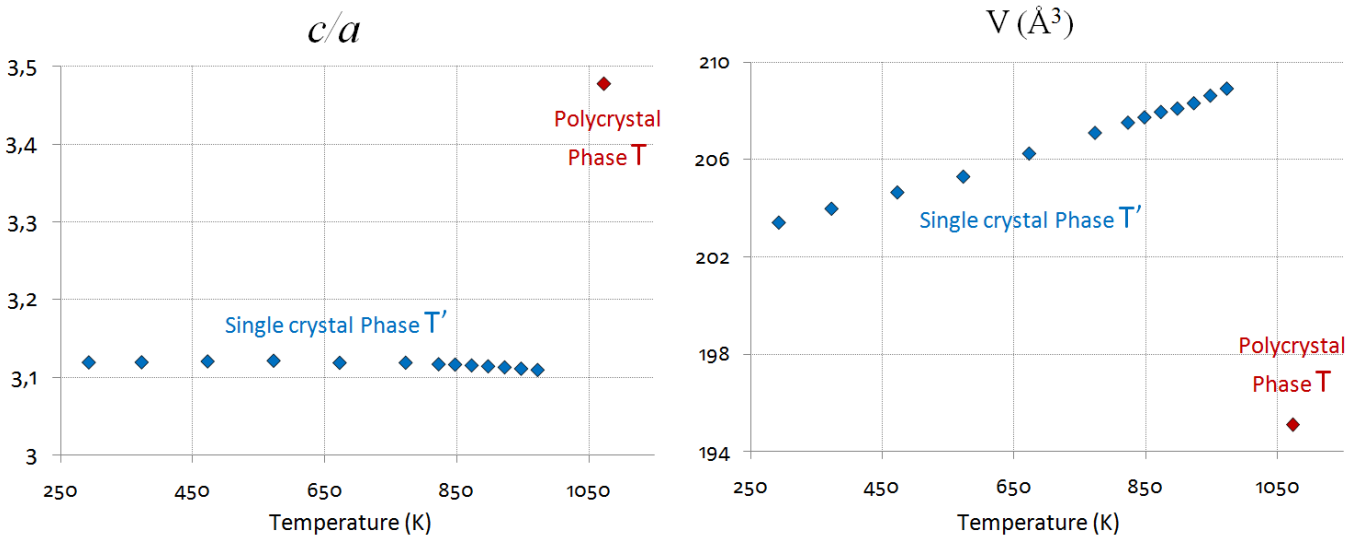

***Figure 5.4**: Temperature dependence of c/a parameter and volume, before and after the transition. The error bar is not bigger than the markers.*

Temperature dependence of interatomic bond distances

The transition from T' to T-type structure necessitates positional shifts of oxygen from interstitial to apical site, involving atomic displacements of ~ 2.2 Å. Hence, the transition is of reconstructive type, which explains the exceptional 'powderization' of the starting crystal at 1000 K. The interatomic bond lengths are submitted to specific variations as function of temperature, far before the transformation to T-phase. Figure 5.5 shows the temperature dependences of the specific bond lengths which undergo particular evolutions. We can see that apparition of the first 'impurity', assumed to be a hybrid tetragonal phase, has no effect on the interatomic bond distances of the T'-prime compound. Until ~700 K every bond lengths increase linearly, but above this temperature, their profiles exhibit different evolutions. For instance, the La-La bond lengths, labeled number 2 on the figure, decrease between 700 and 1000 K. The other temperature dependence profiles of interatomic distances still increase but show variations of slope. Above 1000 K, the sample has turned into T-phase and, like for the cell-parameters profiles, the distances between atoms change drastically above the transition. The transformation from T' to T does not only involve the migration of oxygen from interstitial to apical site, but also a positional shift of La atoms.

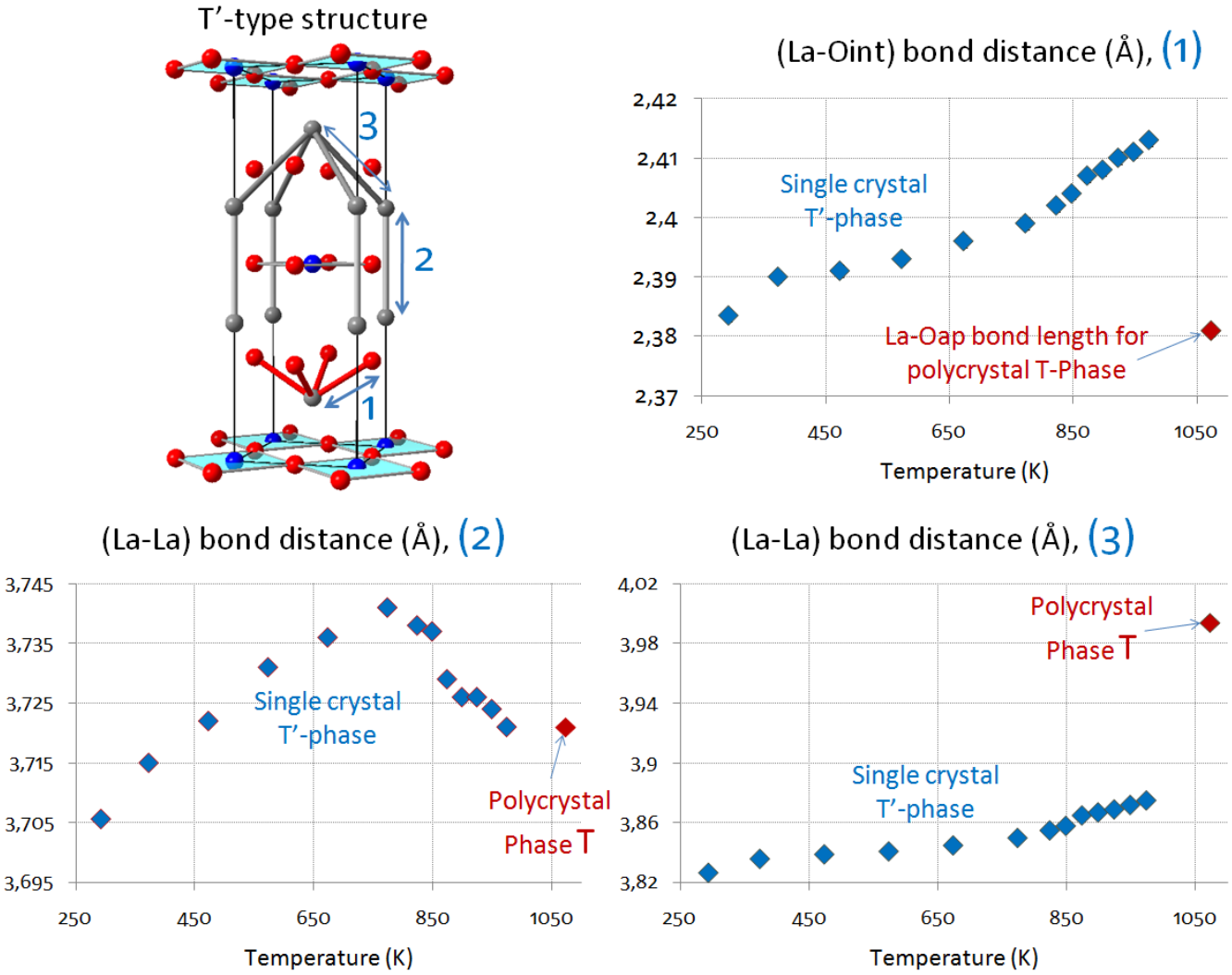

***Figure 5.5**: Temperature dependence of the interatomic bond distances that exhibit non linear evolution.*

Temperature dependence of anisotropic displacement factors for the T'-phase

The synchrotron X-ray diffraction data allowed us to refine anisotropic displacement factors for each temperature with good precision. They are given in Table 5.1 together with the *z/c* value of La position in the unit-cell and the respective agreement factors. U_{11} is equal to U_{22} for La, Cu and O_{int} atoms but not for O_{eq} whose displacements toward $\vec{b}$ is a bit superior than toward $\vec{a}$. All U_{ii} values increase quite linearly with temperature. The oxygen atoms on interstitial sites undergo stronger displacements toward $\vec{c}^*$ than in the plane, in particular for temperatures close to the transition, which goes in the sense of migration to apical site.

***Table 5.1**: Anisotropic displacement parameters in the T'-phase refined for the different temperatures.*

Atom	La			Cu		Oeq			Oint		Agreement	
T(K)	*z/c*	U_{11}	U_{33}	U_{11}	U_{33}	U_{11}	U_{22}	U_{33}	U_{11}	U_{33}	R_F	R_{WF}
293	0,3523(4)	7.9(3)	9.4(2)	5.1(2)	10.4(2)	7.(2)	6.(6)	12.(1)	6.(4)	9.(0)	5.09	4.99
373	0,3522(1)	9.8(7)	10.6(6)	7.2(5)	9.5(6)	9.(7)	12.(5)	13.(2)	10.(3)	11.(7)	4.86	4.74
473	0,3521(3)	11.4(9)	12.5(7)	8.7(4)	12.6(8)	9.(6)	13.(6)	17.(5)	9.(2)	15.(3)	4.65	4.15
573	0,3519(7)	13.4(7)	14.8(2)	10.8(2)	16.3(1)	14.(5)	19.(1)	20.(5)	13.(7)	13.(3)	5.75	5.90
673	0,3519(1)	15.4(1)	16.9(5)	12.8(6)	18.4(2)	14.(9)	20.(3)	24.(3)	13.(9)	19.(8)	5.05	4.55
773	0,3519(1)	16.7(7)	17.9(0)	14.4(7)	19.8(6)	17.(4)	23.(2)	26.(0)	14.(2)	21.(7)	4.76	4.68
823	0,3520(5)	17.3(6)	19.0(2)	15.5(5)	20.4(9)	21.(1)	19.(6)	28.(8)	15.(7)	22.(4)	4.59	4.35
848	0,3521(6)	18.2(0)	19.8(3)	16.1(5)	20.0(2)	20.(4)	23.(3)	31.(0)	17.(2)	23.(2)	4.51	4.40
873	0,3524(8)	17.7(7)	19.1(1)	15.8(3)	21.7(2)	24.(3)	25.(2)	34.(8)	14.(4)	25.(4)	4.59	4.13
898	0,3525(9)	18.7(9)	20.2(6)	16.6(4)	23.2(1)	21.(9)	24.(0)	30.(6)	16.(0)	25.(7)	4.18	3.98
923	0,3526(1)	19.2(7)	20.4(6)	17.1(7)	24.0(5)	25.(4)	26.(3)	29.(8)	18.(2)	24.(3)	4.01	4.15
948	0,3527(1)	19.8(1)	21.0(8)	18.0(1)	24.2(4)	23.(7)	28.(4)	33.(0)	18.(5)	25.(7)	3.99	3.76
973	0,3527(7)	20.8(5)	22.2(1)	18.9(3)	25.5(8)	21.(4)	28.(0)	34.(7)	18.(5)	29.(4)	4.84	4.74

Unit-cell refined with *I4/mmm* space group on, in average, 150 unique reflections with R_{int} < 6 % for all dataset. *Uij* values are given in 10^{-3} Å^2. Synchrotron X-ray diffraction (ID11@ESRF) Wavelength of X-rays: 0.17723 Å.

1.2.2. Second sample: continuous transformation of T'-phases into T-phase by crystal intergrowth, starting at 900 K.

Experimental procedure

The experimental procedure used for the second T'-type La_2CuO_4 sample was quite similar to the settings used for the first sample except few details. Here, λ = 0.2072 Å, and the experimental diffraction data have been collected each 50 K in the whole range explored (RT to 1073 K). The data acquisitions have systematically been performed for isothermal steps of 30 minutes between each heating ramp. No hitch occurred during operation this time, which facilitates interpretations.

Evolution of the reciprocal lattice

On contrary to what has been observed for the first sample, the reciprocal planes reconstructed for the second one does not exhibit neither formation of a hybrid phase nor traces of La_2O_3 impurity. The phase transition to T-structure occurs ~900 K which is 100 K less than before. This time, impurities or other phases do not appear but the sample remains pure single crystal T'-phase until 900 K. At 923 K, reflections corresponding to the T-phase have appeared besides the T'-lattice. This time, reflections are observable not only toward $\vec{c}$* but also in the $\vec{a}$-$\vec{b}$ plane, testifying emergence of real T-phase and not of the hybrid one. Figure 5.6 displays the (0*kl*) and (*hk*0) planes at RT, 923 K and 1073 K, illustrating the presence of both phases in the sample at high temperature, for which the two *I*4/*mmm* sublattices with distinct cell-parameters are observable. This type of diffraction pattern is

characteristic of composite crystals. Astonishingly, this time the sample does not fragment into polycrystal but remains single grain, being an intergrowth of the two types of structure forming two different types of domains with different atomic structure.

Even if their respective values of cell-parameters differ, the colinearity is surprisingly preserved between the unit-cell vectors, *i.e.* $\vec{a}_{T'}$ collinear to $\vec{a}_T$ and $\vec{c}_{T'}$ collinear to $\vec{c}_T$. Still, the size and number of grains were not clarified. While the diffraction spots of the T-phase arising at 923 K are broad and diffused in ω, they are well defined and sharper at 1073 K indicating an improvement of crystallinity for the T-domains. The T-lattice's peaks become sharp enough for integration only at 1023 K, for which refinements could be successfully performed, as well as for 1073 K. The intensity of the T-type reflections increases proportionally to the decrease of the T'-type reflections. It indicates that interstitial oxygen atoms are more and more migrating to the apical site, yielding continuous reconstructive transformation to T-structure. However a complete transition to T-phase was not achieved in the range of temperature explored.

The reconstructions presented on Figure 5.6 also indicate that the sample has moved in the capillary at the transition, probably due to the change of volume. Indeed, the way the area detector cut the Ewald sphere at RT is different from the one at 923 K; this can be viewed not only through the background of the map at RT which exhibit circular shapes, but also through Bragg reflections which appear broad when they are inside those circles. These deformations result from a random but particular orientation of the sample with regards to the detector, *i.e.* with *c*-axis nearly perpendicular to the 2D-detector at 300 K.

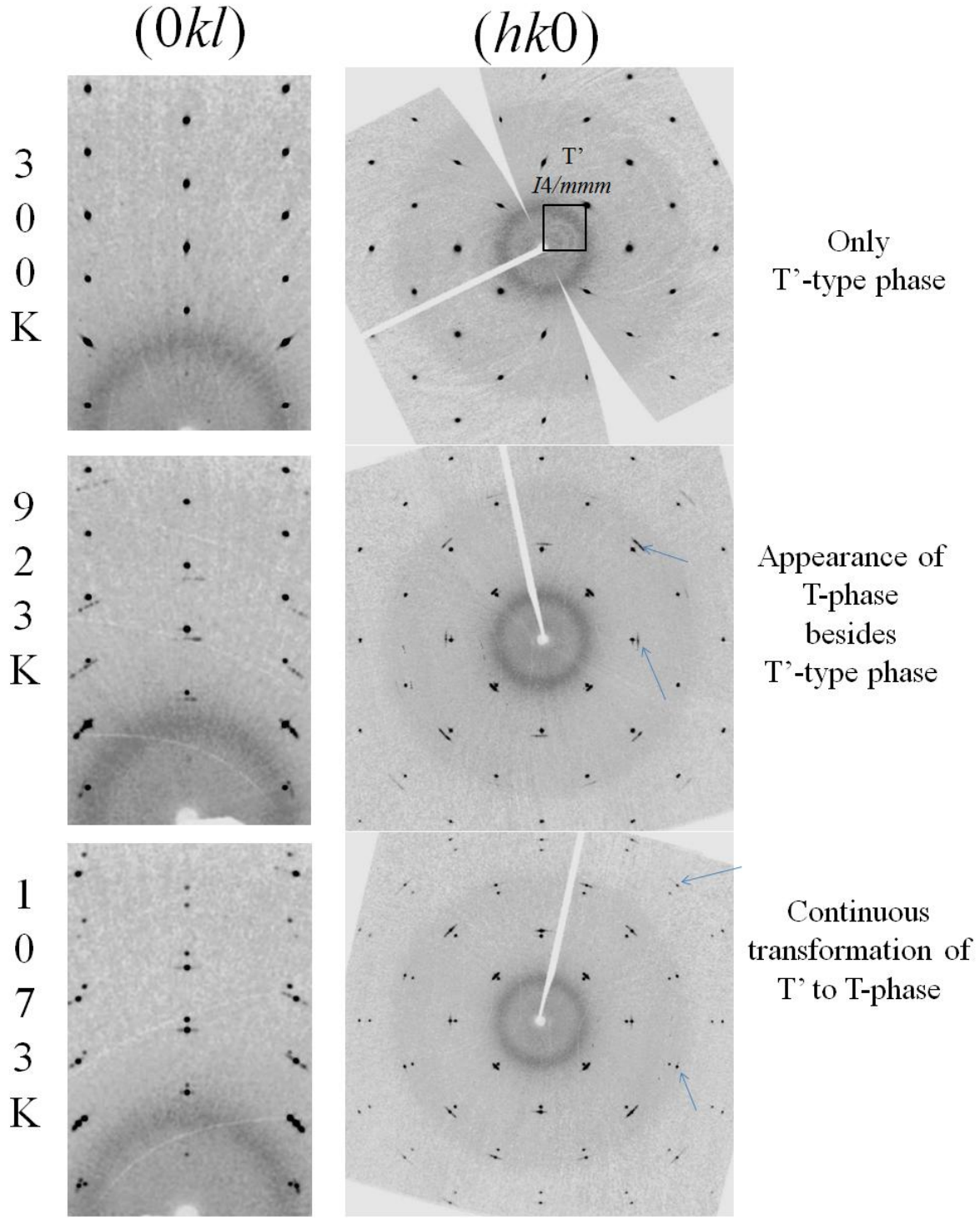

Figure 5.6*: (0kl) and (hk0) reciprocal space planes of T'-La_2CuO_4 single crystal, reconstructed from synchrotron X-ray diffraction data collected at different temperature (ID11@ESRF).*

Temperature dependence of cell parameters

The profiles of the temperature dependences of the ratio *c/a* and of the volume V are shown on Figure 5.7 (error bars are not bigger than the markers which are of the same color than their respective coordinate-axis). While the volume evolves linearly with a slope of 8.5×10^{-3}

$Å^3K^{-1}$, the *c/a* ratio for the T'-phase exhibits a bump between 623 and 873 K, before drastic decreasing at 923 K, *i.e.* when the transition starts. Pre-transitional effects happen for the T'-lattice prior to partial transformation into T-phase, involving competition between enlargements of *a*- and *c*-axis.

Temperature dependence of interatomic bond distances

Figure 5.8 displays the plots of the bond distances which undergo particular evolution with temperature. It is accompanied with a pictorial view of the unit-cells of each phase, where each bond involved is labeled by the number of its respective profile (again, the experimental errors are not bigger than the markers). Since integrating intensity diffracted by the T-phase was only relevant above 1000 K when peaks are sharp enough, no values are given for bond lengths of the T-phase at 923 and 973 K. The values above 1000 K are anyway sufficient, and are just given for comparison. The thermal evolution of distances in the single T'-phase before the transition exhibit a significant wobbling, pointed out by the blue arrows on the figure. The bond lengths oscillate before the transition for 623 < T < 873 K, *i.e.* in range of temperature where the profile of the *c/a* ratio makes a bump. The variations of interatomic distances involve a correlated alteration of the crystal lattice. Hence it demonstrates again that the single crystal sample of T'-La_2CuO_4 does not evolve linearly with temperature. Even if no impurity appears this time, the transformations of the atomic structure induced by temperature provoke non continuous positional shifts. The T'-lattice is much less flexible than the T-lattice.

Temperature dependence of anisotropic displacement factors

The values for anisotropic displacement factors resulting from least-square refinements are given in Table 5.2, together with the *z/c* position of the La atom in the unit-cell and with the agreement factors obtained for each temperature after convergence. The structural refinements permitted to phase the observed (*hkl*) intensities. Then the electronic densities have been calculated in direct space by the Maximum Entropy Method. The Figure 5.9 shows the isosurfaces of the 3D electronic density profiles for both unit-cells refined at 1023 K (for T'-phase: F_{max}= 430, isosurfaces cut at 6, for T-phase: F_{max}= 317, isosurfaces cut at 5). This figure allows to visualize the preferred displacement orientations for each atom, even if it does not correspond to the nuclear intensity this time. But for instance, the interstitial oxygen site of the T'-unit-cell exhibit strong elongation along *c*-axis. Additionally, in the T-phase, the shape of density around the apical oxygen site is strongly anisotropic, smeared out and square shaped in the $\vec{a}$-$\vec{b}$ plane. The tilt toward the $[\pm1\pm10]_{HTT}$ directions are even discernible, in total

accordance with the dynamic switching of CuO_6 octahedra involved by soft-phonon modes of the HTT phase[227].

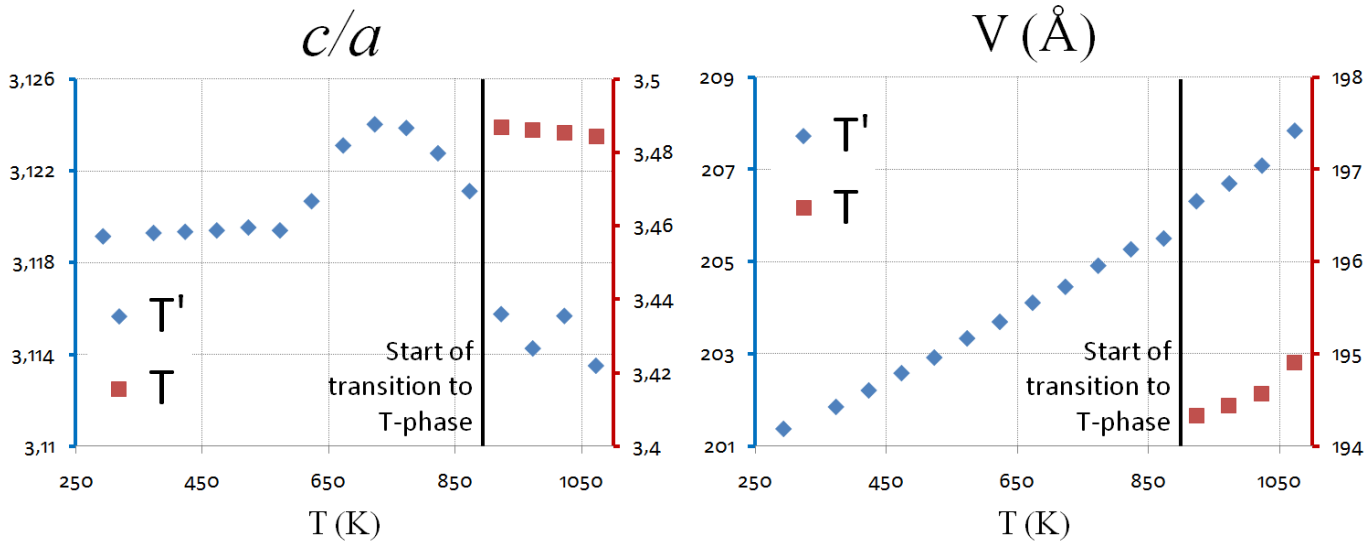

***Figure 5.7**: Temperature dependence of two specific criteria, c/a ratio and volume of the unit-cell.*

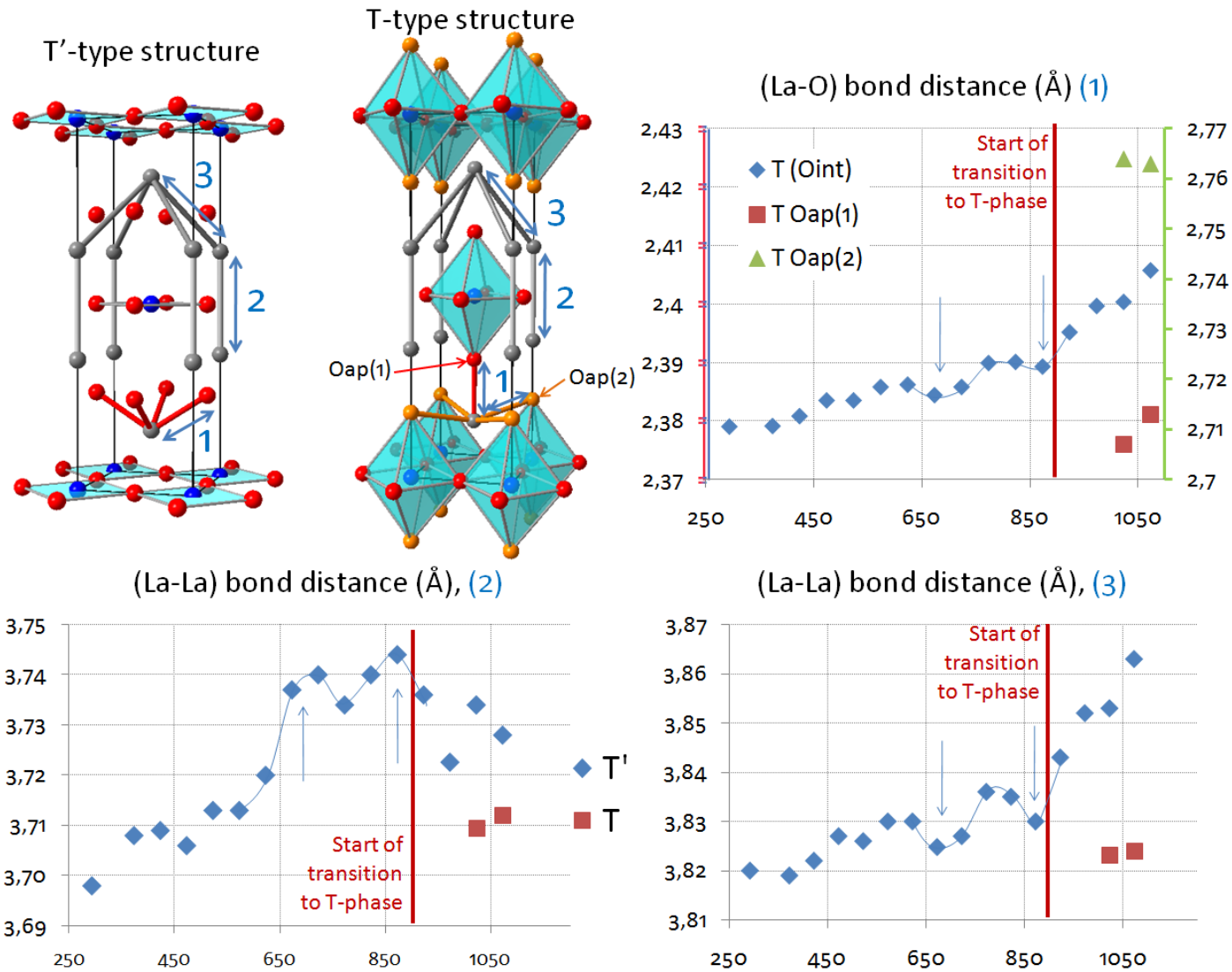

***Figure 5.8**: Temperature dependence of the interatomic bond distances showing particular evolution. The error bars are not bigger than the size of the markers.*

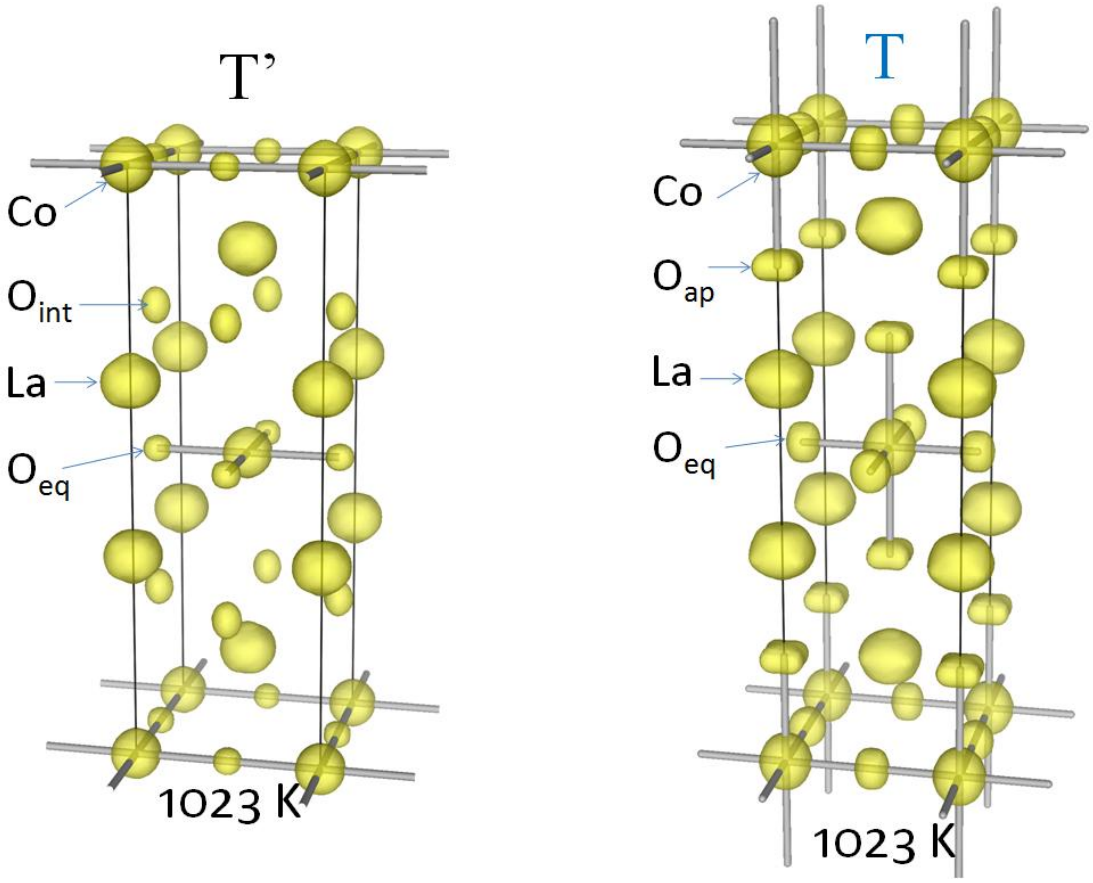

***Figure 5.9**: 3D profiles of electronic densities reconstructed by MEM from X-ray diffraction data (ID11@ESRF) at 1023 K.*

***Table 5.2**: Anisotropic displacement factors depending on temperature. Uij coefficients are given in $10^{-3}Å^2$.*

		La			Cu		Oeq			Oap		Agreement	
Phase	T (K)	*z/c*	U_{11}	U_{33}	U_{11}	U_{33}	U_{11}	U_{22}	U_{33}	U_{11}	U_{33}	R_F (%)	R_{wF} (%)
T'	293	0.35224(1)	6.5(5)	7.1(9)	8.9(0)	8.5(5)	11.(1)	12.(1)	20.(9)	9.(4)	5.(1)	4,40	4,73
	373	0.35196(9)	7.5(2)	8.6(3)	9.4(9)	11.1(3)	11.(6)	15.(8)	24.(9)	12.(8)	7.(1)	4,90	4,42
	423	0.35201(4)	8.4(1)	9.4(8)	9.9(5)	12.3(3)	12.(5)	9.(7)	24.(3)	9.(2)	10.(2)	4,88	4,52
	473	0.35220(5)	8.9(9)	9.1(3)	10.7(7)	13.0(8)	17.(5)	16.(9)	21.(9)	13.(2)	10.(1)	4,82	4,32
	523	0.35200(4)	10.1(7)	10.7(2)	12.5(4)	13.6(9)	19.(9)	15.(4)	28.(4)	14.(3)	12.(3)	4,33	4,75
	573	0.35210(3)	10.2(9)	10.5(8)	12.7(6)	13.4(8)	16.(8)	15.(9)	34.(6)	13.(5)	12.(8)	5,01	4,69
	623	0.35195(9)	10.7(6)	12.1(0)	12.1(9)	14.8(1)	17.(5)	11.(1)	28.(0)	12.(5)	17.(6)	4,91	4,64
	673	0.35146(6)	13.1(0)	14.9(3)	14.9(2)	18.2(0)	18.(8)	20.(5)	28.(9)	14.(2)	34.(5)	3,68	3,63
	723	0.35147(8)	13.0(1)	12.6(1)	15.9(7)	17.0(7)	26.(3)	16.(8)	31.(8)	16.(1)	16.(7)	4,18	4,84
	773	0.35181(9)	13.8(3)	12.7(4)	16.9(4)	18.3(5)	22.(7)	20.(5)	41.(5)	15.(6)	13.(4)	4,14	4,87
	823	0.35162(9)	14.5(3)	15.4(2)	17.7(1)	21.1(4)	29.(6)	22.(3)	43.(2)	16.(4)	18.(5)	4,83	5,00
	873	0.35171(5)	18.6(2)	39.4(5)	20.5(8)	41.1(8)	28.(3)	41.(2)	49.(7)	27.(1)	49.(2)	4,97	4,37
	923	0.35179(7)	23.8(2)	23.6(1)	26.1(0)	32.4(9)	36.(4)	28.(7)	58.(8)	29.(8)	26.(6)	3,64	4,69
	973	0.35225(8)	25.7(5)	23.6(7)	27.4(2)	33.4(1)	46.(3)	39.(7)	38.(0)	33.(1)	31.(5)	3,40	3,80
	1023	0.35207(3)	24.8(5)	21.8(1)	27.7(6)	29.0(3)	37.(3)	29.(4)	40.(8)	24.(1)	38.(5)	3,94	4,26
	1073	0.35243(1)	29.5(1)	30.3(2)	32.1(6)	40.4(9)	49.(9)	45.(2)	46.(8)	25.(1)	51.(5)	2,91	2,89
T	1023	0.36076(8)	33.1(0)	21.8(9)	20.3(1)	35.6(8)	24.(7)	27.(2)	42.(9)	57.(8)	21.(3)	3,92	4,61
	1073	0.36071(8)	31.7(8)	24.2(4)	19.2(7)	38.2(2)	37.(8)	19.(1)	52.(6)	57.(3)	34.(7)	3,25	3,55

1.3.Global outcomes about the transformation from T' to T-phase.

The two T'-type crystal samples of high quality exhibit a distinct evolution with temperature. Even if they both transit irreversibly to the T-phase at high temperature, the nature of the final product remains different: pure polycrystal of T-phase in the first case, and intergrowth of T and T'-type phase in the second case. Although these behaviors appear to be rather dissimilar, they must be regulated by some common underlying phenomena. We can see from the structural results that the transition is governed by the transfer of interstitial atoms to apical sites. Theoretically, such migration of atoms during reconstructive phase transitions of this type is activated when their displacement factors reach a limit value induced by thermal motion[228]. This is precisely what we observe in T'-La_2CuO_4: the values refined for U_{33} coefficient of O_{int} (Tables 5.1 and 5.2), which are related to oxygen displacements toward the layers of apical sites, increase with temperature and undergo anisotropic deformation directed along *c*-axis at high temperature. It is also shown in Figure 5.9 through the MEM reconstructions of electronic densities. So, at one point oxygen atoms are able to overcome the energy barrier of the crystal field; they can diffuse through a pathway of ~ 2.2 Å long until being trapped in the minima of potential corresponding to the apical site. This structural changing does not modify the symmetry of the unit-cell and thus does not involve group-subgroup intermediate transformation which is generally the case for reconstructive transitions[228]. Though, the lattice undergoes strong deformations. Indeed, the coming of oxygen on apical sites modifies the valence of copper atoms yielding elongation of Cu-O_{ap} distances by Jahn-Teller effect. Furthermore, the whole atomic structure is modified; it is illustrated by the strong variations of La-La bond lengths between the two phases. Therefore, the subsequent strains oblige the *c*-axis to elongate from 12.60 Å to 13.30 Å at 900 K, leaving more freedom in the $\vec{a}$-$\vec{b}$ plane which thus contracts from a = 4.02 to 3.82 Å. Consequently, the crystal lattice is strongly distorted by the transfer of oxygen.

The divergences observed between the structural transformations of the two T'-samples can be attributed to the long exposure of the first sample at the constant temperature of 673 K resulting from the technical hitch. In comparison, the second sample remained pure T'-phase until ~900 K and exhibit non negligible fluctuations of bond distances starting already around 650 K (*cf.* figure 5.8). So, it becomes conceivable that letting a sample at 673 K for long time allow slow relaxation of the phase, yielding structural stabilizations which can involve not only apparition of impurities but also alteration of the crystal structure. Hence, subsequent internal changes experienced by the compound could be responsible of the complete fragmentation of crystal bulk into polycrystalline compound at 1000 K. This 'powderization'

indicates that the transformations occurred at a local level yielding loss of coherency between grains. This suggests a transition with a strong 1st order character (T_c>>T_0). Conversely, the second crystal sample did not crack but transited continuously to T-phase by crystal intergrowth of the grains, *i.e.* with coexistence of T' and T-phase in the sample for an undetermined range of temperature (starting at ~ 900 K and at least until 1073 K). At 923 K, the diffracted pattern of the T-phase starts to appear and exhibits rather strong diffused intensity around the maxima of reflections, suggesting presence of different grains not perfectly aligned. Then, the diffuse scattering disappears at higher temperature and the Bragg reflections are much sharper, indicating a better crystallinity and better alignment of the grains when their volume increases. Furthermore, the intensity of the T-lattice become stronger with temperature, to the detriment of T'-lattice illustrating the continuous transformation from one to the other.

Therefore, on a phenomenological approach the transformations exhibited on a microscopic scale by the two samples appear to be similar, although macroscopically the distinction is manifest. The transition could start at different positions in the bulk, creating several grains which gain in quality while they grow and transform the T'-matrix into T-type structure. For the first sample, the coherency is lost between the grains while they are kept aligned for the second sample. It is regrettable that we did not explore higher temperatures for the latter, which could have provided observation, or not, of complete transformation to T-phase (since data treatments are time consuming and because we did not expect such high temperatures of transition, we understood the incompleteness of the transition late after experiments). However, not only the transition itself is interesting, but also all the pre-transitional effects we observed. The strange evolution of the *c/a* ratio together with the fluctuations of interatomic bond lengths indicate that structural instabilities start already at 650 K, *i.e.* 250 K below the temperature of transition. In addition, the structural transformations result either in the decomposition of the crystal into powder or in pseudo-epitaxial intergrowth demanding a long duration of process and high temperatures. All these considerations are consistent with sluggish kinetics of reaction observed in various inorganic compounds or metal alloys under high pressure[229,230,231,232].

The reconstructive phase transition with sluggish kinetics starts at ~ 900 K or more, which is at first sight contradictory with the assumption of fast oxygen diffusion at moderate temperature through the same O_{int}-O_{ap} pathway. But it indicates that the diffusion of oxygen ions in the crystal lattice is compromised at moderate temperature when apical sites are empty, and thus the presence of oxygen atoms on apical site can be seen as a criterion for

amplification of oxygen diffusion. Therefore, the occupation of apical sites appears to be compulsory for occurrence of fast diffusion at moderate temperatures. The latter assumption shows that the instabilities of the lattice, responsible of intensification of oxygen mobility, ensues in fact from the apical atoms which occupy a lattice site with shallow potential of energy surface in the T-phase.

When synthesized at 673 K, the compound with La_2CuO_4 stoichiometry stabilizes its atomic structure in the T'-phase whereas it takes the form of T-phase for higher temperatures of synthesis. Hence, the interstitial site seems to be more stable at RT and the apical site more for higher temperatures. However, the transition from T' to T-phase is irreversible, and when cooled back to RT, the product transits to usual LTO phase with tilted octahedra. Oxygen atoms on apical site do not return back to interstitial sites. It is, until now, impossible to transform directly the T-phase into T'. However, there is an indirect method, exposed in chapter 2 section 2.1, consisting in reducing the T-phase for taking out as much as oxygen as possible, yielding distorted lattice with vacancies (pseudo S-phase); and then re-oxidizing at 673 K, *i.e.* re-filling the atomic network with oxygen atoms at low temperature, producing polycrystalline T'-phase of bad quality. So it appears that the T-phase is metastable at RT while the T'-phase is more stable, which is also true for the comparison between apical and interstitial sites respectively. So the phenomenon of diffusion can be seen this way: the T-phase, which has an instable apical site (presence of soft phonon modes already at RT), can accept extra oxygen on interstitial sites in order to stabilize the structure at moderate temperatures, yielding oxygen diffusion. Conversely the T'-phase is already stable, static, and does not need to relax.

2. Successive structural phase transitions undergone by the *as grown* $La_2CoO_{4+\delta}$ as function of temperature

The previous works concerning the phase transitions undergone by $La_2CoO_{4+\delta}$ on heating have been exclusively focused on the LTO to HTT phase transition. While the structural modulation at RT in oxygen rich $La_2CoO_{4+\delta}$ has been partially detected at RT and analysed by R. Le Toquin during his Ph. D thesis[8], the structural evolution of the compound with temperature has not been explored. The description of the real atomic structure for $La_2CoO_{4+\delta}$ (structural modulation, twinning, disorder...) and its evolution as function of T and δ would obviously bear structural key information concerning the phase diagram of this compound.

This can provide new results with respect to low temperature bulk oxygen ion transport, in close relation to physical properties and chemical reactivity.

But only few studies have been focused on the long range ordering, and most of them were concerning only the spin correlations below RT. For instance, K. Yamada *et al.*[91] have observed an antiferromagnetic ordering occurring at 275 K on cooling for a stoichiometric $La_2CoO_{4.0}$ crystal sample by neutron diffraction, as well as a spin flip transition occurring at 135 K. Similarly, J.S. Gardner *et al.*[93] have reproduced the latter studies on oxygen-enriched $La_2CoO_{4.15}$ sample and found different temperatures for the two transitions, respectively 227 K and 103 K. These differences come from the distinct extra-oxygen contents of the two samples (respectively of δ = 0.0 and 0.15), which illustrates how the thermal evolution of the material depends strongly on the value of δ. The single study concerning structural modulation in $La_2CoO_{4+\delta}$ has been reported by R. Le Toquin *et al*[10] who evoked a (3+2) incommensurate phase for δ = 0.20 at RT, with two symmetric propagation vectors $\vec{q}_1$ = -0.769 $\vec{a}$*+ 0.559 $\vec{b}$* and $\vec{q}_2$ = 0.769 $\vec{a}$*+ 0.559 $\vec{b}$* in the basic LTO unit-cell[10], space group *Fmmm*. This extra oxygen stoichiometry was achieved by electrochemical oxidation at RT in an aqueous KOH electrolyte. The orthorhombicity of this oxygen-rich sample has been shown[8] to vary on heating, indicating structural changes that we propose to study in more details here, by taking the modulation in account.

The temperature dependences of various samples of $La_2CoO_{4+\delta}$ with different oxygen content δ are presented hereafter, revealing a complex phase diagram. The particularity of this compound is to undergo variations of oxygen content with temperature. So, in addition to diffraction experiments, thermogravimetric studies have been carried out in parallel for determining the concentrations of interstitial oxygen for each stable phase.

2.1. Low temperatures: in the range of 10K to RT

On cooling, the stoichiometric La_2CoO_4 compound has been reported to undergo a structural phase transition at 110 K[91], from LTO phase, space group *Bmab*, to LTT phase, space group $P4_2/ncm$. Moreover, the presence of magnetic super-ordering has been shown to occur in $La_2CoO_{4.15}$ at the same temperature than the structural phase transition[93] to LTT state, consisting in the appearance of supplementary (100) magnetic peak. Even if our studies are rather focused on the range of temperature between RT and 800 K at which oxygen diffusion is significant, we decided to explore the structural evolution of our *as grown* sample at low

temperature by neutron diffraction in order to check the evolution of modulation below RT, in order to correlate structural changes with magnetic effects. It appeared that the behavior of $La_2CoO_{4.14}$ resulting from our measurements at low temperatures is absolutely dissimilar to what has been reported by J.S. Gardner *et al.*[93]: no structural transition to tetragonal phase could be detected and no magnetic super-ordering was observed. It might be due to different content of extra-oxygen in our respective samples. It is possible that the sample used by J.S. Gardner contains higher amount of extra-oxygen than δ = 0.15, yielding coming back of magnetic ordering (cf. section 3.1 of this chapter).

A set of specific reflections have been followed by neutron diffraction ω-scan (TriCS@PSI) on cooling from RT to 10 K, each 10 K, and a full data collection has been performed at the final temperature (10 K). The splitting of (*hhl*) basic reflections remains until 10 K without changing, except continuous increase of angular separation from 2Δ = 1.12° at RT to 1.21° at 10 K, induced by the increasing differentiation between the values of *a*- and *b*-parameters. No transition to tetragonal unit-cell occurred, the basic structure staying orthorhombic. The few satellites which have been followed until 10 K did not show any positional changing, even if a weak linear increase of intensity has been observed on cooling, indicating similar long-range ordering than at RT but slightly better defined due to the lower thermal agitations at 10 K. Reciprocal space maps could not be obtained by X-ray diffraction at low temperature since no cryostat have been installed on ID11 beamline. The full dataset resulting from neutron diffraction experiments at 10 K has been collected with low symmetry space group, *Pmmm*, in order to detect eventual supplementary reflections, either from atomic or magnetic structures. However, no extra reflection could be found at the positions reported by J.S Gardner *et al.*, and all the diffracted intensity detected corresponded to positions of the *F*-centered lattice and to satellites with $\vec{q}_1$ = (0.85, 0.53, 0). The 539 observed main reflections (113 unique) were refined with the average space group *F*4/*mmm*, *i.e.* averaging the twinned domains in a single unit-cell, R_F = 3.41 %, R_{wF} = 3.86 %. The resulting structural model is presented in Table 5.3. A split model was used for apical oxygen.

The observed (*hkl*) reflections have been phased according to the structural model presented in Table 5.3, and nuclear densities have been reconstructed by Maximum Entropy Method (MEM, *cf.* chapter 3, section 5.2), R_F = 2.73 %, R_{WF} = 2.83 % and C_N = 1.47. Figure 5.10 shows the resulting 3D profiles of the nuclear isodensities of CoO_6 octahedra and interstitial sites (F_{max} = 825.5 and the isosurfaces were cut at 5). The projections of densities on the $\vec{a}$-$\vec{b}$ plane are also shown for different slices of the cell. The shape of apical site is comparable to the one at RT (*cf.* section 3.1, chapter 4), in the sense that the isosurface of nuclear density is

smeared out in $\vec{a}$-$\vec{b}$ plane around the centroid of apical site, and exhibits a complex shape; the two orientations of tilt [100]-type and [110]-type being distinguishable.

Table 5.3: *Structural model resulting from LS refinements of neutron diffraction data (TriCS@PSI)*

T = 10 K

Atom	*x/a*	*y/b*	*z/c*	*Occ*	U_{11}	U_{22}	U_{33}	U_{12}	U_{eq}
La	0	0	0.3612(1)	2	10.1(1)	10.1(1)	2.2(2)	-	7.43(2)
Co	0	0	0	1	8.1(1)	8.1(1)	6.3(4)	-	7.57(2)
Oeq	¼	¼	0	2	11.3(5)	11.3(5)	30.7(8)	-1.(1)	17.2(6)
Oap (1)	0	0	0.1734(1)	1.41(2)	25.6(5)	25.6(5)	6.7(5)	-	19.3(5)
Oap (2)	0.071(2)	0.071(2)	0.1766(6)	0.58(1)	35.(7)	-	-	-	35.(7)
Oint	¼	¼	¼	0.014(5)	32.(6)	32.(6)	1(7)	-	24.(7)

$a = b = 5.48(7)$ Å and $c = 12.62(5)$ Å, $\alpha = \beta = \gamma = 90°$. V = 380.1(1) Å^3, angular splitting 2Δ = 1.21°.Average structure refined in *F*4/*mmm* on 112 independent main reflections. R_{int} = 3.6 %. Agreement factors on LS refinements: R_F = 3.41 %, R_{wF} = 3.86 %. *Uij* are given in 10^{-3} Å^2. U_{iso} for O(ap2).

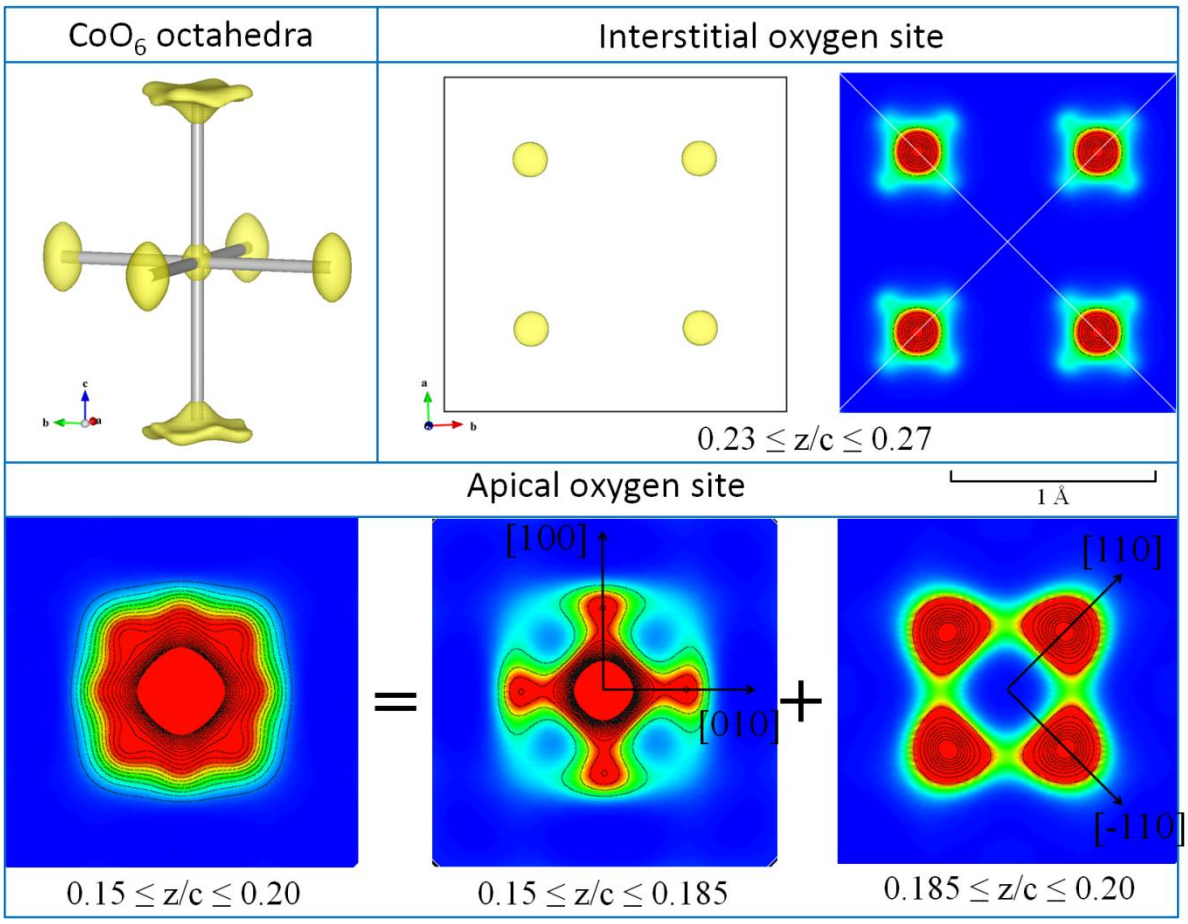

Figure 5.10*: Nuclear densities reconstructed by MEM applied on neutron diffraction data (TriCS@PSI) of* $La_2CoO_{4.14}$ *at 10 K.*

The two directions of apical atoms displacements are not perfectly lying in the same plane; the apical site can be divided into two distinct parts along *c*-axis as shown on the figure: the lower part of the site, *i.e.* with $0.15 \leq z/c \leq 0.185$, show atomic displacements toward [100]-type directions, while the upper part, *i.e.* with $0.185 \leq z/c \leq 0.20$, portrays atomic displacements toward diagonal [110]-type directions of the *F*-centered unit-cell. It demonstrates that the two types of displacements can be differentiated as function of their distinct Co-O_{ap} bond distances depending on their tilts' orientation. According to maximum entropy results, Co-O_{ap} interatomic bond lengths are of 2.20 Å for a tilt of ~13° toward [100]-type axes and of 2.34 Å for a tilt of ~16° toward [110]-type axes. The two latter orientations of tilting remain at RT, with different bond lengths, as previously shown. However, at 10 K, displacements around the site can be reasonably imputed in majority to static distortions. The interstitial sites are broad in the plane, evidencing displacive effects with static contribution. It is noticeable that such delocalization of the nuclear density of interstitial site occurs only when a part of octahedra are tilted toward to [100]-type direction.

2.2.Transitions from RT to 773 K

First, thermogravimetric measurements have been performed on highly pure $La_2CoO_{4.14}$ sample, from RT to 773 K, under mixed gas flow He/O_2 with same proportion and partial pressure of oxygen than in atmospheric conditions. It allowed dividing the thermal evolution of $La_2CoO_{4.14}$ into two distinct parts:

i) From RT to 473 K the phase transitions occur reversibly with constant oxygen content $\delta = 0.14$,

ii) From 473 K to 773 K, the phase transitions are this time accompanied by irreversible increase of oxygen stoichiometry, involving oxygen absorption from atmosphere.

Figure 5.11 shows the gain in mass (in %) on heating measured on a powderized sample of 48.5 mg of $La_2CoO_{4.14}$; the TG profile is accompanied by the corresponding DTA curve (Differential Thermal Analysis) measured simultaneously. The intervals of temperature corresponding to the different phases that could be distinguished through the results of diffraction experiments are shown by different coloured area on the figure for highlighting the numerous phase transitions undergone by the sample during heating process. The different stable states of $La_2CoO_{4+\delta}$ are named with a simple nomenclature used for clarity during this chapter. It should be read this way: (3+*d*): *d* dimension of modulation, *i.e.* number of

propagation vector(s), INC or COM: for INCommensurate or COMmensurate modulation, HT: High Temperature LT: Low Temperature, T: Tetragonal, O: Orthorhombic, LO: Less Orthorhombic. The extra oxygen content δ has been calculated for each isomass stage of the diagram assuming that uptaking extra oxygen atoms from atmosphere is the only cause of mass changing. Calculations are based on the oxygen content value of the starting sample δ = 0.14, previously determined *via* thermogravimetry under reducing gas flow, and confirmed by neutron diffraction refinements of the *as grown* crystal.

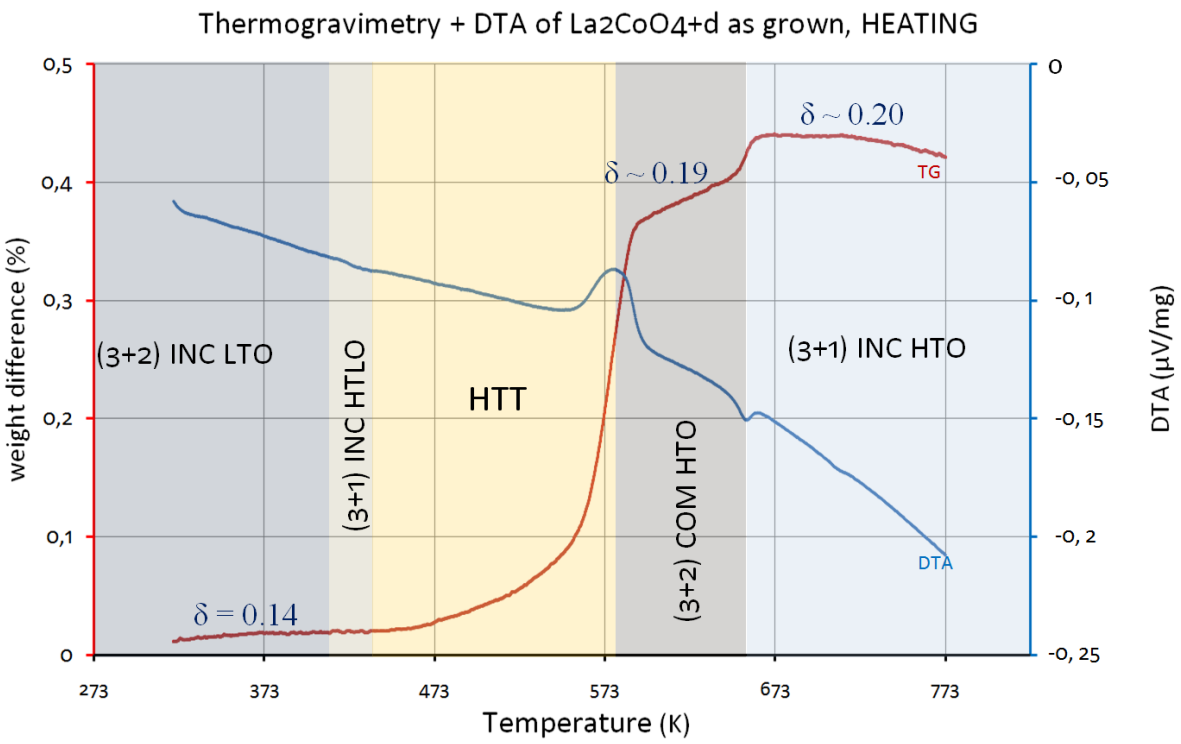

***Figure 5.11**: Temperature dependence of $La_2CoO_{4+\delta}$ measured by thermogravimetry from δ = 0.14 to δ = 0.2. The corresponding DTA curve is superposed on the diagram (LDM@PSI).*

A single-crystal sample of 100 µm, taken from the *as grown* crystal bulk has then been measured with isothermal steps each 50 K between 323 K and 773 K by synchrotron X-ray diffraction experiment (ID11@ESRF), exposed to air. The temperature was controlled by a heat blower apparatus. The data have been collected in the same experimental conditions for each temperature, *i.e.* rotation of 280° in φ with a step $\Delta\varphi$ of 0.2° (1400 scans per temperature) with an exposure time of 0.3 seconds per scan, optimized for clear detection of satellites. In parallel, neutron single crystal diffraction experiments have been carried out in the temperature range of RT-470 K on a *as grown* single crystal sample (3x3x5 mm^3), again with air as external environment.

Investigating structural modifications at higher temperature than 470 K by neutron diffraction was not possible for the following reasons: above the latter value, the phase transitions are not only driven by temperature but are also induced by the variations of extra-oxygen content in the material, involving chemical oxidation of the crystal. Soaking oxygen up from atmosphere together with subsequent diffusion and re-ordering of interstitial oxygen ions in the crystal bulk are easily achieved in microscopic samples which served for X-ray experiments; however circumstances are totally different for centimetric size samples, necessary for neutron experiments, which are much more volumic and have much less effective surface for exchanges with external medium. Therefore, increasing the concentration of interstitial ions and re-ordering homogeneously the whole structure require much longer time for big crystals bulk, as well as extremely stable thermodynamic conditions. Furthermore, it is not obvious that such big samples would undergo the phase transitions similarly than the microscopic one. Indeed problems could arise from inhomogeneity of extra oxygen concentration, which tends to be higher close to the surface, and could involve phase separations implying different phase transitions with temperature occurring simultaneously for various domains of distinct oxygen contents. Besides, these effects can lead to deterioration of the crystal sample. That is why exploring the structural transformations of $La_2CoO_{4+\delta}$ with temperature by the mean of neutron diffraction was limited to the study of phase transitions with constant oxygen content, *i.e.* below 470 K.

The structural investigations coupled with thermogravimetric experiments enabled to distinguish new regions in the phase diagram of $La_2CoO_{4+\delta}$. Concerning the lower temperatures for which δ remains constant, an intermediate state has been observed in a narrow range of temperature (*circa* 20 K), between the LTO and HTT phases. Indeed, starting at RT from the (3+2) INC LTO phase (chapter 4, section 3), two reversible phase transitions have been detected on heating:

- at 413 K: transition from LTO to an intermediate phase, named here High Temperature Less Orthorhombic phase (HTLO), accompanied by the loss of modulation toward $\vec{c}^*$, turning the structure into (3+1) incommensurately modulated;
- at 433 K: transition from the latter HTLO phase to a non-modulated HTT phase with total disappearance of not only superlattice reflections but also twinning.

Hence, for higher temperatures, when δ increases, two new modulated phases have been isolated:

- High Temperature Orthorhombic (3+2) commensurately modulated state in the range of 580-653 K with $\delta \sim 0.19$.
- High Temperature Orthorhombic (3+1) incommensurately modulated state above 653 K accompanied by slight increase of δ to ~ 0.20.

All the samples that have been heated at 773 K systematically stabilize in the $La_2CoO_{4.19}$ phase, at RT, with commensurate monoclinic supercell $\vec{a} = 2\vec{a}_b$, $\vec{b} = 2\vec{b}_b - \vec{a}_b$, $\vec{c} = 4\vec{c}_b$, space group *B*2/*n* (this phase is extensively described in chapter 4, section 5).

2.2.1. Reversible transitions with δ constant from (3+2) incommensurate LTO to HTT phase, via intermediate (3+1) incommensurate HTLO phase.

DSC and temperatures of the phase transitions

Contrary to what has been always observed in $La_2MO_{4+\delta}$ oxides, the transition from LTO to HTT phase undergone by the $La_2CoO_{4.14}$ compound involves a primary transformation *via* one intermediate phase, stable in a narrow range of temperature (20 K). In order to measure precisely the temperatures of the two transitions, Differential Scanning Calorimetry (DSC) experiments were performed with a NETZSCH DSC 204F1 system: 26.74 mg of sample was placed in alumina crucible under sealed Argon atmosphere and heated up from RT to 523 K with a ramp of 5 K/min. The experiment has been performed three times consecutively for checking the reversibility; Figure 5.12 shows the profiles on heating. The two endothermic peaks portray the two phase transitions undergone by the sample, the first one at 413 K from LTO to HTLO, followed by the second one at 433 K to HTT state. The profile of the DSC curve and the presence of a hysteresis of 4-5 K on cooling suggest that the two transitions are of 1st order. In addition, the discontinuities of the DSC profile depict the discontinuities of the entropy at the two temperatures, theoretically characteristic of a 1st order phase transitions. It is rather surprising to detect such endothermic peak even for the transformation into HTT, which is usually attributed to a 2nd order phase transition[233]. However, in the present context, the LTO phase does not directly transit to HTT but passes through the intermediate HTLO phase that may involves a different order of transition. Moreover, the abrupt increase of the DSC signal after the transition can put the order of the transition into question.

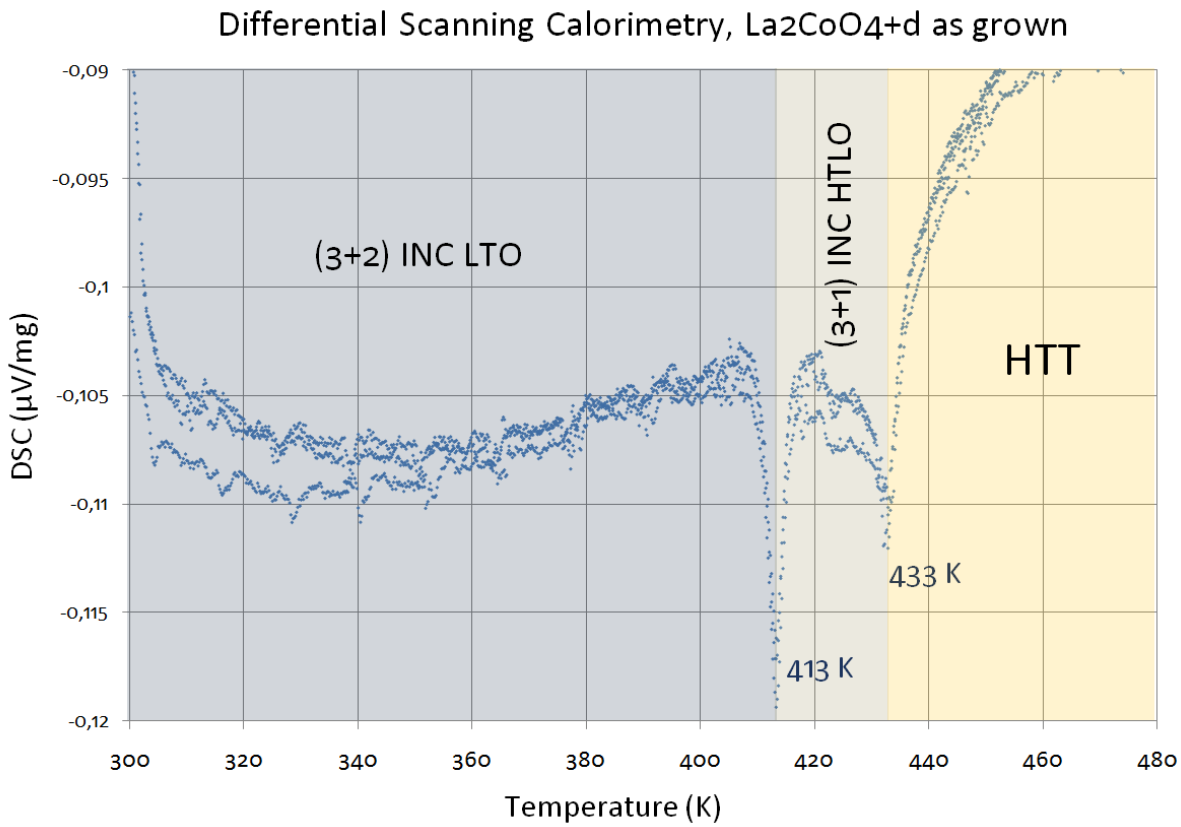

***Figure 5.12**: Differential Scanning Calorimetry (LDM@PSI) of $La_2CoO_{4.14}$, allowing to distinguish precisely temperatures of phase transitions.*

Synchrotron X-ray diffraction results, modulation and symmetry

According to the results of diffraction experiments, the space group of the basic structure remains *Fmmm* for the first two phases, *i.e.* below 433 K, and becomes *F4/mmm* above this temperature (HTT phase equivalent to *I4/mmm* with $a_I = a_F/\sqrt{2}$). The cell parameters of the basic unit-cell for each of the three phases are given below:

T (K)	Basic s.g.	a (Å)	b (Å)	c (Å)	V (Å3)
300	Fmmm	5.473(3)	5.527(2)	12.642(4)	382.41(1)
423	Fmmm	5.497(2)	5.513(3)	12.675(4)	384.11(5)
450	F4/mmm	5.510(1)	5.510(1)	12.697(3)	385.48(2)

The reciprocal space maps reconstructed from synchrotron X-ray diffraction data give the first mandatory details about real symmetries ensuing from modulation of each phase. A complete set of (*hkl*) reciprocal planes has been reconstructed pixel by pixel at RT, 423 K and 473 K. Diffuse strikes have been observed along $\vec{c}^*$ essentially between the Bragg reflections of (*hh*6) and (*hh*8)-type. Conversely the planes perpendicular to $\vec{c}^*$, *i.e.* in the $\vec{a}^*$-$\vec{b}^*$ plane,

exhibit superlattice reflections for the first two phases and only main reflections for the tetragonal one. Figure 5.13 shows the experimental (*hk*1) planes for the three phases: at RT, 423 K and 473 K. The corresponding pattern idealized for a single pseudo-merohedral twin orientation is shown on the right side of each plane.

It has to be underlined that, as explained in chapter 4 (section 3.2), each pseudo-merohedral twin individual is in his turn split into two domains by partial merohedral twinning, involving a complete covering of main reflections while satellites are separated (distinguished by blue and red spots on the idealize pattern). The crosses symbolize the absence of superlattice reflections corresponding of the vector sum $\vec{q}_{1a} + \vec{q}_{1b}$.

The phase named (3+2) INC LTO relates to the *as grown* $La_2CoO_{4.14}$ structure at RT and is extensively described in chapter 4 (section 3). Above 413 K, the (3+1) INC HTLO still presents satellite reflections, but the propagation vectors has shifted from $\vec{q}_1 = 0.53\ \vec{a}^* + 0.85\ \vec{b}^*$ below the transition to $\vec{q}_1 = 0.57\ \vec{a}^* + 0.76\ \vec{b}^*$ above the transition (the modulation period in direct space goes from ~5.50 Å at RT to ~5.76 Å at 423 K). In this intermediate state, the satellites of 3rd order of the pseudo-merohedral domains are overlapped in the left side of the planes but partially or totally split on the right side, as for main reflections; this similarity is a coincidence induced by the specific values of $\alpha_1 = 0.57$ and $\beta_1 = 0.76$ between 413 and 433 K. The shift of the in-plane propagation vector at the transition is accompanied by a decrease of orthorhombicity from $2\Delta = 1.12°$ to 0.81°. Moreover the second vector $\vec{q}_2$ at RT disappears since the superlattice reflections in the reciprocal planes perpendicular to $\vec{c}^*$ with $l = n + ½$ (n integer) are no longer present above 413 K. Consequently, at 423 K the indexation of all reflections can be done by using a single modulation vector $\vec{q}_1$ lying in the $\vec{a}$-$\vec{b}$ plane for each single domain (4 twinned domains in total), with a global reciprocal vector $\vec{H} = h\ \vec{a}^* + k\ \vec{b}^* + l\ \vec{c}^* + m_1\ \vec{q}_1$, until $|m_1| = 3$. Hence, the HTLO intermediate phase has in-plane (3+1) incommensurately modulated structure. This phase is rather close to the starting $La_2CoO_{4.14}$ at RT, even less complex since only a single propagation vector modulates the structure. At RT the superspace group has been suggested to be $F2/m(\alpha_2\beta_2½)00(\alpha_1\beta_1 0)0s$. Between 413 and 433 K, the reflection conditions related to the systematic extinctions and the equivalences between reflections are the same than at RT, the only differences being the loss of $\vec{q}_2$ and the different values of α_1 and β_1. Consequently, the superspace group labelled $F2/m(\alpha\beta 0)0s$, derived from the conventional $B2/m(\alpha\beta 0)0s$ based on a different basic unit-cell with a'= (0, -1, 0), b'= (½, ½, 0) and c'= (0, 0, 1), can be proposed for the (3+1) INC HTLO phase. Even if non-conventional, the *F*-centered superspace group is perfectly acceptable and is even more

convenient since it is based on the usual LTO unit-cell. In the intermediate HTLO phase, only the planar wave deformation persists in the layers, but super-ordering toward *c*-axis disappears. The loss of $\vec{q}_2$ and shift of $\vec{q}_1$ do not affect drastically the basic structure; only orthorhombicity evolves slightly. Nevertheless, the long range ordering is modified, and thus atomic positions in the unit-cell are different, as shown later by neutron diffraction.

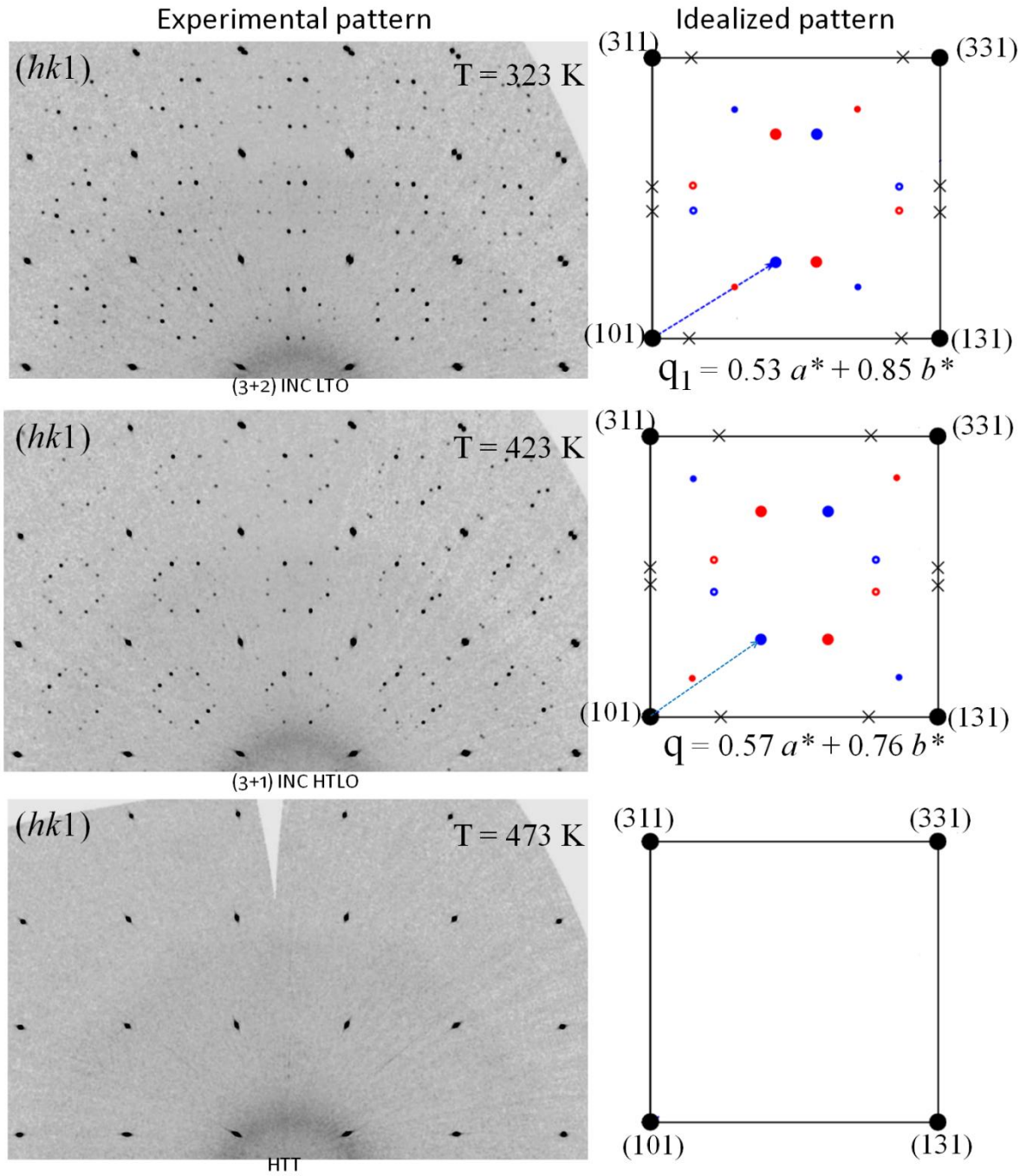

***Figure 5.13**: (hk1) reciprocal space maps of $La_2CoO_{4.14}$ reconstructed from synchrotron X-ray diffraction data (ID11@ESRF), in the three different phases LTO, HTLO, HTT, together with the corresponding idealized reciprocal pattern for one pseudo-merohedral individual.*

At 433 K all superlattice reflections vanish together with the twinning effects, the phase becomes non-modulated and tetragonal. The reciprocal maps reconstructed for this temperature consist only of *F4/mmm* basic reflections, identical to the reciprocal pattern of the so-called HTT phase. The long-range is completely lost in this phase although the oxygen content remained $\delta = 0.14$.

So, to sum up, the *as grown* $La_2CoO_{4.14}$ single crystal undergoes a first transition on heating around 413 K from a (3+2) incommensurately modulated orthorhombic structure (LTO), to (3+1) incommensurate modulated less orthorhombic (HTLO) by loss of modulation toward *c*-axis accompanied by shift of in plane modulation vector. The volume proportion of each twin individual is conserved during the latter structural transformation. When heating further, at 433 K $La_2CoO_{4.14}$ transits to non-modulated, single domain, tetragonal structure (HTT), space group *F*4/*mmm*.

Neutron diffraction refinements, maximum entropy, static and dynamic disorder

A full set of 434 basic reflections (112 unique) has been measured with the *as grown* $La_2CoO_{4.14}$ single crystal sample (3×3×5 mm^3) at RT, 420 K and 450 K (same sample that was measured at 10 K). For the two first data sets, the diffraction pattern has been collected with a wide scale range in ω, namely of 3.6°, in order to fully collect the split reflections which are broader, and refined in the average *F4/mmm* space group. Upon convergence of refinements, the occupancy of interstitial oxygen confirmed the constancy of δ during the two transitions. A split model for the apical site was used, consisting of adding a supplementary site at the Fourier difference maxima position (*x*, *x*, *z*, Wyckoff site *32m*) sharing the total occupancy of apical oxygen with the normal site (0, 0, *z*, Wyckoff site *8e*). The resulting structural models were in better accordance with the experimental data when the supplementary position is partially occupied (17% at 420 K and 29% at 450 K), meaning that a percentage of octahedra are not aligned toward the *c*-axis but remain tilted, and even in the HTT state. According to the atomic positions found in the unit-cell, resulting from structural refinements, the O_{ap}-O_{int} bond distances for the HTLO phase enlarge from 2.16 Å for an empty interstitial site (O_{ap} in (0, 0, *z*)), to 2.79 Å when occupied (O_{ap} in (*x*, *x*, *z*)), corresponding to a tilt of octahedra of about 17.2° from the *c*-axis. For the HTT phase the respective O_{ap}-O_{int} distances are of 2.17 Å and 2.71 Å, *i.e.* tilting of 14.6° at 450 K. For reference, the average value of tilt refined from neutron diffraction at RT in $La_2CoO_{4.14}$ is of

17.7°. The average value of the angle of tilt slightly decreases with temperature while the percentage of tilted octahedra increases.

***Table 5.4**: Structural model of $La_2CoO_{4.14}$ at 420 K and 450 K, resulting from least square refinements carried out on single crystal neutron diffraction data (TriCS@PSI).*

T = 420 K

Atom	*x/a*	*y/b*	*z/c*	*Occ*	U_{11}	U_{22}	U_{33}	U_{12}	*Ueq*
La	0	0	0.3611(2)	2	14.3(2)	14.3(2)	7.1(1)	-	11.2(9)
Co	0	0	0	1	8.7(1)	8.7(1)	35.4(3)	-	17.8(3)
Oeq	¼	¼	0	2	15.3(4)	15.3(4)	29.6(2)	-2.(4)	20.3(2)
Oap (1)	0	0	0.1746(8)	1.591(1)	44.2(1)	44.2(1)	9.5(6)	-	32.4(6)
Oap (2)	0.089(3)	0.089(3)	0.1762(2)	0.342(7)	36.(4)	-	-	-	36.(4)
Oint	¼	¼	¼	0.014(2)	9.(2)	9.(2)	1(6)	-	11.(4)

a = b = 5.50(5) Å and c = 12.675(4) Å, $\alpha = \beta = \gamma = 90°$. V = 384.1(1) Å^3, angular splitting of (*hhl*): 2Δ = 0.81°. Average tilt angle of CoO_6 octahedra: 17.2°. Average structure refined in *F*4/*mmm* on 112 independent main reflections. R_{int} = 3.1 %. Agreement factors on LS refinements: R = 3.76 %, R_w = 4.14 %.

T = 450 K

Atom	*x/a*	*y/b*	*z/c*	*Occ*	U_{11}	U_{22}	U_{33}	U_{12}	U_{eq}
La	0	0	0.3614(3)	2	10.6(3)	10.6(3)	4.1(1)	-	8.2(4)
Co	0	0	0	1	5.7(4)	5.7(4)	14.5(6)	-	8.7(5)
Oeq	¼	¼	0	2	9.2(9)	9.2(9)	32.1(5)	-2.(3)	17.(4)
Oap (1)	0	0	0.1748(3)	1.376(1)	31.5(6)	31.5(6)	6.4(8)	-	21.(6)
Oap (2)	0.078(1)	0.078(1)	0.1779(2)	0.544(1)	34.(5)	-	-	-	34.(5)
Oint	¼	¼	¼	0.014(1)	7.(2)	7.(2)	3.(8)	-	6.(1)

a = *b* = 5.510(1) Å and *c* = 12.697(3) Å, $\alpha = \beta = \gamma = 90°$. V = 385.4(9) Å^3, angular splitting of (*hhl*): 2Δ = 0°. Average tilt angle of CoO_6 octahedra: 14.6°. Space group *F*4/*mmm*, 112 independent main reflections. R_{int} = 4.2 %. Agreement factors on LS refinements: R = 3.93 %, R_w = 3.72 %.
U_{iso} for O(ap2), Uij are given in 10^{-3} Å^2. $U_{13} = U_{23} = 0$ for all atoms. λ = 1.178 Å. Refinements carried out with JANA2006.

Complementary to classical structural refinements, the Maximum Entropy Method (MEM) has been used to reconstruct nuclear densities from experimental (*hkl*) intensities phased *via* the model shown in Table 5.4. In the three cases, only main reflections have been used for MEM calculations (*i.e.* excluding satellites for RT and 420 K). Consequently, the nuclear density distribution ensuing from these data treatments correspond to the average structure at 420 K and RT, whereas the full diffracted intensity is taken in account for the phase at 450 K (no satellite for the latter temperature). All the MEM refinements converged with satisfactory agreement factors: at RT: R_F = 2.71 % R_w = 2.62 % and C_N = 1.29; at 420 K: R_F = 3.65 % R_w = 2.83 % and C_N = 1.14; at 450 K: R_F = 3.86 % R_w = 4.20 % and C_N = 1.30. Figure 5.14

shows the 3D nuclear density profiles of CoO_6 octahedra, for each temperature, together with the respective projection on the $\vec{a}$-$\vec{b}$ plane of the density around apical site (densities integrated between $0.15 \leq z/c \leq 0.20$) and interstitial site (densities integrated for $0.23 \leq z/c \leq 0.27$).

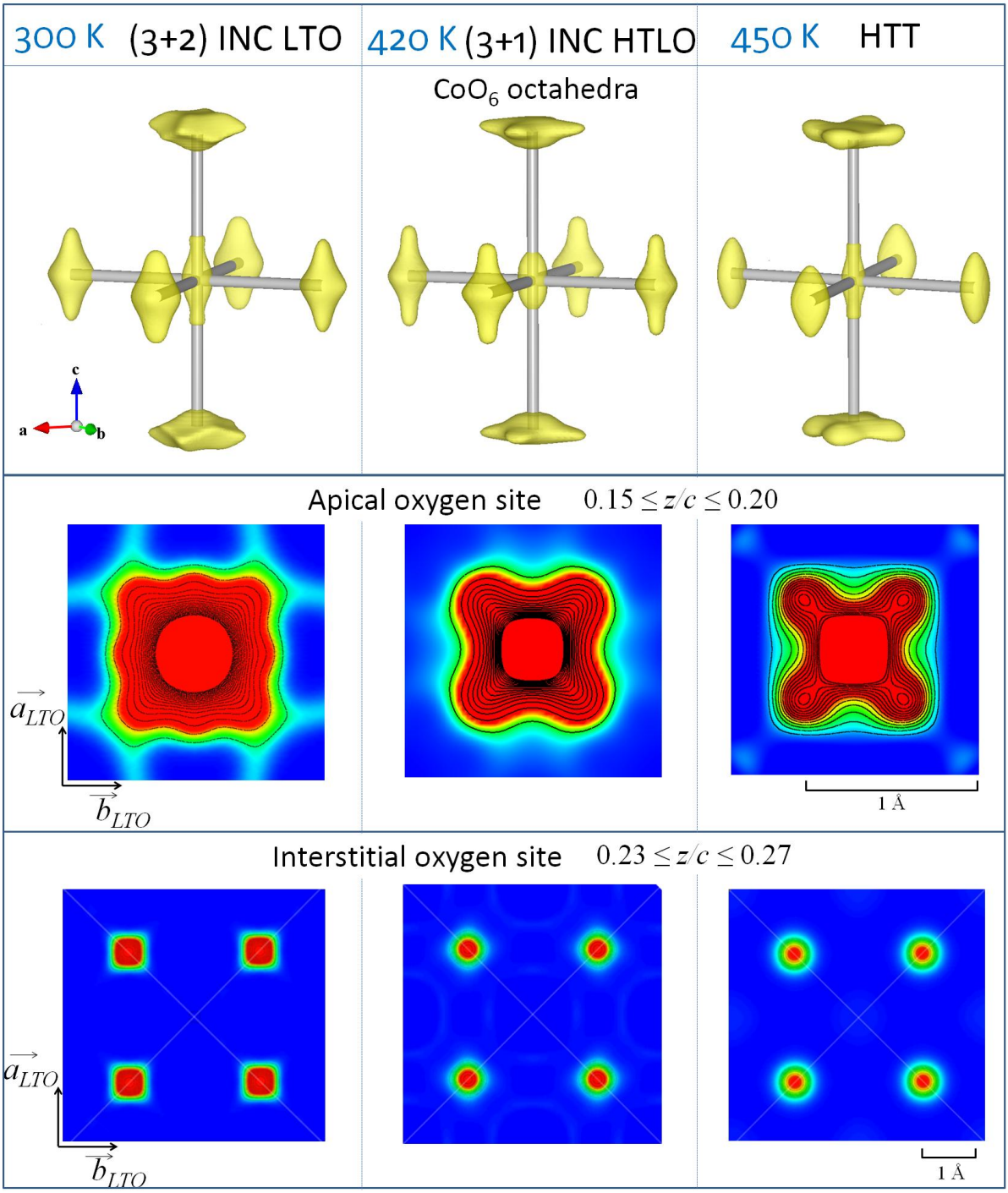

***Figure 5.14**: Nuclear density profiles of $La_2CoO_{4.14}$ for different temperatures, reconstructed by maximum entropy method applied on neutron diffraction data (TriCS@PSI). 3D profiles: RT: F_{max} 321, isosurfaces cut at 3; 420K: F_{max} 680, isosurface cut at 5; 450K: F_{max} 881, isosurface cut at 5. 2D projections: RT and 420 K: densities shown in the range 3-20% of ρ_{max}, 450 K: densities shown in the range 3-50% of ρ_{max}.*

As already stated, at RT the shape of the 3D density profile of O_{ap} exhibit two main orientations of displacements: along the [110]-type and [100]-type directions, with similar amplitude. But, in HTLO state only displacements toward the diagonal [110]-type direction is observable, like for $La_2NiO_{4.125}$ at RT[49,220]. Moreover the displacements are flat, *i.e.* well oriented in the plane. The simultaneous disappearance of O_{ap} displacements toward [100]-type axes, and of the modulation vector $\vec{q}_2$ at the transition, suggests a link between the latter direction of tilt and the modulation toward $\vec{c}^*$ depicted by $\vec{q}_2$ in the as grown sample at RT. The equatorial oxygen atoms are delocalized toward *c*-axis (up and down), depicting the rigidity of CoO_6 octahedra, with a slight tendency to be less delocalized in HTT state, involving more flexible octahedra and thus variations of bond lengths.

At 450 K, displacements of O_{ap} points in the same directions than in HTLO, however it slightly deviates upward, toward the interstitial layer. In addition, the density corresponding to the split positions are very well defined in comparison with the other temperatures. Indeed, the aside-apical site at (*x*, *x*, *z*) appears to form a nice shaped bowl well separated from the average (0, 0, *z*) site. Each of the four sites aside represents 20% of the density of the central peak; for comparison it is only of 4% at 423 K. It is worth mentioning that the HTT phase is generally considered to be highly symmetric, and portrayed with octahedra strictly aligned along *c*-axis. On the contrary, here, it is clear that tilting of octahedra persists even if the vanishing of satellites indicates a total loss of coherency and ordering between tilts which are even more pronounced than at lower temperature. The anisotropic tilts of CoO_6 octahedra do not break the fourfold symmetry axis collinear to *c*-axis. On the contrary to the maximum entropy reconstruction of the modulated phases, the ones of the HTT phase take the whole diffracted intensity in account (no satellites in this phase) implying that the strong anisotropic disorder of apical oxygen atoms is the same for all apical atoms since they are identical by symmetry. Hence, the apparent high symmetry is deceptive since it results in fact from an average of the statistic disorder of the site.

Since we have shown in the previous chapter that the displacive modulation of octahedra is correlated to the occupational modulation of interstitial atoms, the statistic disorder of apical site forbids the determination of the positions of extra-oxygen atoms. The question is: is there still an arrangement at long-range of interstitial atoms in the HTT phase? If not, it logically involves a complete and sudden disordering of interstitial oxygen atoms at the transition, involving large atomic displacements. It is hard to admit that such a reconstructive phase transition by random ionic diffusion occur simultaneously and homogeneously in the whole

crystal bulk. A situation where local but inhomogeneous ordering is kept, appears more conceivable.

The stretching of the *c*-axis yields bond length to elongate, which relaxes the internal strains. Hence the repulsive effect between apical atoms and interstitial ones diminishes. These considerations provide better comprehension of the rather strange evolution of O_{int} nuclear densities, calculated by MEM, with temperature. The centroid of the interstitial site has been found to be located exactly at the (¼, ¼, ¼) position in all cases. But an intriguing temperature dependence of the nuclear density distribution can be noticed (*cf.* Figure 5.14). Interstitial atoms appear indeed more localized at 450 K and 420 K than at RT and 10 K, *i.e.*, even though the opposite trend would be intuitively expected. Indeed, atomic displacement factors usually increases with temperature by thermal motion, but here the nuclear density around O_{int} site is spread out at RT and more contracted at higher temperatures. The localization of O_{int} can be associated to the dynamical delocalization of O_{ap} induced by activation of soft phonon mode, withdrawing strains of O_{ap}-O_{int} bonds and thus explaining the loss of static disorder around O_{int} site, resulting in stretching of nuclear density volume. It is, in fact, similar to what happens for the equatorial oxygen atoms.

The apical oxygen atoms are freer. The maximum entropy method does not intrinsically allow us to differentiate static or dynamic contributions. The LTO/HTT transition in the isostructural compounds La_2NiO_4 and La_2CuO_4 has been shown to be driven by activation of particular soft phonon mode at the transition consisting of coherent tilting of rigid MO_6 octahedra[234,85,86,87,218]. It has never been done for the cobaltate; however, extrapolating such concept of phase transition as hypothesis for the present case appears to be relevant. Furthermore, an inclusive study of structural phase transitions in perovskite-related oxides by neutron scattering techniques has been published by G. Shirane *et al.*[235] summarizing several results accumulated after several years of research at Brookhaven research laboratories (NY, US). Correlated to theoretical studies of condensed matter phases, they show that the concept of displacive phase transitions explained through activation/deactivation of soft-phonon modes is a key for explaining diverse structural transformations undergone by many type of crystal phases, which were remaining inexplicable by static considerations.

Hence, the dynamic disorder of the HTT phase remains the prominent candidate for explaining the shape of the anisotropic nuclear density of the apical site. Activation of soft-phonons modes at the transition involving tilting of octahedra explains the vanishing of satellites. Inelastic neutron scattering experiments could validate this hypothesis. First tries

have been attempted, but since no theoretical calculations have ever been carried out beforehand, finding the location of the softening of the phonon peak in the Brillouin zone was arduous. This is discussed further later.

Neutron diffraction studies of the two phase transitions, twinning, and displacive effects

If $La_2CoO_{4.14}$ is kept in the range of temperature for which δ remains constant (below ~ 500 K), the two phase transitions are reversible. Hence, the single crystal sample has been heated up to 450 K and the structural transitions have been followed on cooling, back to RT. A set of characteristic reflections: (*hh*0) and (00*l*), plus few satellites have been measured by neutron ω-scans every 2 K from 470 K to 370 K and every 10 K from 370 K down to RT.

The family of (*hhl*) reflections, consisting in a single peak at 470 K in the HTT phase, split into 3 distinct peaks below the tetragonal to orthorhombic transition (around 433 K) as visible for the (220) reflection on Figure 5.15. Conversely, the (00*l*) reflections undergo a shift but no splitting, which is expected since this type of reflections is not affected by twinning. The split of (220) reflection into three peaks instead of two implies a different number of twin individuals than in the starting sample. An additional set of two pseudo-merohedrally twinned domains appear, *i.e*. 4 individual orientations of the basic unit-cell in total (and 8 if we take into account the partial merohedral twinning law separating satellites, but here we speak only about main reflections so the second twinning is temporary put aside for the sake of clarity). The middle peak is the superimposition of two domains while the ones on the sides belong to the two other domains each (*cf*. Figure 3.3). According to the twinning law and to the experimental intensities, the volumic ratios of each twin at RT with regards to the total volume of the sample are: I: 46 % - II: 10 % for the first set, and III: 14 % - IV: 30% for the second set.

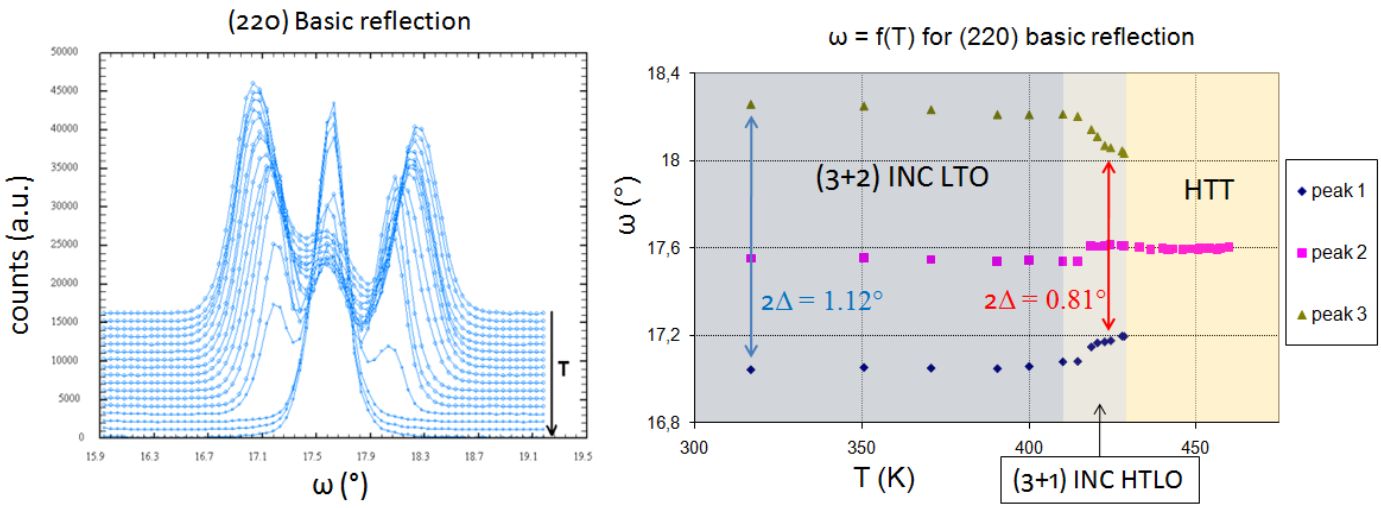

***Figure 5.15**: Left: thermal evolution of (220) reflection measured by neutron diffraction ω-scan (TriCS@PSI), Right: plot of the position of each peak as function of temperature, showing evolution of orthorhombicity.*

So, to sum up, the reversibility of the transition does not involve conservation of twinned components. Once $La_2CoO_{4.14}$ compound is brought into HTT state, twinning vanishes and the crystal consists of a single domain; therefore, the different orientations of the basic orthorhombic unit-cell below the transition are not memorized by the material. When cooling down, domains reappear but with variable numbers and volumes. Figure 5.16 shows the temperature dependence of the (220) integrated intensity, which is twice lower above the transition. This tendency is also followed by the FWHM (Full Width at Half Maximum) profiles, shown on the right side of the figure. In HTT state, reflections are less intense and sharper. As the structure factor does not change, this phenomenon can be assigned to primary extinction, related to the perfection of the atomic lattice. The crystal tends to be more perfect above 433 K, while twinning lowers its quality below the transition. These results go in the sense of dynamical disorder of octahedra in HTT state, since if tilts of octahedra would be kept statically tilted, the perfection of the crystal would not be increased and primary extinction would not be so strong.

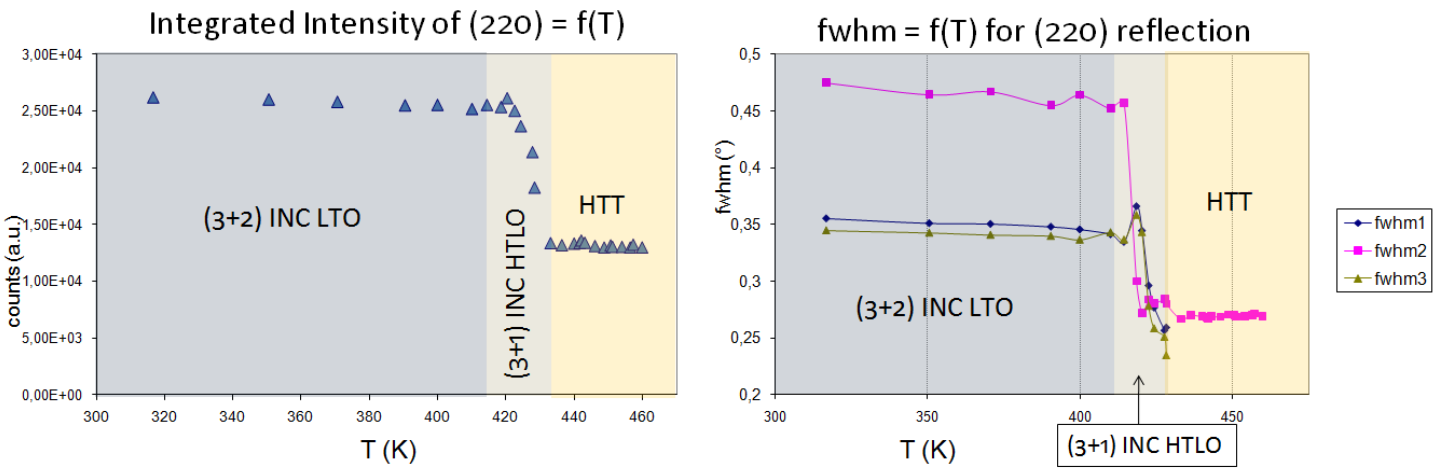

***Figure 5.16**: Temperature dependence of the integrated intensity of (220) reflection, and of FWHM of each peak.*

Figure 5.17 shows the thermal evolution of the strong (02110) satellite measured by ω-scan together with the respective integrated intensity versus temperature. The shift of the peak in ω related to the shift of $\vec{q}_1$ from LTO to HTLO phase is clearly visible, followed by the total disappearance of the satellite above 433 K. The dynamically disordered state above 433 K permits to explain the transformation from HTT to incommensurately modulated structure on cooling in terms of displacive phase transition driven by the freezing of a soft-phonon mode. When cooling from HTT to HTLO, the dynamic mode condenses into static wave deformation of the basic structure, yielding the incommensurate vector $\vec{q}_1$. At the HTT/HTLO transition, the inelastic peak of low-energy corresponding to the phonon becomes elastic and is converted to a superlattice point[235]. Even if phonons are sinusoidal displacement waves, higher harmonic displacements develop within the incommensurate phase, as established for instance in Rb_2ZnCl_4[236]. When $\vec{q}_1$ shifts at 413 K, the intensity of the satellite does not collapse to 0, but remains, as shown on the right side of the Figure 5.17. This implies that super-ordering induced by atomic displacements is kept during the HTLO/LTO transition. The transition can be seen as a coherent and continuous structural re-arrangement to more stable state of lower energy[237].

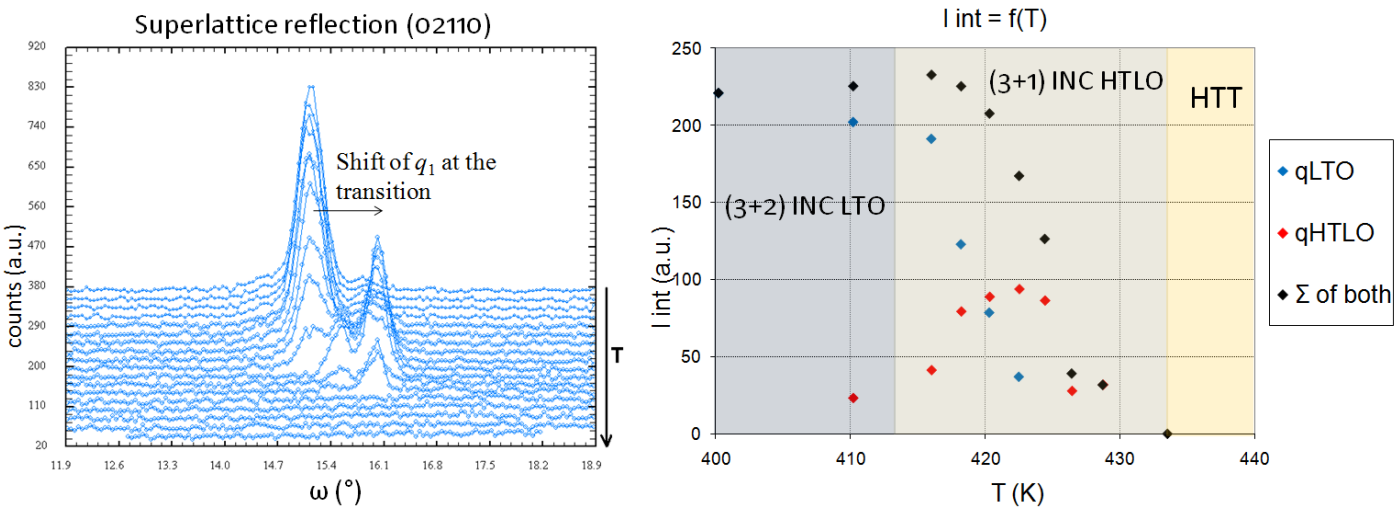

***Figure 5.17**: Temperature dependence of a satellite measured by neutron diffraction (TriCS@PSI), the shift of position on the ω-scan corresponds to the variation of $\vec{q}_1$ at the transition. The right side of the figure shows the plot of integrated intensities as function of temperature.*

Important outcome

The presence of extra oxygen atoms on interstitial sites lowers the temperature of transition from orthorhombic to tetragonal unit-cell which is of 433 K when δ = 0.14 and 850 K for δ = 0[47]. It shows that the presence of extra-oxygen atoms in the material favors the transition to HTT phase. The latter is definitely of first importance for understanding the mechanism of oxygen diffusion at such low temperature. Indeed, as visible on TG profile of Figure 5.11, the increase of oxygen stoichiometry from δ = 0.14 to 0.19 occurs when the compound is in HTT state. The crystal undergoes topotactic oxidation reaction, by uptaking oxygen from atmosphere, involving sudden increase of oxygen concentration in the material.

The concept of dynamic disorder of octahedra by soft-phonon mode in the HTT phase not only provides explanations about all structural effects entering the game during phase transitions but also give better insight about the origin of fast oxygen diffusion properties. Indeed, similarly to what has been recently shown[18] for the Brownmillerite $SrFeO_{2.5}$, phonon modes would supply necessary energy to interstitial oxygen yielding their diffusion within layers. Since positions of interstitial oxygen and apical oxygen are linked, the coherent motion of octahedra triggers the opening and closing of tetrahedral site, amplifying oxygen diffusion through low-energy lattice dynamics. Enlarging the phonon-assisted diffusion model stressed for Brownmillerites to the Ruddlesden-Popper type phases emphasizes the mandatory role of

lattice instabilities allowing oxygen diffusion at moderate temperatures. It goes in the sense of a unified approach to describe oxygen at moderate temperatures.

2.2.2. Transition from HTT to (3+2) commensurate HTO phase with δ ~ 0.19, at 580 K.

As explained beforehand, the content of extra oxygen increases strongly when the sample is in HTT phase. Above 580 K, it reaches the approximate value of δ ~ 0.19, and remains approximately constant until 640 K according to results of TG experiments (Figure 5.11). At 580 K, the tetragonal unit-cell transits back to orthorhombic, a = 5.48(1) Å, b = 5.52(4) Å, c = 12.65(3) Å, together with reappearance of twinning and also satellites at commensurate positions. The basic structure is then twinned into two orthorhombic domains, space group *Fmmm*, testified by the splitting into two peaks of *(hhl)* main reflections. The average structure refined in the *F*4/*mmm* space group is shown in Table 5.5.

Table 5.5: *Structural model of $La_2CoO_{4+\delta}$ single crystal with δ ~ 0.19 at 623 K, refined only with main reflections collected by synchrotron X-ray diffraction (ID11@ESRF).*

Atom	*x/a*	*y/b*	*z/c*	*Occ*	U_{11}	U_{22}	U_{33}	U_{12}	U_{eq}
La	0	0	0.35965(3)	2	22.3(5)	22.3(5)	15.7(7)	-	19.6(7)
Co	0	0	0	1	17.1(4)	17.1(4)	29.3(3)	-	21.4(3)
O (eq)	¼	¼	0	2	22.(7)	22.(7)	47.(8)	-3.(2)	32.(3)
O (ap1)	0	0	0.177(1)	0.4(3)	53.(1)	53.(1)	20.(3)	-	42.(3)
O (ap2)	0.060(8)	0.060(8)	0.171(2)	1.6(1)	3(5)	-	-	-	3(5)
O (int)	¼	¼	¼	0.19	1(8)	-	-	-	1(8)

Average cell parameters: a = b = 5.50(3) Å and c = 12.65(3) Å, α = β = γ = 90°. V = 383.17(1) Å^3, 2Δ = 1.2°.Average structure refined in *F*4/*mmm* on 589 main reflections (145 unique). R_{int} = 4.1 %. Wavelength of X-rays: 0.2072 Å. Agreement factors: R_F = 4.15 %, R_{WF} = 3.98 %. U_{iso} for O(ap2) and O(int). *Uij* are given in 10^{-3} Å^2.

Concerning superlattice reflections, the reciprocal space maps reconstructed for this phase at 623 K exhibit a different diffraction pattern than the one of same stoichiometry (δ = 0.19) at RT (chap 4 section 5). The propagation vectors providing indexation of all satellites are the same, *i.e.* $\vec{q}_1$ = ½ $\vec{a}$* + ¾ $\vec{b}$* and $\vec{q}_2$ = ¼ $\vec{c}$*, but the systematic extinctions differ. At first sight, the (*hk*1) reciprocal map presented in Figure 5.18 looks more like the one of $La_2CoO_{4.25}$ (Figure 4.18), but a major difference distinguish them: here, the satellites corresponding to the vector sum $\vec{q}_1 \pm \vec{q}_2$ are totally absent (pointed by crosses on the figure). This highlights the occurrence of the second twinning effect (already observed in $La_2CoO_{4.14}$ at RT), involving breaking of the (100) mirror plane in addition to the (110) mirror plane. This results in the presence of four individual twin orientations in the sample in total. It is the only

commensurate phase of $La_2CoO_{4+\delta}$ to show this particularity, the second twinning law being usually observed in incommensurate phases. Here, due to the specific rational values of α_1 and β_1 of the in-plane vector $\vec{q}_1$, only satellites with $|m_1|$ odd are separated while those with $|m_1|$ even are overlapped. It is validated by experimental intensities of satellites: the ($hk12m_2$)-type reflections, which are symmetrical by the (100) mirror plane, appear with similar intensity on the map in opposition to the reflections of ($hk11m_2$)-type and ($hk13m_2$)-type which are unique and thus of different intensity, as visible on the figure. Because of the second twinning law, the symmetry of the basic structure lowers to $F2/m$.

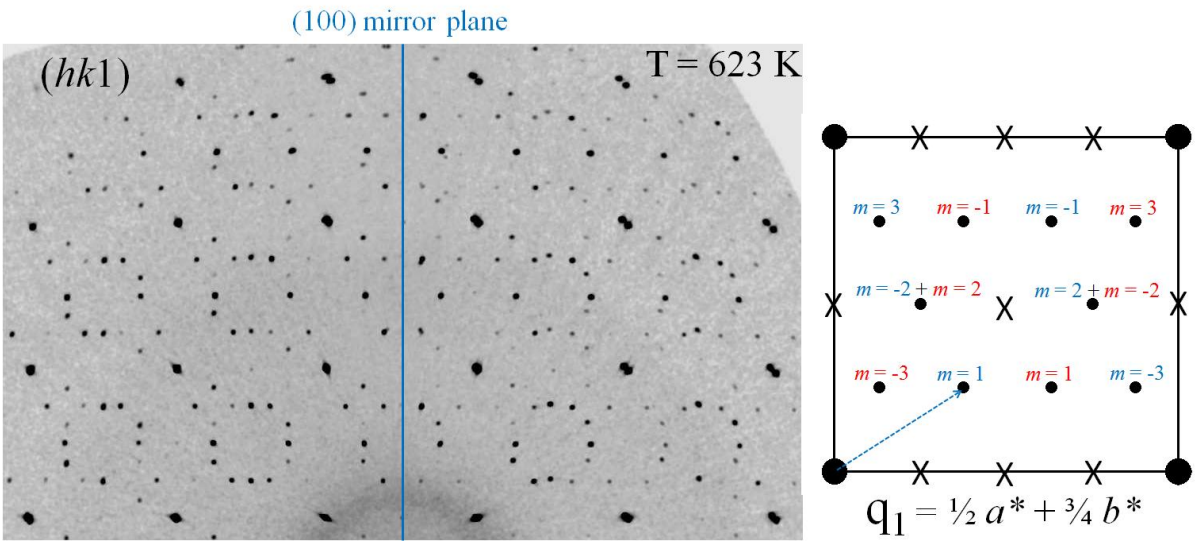

***Figure 5.18**: (hk1) reciprocal space plane of $La_2CoO_{4+\delta}$ with $\delta \sim 0.19$ at 623 K reconstructed from synchrotron X-ray diffraction data (ID11@ESRF). The idealized pattern for two twin domains symmetric by (100) mirror plane is shown, with related indexation of satellites in blue for domain 1 and red for domain 2.*

A second aspect discriminating the present phase to the $La_2CoO_{4.25}$ at RT, is that satellites generated by the second modulation vector $\vec{q}_2$ are very clearly observable until the 2nd order and less but still with $m_2 = 3$, instead of $m_{2max} = 1$ for $\delta = 0.25$ at RT. Figure 5.19 shows the ($h¾l$) reciprocal space map (indexes of the basic cell), composed only of satellites. It demonstrates that $\vec{q}_1$ and $\vec{q}_2$ modulate the same domain since their vector sum clearly generates diffracted intensities. Superstructure reflections with $|m_1| = 1$ of two domains are observable on the map, all satellites aligned vertically belong to the same domain but alternate horizontally, as depicted by the indexation in red or blue above the picture.

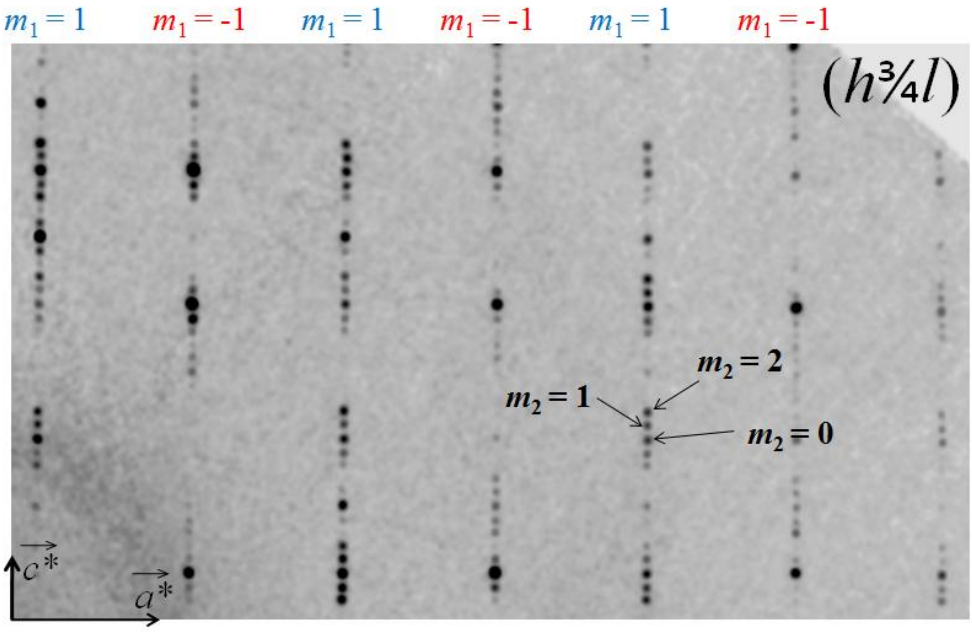

***Figure 5.19**: (h¾l) experimental reciprocal space map of $La_2CoO_{4+\delta}$ with $\delta \sim 0.19$ at 623 K reconstructed from synchrotron X-ray diffraction data (ID11@ESRF), showing only superstructure reflections portraying the commensurate modulation toward c*.*

The systematic extinctions of satellites and their equivalences determined from experimental intensities lead to the same reflection conditions than at RT: ($hklm_1m_2$): $h + k = 2n$, $h + l = 2n$, $k + l = 2n$; and ($hk0m_1m_2$): $m_1 = 2n$. However the propagation vectors are different: $\vec{q}_1$ = (½, ¾, 0) and $\vec{q}_2$ = (0, 0, ¼), consequently, the superspace group can be $F2/m(\alpha_1\beta_10)0s(00\gamma_2)00$. It derivates from the conventional superspace group $B2/m(\alpha_1\beta_10)0s(00\gamma_2)00$ based on a unit-cell with a'= (0, -1, 0), b'= (½, ½, 0) and c'= (0, 0, 1), and with α_1 = ¼, β_1 = ½ and γ_2 = ¼. The twinning effects involving partial overlap of basic reflections, together with complete overlap of satellites with m_1 = 2, make structural refinements difficult.

The transition from HTT to (3+2) COM HTO, driven by simultaneous increase of temperature and oxygen content, raises phenomenological questions about interpretations of the structural transformation. It is clear that re-ordering occurs from the completely disordered HTT phase to very well defined long-range order. It is even surprising to observe simultaneous coming back of such strong and well defined satellites until very high angles. The transition is caused by displacive effects caused by complete re-ordering of the structural arrangement at long-range. The hypothetical dynamic coherency of atomic vibrations would be converted into cooperative small static displacements of atoms from their respective average site, at the origin of long-range ordering.

However, these types of transitions usually happen on cooling and here the long-range ordering occurs on on heating. But the as mentioned before, temperature is not the only criterion: it is accompanied by simultaneous increase of oxygen content in the material.

It is quite conceivable that the incoming of supplementary extra oxygen atoms during the chemical oxidation has an impact of the stability of the structure. At the HTT/HTO transition, a limit is reached for which interstitial atoms become too numerous, and the crystal structure adopts a more stable configuration that necessitate the return of 3D ordering at long range. So, not only the temperature but also the oxygen content δ determines the order/disorder transitions from possible dynamic regime to static arrangement, involving displacive phase transitions in oxygen-enriched $La_2CoO_{4+\delta}$. The softening of a low-energy phonon mode at this transition would be unfortunately hard to measure experimentally by inelastic neutron scattering experiments, because, as already explained, the transitions involving drastic modification of oxygen content give rise to problems with volumic samples necessary for such measurements.

2.2.3. Irreversible transition from (3+2) commensurate HTO to (3+1) incommensurate HTO phase with $\delta \sim 0.2$, at 653 K on heating.

The commensurate phase described in the previous section is not the final state, but can be viewed as intermediate one which undergoes a last structural transformation to incommensurate phase at higher temperature. The transition at 653 K is not reversible and is combined with slight rising up of oxygen content about $\delta + 0.01 \sim 0.20$. The extra-oxygen stoichiometry increases promptly in a short range of temperature (< 10°), and stabilizes above 660 K as testified by the TG curve shown in Figure 5.11. At 653 K, the (3+2) COM HTO phase undergoes a transition to the phase labeled (3+1) INC HTO on the figures, accompanied with strong increase of orthorhombicity from 2Δ = 1.1° to 2.1°. The cell parameters turn to a = 5.50(3) Å, b = 5.57(8) Å, c = 12.70(8) Å. Table 5.6 gives the structural model resulting from refinements of basic reflections only, in average $F4/mmm$ space group.

The typical ($hk1$) reciprocal space map reconstructed from the X-ray diffraction data collected at 673 K is shown on Figure 5.20. Astonishingly the proportion of individual twin components has changed at the transition. When comparing the ($hk1$) plane of the (3+2) COM HTO phase below 653 K (Figure 5.18) with the present one above the transition, the disappearance of the satellites on two domains, pointed out by the red quotes, is significant.

When looking carefully, it is possible to see that just few remaining traces, but with extremely weak intensity. Hence, one set of two twin domains has practically vanished; and here, almost only two twin domains are present in total in the sample, and only a single one is portrayed in blue on the figure. It definitively confirms the presence of only one modulation vector in the $\vec{a}$-$\vec{b}$ plane.

Table 5.6: *Structural model of as grown $La_2CoO_{4+\delta}$ single crystal with δ ~ 0.20 at 673 K, refined only with main reflections collected by synchrotron X-ray diffraction (ID11@ESRF).*

Atom	*x/a*	*y/b*	*z/c*	*Occ*	U_{11}	U_{22}	U_{33}	U_{12}	U_{eq}
La	0	0	0.36031(3)	2	27.4(5)	27.4(5)	19.4(8)	-	24.7(3)
Co	0	0	0	1	19.2(7)	19.2(7)	33.7(5)	-	24.8(3)
O (eq)	¼	¼	0	2	31.(2)	31.(2)	47.(5)	-4.(1)	36.(3)
O (ap1)	0	0	0.179(3)	0.9(9)	53.(8)	53.(8)	27.(6)	-	44.(7)
O (ap2)	0.078(5)	0.078(5)	0.173(1)	1.1(6)	3(1)	-	-	-	3(1)
O (int)	¼	¼	¼	0.20	3(9)	-	-	-	3(9)

Average cell parameters: $a = b = 5.54(1)$ Å and $c = 12.70(8)$ Å, $\alpha = \beta = \gamma = 90°$. V = 390.16(9) Å^3, $2\Delta = 2.1°$.Average structure refined in *F*4/*mmm* on 587 main reflections (143 unique). R_{int} = 4.5 %. Wavelength of X-rays: 0.2072 Å. Agreement factors: R_F = 4.23 %, R_{WF} = 4.05 %. U_{iso} for O(ap2) and O(int). *Uij* are given in 10^{-3} Å^2.

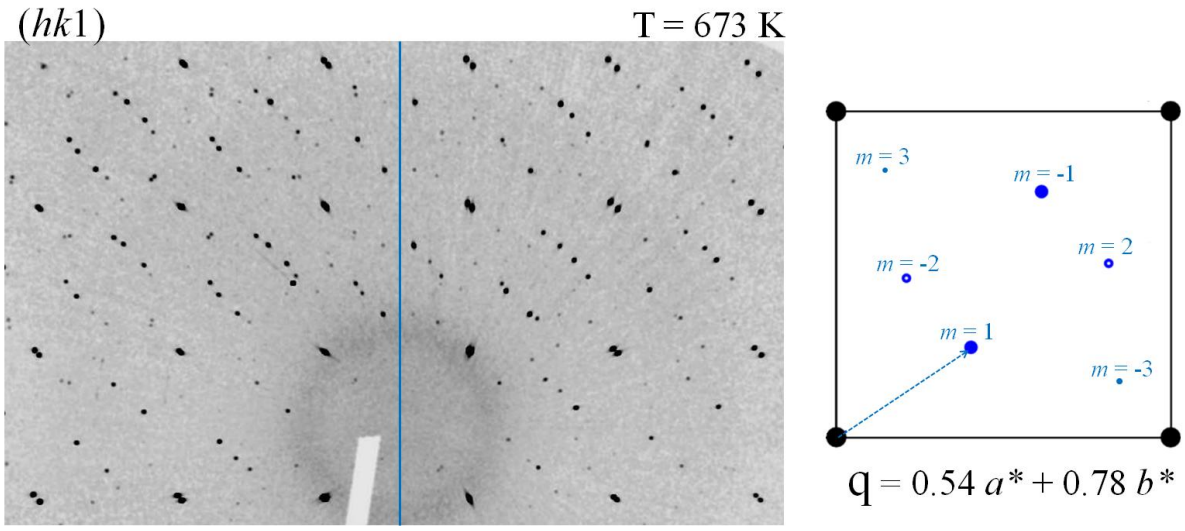

Figure 5.20: *(hk1) reciprocal space map of $La_2CoO_{4+\delta}$ at 723 K reconstructed from X-ray synchrotron diffraction data (ID11@ESRF). The idealized pattern for a single individual is shown on the side with indexation of satellites.*

Figure 5.21 shows the (*h* 0.78 *l*) reciprocal map, which is comparable to the plane of Figure 5.19 for the previous phase, and confirms the presence of only one set of two domains. Only satellites of 1st order are visible, but this time they all belong to the same individual orientation; the absent satellites of the second twin with m_1 = -1 are quoted by red crosses. This plane also shows the disappearance of modulation toward $\vec{c}$*.

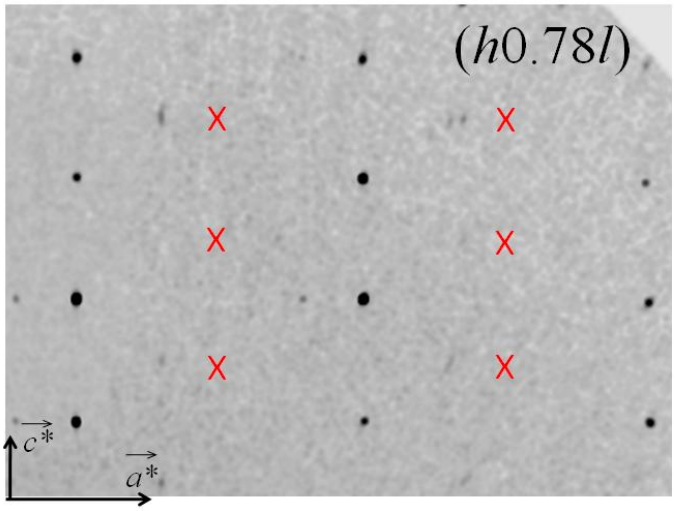

***Figure 5.21**: (1.54 kl) reciprocal space plane of $La_2CoO_{4+\delta}$ with δ ~ 0.2 at 673 K, reconstructed from synchrotron X-ray diffraction data (ID11@ESRF), showing satellites with m = 1 of a single twin individual.*

The systematic extinction conditions of the experimental diffraction pattern are the same than the previous phase and permit to propose a superspace group for the incommensurate symmetry: $F2/m(\alpha\beta0)0s$, which is similar to the intermediate (3+1) INC HTLO phase. Structural refinements have been carried out on data collected from similar phase but with different twinning composition. It is introduced in section 3.2.2 of this chapter.

All together, the structural transformations from 2D commensurate modulation to 1D incommensurate in-plane modulation indicate different arrangements of atomic displacements at long-range in the plane (shift of $\vec{q}_1$) together with a re-ordering of the stacking alternation of layers (vanishing of $\vec{q}_2$). The structural super-ordering has been demonstrated to be strongly correlated to the positions of interstitial atoms, linked to opening or closing of O_{int}-4(O_{ap}) tetrahedral site which locally distort CoO_6 octahedra arrangement provoking tilts, and also distorting rows of Co and La atoms, at the origin of satellites besides main reflections. Since the concentration of O_{int} increases at the transition, oxygen atoms are pushed out from their sites by upcoming of supplementary atoms, involving re-ordering by diffusion in the bulk. Oxygen migration and re-ordering occurs in such manner that the volumes of the twin domains change, and the crystal becomes more homogeneous (disappearance of one set of twinned orientations). What is surprising is that coherency and long-range orders are kept during the transition, as mentioned for the LTO/HTLO transformation. But here it occurs with changing of δ, meaning that increasing of oxygen concentration takes place homogenously in

the crystal. It is fascinating to observe such long-range correlation between atoms separated by more than 5 Å, even when they diffuse through the crystal lattice.

Finally, it remains significant that increasing of oxygen content by topotactic oxidation reaction can occur even in highly ordered phases without loss of structural modulation. Indeed it proves that static arrangements of interstitial atoms do not block their diffusion, but can still provide ionic conduction depending on temperature.

2.2.4. Transition on cooling from (3+1) incommensurate HTO phase to commensurate $La_2CoO_{4.19}$ LTO phase at 610 K.

Once the (3+1) INC HTO phase is reached above 653 K, cooling the temperature systematically lead to transformation into the $La_2CoO_{4.19}$ phase, similar than the one at RT extensively described in chapter 4, with monoclinic supercell space group *B*2/*n*. This phase transition takes place at 610 K, which is lower than the transition temperature on heating, and involves several transformations. First, the decreasing of oxygen content, back to δ = 0.19, occurs as pictured on the Figure 5.22 showing the thermogravimetric profile of the sample on cooling together with the corresponding DTA profile measured simultaneously.

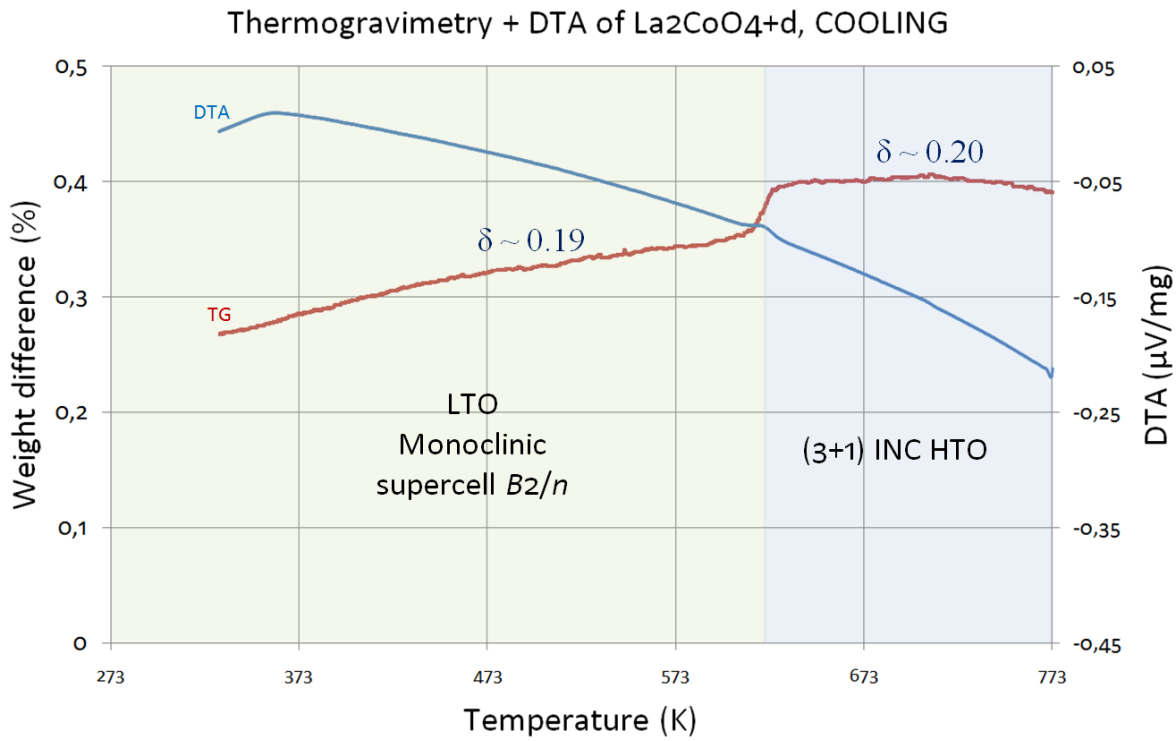

***Figure 5.22**: TG + DTA profile of $La_2CoO_{4+\delta}$ on cooling from 773 K to RT (LDM@PSI).*

The step in the mass difference's curve is visible at the transition together with the small exothermic peak of the DTA profile at ~ 610 K. It seems that oxygen content does not remain stable after the transition, but instead continues decreasing linearly with temperature. The values of δ are approximated and the small deviation of the TG curve from 573 K to RT only involve oxygen content modification of $\Delta\delta$ ~ 0.005, which is very weak, and thus will be neglected. The calculated value of δ = 0.19 is averaged in the range 573 K – RT.

Concerning the basic unit-cell, orthorhombicity decreases back to an angular separation of 2Δ = 1.2° for (*hhl*) reflections, with basic cell-parameters of a = 5.49(4) Å, b = 5.51(3), c = 12.61(2) Å. The incommensurate superlattice reflections lock in commensurate positions, *i.e.* with variation of propagation vector from α = 0.54 and β = 0.78 above the transition, to α = ½ and β = ¾ below the transition. In addition to the 'lock in' of $\vec{q}_1$, additional modulation along $\vec{c}$* re-appears, with $\vec{q}_2$ = ¼. Systematic extinctions related to the superstructure reflections correspond to the commensurate monoclinic supercell *B*2/*n* of volume 6071 Å^3, which remains stable until cooling to ambient temperature.

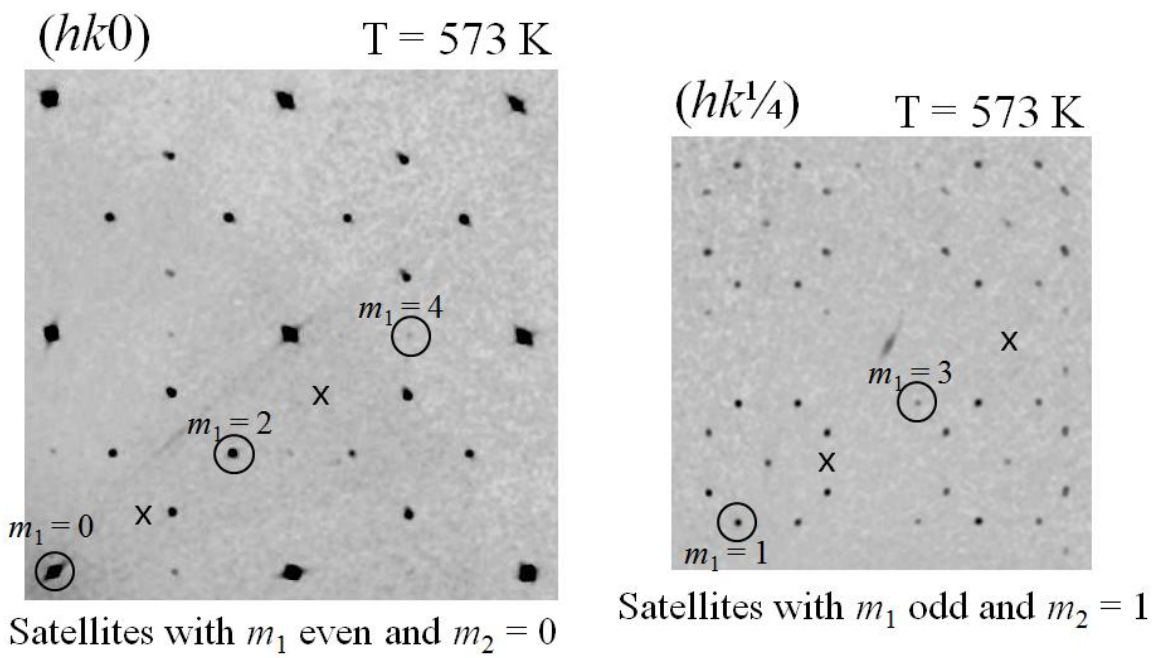

***Figure 5.23**: Reciprocal space maps of $La_2CoO_{4.19}$ at 573 K on cooling from 773 K, reconstructed from synchrotron diffraction experiments (ID11@ESRF). The reflection conditions are consistent with the monoclinic supercell, space group B2/n, corresponding to the structure of $La_2CoO_{4.19}$ at RT described in chapter 4.*

The phase transition implies a homogeneous re-ordering process involved by the departure of oxygen atoms from the crystal to the external medium. When considering the extra oxygen content and the propagation vectors, the transition seems to be reversible. However, the reflection conditions deduced from experimental reciprocal space maps are different between the intermediate (3+2) COM HTO phase and the present one reached on cooling. Therefore, their respective space groups are not the same and thus their structures are different. Consequently, the transition between commensurate and incommensurate states at high temperature is not reversible when the starting sample is (3+2) INC LTO phase, *i.e.* $La_2CoO_{4.14}$ *as grown*.

2.2.5. Global thermal evolution of significant parameters, from RT to 773 K.

Globally, the evolution of the *as grown* sample from RT to 773 K under air involves various phase transitions of different kinds between distinct phases having complex local structures. It is astonishing to observe so many unexpected structural transformations in this rather short range of temperature. Indeed, the scenario is now much more complicated than the simple LTO/HTT transition undergone by stoichiometric samples. The presence of interstitial oxygen atoms modifies drastically the thermal evolution of the $La_2CoO_{4+\delta}$ compound. We can see that the phase diagram T vs. δ involves several structural transformations through many stable states that must be very close in energy, like what has been proposed for parent compounds by S Stolen *et al.*[238,239]. These studies suggested that the possibility of many different oxygen orderings associated with a variety of low-energy connectivity schemes within tetrahedral layers such as in the Brownmillerite-type structures of $Sr_2Fe_2O_5$ and $Ba_2In_2O_5$ is a prerequisite for high ionic conductivity in perovskite-related oxides.

Orthorhombicity

The orthorhombicity of the $\vec{a}$-$\vec{b}$ plane is a very convenient criterion for distinguishing easily the different phases. Figure 5.24 shows the temperature dependence of the angular separation between the split (*hhl*) peaks of twinned samples, measurable by simple ω-scan when the crystal sample has the *c*-axis perpendicular to the diffraction plane. It is directly linked to evolution of orthorhombicity by the equation 3 (chapter 3). A tendency curve has been superimposed on the discrete spots corresponding to experimental values, but a step-like evolution is conceivable too. The re-appearance of orthorhombicity at 580 K is triggered by the extra oxygen content δ, while the O/T transition at 433 K occurs for constant δ.

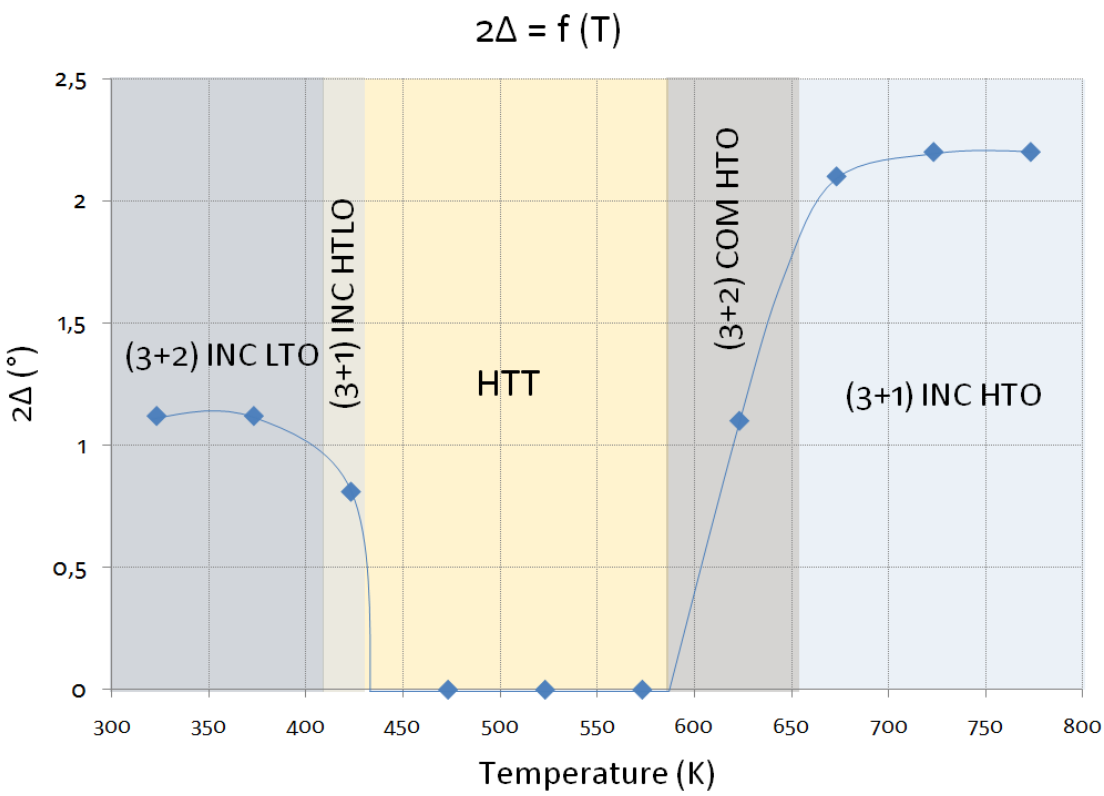

***Figure 5.24**: Evolution of angular separation of (hhl) reflection on heating, which is directly proportional to evolution of orthorhombicity.*

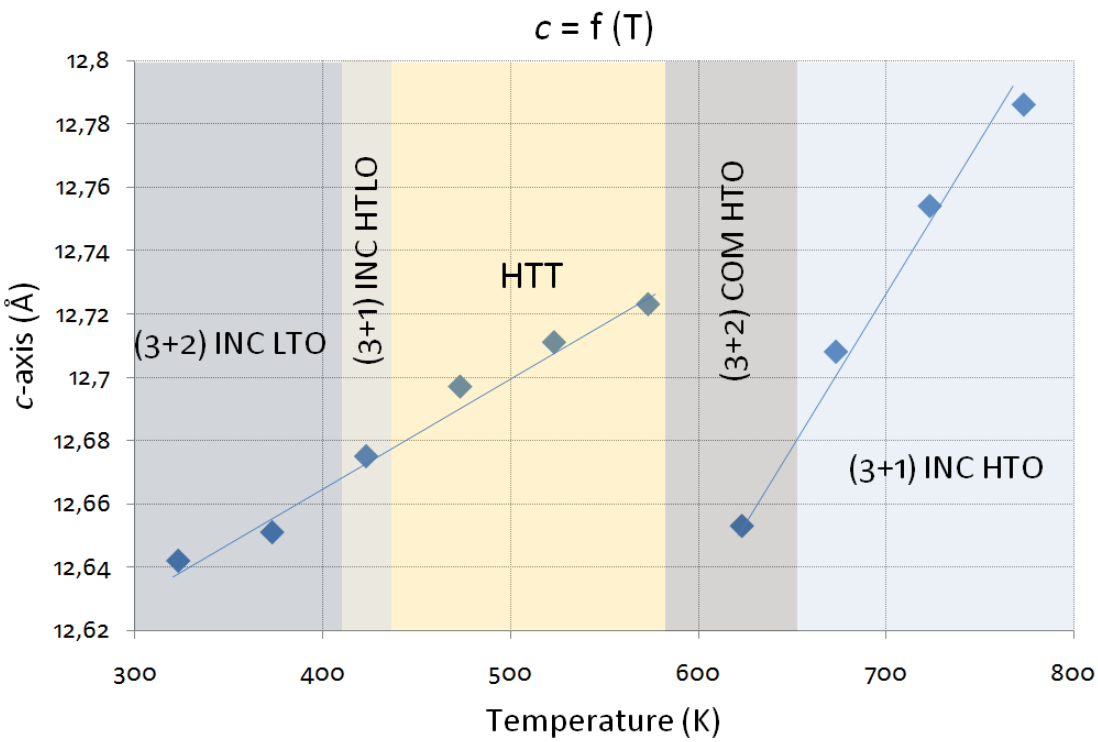

***Figure 5.25**: Evolution of c-parameter on heating.*

The c-parameter, lattice instabilities

Similarly to the variations of *a*- and *b*-parameters, the *c*-parameter exhibits a singular temperature dependence, displayed by the Figure 5.25. The *c*-parameter increases approximately linearly between RT and 580 K (~ 3.2×10^{-4} Å/K), *i.e.* during the first two structural transformations undergone by $La_2CoO_{4.14}$. It suddenly decreases at the HTT/HTO transition. Then, in the high temperature regime, *c*-parameter increases again, however with a more pronounced slope than in the low temperature regime (~ 8.8×10^{-4} Å/K).

When heating, atomic displacement factors are amplified by thermal motion yielding elongation of interatomic bond distances, which cumulated, increase the volume of the unit-cell. The continuous expansion of *c*-axis stretches interlayer distances and relaxes strains, which directly influences rotation of CoO_6 octahedra. At the LTO/HTLO transition (413 K), the tilts toward [±100]-type direction vanishes while the diagonal tilt along [±1±10]-type directions are kept. At the HTLO/HTT transition (433 K), Co-O_{ap} and La-O_{ap} bond distances get broad enough to place apical oxygen atoms in a situation where they are able to fluctuate between different sites with a shallow potential of energy surface[18,219]; *i.e.* large distortions are possible with very small expenditure of energy. Therefore, anisotropic motions of O_{ap} is activated, consisting of positional switching. Comparing *c*-axis evolution with the TG profile (Figures 5.11 and 5.25) demonstrates that the rate of oxygen absorption is proportional to the value of *c*-parameter for the HTT phase. At the HTT/HTO transition (580 K), the extra oxygen content δ reaches a limit of concentration, the c-axis shrinks which compresses layers yielding reappearance of static modulation. The discontinuous evolution of *c*-axis at the transition, corresponding to a decrease of volume from 386.27 $Å^3$ to 383.17 $Å^3$, denotes the 1st order character of the transition[240]. Above 580 K, the apical oxygen atoms are forced to stay on one specific site because of the coming back of energetic differentiation between (0, 0, *z*) and (*x*, *x*, *z*) sites. This transition involves an inverse process than the HTLO/HTT transformation.

Finally the (3+2) COM to (3+1) INC transition (653 K) involves homogeneous re-ordering at long range depicted by the shift of the in-plane propagation vector together with vanishing of modulation toward *c*-axis, implied by disappearance of $\vec{q}_2$. All the phase transitions observed on heating seem to be ruled by the degrees of freedom of apical sites. One neutron inelastic scattering study concerning $La_{2-x}Sr_xCuO_4$ has been reported by Kimura *et al.*[227] where it is very well explained how the activation of different modes of octahedra tilting triggers the structural transformations in the parent compound.

Propagation vectors

The evolution of the propagation vectors' coefficients are plotted on Figure 4.26 (lozenges for the in-plane modulation vector $\vec{q}_1$ and triangles for the modulation toward c*-axis $\vec{q}_2$), depicting the transitions undergone by the modulation with temperature. While α_1 and β_1 show an inverse evolution below 433K, they follow the same tendency above 580 K. A rule can be sorted from the comparison between the temperature dependence of orthorhombicity and the one of propagation vectors: the smaller the angle is between the modulation vector and the b-axis, the higher is the orthorhombicity (this hypothesis is in agreement with the stoichiometric phase for which $\delta = 0$, $\vec{\boldsymbol{q}} \,//\, \vec{\boldsymbol{b}}$ and $2\Delta = 3°$ is the maximum value).

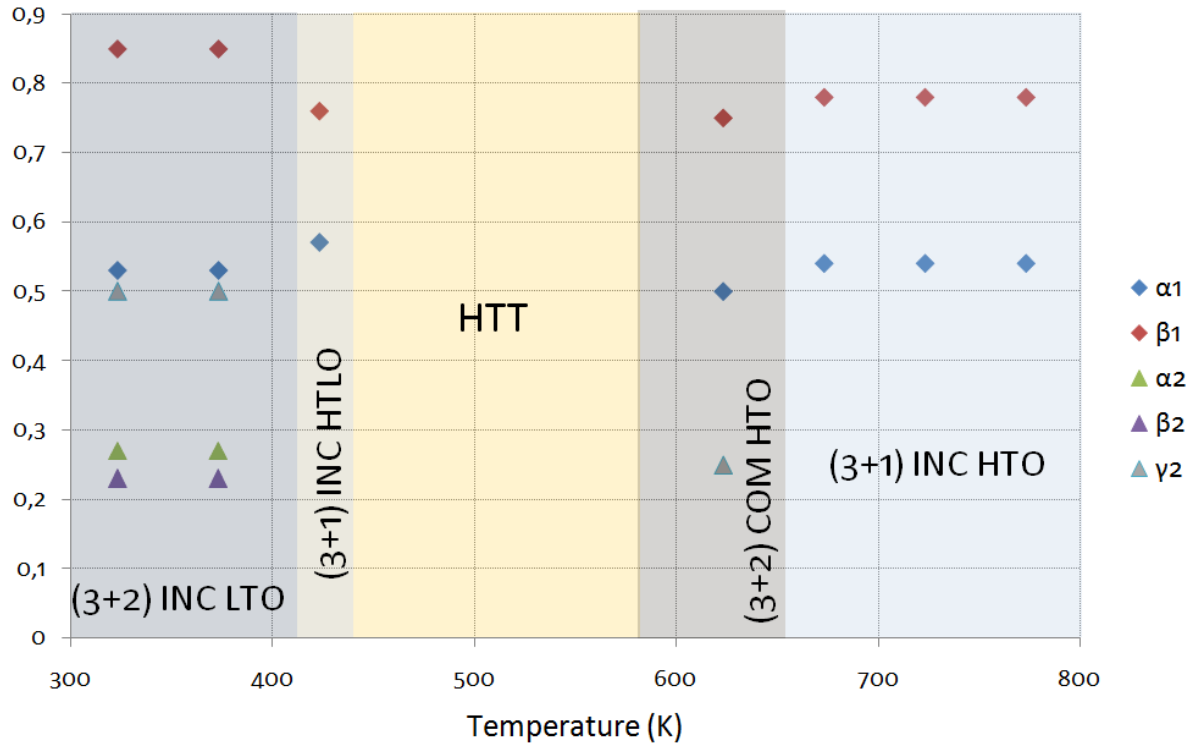

***Figure 4.26**: Evolution of modulation components with temperature.*

Except the (3+2) INC LTO phase obtained *as grown*, the two other incommensurate phases of $La_2CoO_{4+\delta}$ are not modulated toward $\vec{c}$*. The *as grown* phase can be seen as an exception, since it is frequent to get unusual states directly after crystal growth[241,184]; indeed, post-treatments are generally performed on *as grown* crystal samples in order to improve the crystallinity and perfection of crystals before scattering experiments.

Diffuse scattering

In addition to the structural transformations evidenced by the evolution of superlattice reflections' pattern, linear diffuse scattering is observable between (*hh*6) and (*hh*8) main reflections, and is also submitted to variations with temperature. The diffuse scattering is present for every phase. Figure 4.27 displays zooms on experimental (*h*0*l*) planes reconstructed pixel by pixel with $\vec{c}$* vertical in the plane, showing the stripes between the two main reflections (006) and (008) which exhibit the strongest diffuse intensity. The streaks are structured into 5 distinguishable maxima and are very similar for the four modulated phases, even if the intensity for the (3+1) INC HTO phase is lower; which might be due to the higher temperature. For the HTT phase, the stripes are less structured, more diffused. At first sight it seems to form a continuous line between (006) and (008) main reflections, but when looking carefully, one can see that it is constituted of a large amount of peaks which are very close and are at the limit of the distinction. Once more, the HTT phase exhibits a particular behavior with respect to the other states. As explained in the section 3.3 of chapter 4, the (006) and (008) planes, in direct space, cut the unit-cell in a way that the La site is taken in sandwich between them (for instance, for La atoms with $z/c \sim 0.14$, $1/6 < 0.14 < 1/8$). Consequently, the diffuse scattering could be due to in-plane disorder of La site (the linear diffuse scattering being theoretically perpendicular to the direction of atomic displacements responsible of disorder[195]).

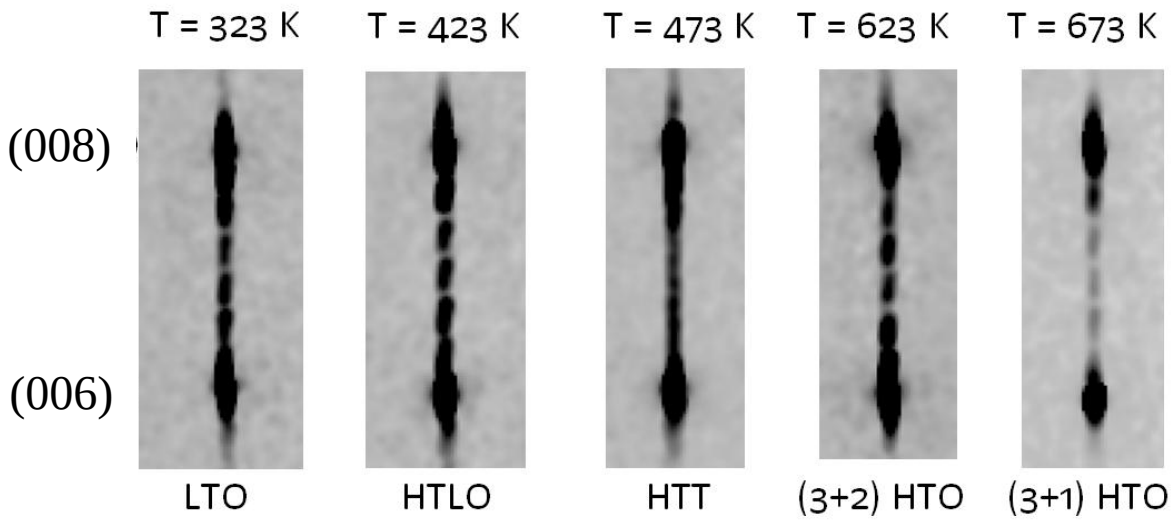

***Figure 4.27**: Evolution of diffuse scattering between (006) and (008) main reflections depending on temperature, reconstructed from synchrotron X-ray diffraction data (ID11@ESRF).*

First tentative of inelastic neutron scattering measurements

Inelastic neutron scattering experiments have been carried out at the IN12 beamline at ILL (Institut Laue Langevin, Grenoble, France). This beamline uses cold neutrons and provides detection of phonons of low energies. The highest energy reachable was 9 meV, k_i was fixed at 1.4 meV while k_f was varying. A germanium filter cooled at 10 K was used to cut harmonics of the incoming neutron beam and thus permitted to avoid any spurion in the experimental signal. Since no theoretical calculations of phonon dispersion curves have ever been performed for $La_2CoO_{4+\delta}$, location of soft modes in the Brillouin zone was unknown.

We probed several characteristic points, in particular the *X*-point which is famous for being the position were phonon modes, corresponding to octahedra tilting, soften at the HTT-LTO transition in La_2NiO_4[85] and La_2CuO_4[86]. However we could not detect any peak for this *X*-point. It might be that the range of energy available with the spectrometer was not wide enough for detecting the phonons. But it is more conceivable that the presence of oxygen atoms on interstitial sites modifies the dynamics of the crystal lattice and thus the locations of soft modes in the Brillouin zones for $\delta \neq 0$. For instance the specific low energy phonon mode that soften in La_2NiO_4 and La_2CuO_4 involve dynamic tilts of octahedra toward [100]-type direction while for the oxygen rich $La_2CoO_{4+\delta}$ the tilts toward [110]-type direction are prominent. Furthermore, the incommensurate character of the propagation vector in $La_2CoO_{4.14}$ below the transition also suggests that the softening do not occur exactly at the boundary of the zone.

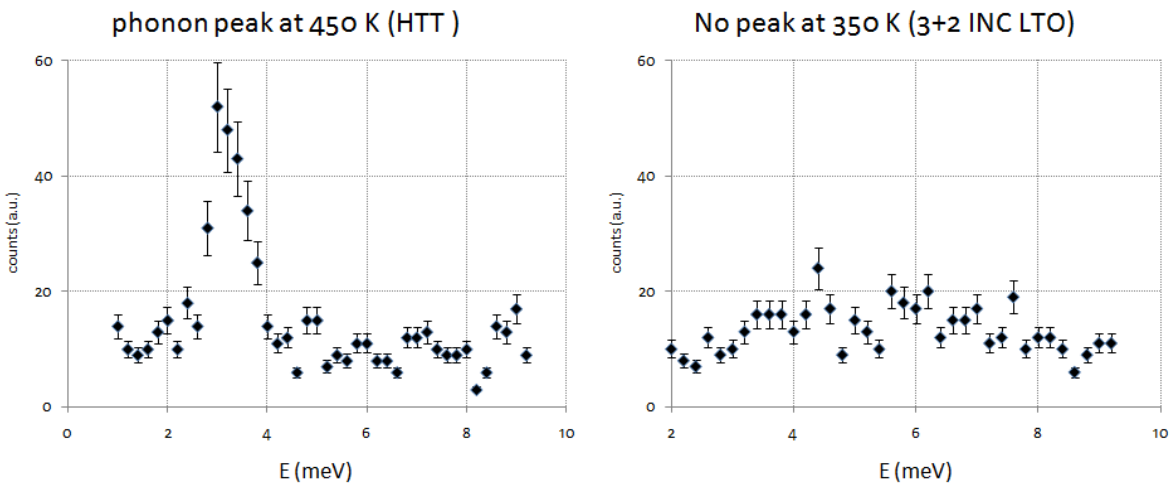

***Figure 4.28**: Inelastic neutron scattering experiments (IN12@ILL) showing the presence of soft-phonon (3meV) at q = (1.1, 1, 0) in $La_2CoO_{4.14}$ at 450 K, while no peak is detected at 350 K in the same conditions. k_i fixed at 1.4 meV, 1.56 < k_f <2.52 meV.*

The energy of the *X*-point has been followed each 2 K during the transition, *i.e.* from 450 K to 400 K. If a specific mode would have softened, even very fast, it would have been at least detected once, since the phonon must pass by low energies. But the signal remained flat for all temperature. However, after performing measurements at several points of the Brillouin zone, a signal was detected at 3 meV above 450 K at q_h = 1.1, q_k = 1 q_l =0. This peak of low energy was not anymore present at 350 K (*cf.* Figure 4.28). Unfortunately we could not follow this changing in details because of the lack of time. Anyway, without primary theoretical simulations it is impossible to attribute any specific eigenvector corresponding to the mode we observed. Inelastic neutron scattering experiments demand long durations and necessitate a lot of work. Further investigations of phonons activation/deactivation in $La_2CoO_{4+\delta}$, not only experimentally but also theoretically would obviously bare key information with regards to the crystal chemistry of this compound. It could definitively validate a Brownmillerite-like phonon-assisted oxygen diffusion process[18] in Ruddlesden-Popper phases.

Important outcome

At this stage of the results, one crucial point must be underlined concerning the phenomenological approach of oxygen diffusion in $La_2MO_{4+\delta}$ compounds. Indeed, here we necessitate a new vision of the basic disordered ionic conduction with regards to the classical migration mechanism activated thermally by following the Arrhenius law. The latter involves activation of fast ionic diffusion at higher temperatures than what is observed in $La_2CoO_{4+\delta}$ and thus do not provide satisfactory explanations of oxygen mobility at moderate temperatures in the Ruddlesden-Popper phases. Furthermore, the common concept of ionic diffusion depicts the phenomena in terms of random push-pull mechanism implying faster diffusion for higher structural disorders. However, in the present study, we clearly demonstrate that ordering plays a prominent role in the phase transitions undergone by oxygen-rich $La_2CoO_{4+\delta}$ phases. These phases are strongly modulated (at least) up to 773 K. Disorder is apparent, but long-range ordering is so extended that, for instance, modeling the real structure of $La_2CoO_{4.19}$ at RT necessitates a unit-cell of 6047.2 $Å^3$, which is 16 times bigger than the basic LTO unit-cell (V = 377.4 $Å^3$). In addition, phase transitions involving exchanges of oxygen with external medium occur between modulated states, involving homogeneous structural re-ordering by anisotropic in-plane diffusion, which is far away from random diffusion and statistic distribution of atoms. The concept of displacive phase

transitions employed to portray structural transformations between disordered states and modulated phases explains the remaining of strong coherency between atomic positions. Therefore, atomic ordering does not anymore break the diffusion but even becomes compulsory for stabilization of the structure.

***Table 5.7**: Summary of the structural evolution of as grown starting $La_2CoO_{4+\delta}$ sample as function of T.*

$La_2CoO_{4+\delta}$		Average cell *F*4/*mmm*					Modulation			
T (K)	δ	T (K)	*a* (Å)	*c* (Å)	V (Å^3)	2*Δ* (°)	Type	$\vec{a}^*$-$\vec{b}^*$ plane	Toward $\vec{c}^*$	Symmetry
323-413	0.14	323	5.508(4)	12.64(9)	383.74(6)	1.12	(3+2) INC	0.53 $\vec{a}^*$ + 0.85 $\vec{b}^*$	0.27 $\vec{a}^*$ - 0.23 $\vec{b}^*$ + ½ $\vec{c}^*$ (only 1st order)	Monoclinic $F2/m(\alpha_2\beta_2½)00(\alpha_1\beta_1 0)0s$ $\alpha_1 = 0.53$, $\beta_1 = 0.85$ $\alpha_2 = 0.27$, $\beta_2 = -0.23$
413-433	0.14	423	5.50(5)	12.675(4)	384.11(5)	0.81	(3+1) INC	0.57 $\vec{a}^*$ + 0.76 $\vec{b}^*$	X	Monoclinic $F2/m(\alpha\beta 0)0s$ $\alpha_1 = 0.57$, $\beta_1 = 0.76$
433-580	0.14 → 0.19	453	5.510(1)	12.697(3)	385.49(8)	0	X	X	X	X
580-653	~0.19	623	5.50(3)	12.65(3)	383.17(1)	1.2	(3+2) COM	½ $\vec{a}^*$ + ¾ $\vec{b}^*$	¼ $\vec{c}^*$	Monoclinic $F2/m(\alpha_1\beta_1 0)0s(00\gamma_2)00$ $\alpha_1 = ½$, $\beta_1 = ¾$, $\gamma_2 = ¼$
> 653	~0.2	723	5.54(1)	12.70(8)	390.16(9)	2.1	(3+1) INC	0.54 $\vec{a}^*$ + 0.78 $\vec{b}^*$	X	Monoclinic $F2/m(\alpha\beta 0)0s$ $\alpha_1 = 0.54$, $\beta_1 = 0.78$
Cooling 610 K → RT	~0.19	323	5.47(4)	12.59(7)	376.70(8)	0.72	3D COM	½ $\vec{a}^*$ + ¾ $\vec{b}^*$ ½ $\vec{a}^*$ - ¾ $\vec{b}^*$	¼ $\vec{c}^*$	Monoclinic (2*a* 2*b*-*a* 4*c*) *B*2/*n*

The coefficients of the modulation vectors are given by taking orthorhombicity in account, i.e. with respect to the cell parameters of the Fmmm basic cell.

3. Successive phase transitions in the oxygen-rich $La_2CoO_{4.25}$

Even if the compound with $La_2CoO_{4.25}$ stoichiometry has already been mentioned in the literature[10,9,12], its atomic structure has never been reported in peer reviews. The work of R. Le Toquin[8] on this compound was the first to really enter in details. He has notably highlight an antiferromagnetic phase transition at low temperature (T_N = 35 K). However, ambiguities were remaining about the real unit-cell and subsequently about the real atomic positions.

Besides, the structural evolution on heating has never been investigated. In Chapter 4 (section 4) we clarified the real structure of this compound at RT, from synchrotron X-ray diffraction experiments; here, we present in one hand complementary results on magnetic structure at low temperature, and on the other hand the structural evolution in the range of RT-800 K, which is accompanied with variations of δ.

3.1. Magnetic structure at low temperature

Neutron Laue diffraction experiments have been carried out on a single crystal of $La_2CoO_{4.25}$ obtained through electrochemistry by R. Le Toquin, with the instrument Vivaldi (Very-Intense Vertical-Axis Laue Diffractometer) at ILL (Grenoble), using a polychromatic beam with λ_{min} = 0.78 Å, λ_{max} = 3.5 Å. The diffraction data were collected by a cylindrical image-plate detector (360°), with a step of 10 K from RT to 50 K and then with a step of 1 K from 50 K to 10 K. The time of exposure was of 900 seconds for each temperature. The Laue diffraction patterns were treated *via LaueGen* program, version 6.0, of the CCP4 suite.

At low temperature, the rising of peaks has been observed at low angles only, suggesting they are of magnetic origin (*cf.* Figure 5.29). Few reflections of this type have been followed versus temperature, their intensity is plotted on Figure 5.30 where we can see that the temperature of transition is around 36 K, as expected[8]. Above 36 K, 100 % of intense reflections can be indexed with the *F*-centered orthorhombic unit-cell, *a* = 5.50 Å, *b* = 5.52 Å and *c* = 12.55 Å. However, below 36 K, indexation of the upcoming magnetic peaks necessitates a Primitive unit-cell 2*a*, 2*b*, 2*c*. Therefore, the magnetic correlations are not only lying in the $\vec{a}$-$\vec{b}$ plane but orders of spins also occur perpendicularly to the layers. The magnetic supercell we have found for $La_2CoO_{4.25}$ is similar to the one previously reported by I.A. Zaliznyak *et al.*[242] for the Sr-doped compound $La_{1.5}Sr_{0.5}CoO_4$ below 30 K. These two systems are very close. Indeed, when δ = 0.25 or if ¼ of La atoms are substituted by Sr, the

valence state of cobalt ions is partially modified the same way: half of them have the +II valence state, in high spin configuration (S = 3/2) and the other half are +III, in low spin configuration (S = 0). Such specific ratio is supposed to be responsible for commensurate arrangement of charge and spins on the cobalt ions at low temperature. Because of the twinning effects which divide the reflections in several spots, no satisfactory intensity integration has been obtained, and thus the magnetic structure unfortunately remains unknown.

It would be interesting to investigate the phenomenological aspects of this magnetic transition. Indeed, it could be due to a freezing of spins only, while the charge would already be ordered at higher temperatures, as for $La_{1.5}Sr_{0.5}CoO_4$[242]. Since the Co-O bond lengths depend on the valence of cobalt, charge ordering directly imply ordering of bond distances. That could be a hint for taking into account possible correlations between mixed valence state and atomic ordering.

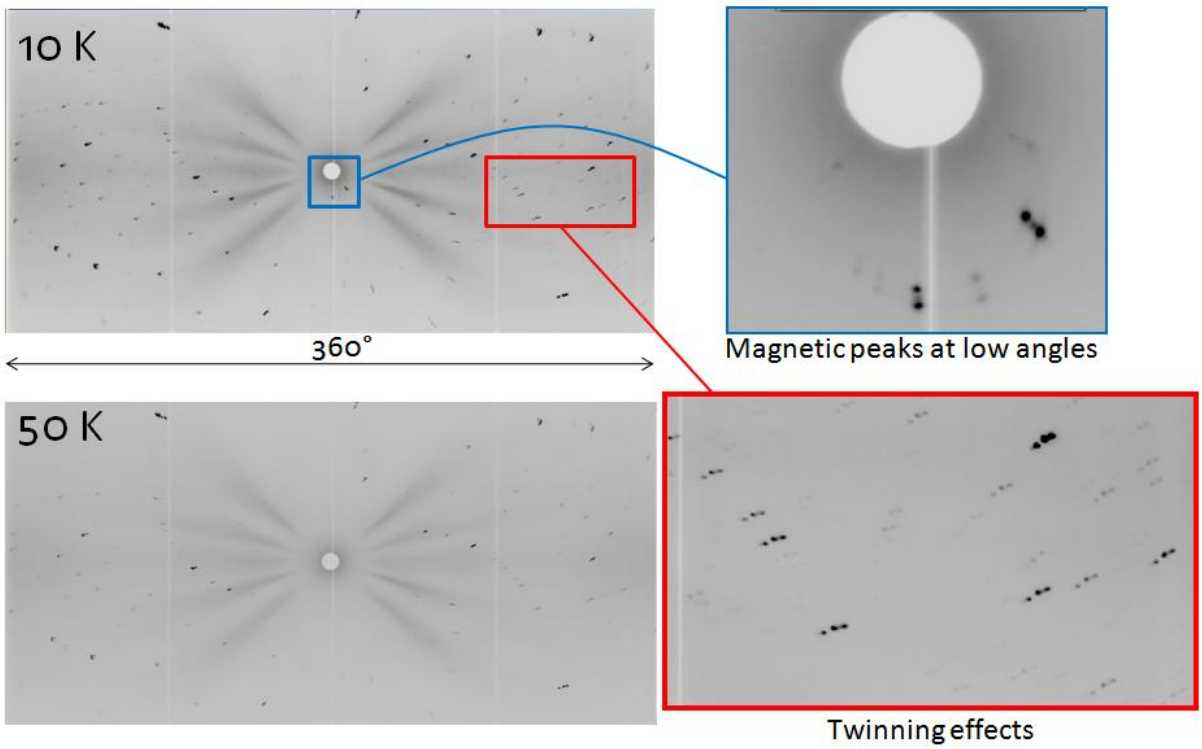

***Figure 5.29**: Experimental neutron Laue diffraction pattern of $La_2CoO_{4.25}$ collected with a cylindrical image plate detector on Vivaldi@ILL. Magnetic reflections are present on the pictures below 36 K.*

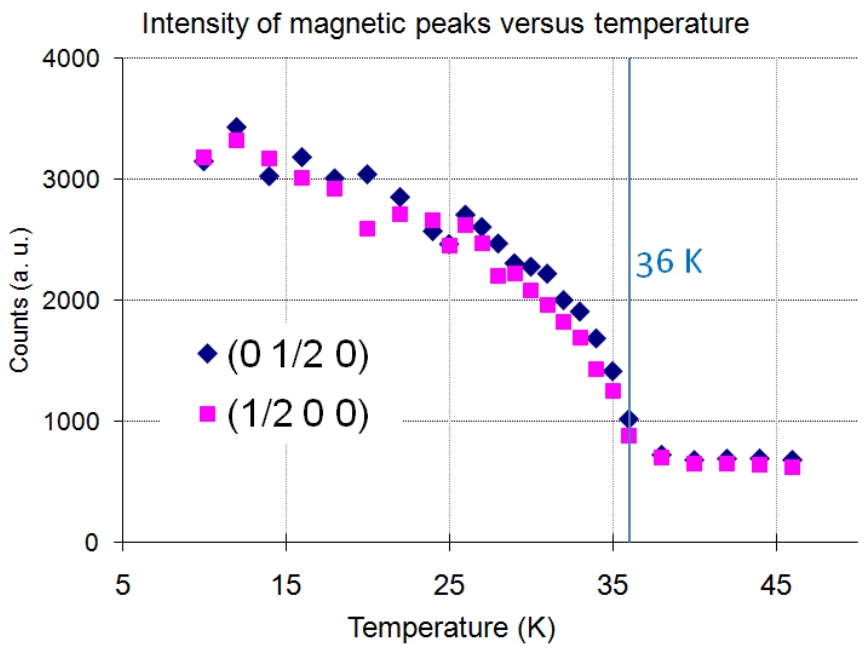

***Figure 5.30**: Temperature dependence of two magnetic reflections, showing arising of spin ordering at 36 K on cooling in $La_2CoO_{4.25}$ (Vivaldi@ILL).*

3.2. Structural evolution in the range of RT-800 K

3.2.1. *Experimental procedure and thermogravimetry*

A small piece of $La_2CoO_{4.14}$ single crystal has been finely grinded, oxidized thermally until the stoichiometry of δ = 0.25 ± 0.01 (according to results of thermogravimetric reduction under He/H_2). Then the $La_2CoO_{4.25}$ powder has been used as starting sample for further thermogravimetric experiments. The measurements have been performed with a NETZSCH thermobalance from RT to 800 K with a speed of 5 K/min, under mixed gas flow He/O_2 with the same proportion and partial pressure of oxygen than in atmospheric conditions. The values of δ have been calculated according to the loss of weight and assuming that variation of oxygen concentration in the sample is the only cause of mass changing. Figure 5.31 displays the resulting TG profile superimposed with coloured area representing the three distinct phases, stable in their respective range of temperature, characterized by single crystal synchrotron X-ray diffraction experiments. A full data collection has been done during isothermal steps each 50 K from RT to 773 K. Reciprocal space plane reconstructions together with structural refinements allowed to distinguish two phase transitions between three different phases in this range of temperature.

On contrary to what has been observed for the *as grown* compound (δ = 0.14) with temperature, the super-oxygenated $La_2CoO_{4.25}$ loses weight on heating. Above 400 K the concentration of extra-oxygen atoms decreases and reaches the value of δ = 0.19 at ~ 550 K. Consequently the structure transits to $La_2CoO_{4.19}$ stoichiometry, and adopts the *B*2/*n* space group with the unit-cell (2*a*, 2*b*-*a*, 4*c*). A second phase transition has been detected at higher temperature: at 623 K, the sample has transited to the (3+1) INC HTO state, similar to the one obtained by heating the *as grown* sample (δ = 0.14) above 650 K.

Astonishingly, the $La_2CoO_{4.25}$ compound does not go through the HTT phase on heating, but the atomic structure remains modulated until (at least) 773 K.

On cooling, the crystal sample transits back to $La_2CoO_{4.19}$ stoichiometry of monoclinic supercell, space group *B*2/*n*, which appears to be the common final state, reached after thermal treatments under air whatever the starting content of extra-oxygen atoms is.

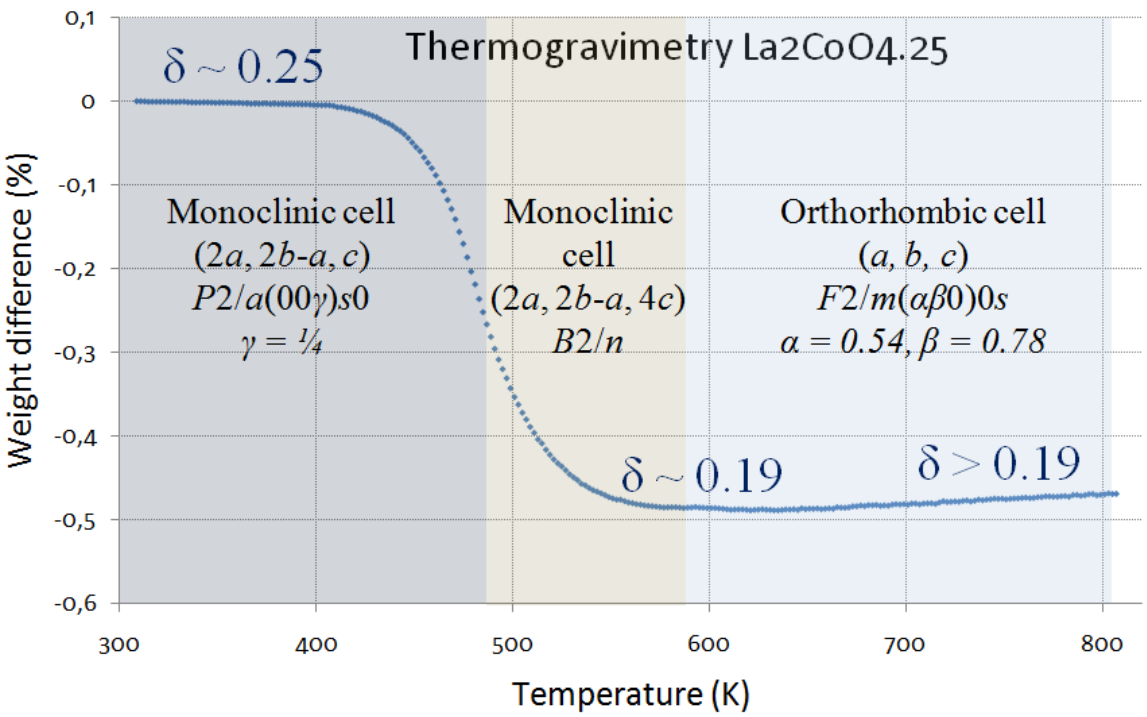

***Figure 5.31**: Thermogravimetric profile (LDM@PSI) of $La_2CoO_{4.25}$ starting sample showing a loss of weight interpreted as a decrease of extra-oxygen concentration in the material.*

3.2.2. Transition from $La_2CoO_{4.25}$ to $La_2CoO_{4.19}$ around 480 K

The first phase transition from $La_2CoO_{4.25}$ to $La_2CoO_{4.19}$, taking place around 480 K, does not alter the size of the supercell but involves a re-ordering of the interstitial oxygen atoms.

Subsequently the rest of the crystal structure is modified. Such transformations between the two commensurately modulated structures with variation of oxygen concentration necessitate large displacements of interstitial atoms. So in addition to the displacive transition undergone by the structure, the increase of interstitial oxygen concentration implies a concomitant reconstructive character. Experimentally, the decrease of oxygen content from δ = 0.25 to δ = 0.19, corresponding to the release of 1.63×10^{-5}mol of oxygen (starting mass m = 52.3 mg, loss of weight of 0.5 %), is completed in about 30 minutes. This is rather fast for such topotactic reduction of the crystal, and it highlights once more the structural flexibility of the crystal lattice which is able to distort in various ways allowing different extra-oxygen contents.

Indeed, according to the structural refinements carried out for the two compounds (*cf.* chapter 4), the transition provokes not only a variation of the repartition of interstitial oxygen atoms in the interlayers but also re-arrangement of octahedra tilts. More precisely, their arrangement passes from a configuration where the rotation axis of octahedra alternates between layers for δ = 0.25 (consecutively between $[\pm110]_F$ and $[1\pm10]_F$) to a configuration where the two axes of rotation coexist in every layers for δ = 0.19. Moreover, the positions found by structural refinements for interstitial oxygen atoms in $La_2CoO_{4.19}$ (chapter 4, section 5.3) indicate an alternation of extra-oxygen concentration between consecutive interlayers. If the refinements presented in chapter 4 are exact, the interstitial atoms are distributed in the crystal structure of $La_2CoO_{4.19}$ in a way that two types of interlayers are stacked toward *c*-axis in alternating sequence of 'oxygen-poor' and 'oxygen-rich' interlayers with a ratio of oxygen content between them equal to (1:2). The oxygen-rich interlayers possess the same amount of interstitial oxygen atoms than all interlayers for δ = 0.25. So, the decrease of δ at the transition can be imputed to the release of extra-oxygen atoms to the external medium selectively by half of the interlayers: the ones which become oxygen-poor. While the oxygen concentration of oxygen-poor interlayers decreases at the transition, the oxygen-rich interlayers undergo internal re-ordering, yielding the opening of adequate tetrahedral interstitial sites which stabilize the *B*2/*n* symmetry of the monoclinic supercell.

One synchrotron X-ray diffraction dataset has been collected at 473 K, for which the content of extra-oxygen has already started to decrease according to the TG profile (*cf.* Figure 5.31). The reciprocal space reconstructions of the $\vec{a}$*-$\vec{b}$* planes remain identical to the one at RT. Conversely, new superlattice reflections appear toward $\vec{c}$*, pointed out by blue arrows on Figure 5.32, with a slight component toward $\vec{b}$*. These incommensurate superlattice points are not observed below the transition and they completely disappear above the transition.

They reveal an intermediate ordering occurring during the topotactic reduction. In addition to this, below the transition superstructure reflections with m_2 = 0 are more intense than ones with m_2 = 1, whereas it is the contrary above the transition. Those variations of modulation toward $\vec{c}*$ are directly connected to re-ordering of layers. In a sense, the reduction of $La_2CoO_{4+\delta}$ from δ = 0.25 to 0.19 oblige the structure to pass through an intermediate phase with different symmetry. Hence the transition is not direct but long-range ordering remains. Again, the diffusion of interstitial atoms does not break the supersymmetries, involves continuous re-ordering.

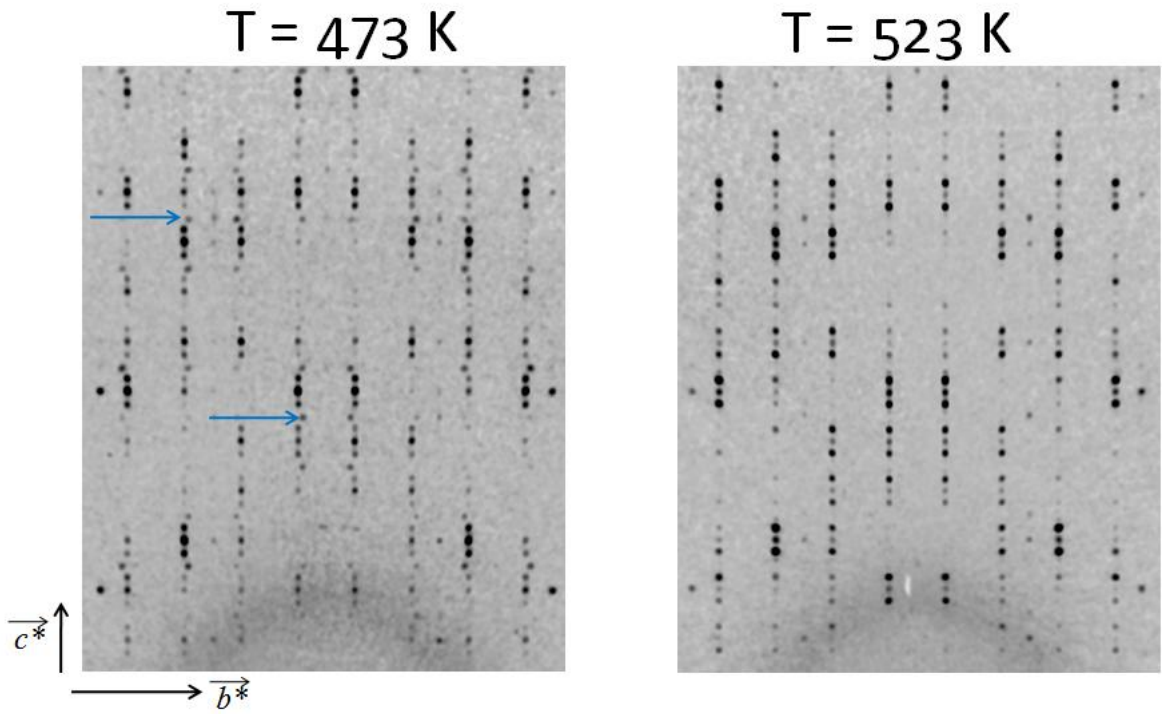

Figure 5.32*: Reciprocal space maps reconstructed from synchrotron X-ray diffraction data (ID11@ESRF) of oxygen rich $La_2CoO_{4+\delta}$ at two different temperatures. The commensurate superlattice reflections toward $\vec{c}*$ depict different symmetries between layers.*

3.2.3. First tentative of structural refinements of the (3+1) INC HTO phase via superspace approach.

Structural refinements in superspace

Above 600 K, the compound transits to the so-called (3+1) INC HTO phase, with orthorhombic basic unit-cell modulated in the plane by the propagation vector $\vec{q}_1$ = (0.54, 0.78, 0). The reader can refer to the section 2.2.3 of the present chapter for further details concerning this phase. Here, complementary results are presented, consisting in tentative of refinements of the incommensurate structure *via* superspace approach using *JANA2006*[206]

software. Indeed, the basic structure of the current sample was not twinned at 773 K, and thus a full experimental dataset of (*hklm*) intensities could have been integrated for a single domain until |*m*| = 3. Therefore, no average symmetries had to be considered, and the superspace group could have been tested. After averaging the experimental reflections with the superspace group $F2/m(\alpha\beta0)0s$, the internal error R_{int} = 4.6 %, which is an acceptable value (it corresponds to the difference of intensity between all reflections equivalent by the superspace group). The results of structural refinements are given in Table 5.8. Positional modulation functions until the third order have been used for La, Co and O_{ap} atoms and a crenel modulation function, with two wave functions, was used for refining the occupational modulation of interstitial atoms.

Table 5.8: *Results of the structural refinements via superspace approach carried out with JANA2006 on synchrotron X-ray diffraction data collected with area detector (ID11@ESRF) on $La_2CoO_{4+\delta}$ at 773 K with δ ~0.19.*

BASIC STRUCTURE *F2/m*							
Atom	*x/a*	*y/b*	*z/c*	U_{11}	U_{22}	U_{33}	U_{12}
La	0	0	0.3586(8)	16.1(9)	14.5(8)	17.1(7)	-1.(6)
Co	0	0	0	15.9(5)	12.0(1)	10.(9)	-1.(2)
Oeq1	¼	¼	0	14.(6)	-	-	-
Oeq2	¾	¼	0	18.(5)	-	-	-
Oap	0	0	0.171(3)	16.(8)	-	-	-
Oint	¼	¼	¼	17.(1)	-	-	-

MODULATION FUNCTIONS $F2/m(\alpha\beta0)0s$							
	Position	*x*sin	*Y*sin	*Z*sin	*x*cos	*y*cos	*Z*cos
La	1st harmonic	0	0	0.00601	0.00329	-0.01446	0
	2nd harmonic	0.00188	0.00316	0	0	0	0.00145
	3rd harmonic	0	0	0.00101	-0.00352	0.00509	0
Co	1st harmonic	0	0	-0.00940	0	0	0
	2nd harmonic	-0.00307	-0.00230	0	0	0	0
	3rd harmonic	0	0	-0.00153	0	0	0
Oap	1st harmonic	0	0	0.00167	0.01136	-0.01142	0
	2nd harmonic	0.00073	0.00829	0	0	0	0.00709
	3rd harmonic	0	0	-0.00306	-0.00639	-0.00229	0
Oint	Occupation	*o*sin	*o*cos				
	1st wave	0.91447	0.24856				
	2nd wave	0.03858	0.07501				

Basic cell parameters: a = 5.48(1) Å b = 5.50(3) Å and c = 12.67(2) Å, $\alpha = \beta = \gamma = 90°$. V = 382.21(2) Å^3. Structure refined in $F2/m(\alpha\beta0)0s$, $\vec{q}_1$ = (0.541, 0.778, 0), on 1290 (*hklm*) reflections averaged from 11216 reflections (166 main reflections R_{int} = 5.4 %, 351 satellites of 1st order R_{int} = 4.7 %, 405 satellites of 2nd order R_{int} = 5.3 %, 368 satellites of 3rd order R_{int} = 3.2 %). Wavelength of X-rays: 0.17723 Å. Global agreement factors: R_F = 6.13 %, R_{WF} = 6.98 %. *Uij* are given in 10^{-3} Å^2.

Basics of data visualization in superspace

Refinements of modulated structures with superspace models involve participation of supplementary dimensions attributing additional coordinates to the lattice points. For instance the current (3+1) incommensurate structure necessitates a 4th coordinate called x_4 besides x, y and z. But, it is very difficult to represent such 4-dimensionnal spaces. Therefore, different manners are generally employed for depicting the periodicity in the extra dimension. The Fourier maps in direct superspace display the electron density toward the x_4 direction, providing good visualization of the modulation functions. Each atom in the basic structure of an incommensurately modulated crystal appears as an undulating string of high density in the Fourier maps. An alternative way to portray the modulation functions is to plot the atomic positions, displacements and bond lengths as a function of the parameter t. The latter corresponds to the distance between the lattice points outside the physical space and the physical space itself[222]. All points with the same distance from the physical space form a three-dimensional space that intersects the fourth coordinate in the point x_s = (0, 0, 0, t). So, the physical space is recovered for t = 0. The periodicity of the modulation implies that any quantity is periodic with t.

Fourier maps and t-plots of the refined modulation functions

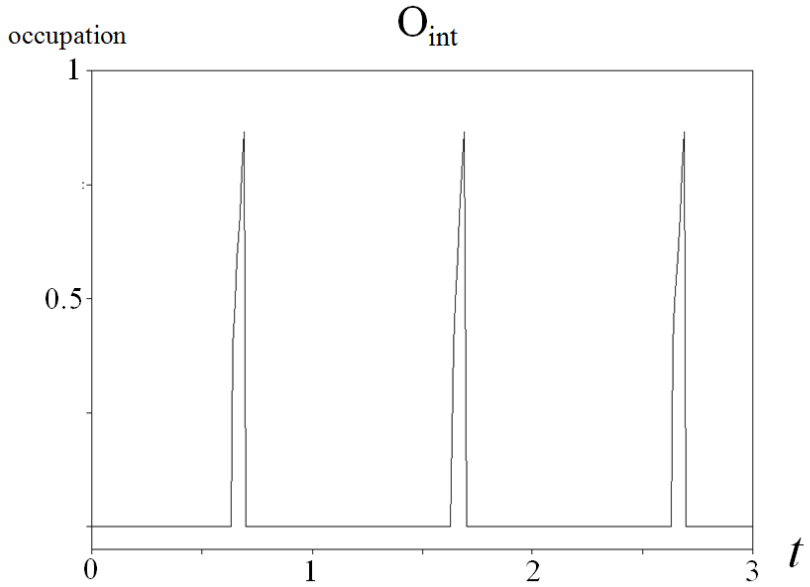

Figure 5.33*: Experimental t-plot of the modulation function refine with a crenel function for the interstitial site.*

The experimental *t*-plot rendering the modulation function of the interstitial site is given in Figure 5.33. It shows a crenel-type function with peaks of occupation centered at $t = n + 0.668$.

Occupational modulations are invariably accompanied by displacive modulations of surrounding atoms (cf. section 2, chapter 3). Special attention is required for the description of the ensuing modulation waves their sites. Consequently, positional modulation functions of other atoms constituting the structure have been refined and are also detailed hereafter.

The (y, x_4)-section in direct space centered on La position, resulting from Fourier calculations (on observed reflections), exhibit particular contours characteristic of a sawtooth function. It is shown on the figure 5.34 together with the corresponding *t*-plot of the *y* coefficient which confirms this tendency. In comparison, the electron density of the (x, x_4)-section is almost rectilinear. Hence, positional modulation of La atoms in the plane involve displacements along $[010]_F$ axis mainly.

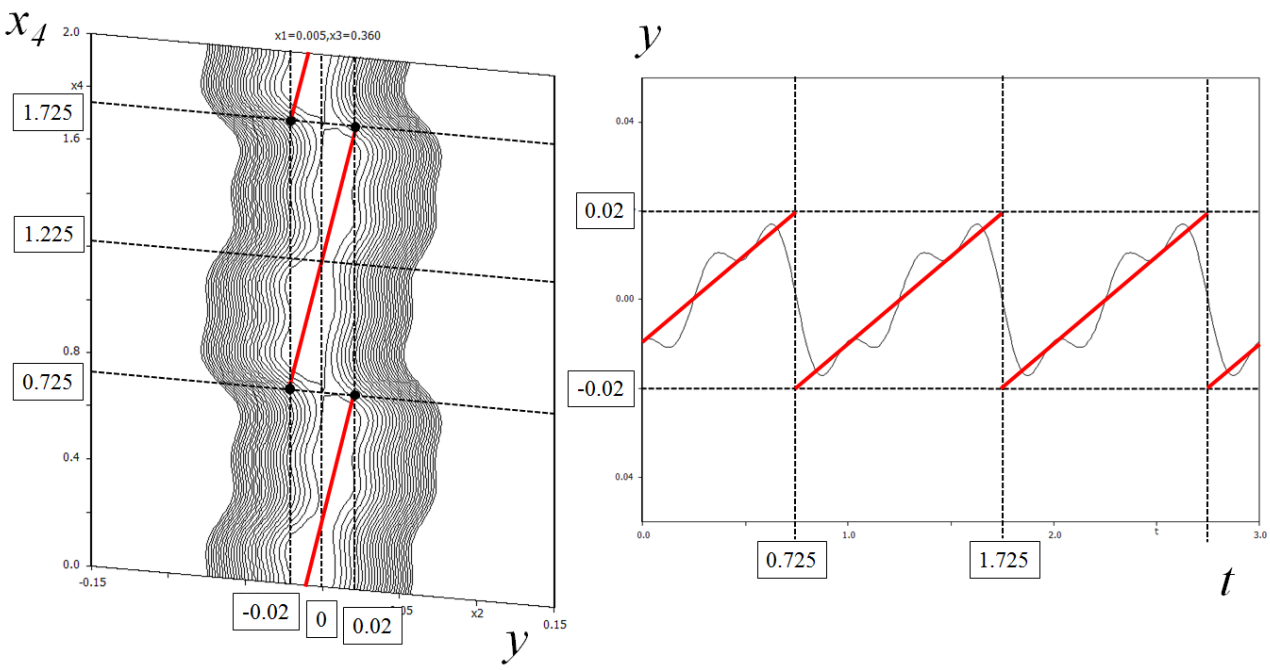

***Figure 5.34**: The electron density of $La_2CoO_{4.19}$ at 773 K in (3+1)-dimensional superspace, a) (y, x_{s4})-section centered on the La atom at (0, 0, 0.3586) showing modulation of saw-tooth type, ρ_{max} = 40 electrons/Å^3, b) t-plot of the displacement of La atoms. The saw-tooth function is symbolized by red lines superimposed on both plots*

The (x, x_4) and (y, x_4) Fourier sections centered on the average position of apical site, displayed on Figure 5.35, exhibit maxima of density which are aside of the centroid position. It denotes the specific ordering of tilts of octahedra. Oxygen atoms occupy alternatively

different precise sites around the average apical site. The subsequent occupational modulation of each of this site can be modeled by a crenel function. The corresponding idealized *t*-plot is shown on the left side of Figure 5.36; it has been constructed on account of maxima of density in the experimental Fourier sections. The right side of the figure shows the experimental *t*-plot of the displacement component along *c*-axis, exhibiting rather strong deviations between -0.15 and +0.10 Å from the centroid position.

The *t*-plots of atomic displacements of La and Co give other interesting details (*cf.* Figure 5.37). First, La atoms are also shifted from their averaged position toward the *c*-axis. Furthermore, Co atoms are even mostly displaced in the latter direction. A crenel function is distinguishable for the *dz* profile.

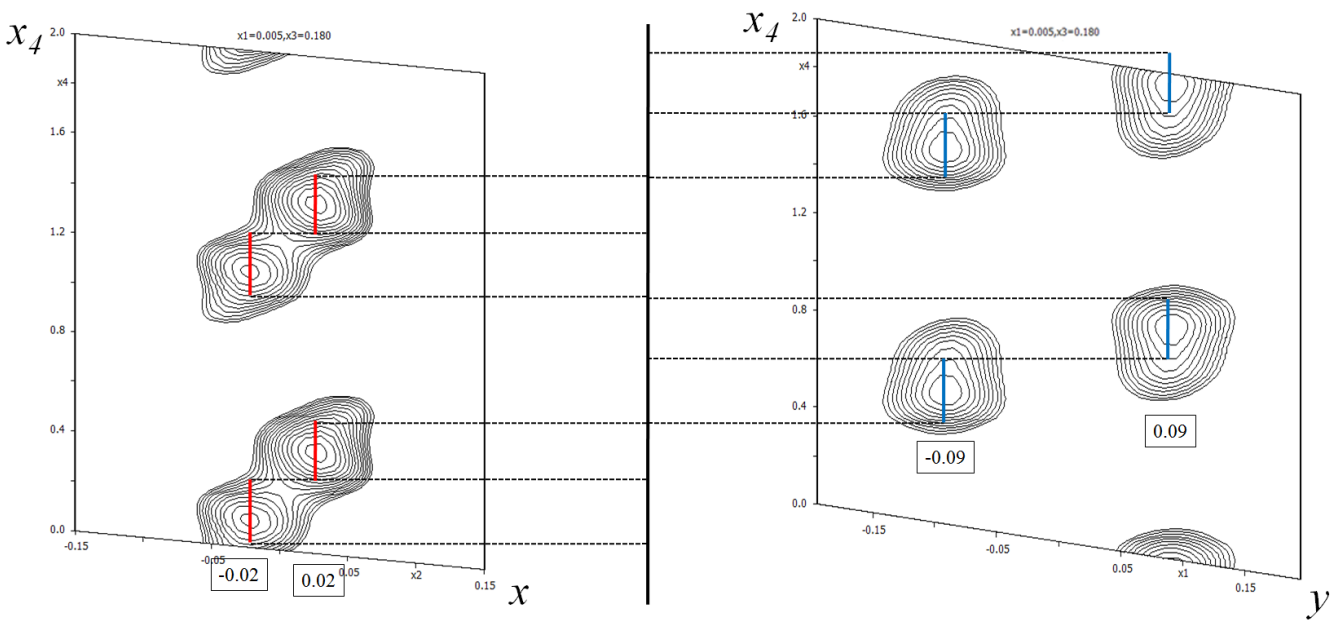

Figure 5.35: *(x, x_4) and (y, x_4)-sections centered on O_{ap} atoms resulting from Fourier calculations, ρ_{max} = 6 electrons/Å^3.*

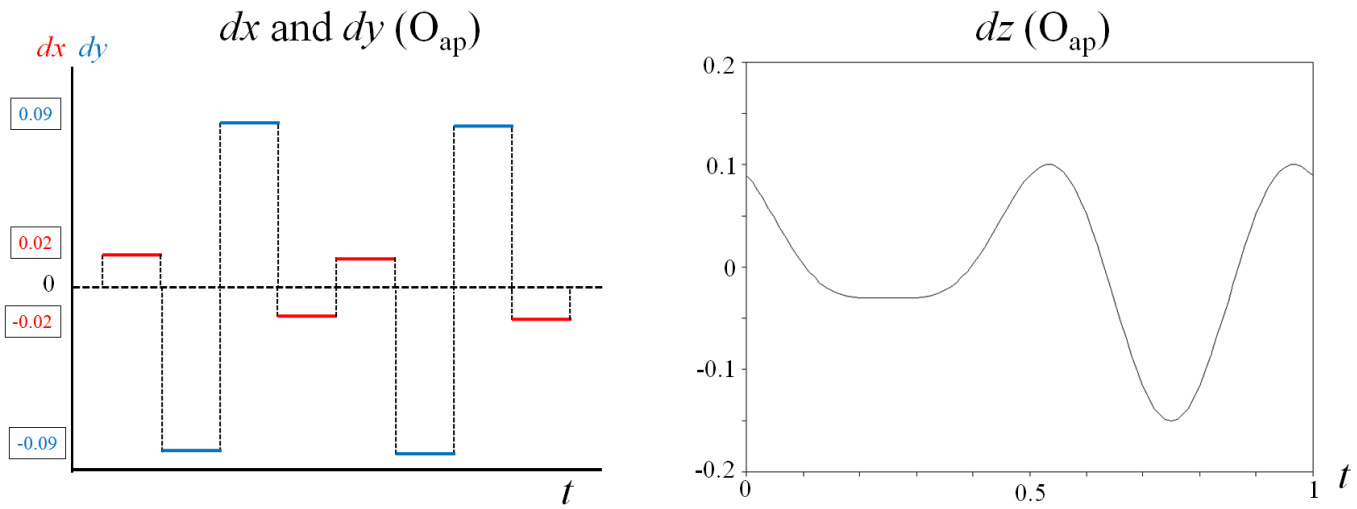

***Figure 5.36**: Left: Idealized t-plot of the crenel function for the apical site, reconstructed from the experimental Fourier sections calculated after structural refinements with superspace approach F2/m(αβ0)0s. Right: experimental t-profile of the atomic displacements of apical oxygen atom toward c-axis.*

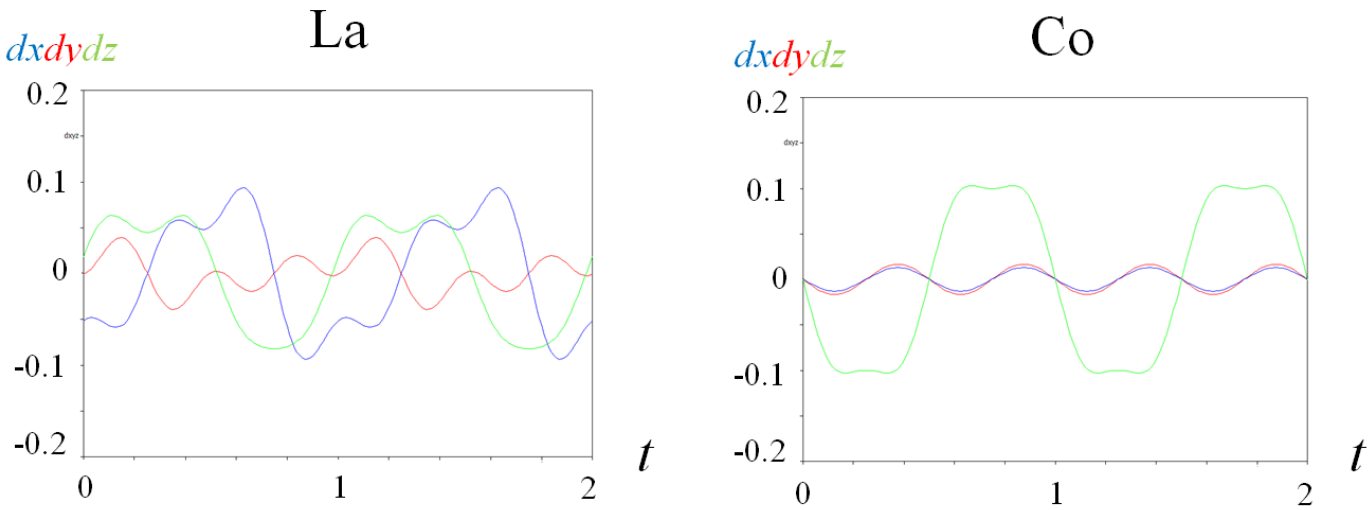

***Figure 5.37**: Modulation functions: t-plot of atomic displacements of La and Co atoms resulting from structural refinements in superspace, carried out with JANA2006 on synchrotron X-ray diffraction data (ID11@ESRF).*

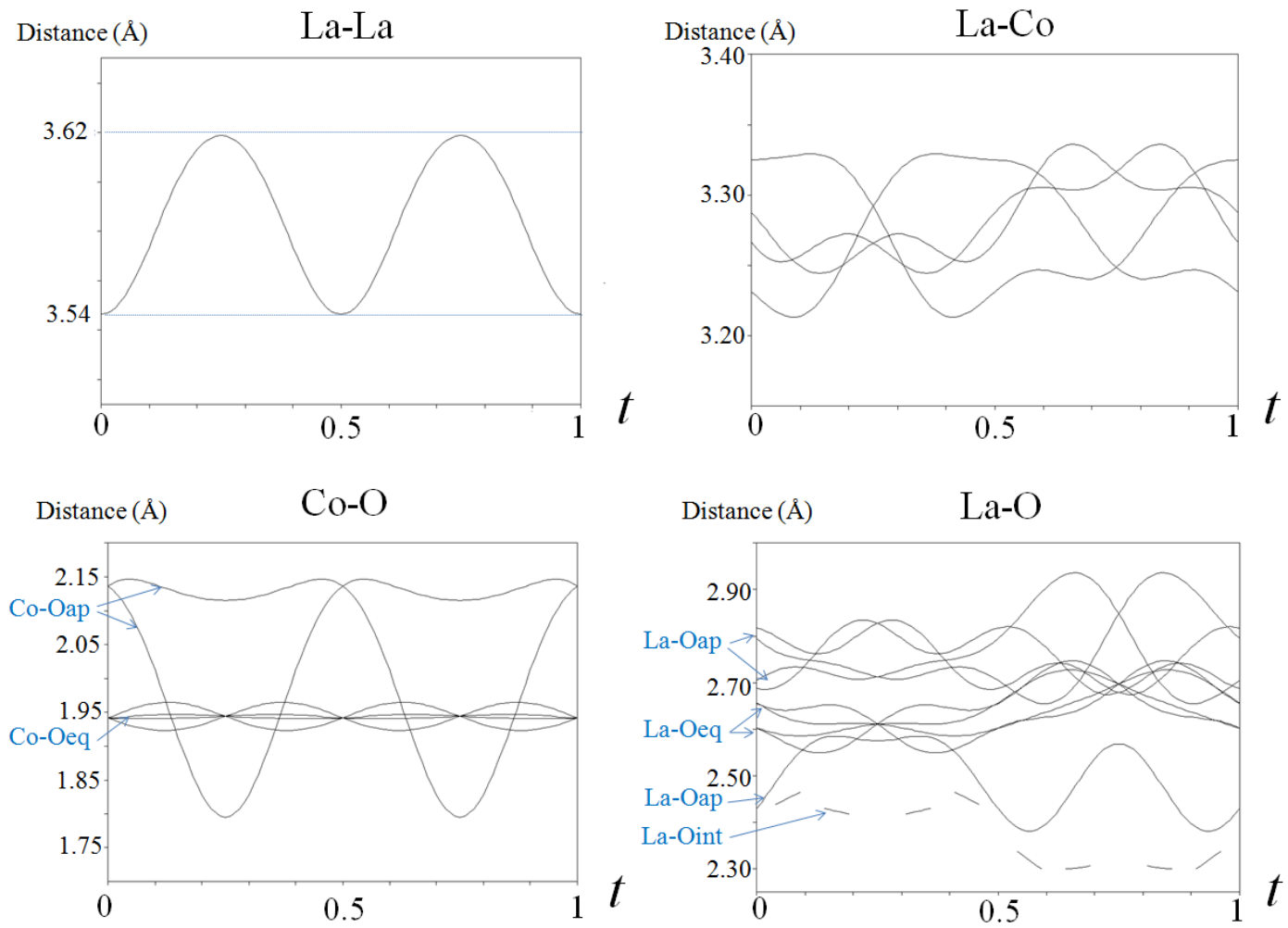

***Figure 5.38**: t-plots of interatomic bond distances resulting from structural refinements in superspace, carried out with JANA2006 on synchrotron X-ray diffraction data (ID11@ESRF).*

The *t*-plots of the interatomic bond distances provide supplementary information. For instance, the *t*-profile of La-La bond distance reveal oscillations consisting of a cosine function with amplitude of 0.08 Å between minima and maxima. The four La-Co distances result from the positional modulations of each atom; their *t*-profiles are rather complex. The bond distances between heavy atoms and oxygen atoms are also shown in Figure 5.38. The positional modulation of equatorial oxygen atoms has not been refined and that is why the Co-O_{eq} bond lengths do not vary a lot. Conversely, the *t*-plots of the Co-O_{ap} distances show strong fluctuations which result from the strong positional shifts of Co atoms toward *c*-axis, and from the simultaneous alternation of occupation of O_{ap} atoms on the different sites around average apical position. The charge ordering of Co^{2+} and Co^{3+} could be at the origin of the modulation of Co-O_{ap} distances (Co^{3+} is more attractive to O^{2-} than Co^{2+}, and thus shrinks the bond lengths). The amplitude of the Co-O_{ap} bond lengths variations appear unusually

elevated: on the experimental profile they are comprised between 1.77 and 2.15 Å. The La-O distances are multiple and complex. The dashed line represents the bond distances with interstitial oxygen atoms which occupation follows a crenel function. Conversely, the La-O_{ap} and La-O_{eq} bond distances are represented by full lines. Their evolution with t can be separated into two parts: *i*) for $0 \leq t \leq 0.5$, the bond distances are contained between 2.55 Å and 2.83 Å, which correspond to a difference of 0.28 Å, *ii*) for $0.5 \leq t \leq 1$, The La-O_{ap} distances are stretched, the difference between the shortest and the longest ones is of 0.56 Å, conversely the La-O_{eq} are very close and they are even all equals for $t = 0.75$.

Interpretations of structural refinements with superspace group are not straightforward. Further data analyses should be done for depicting the real atomic structure in direct space. The results of superspace approach have been presented in order to demonstrate that this thesis is absolutely not exhaustive, and to encourage further structural investigations of the incommensurate phases of $La_2CoO_{4+\delta}$.

3.3.Global outcomes concerning the thermal evolution of $La_2CoO_{4.25}$

The $La_2CoO_{4.25}$ crystal compound does not undergo the transition to the HTT phase. The concentration of interstitial atoms appears to be too elevated, which distort too much the basic structure, preventing the complete disorder characteristic of the HTT phase. A static contribution of atomic displacement persists, but the atomic structure can remain stable with various atomic configurations and oxygen content. The strong structural modulation is prominent until (at least) 773 K. The topotactic reduction stabilizes the $La_2CoO_{4.19}$ stoichiometry through homogenous transformations implying a selective release of interstitial oxygen atoms by half of interlayers. A complete disorder of the atomic structure is not compulsory for allowing variation of oxygen content, but the structural instabilities still play a great role in the process. Even if the extra oxygen content $\delta = 0.25$ can be reached by forcing the topotactic oxidation, either *via* electrochemistry or by oxygen pressure on heating, the subsequent phase is metastable at RT. Consequently, a temperature of 400 K is already sufficient to provoke the transition back to the stoichiometry of $\delta = 0.19$, which appears to be the one with most stable structure. It is very impressive to see the numerous possible atomic configurations available and the facility the compound has to transit from one to the other. The different structures must be very close in energy.

General conclusion

One major outcome of this thesis was the successful growth of high quality single crystals of $La_2CoO_{4+\delta}$ using the Travelling Solvent Floating Zone technique, achieved with optical furnace. Taking advantage of this method allowed us to overcome several obstacles that usually preclude the synthesis of such crystals. As a result, we managed to develop for the first time a reproducible method for the growth of $La_2CoO_{4+\delta}$ single crystals of centimetric size, that open new possibilities for experimental analyses that are unachievable with polycrystalline samples. All precursors have been characterized by X-ray powder diffraction. The quality of the *as grown* single crystals was verified by X-ray Laue and neutron single crystal diffraction; grinded crystal parts were systematically checked by X-ray powder diffraction and thermogravimetric studies for the overall composition, especially for oxygen content.

For $La_2CoO_{4+\delta}$ a variety of complex superstructures have been found as a function of oxygen content δ and temperature. With respect to the pseudo-tetragonal symmetry, crystals were usually pseudo-merohedrically twinned. The splitting of selected reflections, which generally hinders data and structure analysis, was also used for the detection of phase transitions especially for the $La_2CoO_{4.14}$ phase.

All $La_2CoO_{4+\delta}$ crystals investigated in the stoichiometric range of $0.14 < \delta < 0.25$ show complex modulated superstructures, incommensurate for $\delta = 0.14$ showing a lock-in transition towards a commensurate ordering for the higher contents $\delta = 0.19$ and 0.25. Remarkably all superstructure reflections were extremely nicely defined in terms of spot size, and this, up to high momentum transfers, *i.e.* high $\sin\Theta/\lambda$ values. This directly implies that the underlying and generally non-stoichiometric phases are very homogeneous concerning the extra oxygen distribution and related 3D ordering of the CoO_6 octahedra. The incommensurate modulation at RT is described by a 2D modulation, which varies with the oxygen stoichiometry δ and temperature. As for thermally prepared $La_2CoO_{4.14}$ we were able to index all reflections in a (3+2) superspace group, the commensurate structure for $La_2CoO_{4.25}$ could have been refined on a single-domain crystal, the latter has been oxidized by electrochemical oxidation at ambient temperature. The corresponding unit-cell of $La_2CoO_{4.25}$ has monoclinic symmetry and its volume is increased by a factor 32 with respect to the parent HTT phase. Remarkably the *c*-axis is increased by a factor of 4. For thermally oxidized $La_2CoO_{4.25}$ a less ordered phase

is obtained as no increase of the *c*-axis is observed. This clearly underlines the strong potential given by solid state reactions carried out at low temperatures, *e.g.* electrochemical oxidation, as it allows to obtain highly ordered phases, not available by reactions at more elevated temperatures.

The intercalated-oxygen atoms are ordered at long-range together with interstitial vacancies, involving 'occupational modulation' that can be modeled by crenel functions. On the contrary to the stage-like models of interstitial ordering reported by J.M. Tranquada *et al.*[142] for $La_2NiO_{4+\delta}$, involving alternations of empty and full interstitial layers, here we found that every layer of $La_2CoO_{4+\delta}$ contains extra-atoms. In this sense, our results are more comparable to the models of interstitial ordering proposed by A. Demourgues *et al.*[127,128,136] for $La_2NiO_{4+\delta}$.

The corresponding thermally obtained $La_2CoO_{4.19}$ phase shows the same monoclinic supercell as found for $La_2CoO_{4.25}$, but as the content of interstitial oxygen differs, the atomic arrangement is not the same. The transition must then be regarded to be driven by the amount of the interstitial oxygen stoichiometry only. To each value of δ we isolated corresponds a specific crystal structure. Easy switching between different oxygen ordering scenarios thus seems a prerequisite for high ionic conductivity[238,239].

Surprisingly the superstructure reflections persist or even re-appear upon heating, for all $La_2CoO_{4+\delta}$ samples with $0.14 < \delta < 0.25$ at least up to 500°C, evidencing an impressive stability of a long-range oxygen ordering with temperature. This is an important issue when discussing the origin of low temperature oxygen mobility based on specific lattice dynamics, *i.e.* phonon assisted diffusion mechanisms, allowing to explain low temperature oxygen diffusion. In this context ordered states may favor the formation of particular lattice modes to be at the origin of oxygen diffusion mechanisms down to ambient temperature. This concept, which has been first postulated for Brownmillerite type frameworks[18], also holds for K_2NiF_4 type oxides, as has been shown for $La_2CuO_{4.07}$[19]. Hence, the results of DFT (Density Functional Theory) and MD (Molecular Dynamics) calculations recently reported[224] for oxygen-rich $La_2CoO_{4+\delta}$ at elevated temperatures, which are based on the only averaged tetragonal *I*4/*mmm* structural model, are idealistic since the real atomic positions are ignored.

3D order of interstitial atoms in $La_2CoO_{4.25}$ is also at the origin of the re-entrant transition of antiferromagnetic ordering below 36 K implying a probable charge ordering. The results obtained from neutron Laue diffraction suggest a magnetic unit-cell of $2a \times 2b \times 2c$, eight

times larger than the magnetic cell of the stoichiometric compound, reported by K. Yamada *et al.*[91]

Different $La_2CoO_{4+\delta}$ phases show similar distortions of the apical oxygen atoms towards the [100] and/or [110] directions with respect to the F-centered cell, as found for electrochemically oxidized $La_2CuO_{4.07}$[19]. They have been evidenced via the reconstruction of the nuclear density using the Maximum Entropy algorithm from neutron diffraction data. This again underlines the more general concept that specific lattice vibrations might be at the origin for a phonon assisted diffusion mechanism to microscopically explain low temperature oxygen mobility in solid oxides.

Preliminary measurements using inelastic neutron scattering have been engaged to investigate the changes of lattice dynamics related to the intercalation of oxygen into La_2CoO_4. As a perspective it should be interesting to follow changes in the appearance/disappearance of phonon branches for $La_2CoO_{4.14}$ as a function of temperature, *i.e.* oxygen ordering below and above the orthorhombic-tetragonal phase transition. This will clearly allow to estimate the influence of oxygen ordering for the existence of soft modes and associated changes in the oxygen mobility. Complementary measurements to determine the anisotropy of the oxygen mobility using the $^{18}O/^{16}O$ tracer method should also be envisaged to allow a better insight in the diffusion mechanism and pathway as a function of temperature.

Complementary studies on the polymorphism of La_2CuO_4 clearly indicate that oxygen can easily move from the apical to interstitial sites in the T phase, but is completely blocked in the T'-phase, although the latter is of lower density. The phase transition from the T'-La_2CuO_4 phase to T-La_2CuO_4 observed at high temperatures, is irreversible and has a reconstructive character. This again underlines the importance of lattice dynamics for oxygen mobility and its dependence from structural instabilities as realized in the T-phase only. For this reason one easily understands that oxygen cannot be intercalated into T'-La_2CuO_4.

APPENDIX A: Structural model for $La_2CoO_{4.25}$ at RT

Structural model for $La_2CoO_{4.25}$ resulting from refinements carried out with JANA2006 on synchrotron X-ray diffraction data (ID11@ESRF)

Atom	*Wick.*	*x/a*	*y/b*	*z/c*	U_{11}	U_{22}	U_{33}	U_{12}	U_{13}	U_{23}
La1	4*g*	0.5602(1)	0.3749(1)	0.3541(2)	16.(2)	17.(5)	13.(3)	1.(5)	3.(2)	1.(4)
La2	4*g*	0.6944(1)	0.1232(1)	0.3566(1)	25.(4)	21.(4)	16.(3)	15.(4)	1.(1)	1.(7)
La3	4*g*	0.1889(1)	0.1232(2)	0.3618(2)	25.(2)	20.(9)	14.(2)	7.(7)	-2.(2)	2.(2)
La4	4*g*	0.1922(1)	0.6270(2)	0.13777(9)	8.(2)	9.(2)	13.(6)	4.(2)	-2.(4)	2.(3)
La5	4*g*	0.0728(1)	0.3742(2)	0.36509(9)	13.(3)	15.(2)	6.(9)	4.(4)	-3.(2)	1.(8)
La6	4*g*	0.5677(1)	0.8799(1)	0.1389(1)	9.(4)	12.(8)	14.(8)	-2.(1)	2.(7)	2.(4)
La7	4*g*	0.0659(1)	0.8721(1)	0.1417(1)	12.(9)	16.(2)	15.(5)	2.(1)	-3.(5)	1.(7)
La8	4*g*	0.6881(1)	0.6238(1)	0.1430(1)	19.(2)	17.(1)	11.(1)	9.(2)	7.(8)	1.(6)
Co1	4*g*	0.1876(2)	0.1276(2)	0.0003(1)	8.(2)	3.(7)	11.(2)	4.(3)	1.(1)	-1.(2)
Co2	4*g*	0.9441(2)	0.1277(2)	0.5021(1)	3.(3)	8.(5)	13.(8)	3.(5)	-4.(3)	-3.(1)
Co3	4*g*	0.8183(2)	0.3765(2)	0.4935(2)	10.(4)	2.(3)	21.(4)	1.(6)	6.(4)	2.(1)
Co4	4*g*	0.0625(2)	0.3763(2)	0.0004(2)	11.(2)	3.(2)	25.(4)	2.(2)	-1.(5)	0.(9)

Atom	*Wick.*	*x/a*	*y/b*	*z/c*	U_{iso}	Tilt (°)	dist Oap-Co (Å)	dist Oap-Oint (Å)
Oap1	4*g*	0.813(2)	0.389(1)	0.6735(5)	21.(8)	1.07	2.25(9)	2.18(4)
Oap2	4*g*	0.959(3)	0.135(3)	0.3265(7)	35.(9)	3.98	2.20(8)	2.26(3)
Oap3	4*g*	0.084(1)	0.387(3)	0.1720(9)	45.(9)	5.82	2.16(2)	2.38(9)
Oap4	4*g*	0.049(1)	0.398(1)	-0.1766(6)	48.(3)	9.16	2.24(8)	2.53(6)
Oap5	4*g*	0.180(1)	0.157(3)	0.1753(6)	54.(2)	10.59	2.22(8)	2.67(5)
Oap6	4*g*	0.199(3)	0.091(2)	-0.1708(8)	53.(9)	13.74	2.21(1)	2.73(6)
Oap7	4*g*	0.874(1)	0.402(2)	0.3204(7)	61.(8)	14.26	2.24(4)	2.74(1)
Oap8	4*g*	0.8608(2)	0.0756(2)	0.6855(8)	64.(4)	20.24	2.44(8)	2.80(8)
Oeq1	4*g*	0.882(2)	0.253(3)	0.509(1)	38.(0)			
Oeq2	4*g*	0.122(2)	0.254(3)	-0.0212(9)	26.(6)			
Oeq3	4*g*	0.364(1)	0.244(4)	-0.008(1)	54.(8)			
Oeq4	4*g*	0.621(3)	0.265(2)	0.474(1)	51.(3)			
Oeq5	2*e*	¼	0	0.0207(8)	29.(1)			
Oeq6	2*e*	¾	0	0.4778(9)	34.(1)			
Oeq7	2*f*	¼	½	-0.0186(8)	42.(4)			
Oeq8	2*d*	½	½	0	35.(4)			
Oeq9	2*f*	¾	½	0.4880(9)	27.(4)			
Oeq10	2*b*	0	½	0.498(1)	27.(5)			
Oeq11	2*c*	0	0	½	43.(6)			
Oeq12	2*a*	0	0	0	41.(3)			
Oint	4*g*	0.621(2)	0.242(3)	0.252(1)	31.(8)			

Cell parameters: a = 11.05(8) Å, b = 12.26(9) Å and c = 12.53(1) Å, $\alpha = \beta = 90°$, γ = 116.6(4)°. V = 1517.73(4) Å^3. Structure refined in *P*112/*a* on 2152 independent reflections. R_{int} = 2.1 %. λ = 0.2072 Å. Agreement factors: R_F = 3.77 %, R_{WF} = 3.59 %. All sites given have full occupation. *Uij* are given in 10^{-3} Å^2.

APPENDIX B: Structural model for $La_2CoO_{4.19}$

Structural model of $La_2CoO_{4.19}$ refined from synchrotron X-ray diffraction data (ID11@ESRF).

a) La and Co atoms in the monoclinic supercell.

Atom	*Wick.*	*x/a*	*y/b*	*z/c*	U_{11}	U_{22}	U_{33}	U_{12}	U_{13}	U_{23}
La1	8f	0.5586(2)	0.1244(2)	0.1528(1)	13.(4)	16.(5)	17.(5)	4.(1)	-6.(3)	0.(4)
La2	8f	-0.0621(2)	-0.1263(2)	0.0282(1)	27.(4)	17.(3)	14.(5)	8.(1)	-0.(5)	-6.(3)
La3	8f	0.5585(3)	0.1217(1)	0.2221(1)	17.(4)	19.(4)	10.(4)	1.(2)	-9.(2)	-7.(4)
La4	8f	0.4433(3)	0.3735(1)	0.222(1)	23.(7)	18.(6)	14.(3)	7.(3)	-2.(3)	6.(5)
La5	8f	0.0593(3)	0.1242(2)	0.1519(2)	17.(6)	18.(5)	22.(5)	8.(1)	-6.(4)	2.(7)
La6	8f	0.4342(2)	-0.1279(2)	0.0968(2)	13.(5)	14.(7)	24.(6)	3.(5)	8.(6)	-1.(3)
La7	8f	-0.0526(1)	-0.1239(3)	0.0985(1)	12.(5)	21.(7)	27.(7)	3.(2)	-0.(5)	6.(4)
La8	8f	0.4443(3)	-0.1236(3)	0.0259(1)	10.(4)	18.(5)	15.(8)	2.(3)	2.(4)	-5.(5)
La9	8f	0.6776(2)	-0.1261(2)	0.1507(1)	16.(6)	18.(5)	17.(8)	6.(4)	-7.(6)	-3.(6)
La10	8f	0.8146(2)	0.1285(2)	0.2794(1)	14.(5)	12.(6)	10.(7)	4.(5)	-8.(3)	-3.(6)
La11	8f	0.316(1)	0.1207(2)	0.2756(2)	16.(4)	15.(7)	11.(5)	9.(6)	7.(2)	-6.(4)
La12	8f	0.1877(3)	-0.1271(2)	0.1530(1)	15.(6)	17.(6)	10.(6)	4.(3)	-8.(4)	7.(3)
La13	8f	0.6817(2)	0.3746(3)	0.0263(2)	18.(6)	12.(5)	21.(7)	8.(4)	-9.(4)	-6.(4)
La14	8f	0.3183(2)	0.1265(2)	0.0975(1)	23.(7)	19.(5)	11.(6)	1.(7)	-2.(4)	-3.(5)
La15	8f	0.6858(2)	0.3793(3)	0.0969(1)	22.(7)	10.(4)	17.(6)	4.(3)	1.(5)	8.(7)
La16	8f	0.6856(3)	-0.1237(3)	-0.0270(1)	13.(6)	18.(4)	11.(5)	3.(3)	8.(4)	6.(6)
Co1	8f	0.6920(4)	0.3715(5)	0.1869(2)	18.(4)	16.(8)	18.(6)	7.(7)	6.(9)	-2.(8)
Co2	8f	0.3078(5)	-0.3753(5)	0.0621(1)	3.(7)	6.(8)	24.(4)	2.(7)	-3.(5)	-6.(7)
Co3	8f	0.6915(5)	-0.1260(4)	0.0621(1)	5.(3)	8.(7)	23.(3)	3.(9)	-0.(7)	0.(4)
Co4	8f	0.432(1)	-0.1295(5)	0.1885(1)	17.(4)	13.(6)	16.(3)	3.(8)	4.(5)	3.(6)
Co5	8f	0.3081(5)	0.1270(4)	0.1876(1)	16.(4)	13.(8)	22.(4)	4.(6)	-2.(8)	2.(7)
Co6	8f	0.5650(4)	0.1261(5)	0.0615(1)	3.(3)	5.(3)	26.(6)	0.(5)	0.(8)	-8.(9)
Co7	8f	0.5618(4)	0.1227(5)	0.3138(2)	23.(3)	16.(3)	14.(7)	8.(7)	5.(9)	9.(8)
Co8	8f	0.0673(4)	0.1271(5)	0.0623(2)	3.(2)	5.(7)	25.(4)	0.(8)	5.(7)	4.(7)

Cell parameters: a = 10.94(8) Å, b = 12.26(7) Å and c = 50.38(8) Å, $\alpha = \beta = 90°$, γ = 116.7(9)°. V = 6047.20(2) $Å^3$. Structure refined in *B2/n* on 4594 independent reflections R_{int} = 2.1 %. λ = 0.2072 Å. Agreement factors: R_F = 5.27 %, R_{WF} = 3.12 %. All sites given have full occupation. *Uij* are given in $Å^2$.

b) Oxygen atoms in the monoclinic supercell.

Atom	*Wick.*	*x/a*	*y/b*	*z/c*	U_{iso}
Oeq1	8f	0.617(7)	0.501(0)	0.064(1)	17.(5)
Oeq2	8f	0.371(8)	0.501(1)	0.0673(8)	20.(6)
Oeq3	8f	0.495(8)	0.748(8)	0.059(2)	30.(7)
Oeq4	4e	¼	¾	0.0602(9)	12.(9)
Oeq5	4e	¼	¼	0.059(1)	39.(4)
Oeq6	8f	0.501(9)	0.25(1)	0.061(1)	29.(7)
Oeq7	4e	¾	¾	0.066(1)	31.(3)
Oeq8	8f	0.111(7)	0.495(8)	0.0634(8)	15.(3)
Oeq9	4e	¾	¼	0.0649(9)	54.(6)
Oeq10	4e	¾	¾	0.1821(9)	17.(3)
Oeq11	8f	0.497(7)	0.747(7)	0.191(1)	18.(5)
Oeq12	8f	0.627(7)	0.492(7)	0.184(1)	26.(8)
Oeq13	8f	0.376(6)	0.501(9)	0.190(1)	26.(8)
Oeq14	4e	¼	¾	0.1924(8)	21.(4)
Oeq15	8f	0.133(9)	0.50(1)	0.1874(8)	30.(8)
Oeq16	4e	¼	¼	0.185(1)	23.(4)
Oeq17	8f	0.502(8)	0.246(8)	0.1887(8)	40.(7)
Oeq18	4e	¾	¼	0.190(1)	20.(6)
Oeq19	8f	0.617(7)	-0.001(8)	0.1865(8)	18.(5)
Oeq20	8f	0.125(7)	-0.002(9)	0.5605(9)	27.(7)
Oap1	8f	0.301(6)	0.620(8)	0.1050(8)	28.(5)
Oap2	8f	0.401(6)	0.356(6)	0.104(1)	27.(4)
Oap3	8f	0.561(8)	0.107(7)	0.105(3)	44.(1)
Oap4	8f	0.847(9)	0.613(9)	0.104(1)	43.(1)
Oap5	8f	0.805(8)	0.613(9)	0.269(2)	36.(4)
Oap6	8f	0.367(7)	0.662(9)	0.270(1)	46.(5)
Oap7	8f	0.420(6)	0.404(8)	0.269(1)	52.(5)
Oap8	8f	0.591(8)	0.122(7)	0.270(2)	36.(5)
Oap9	8f	0.691(9)	0.864(8)	0.0211(9)	42.(7)
Oap10	8f	0.438(8)	0.38(1)	0.0191(8)	27.(8)
Oap11	8f	0.342(7)	0.629(9)	0.019(3)	49.(4)
Oap12	8f	0.584(7)	0.147(9)	0.021(0)	46.(7)
Oap13	8f	0.42(1)	0.872(9)	0.1450(9)	23.(3)
Oap14	8f	0.203(8)	0.390(9)	0.1435(8)	35.(3)
Oap15	8f	0.526(8)	0.628(8)	0.1478(8)	36.(5)
Oap16	8f	0.715(8)	0.372(8)	0.145(1)	37.(6)
Oint1	4e	¾	¼	⅛	31.(5)
Oint2	4e	¾	¼	½	42.(4)
Oint3	4e	¼	¾	¼	23(3)

Bibliography

(1) Colville, A. A.; Geller, S. *Acta Crystallogr B Struct Crystallogr Cryst Chem* **1971**, *27*, 2311-2315.
(2) Ruddlesden, S. N.; Popper, P. *Acta Cryst* **1957**, *10*, 538-539.
(3) Ruddlesden, S. N.; Popper, P. *Acta Cryst* **1958**, *11*, 54-55.
(4) Nemudry, A.; Weiss, M.; Gainutdinov, I.; Boldyrev, V.; Schöllhorn, R. *Chemistry of Materials* **1998**, *10*, 2403-2411.
(5) Grenier, J.; Wattiaux, A.; Doumerc, J.; Dordor, P.; Fournes, L.; Chaminade, J.; Pouchard, M. *Journal of Solid State Chemistry* **1992**, *96*, 20-30.
(6) Grenier, J. C.; Wattiaux, A.; Monroux, C.; Pouchard, M.; Locquet, J. P. *Physica C: Superconductivity* **1994**, *235-240*, 79-82.
(7) Demourgues, A.; Wattiaux, A.; Grenier, J. C.; Pouchard, M.; Soubeyroux, J. L.; Dance, J. M.; Hagenmuller, P. *Journal of Solid State Chemistry* **1993**, *105*, 458-468.
(8) Le Toquin, R. L. réactivité, structure et propriétés physiques de SrCo2.5+d et LA2CoO4+d, étude par diffraction des rayons x et des neutrons in situ, Rennes 1: France, 2003.
(9) Girgsdies, F. *Solid State Commun.* **1994**, *91*, 111-112.
(10) Le Toquin, R.; Paulus, W.; Cousson, A.; Dhalenne, G.; Revcolevschi, A. *Physica B: Condensed Matter* **2004**, *350*, E269-E272.
(11) Le Toquin, R.; Paulus, W.; Cousson, A.; Prestipino, C.; Lamberti, C. *J. Am. Chem. Soc* **2006**, *128*, 13161-13174.
(12) Nemudry, A.; Rudolf, P.; Schöllhorn, R. *Solid State Ionics* **1998**, *109*, 213-222.
(13) Chou, F.; Cho, J.; Miller, L.; Johnston, D. *Phys. Rev. B* **1990**, *42*, 6172-6180.
(14) Matei, C.; Berger, D.; Marote, P.; Deloume, J. *J Electroceram* **2008**, *24*, 64-66.
(15) Das, H.; Saha-Dasgupta, T. *Phys. Rev. B* **2009**, *79*, 134522.
(16) Yamamoto, H.; Matsumoto, O.; Tsukada, A.; Naito, M. *Physica C: Superconductivity* **2010**, *470*, 1025-1028.
(17) Hord, R.; Luetkens, H.; Pascua, G.; Buckow, A.; Hofmann, K.; Krockenberger, Y.; Kurian, J.; Maeter, H.; Klauss, H.; Pomjakushin, V.; Suter, A.; Albert, B.; Alff, L. *Phys. Rev. B* **2010**, *82*, 180508.
(18) Paulus, W.; Schober, H.; Eibl, S.; Johnson, M.; Berthier, T.; Hernandez, O.; Ceretti, M.; Plazanet, M.; Conder, K.; Lamberti, C. *Journal of the American Chemical Society* **2008**, *130*, 16080-16085.
(19) Villesuzanne, A.; Paulus, W.; Cousson, A.; Hosoya, S.; Dréau, L.; Hernandez, O.; Prestipino, C.; Ikbel Houchati, M.; Schefer, J. *J Solid State Electrochem* **2010**, *15*, 357-366.
(20) Kay, H. F.; Bailey, P. C. *Acta Cryst* **1957**, *10*, 219-226.
(21) Glazer, A. M. *Acta Crystallogr B Struct Crystallogr Cryst Chem* **1972**, *28*, 3384-3392.
(22) Newnham, R.; Cross, L. *Materials Research Bulletin* **1974**, *9*, 927-933.
(23) Megaw, H. D. *Acta Cryst* **1952**, *5*, 739-749.
(24) Taguchi, Y.; Tokura, Y.; Arima, T.; Inaba, F. *Phys. Rev. B* **1993**, *48*, 511.
(25) Kanno, I.; Fujii, S.; Kamada, T.; Takayama, R. *Appl. Phys. Lett.* **1997**, *70*, 1378.
(26) Sadel, A.; Von Der Mühll, R.; Ravez, J.; Hagenmuller, P. *Materials Research Bulletin* **1980**, *15*, 1789-1796.
(27) Burns, G.; Gläzer Space Group for Solid State Scientist. *Academin Press Inc*.
(28) Goldschmidt, V. Geochemische Verteilungegesetze der Elemente VII, VIII. **1927**.
(29) Woodward, P. M. *Acta Crystallogr B Struct Sci* **1997**, *53*, 32-43.
(30) Woodward, P. M. *Acta Crystallogr B Struct Sci* **1997**, *53*, 44-66.
(31) Hodges, J. P.; Short, S.; Jorgensen, J. D.; Xiong, X.; Dabrowski, B.; Mini, S. M.; Kimball, C. W. *Journal of Solid State Chemistry* **2000**, *151*, 190-209.
(32) Kharton, V. V.; Marozau, I. P.; Vyshatko, N. P.; Shaula, A. L.; Viskup, A. P.; Naumovich, E.

N.; Marques, F. M. B. *Materials Research Bulletin* **2003**, *38*, 773-782.
(33) Inoue, S.; Kawai, M.; Ichikawa, N.; Kageyama, H.; Paulus, W.; Shimakawa, Y. *Nat Chem* **2010**, *2*, 213-217.
(34) Fisher, C. A. J.; Islam, M. S. *Solid State Ionics* **1999**, *118*, 355-363.
(35) D'Hondt, H.; Abakumov, A. M.; Hadermann, J.; Kalyuzhnaya, A. S.; Rozova, M. G.; Antipov, E. V.; Van Tendeloo, G. *Chem. Mater.* **2008**, *20*, 7188-7194.
(36) Abakumov, A. M.; Alekseeva, A. M.; Rozova, M. G.; Antipov, E. V.; Lebedev, O. I.; Tendeloo, G. V. *Journal of Solid State Chemistry* **2003**, *174*, 319-328.
(37) Tsujimoto, Y.; Tassel, C.; Hayashi, N.; Watanabe, T.; Kageyama, H.; Yoshimura, K.; Takano, M.; Ceretti, M.; Ritter, C.; Paulus, W. *Nature* **2007**, *450*, 1062-1065.
(38) Siegrist, T.; Zahurak, S. M.; Murphy, D. W.; Roth, R. S. *Nature* **1988**, *334*, 231-232.
(39) Takano, M.; Takeda, Y.; Okada, H.; Miyamoto, M.; Kusaka, T. *Physica C: Superconductivity* **1989**, *159*, 375-378.
(40) Smith, M. G.; Manthiram, A.; Zhou, J.; Goodenough, J. B.; Markert, J. T. *Nature* **1991**, *351*, 549-551.
(41) Tassel, C.; Pruneda, J. M.; Hayashi, N.; Watanabe, T.; Kitada, A.; Tsujimoto, Y.; Kageyama, H.; Yoshimura, K.; Takano, M.; Nishi, M.; Ohoyama, K.; Mizumaki, M.; Kawamura, N.; Íñiguez, J.; Canadell, E. *Journal of the American Chemical Society* **2009**, *131*, 221-229.
(42) Inoue, S.; Kawai, M.; Shimakawa, Y.; Mizumaki, M.; Kawamura, N.; Watanabe, T.; Tsujimoto, Y.; Kageyama, H.; Yoshimura, K. *Appl. Phys. Lett.* **2008**, *92*, 161911.
(43) Beznosikov, B. V.; Aleksandrov, K. S. *Crystallography Reports* **2000**, *45*, 792–798.
(44) Bednorz, J. G.; Müller, K. A. *Z Phys B Con Mat* **1986**, *64*, 189–193.
(45) Fisher, R. A.; Gordon, J. E.; Phillips, N. E. *Annu. Rev. Phys. Chem.* **1996**, *47*, 283-325.
(46) Hayashi, A.; Tamura, H.; Ueda, Y. *Physica C: Superconductivity* **1993**, *216*, 77-82.
(47) Ram, R.; Ganguly, P.; Rao, C.; Honig, J. *Materials Research Bulletin* **1988**, *23*, 501-506.
(48) Paulus, W.; Heger, G.; Rudolf, P.; Schöllhorn, R. *Physica C: Superconductivity* **1994**, *235-240*, 861-862.
(49) Paulus, W.; Cousson, A.; Dhalenne, G.; Berthon, J.; Revcolevschi, A.; Hosoya, S.; Treutmann, W.; Heger, G.; Le Toquin, R. *Solid State Sciences* **2002**, *4*, 565-573.
(50) *Ternary Compounds, Organic Semiconductors*; Madelung, O.; Rössler, U.; Schulz, M., Éd.; Springer-Verlag: Berlin/Heidelberg, 2000; Vol. 41E.
(51) Tokura, Y.; Takagi, H.; Uchida, S. *Nature* **1989**, *337*, 345-347.
(52) Imai, Y.; Kato, M.; Takarabe, Y.; Noji, T.; Koike, Y. *Chemistry of Materials* **2007**, *19*, 3584-3585.
(53) Luce, J. L.; Stacy, A. M. *Chemistry of Materials* **1997**, *9*, 1508-1515.
(54) Chou, F. C.; Cho, J. H.; Miller, L. L.; Johnston, D. C. *Phys. Rev. B* **1990**, *42*, 6172-6180.
(55) Yamamoto, H.; Matsumoto, O.; Tsukada, A.; Naito, M. *Physica C: Superconductivity* **2010**, *470*, 1025-1028.
(56) Braden, M.; Paulus, W.; Cousson, A.; Vigoureux, P.; Heger, G.; Goukassov, A.; Bourges, P.; Petitgrand, D. *Europhys. Lett.* **1994**, *25*, 625-630.
(57) Manthiram, A.; Goodenough, J. B. *Journal of Solid State Chemistry* **1990**, *87*, 402-407.
(58) Manthiram, A.; Goodenough, J. B. *Journal of Solid State Chemistry* **1991**, *92*, 231-236.
(59) Tokura, Y.; Takagi, H.; Watabe, H.; Matsubara, H.; Uchida, S.; Hiraga, K.; Oku, T.; Mochiku, T.; Asano, H. *Phys. Rev. B* **1989**, *40*, 2568.
(60) Hiroi, Z.; Takano, M.; Azuma, M.; Takeda, Y. *Nature* **1993**, *364*, 315-317.
(61) Hiroi, Z.; Azuma, M.; Takano, M.; Bando, Y. *Journal of Solid State Chemistry* **1991**, *95*, 230-238.
(62) Wang, Y. Y.; Zhang, H.; Dravid, V. P.; Marks, L. D.; Han, P. D.; Payne, D. A. *Physica C: Superconductivity* **1995**, *255*, 247-256.
(63) Yang, H.; Liu, Q. Q.; Li, F. Y.; Jin, C. Q.; Yu, R. C. *Supercond. Sci. Technol.* **2006**, *19*, 934-940.

(64) Van Tendeloo, G.; Amelinckx, S. *Physica C: Superconductivity* **1991**, *176*, 575–595.
(65) Chen, B. *Journal of Solid State Chemistry* **1996**, *125*, 63-66.
(66) Tarascon, J. M.; Greene, L. H.; Mckinnon, W. R.; Hull, G. W.; Geballe, T. H. *Science* **1987**, *235*, 1373-1376.
(67) Tokura, Y.; Fujimori, A.; Matsubara, H.; Watabe, H.; Takagi, H.; Uchida, S.; Sakai, M.; Ikeda, H.; Okuda, S.; Tanaka, S. *Phys. Rev. B* **1989**, *39*, 9704.
(68) Luke, G. M.; Le, L. P.; Sternlieb, B. J.; Uemura, Y. J.; Brewer, J. H.; Kadono, R.; Kiefl, R. F.; Kreitzman, S. R.; Riseman, T. M.; Stronach, C. E.; Davis, M. R.; Uchida, S.; Takagi, H.; Tokura, Y.; Hidaka, Y.; Murakami, T.; Gopalakrishnan, J.; Sleight, A. W.; Subramanian, M. A.; Early, E. A.; Markert, J. T.; Maple, M. B.; Seaman, C. L. *Phys. Rev. B* **1990**, *42*, 7981.
(69) Tsukada, A.; Krockenberger, Y.; Yamamoto, H.; Naito, M. *Arxiv preprint cond-mat/0401120* **2004**.
(70) Muller-Buschbaum; Wollschlager *Zeitschrift für anorganische und allgemeine Chemie* **1975**, *414*, 76.
(71) Takayama-Muromachi, E.; Uchida, Y.; Kobayashi, M.; Kato, K. *Physica C: Superconductivity* **1989**, *158*, 449-452.
(72) Tan, Z.; Budnick, J. I.; Luo, S.; Chen, W. Q.; Cheong, S.; Cooper, A. S.; Canfield, P. C.; Fisk, Z. *Phys. Rev. B* **1991**, *44*, 7008.
(73) Ramanujachary, K.; Greaney, M.; Fuller, R.; Greenblatt, M. *Journal of Solid State Chemistry* **1991**, *93*, 263-266.
(74) Okamoto, S.; Millis, A. J. *cond-mat/0404275* **2004**.
(75) Kancharla, S.; Okamoto, S. *Phys. Rev. B* **2007**, *75*.
(76) Sreedhar, K.; Ganguly, P. *Phys. Rev. B* **1990**, *41*, 371.
(77) Szotek, Z.; Guo, G. Y.; Temmerman, W. M. *Physica C: Superconductivity* **1991**, *175*, 1-11.
(78) Tsukada, A.; Shibata, H.; Noda, M.; Yamamoto, H.; Naito, M. *Physica C: Superconductivity* **2006**, *445-448*, 94-96.
(79) Das, H.; Saha-Dasgupta, T. *Phys. Rev. B* **2009**, *79*, 134522.
(80) Shannon Radii.
(81) Yashima, M.; Enoki, M.; Wakita, T.; Ali, R.; Matsushita, Y.; Izumi, F.; Ishihara, T. *Journal of the American Chemical Society* **2008**, *130*, 2762-2763.
(82) Yashima, M.; Sirikanda, N.; Ishihara, T. *Journal of the American Chemical Society* **2010**, *132*, 2385-2392.
(83) Chroneos, A.; Parfitt, D.; Kilner, J. A.; Grimes, R. W. *J. Mater. Chem.* **2010**, *20*, 266.
(84) Chroneos, A.; Vovk, R.; Goulatis, I.; Goulatis, L. *Journal of Alloys and Compounds* **2010**, *494*, 190-195.
(85) Pintschovius, L.; Bassat, J. M.; Odier, P.; Gervais, F.; Chevrier, G.; Reichardt, W.; Gompf, F. *Phys. Rev. B* **1989**, *40*, 2229.
(86) Birgeneau, R. J.; Chen, C. Y.; Gabbe, D. R.; Jenssen, H. P.; Kastner, M. A.; Peters, C. J.; Picone, P. J.; Thio, T.; Thurston, T. R.; Tuller, H. L.; Axe, J. D.; Böni, P.; Shirane, G. *Phys. Rev. Lett.* **1987**, *59*, 1329.
(87) Böni, P.; Axe, J. D.; Shirane, G.; Birgeneau, R. J.; Gabbe, D. R.; Jenssen, H. P.; Kastner, M. A.; Peters, C. J.; Picone, P. J.; Thurston, T. R. *Phys. Rev. B* **1988**, *38*, 185.
(88) Yu, J.; Freeman, A. J.; Xu, J. -. *Phys. Rev. Lett.* **1987**, *58*, 1035.
(89) Kajitani, T.; Hosoya, S.; Hiraga, K.; Fukuda, T. *J. Phys. Soc. Jpn.* **1990**, *59*, 562-570.
(90) Hücker, M.; Chung, K.; Chand, M.; Vogt, T.; Tranquada, J. M.; Buttrey, D. J. *Phys. Rev. B* **2004**, *70*, 064105.
(91) Yamada, K.; Matsuda, M.; Endoh, Y.; Keimer, B.; Birgeneau, R. J.; Onodera, S.; Mizusaki, J.; Matsuura, T.; Shirane, G. *Phys. Rev. B* **1989**, *39*, 2336.
(92) Tranquada, J. M.; Axe, J. D.; Ichikawa, N.; Moodenbaugh, A. R.; Nakamura, Y.; Uchida, S. *Phys. Rev. Lett.* **1997**, *78*, 338.
(93) Gardner, J. S.; Paul, D. M.; Lcbech, B. *Physica B: Condensed Matter* **1997**, *234-236*, 721-

722.
(94) Axe, J. D.; Moudden, A. H.; Hohlwein, D.; Cox, D. E.; Mohanty, K. M.; Moodenbaugh, A. R.; Xu, Y. *Phys. Rev. Lett.* **1989**, *62*, 2751.
(95) Axe, J. D.; Cox, D. E.; Mohanty, K.; Mouden, H.; Moodenbaugh, A.; Xu, Y.; Thurston, T. *IBM J. Res. Dev.* **1989**, *33*, 382-388.
(96) Maeno, Y.; Kakehi, N.; Odagawa, A.; Fujita, T. *Physica B: Condensed Matter* **1990**, *165-166*, 1689-1690.
(97) Fernández-Díaz, M. T.; Sáez-Puche, R. *Physica B: Condensed Matter* **1997**, *241-243*, 364-366.
(98) Fernández-Díaz, M.; Martínez, J.; Rodríguez-Carvajal, J. *Solid State Ionics* **1993**, *63-65*, 902-906.
(99) Goka, H.; Fujita, M.; Ikeda, Y.; Yamada, K. *Physica C: Superconductivity* **2001**, *357-360*, 256-259.
(100) Horibe, Y.; Inoue, Y.; Koyama, Y. *J Supercond* **1997**, *10*, 461-466.
(101) Keimer, B.; Birgeneau, R. J.; Cassanho, A.; Endoh, Y.; Greven, M.; Kastner, M. A.; Shirane, G. *Z. Physik B - Condensed Matter* **1993**, *91*, 373-382.
(102) Kimura, H.; Noda, Y.; Goka, H.; Fujita, M.; Yamada, K.; Shirane, G. *J. Phys. Soc. Jpn.* **2005**, *74*, 445-449.
(103) Kwei, G. H.; Lawson, A. C.; Mostoller, M. *Physica C: Superconductivity* **1991**, *175*, 135-142.
(104) Balz, D.; Plieth, K. *Z. Electrochem. Ber. Bunsenges., Phys. Chem.* **1955**, *59*, 545.
(105) Leary, K. J.; zur Loye, H.; Keller, S. W.; Faltens, T. A.; Ham, W. K.; Michaels, J. N.; Stacy, A. M. *Phys. Rev. Lett.* **1987**, *59*, 1236.
(106) François, M.; Junod, A.; Yvon, K.; Hewat, A. W.; Capponi, J. J.; Strobel, P.; Marezio, M.; Fischer, P. *Solid State Communications* **1988**, *66*, 1117-1125.
(107) Jarlborg, T. *Solid State Communications* **1988**, *67*, 297-300.
(108) Bardeen, J.; Cooper, L. N.; Schrieffer, J. R. *Phys. Rev.* **1957**, *108*, 1175-1204.
(109) Weber, W. *Phys. Rev. Lett.* **1987**, *58*, 1371.
(110) Chu, C. W.; Gao, L.; chen, F.; Huang, Z. J.; Meng, R. L.; Xue, Y. Y. *Nature 365*, 323.
(111) Gao, Y.; Xue, Y. Y.; Chen, F.; Xiong, R.; Meng, R. L.; Ramirez, M. L.; Chu, C. W. *Phys. Rev. B* **1994**, *50*, 4260-4263.
(112) Sekizawa, K.; Takano, Y.; Takigami, H.; Tasaki, S.; Inaba, T. *Jpn. J. Appl. Phys.* **1987**, *26*, L840-L841.
(113) Shaheen, S. A.; Jisrawi, N.; Lee, Y. H.; Zhang, Y. Z.; Croft, M.; McLean, W. L.; Zhen, H.; Rebelsky, L.; Horn, S. *Phys. Rev. B* **1987**, *36*, 7214.
(114) Grant, P. M.; Parkin, S. S. P.; Lee, V. Y.; Engler, E. M.; Ramirez, M. L.; Vazquez, J. E.; Lim, G.; Jacowitz, R. D.; Greene, R. L. *Phys. Rev. Lett.* **1987**, *58*, 2482.
(115) Demazeau, G.; Tresse, F.; Plante, T.; Chevalier, B.; Etourneau, J.; Michel, C.; Hervieu, M.; Raveau, B.; Lejay, P.; Sulpice, A.; Tournier, R. *Physica C: Superconductivity* **1988**, *153-155*, 824-825.
(116) Schirber, J.; Morosin, B.; Merrill, R.; Hlava, P.; Venturini, E.; Kwak, J.; Nigrey, P.; Baughman, R.; Ginley, D. *Physica C: Superconductivity* **1988**, *152*, 121-123.
(117) Grenier, J.; Wattiaux, A.; Lagueyte, N.; Park, J.; Marquestaut, E.; Etourneau, J.; Pouchard, M. *Physica C: Superconductivity* **1991**, *173*, 139-144.
(118) Park, J.; Kang, S.; Choy, J.; Wattiaux, A.; Grenier, J. *Physica C: Superconductivity* **1991**, *185/89*, 567-568.
(119) Grenier, J.; Lagueyte, N.; Wattiaux, A.; Doumerc, J.; Dordor, P.; Etourneau, J.; Pouchard, M.; Goodenough, J.; Zhou, J. *Physica C: Superconductivity* **1992**, *202*, 209-218.
(120) Jorgensen, J. D.; Dabrowski, B.; Pei, S.; Richards, D. R.; Hinks, D. G. *Phys. Rev. B* **1989**, *40*, 2187.
(121) Crank, J. *The Mathematics of Diffusion*; 2 éd.; Oxford University Press, USA, 1980.
(122) Kilner, J. A. *Solid State Ionics* **2000**, *129*, 13-23.

(123) Munnings, C.; Skinner, S.; Amow, G.; Whitfield, P.; Davidson, I. *Solid State Ionics* **2005**, *176*, 1895-1901.
(124) Boehm, E.; Bassat, J.; Steil, M.; Dordor, P.; Mauvy, F.; Grenier, J. *Solid State Sciences* **2003**, *5*, 973-981.
(125) Reyes, A.; Hammel, P.; Ahrens, E.; Thompson, J.; Canfield, P.; Fisk, Z.; Schirber, J. *Journal of Physics and Chemistry of Solids* **1993**, *54*, 1393-1402.
(126) Cyrot, M. *Solid State Communications* **1987**, *62*, 821-823.
(127) Demourgues, A.; Weill, F.; Grenier, J. C.; Wattiaux, A.; Pouchard, M. *Physica C* **1992**, *192*, 425–434.
(128) Demourgues, A.; Wattiaux, A.; Grenier, J. C.; Pouchard, M.; Soubeyroux, J. L.; Dance, J. M.; Hagenmuller, P. *J. Solid State Chem.* **1993**, *105*, 458-468.
(129) Rao, C. N. R.; Ganguly, P.; Singh, K. K.; Ram, R. A. M. *Journal of Solid State Chemistry* **1988**, *72*, 14-23.
(130) Chaillout, C.; Cheong, S. W.; Fisk, Z.; Lehmann, M. S.; Marezio, M.; Morosin, B.; Schirber, J. E. *Physica C: Superconductivity* **1989**, *158*, 183-191.
(131) Rogers, J. W.; Shinn, N. D.; Schirber, J. E.; Venturini, E. L.; Ginley, D. S.; Morosin, B. *Phys. Rev. B* **1988**, *38*, 5021.
(132) Lander, G. H.; Brown, P. J.; Spal/ek, J.; Honig, J. M. *Phys. Rev. B* **1989**, *40*, 4463.
(133) Radaelli, P. G.; Jorgensen, J. D.; Schultz, A. J.; Hunter, B. A.; Wagner, J. L.; Chou, F. C.; Johnston, D. C. *Phys. Rev. B* **1993**, *48*, 499.
(134) Paulus, W.; Heger, G.; Rudolf, P.; Schöllhorn, R. *Physica C: Superconductivity* **1994**, *235-240*, 861-862.
(135) Tamura, H.; Hayashi, A.; Ueda, Y. *Physica C* **1993**, *216*, 83-88.
(136) Demourgues, A.; Weill, F.; Darriet, B.; Wattiaux, A.; Grenier, J. C.; Gravereau, P.; Pouchard, M. *J. Solid State Chem.* **1993**, *106*, 330-338.
(137) Dabrowski, B.; Jorgensen, J.; Hinks, D.; Pei, S.; Richards, D.; Vanfleet, H.; Decker, D. *Physica C: Superconductivity* **1989**, *162-164*, 99-100.
(138) Koga, K.; Fujita, M.; Ohshima, K.; Nishihara, Y. *J. Phys. Soc. Jpn.* **1995**, *64*, 3365-3375.
(139) Balagurov, A. M.; Pomjakushin, V. Y.; Simkin, V. G.; Zakharov, A. A. *Physica C: Superconductivity* **1996**, *272*, 277-284.
(140) Gao, M.; Liu, G. D.; Che, G. C.; Zhao, Z. X.; Peng, L. *Phys. Rev. B* **2001**, *64*, 224113.
(141) Hiroi, Z.; Obata, T.; Takano, M.; Bando, Y.; Takeda, Y.; Yamamoto, O. *Phys. Rev. B* **1990**, *41*, 11665.
(142) Tranquada, J. M.; Kong, Y.; Lorenzo, J. E.; Buttrey, D. J.; Rice, D. E.; Sachan, V. *Phys. Rev. B* **1994**, *50*, 6340.
(143) Yamada, K.; Omata, T.; Nakajima, K.; Endoh, Y.; Hosoya, S. *Physica C* **1994**, *221*, 355-362.
(144) Demourgues, A.; Weill, F.; Darriet, B.; Wattiaux, A.; Grenier, J. C.; Gravereau, P.; Pouchard, M. *Journal of Solid State Chemistry* **1993**, *106*, 330-338.
(145) Depmeier, W. *Acta Crystallogr B Struct Crystallogr Cryst Chem* **1981**, *37*, 330-339.
(146) Steurer, W.; Depmeier, W. *Acta Crystallogr B Struct Sci* **1989**, *45*, 555-562.
(147) Poeppelmeier, K. R.; Leonowicz, M. E.; Longo, J. M. *Journal of Solid State Chemistry* **1982**, *44*, 89-98.
(148) Poeppelmeier, K. R.; Leonowicz, M. E.; Scanlon, J. C.; Longo, J. M.; Yelon, W. B. *Journal of Solid State Chemistry* **1982**, *45*, 71-79.
(149) Grenier, J.; Pouchard, M.; Hagenmuller, P. .
(150) Sayagués, M. J.; Vallet-Regí, M.; Hutchison, J. L.; González-Calbet, J. M. *Journal of Solid State Chemistry* **1996**, *125*, 133-139.
(151) Tranquada, J. M.; Buttrey, D. J.; Sachan, V.; Lorenzo, J. E. *Phys. Rev. Lett.* **1994**, *73*, 1003.
(152) Tranquada, J. M.; Lorenzo, J. E.; Buttrey, D. J.; Sachan, V. *Phys. Rev. B* **1995**, *52*, 3581.
(153) Tranquada, J. M.; Sternlieb, B. J.; Axe, J. D.; Nakamura, Y.; Uchida, S. *Nature* **1995**, *375*, 561-563.

(154) Tranquada, J. M.; Woo, H.; Perring, T. G.; Goka, H.; Gu, G. D.; Xu, G.; Fujita, M.; Yamada, K. *Nature* **2004**, *429*, 534-538.
(155) Carlson, E. W.; Emery, V. J.; Kivelson, S. A.; Orgad, D. Concepts in High Temperature Superconductivity **2002**.
(156) Billaud, D.; Herold, A. *Carbon* **1978**, *16*, 301-302.
(157) Rial, C.; Arroyo, E.; Morán, E.; Alario-Franco, M. A.; Amador, U.; Ehrenberg, H.; Fuess, H. *Physica C: Superconductivity* **1999**, *319*, 21-33.
(158) Crawford, M. K.; Harlow, R. L.; McCarron, E. M.; Herron, N.; Farneth, W. E.; Donahue, W. J.; Parkinson, B. A.; Schirber, J. *Journal of Physics and Chemistry of Solids* **1995**, *56*, 1459-1469.
(159) Hervieu, M.; Michel, C.; Pelloquin, D.; Maignan, A.; Raveau, B. *Journal of Solid State Chemistry* **2000**, *149*, 226-235.
(160) Rodriguez-Carvajal Toulouse, 1990; p. 127.
(161) Rodríguez-Carvajal, J. *Physica B: Condensed Matter* **1993**, *192*, 55-69.
(162) Changkang, C. *Progress in Crystal Growth and Characterization of Materials* **1992**, *24*, 213-267.
(163) Shamoto, S.; Hosoya, S.; Sato, M. *Solid State Communications* **1988**, *66*, 195-199.
(164) Tanaka, I.; Watanabe, T.; Komai, N.; Kojima, H. *Physica C: Superconductivity* **1991**, *185-189*, 437-438.
(165) Revcolevschi, A.; Ammerahl, U.; Dhalenne, G. *Journal of Crystal Growth* **1999**, *198-199*, 593-599.
(166) Czochralski, J. *Zeitschrift furMetallographie* **1916**, *8*, 1-43.
(167) Czochralski, J. *Zeitschrift des Vereines Deutscher Ingenieure* **1917**, *61*, 345-351.
(168) Teal, G. K.; Little, J. B. *Phys. Rev.* **1950**, *78*.
(169) Balbashov, A. M.; Egorov, S. K. *Journal of Crystal Growth* **1981**, *52*, 498-504.
(170) Poplawsky, R. P.; Thomas, J. E. *Rev. Sci. Instrum.* **1960**, *31*, 1303.
(171) Halden, F. A.; Sedlacek, R. *Rev. Sci. Instrum.* **1963**, *34*, 622.
(172) Field, W. G.; Wagner, R. W. *Journal of Crystal Growth* **1968**, *3-4*, 799-803.
(173) Eyer, A.; Nitsche, R.; Zimmermann, H. *Journal of Crystal Growth* **1979**, *47*, 219-229.
(174) Kimura, S.; Shindo, I. *Journal of Crystal Growth* **1977**, *41*, 192-198.
(175) Tanaka, I.; Yamane, K.; Kojima, H. *Journal of Crystal Growth* **1989**, *96*, 711-715.
(176) Janecek, J. J.; Wirtz, G. P. *J American Ceramic Society* **1978**, *61*, 242-244.
(177) Kitayama, K. *Journal of Solid State Chemistry* **1988**, *73*, 381-387.
(178) Pfann, W. G. Wiley: New York, NY, 1966.
(179) Humphreys, L. B.; Heminger, J. A.; Young, G. W. *Journal of Crystal Growth* **1990**, *100*, 31-50.
(180) Rivas, D.; Vázquez-EspI[combining acute accent], C. *Journal of Crystal Growth* **2001**, *223*, 433-445.
(181) Ito, T.; Oka, K. *Physica C: Superconductivity* **1994**, *231*, 305-310.
(182) Kuo, V. H. S.; Wilcox, W. R. *Journal of Crystal Growth* **1972**, *12*, 191-194.
(183) Lee, C. H.; Kaneko, N.; Hosoya, S.; Kurahashi, K.; Wakimoto, S.; Yamada, K.; Endoh, Y. *Supercond. Sci. Tech.* **1998**, *11*, 891-897.
(184) Hosoya, S.; Lee, C. H.; Wakimoto, S.; Yamada, K.; Endoh, Y. *Physica C: Superconductivity* **1994**, *235-240*, 547-548.
(185) Kobayashi, N. *Journal of Crystal Growth* **1978**, *43*, 417-424.
(186) Jurisch, M.; Löser, W. *Journal of Crystal Growth* **1990**, *102*, 214-222.
(187) Lan, C. W. *Journal of Crystal Growth* **2003**, *247*, 597-612.
(188) Louchev, O. A.; Otani, S.; Ishizawa, Y. *Journal of Crystal Growth* **1996**, *167*, 333-344.
(189) Hermann, R.; Priede, J.; Behr, G.; Gerbeth, G.; Schultz, L. *Journal of Crystal Growth* **2001**, *223*, 577-587.
(190) Munakata, T.; Tanasawa, I. *Journal of Crystal Growth* **1999**, *206*, 27-36.

(191) Roisnel, T.; Rodriguez-Carvajal R. Delhez and E. J. Mittenmeijer, 2000; p. 118-123.
(192) Laughier, J.; Filhol, A. *J Appl Crystallogr* **1983**, *16*, 281-283.
(193) CCP14 Homepage - Tutorials and Examples - LMGP suite for Windows by Jean Laugier and Bernard Bochu - Basic Demonstration of OrientExpress for orienting a single crystal from a single Laue Photograph.
(194) Laue: X-ray Diffractometer at Paul Scherrer Institute, CH-5232 Villigen PSI.
(195) *International Tables for Crystallography*; Prince, E.; Fuess, H.; Hahn, T.; Wondratschek, H.; Müller, U.; Shmueli, U.; Prince, E.; Authier, A.; Kopský, V.; Litvin, D. B.; Rossmann, M. G.; Arnold, E.; Hall, S.; McMahon, B., Éd.; 1er éd.; International Union of Crystallography: Chester, England, 2006; Vol. C.
(196) Massa, W. Dans *crystal structure determination*; Springer-Verlag, 2004.
(197) Braden, M.; Heger, G.; Schweiss, P.; Fisk, Z.; Gamayunov, K.; Tanaka, I.; Kojima, H. *PHYSICA C* **1992**, *191*, 455-468.
(198) McIntyre, G. J.; Renault, A.; Collin, G. *Phys. Rev. B* **1988**, *37*, 5148.
(199) Van Tendeloo, G.; Zandbergen, H.; Amelinckx, S. *Solid State Communications* **1987**, *63*, 389-393.
(200) Hücker, M.; Zimmermann, M. V.; Klingeler, R.; Kiele, S.; Geck, J.; Bakehe, S. N.; Zhang, J. Z.; Hill, J. P.; Revcolevschi, A.; Buttrey, D. J.; Büchner, B.; Tranquada, J. M. *Phys. Rev. B* **2006**, *74*, 085112.
(201) *International Tables for Crystallography*; Hahn, T.; Fuess, H.; Hahn, T.; Wondratschek, H.; Müller, U.; Shmueli, U.; Prince, E.; Authier, A.; Kopský, V.; Litvin, D. B.; Rossmann, M. G.; Arnold, E.; Hall, S.; McMahon, B., Éd.; 1er éd.; International Union of Crystallography: Chester, England, 2006; Vol. A.
(202) Duisenberg, A. *J. appl. cryst.* **1992**, *25*, 92-96.
(203) Duisenberg, A.; Kroon-Batenburg, L.; Schreurs, A. M. M. *J. appl. cryst.* **2003**, *36*, 220-229.
(204) Labiche, J.; Mathon, O.; Pascarelli, S.; Newton, M. A.; Ferre, G. G.; Curfs, C.; Vaughan, G.; Homs, A.; Carreiras, D. F. *Rev Sci Instrum* **2007**, *78*, 091301.
(205) Petricek, V.; Dusek, M.; Palatinus, L. The crystallographic computing system.: Institute of Physics, Praha, Czech Republic., 2006.
(207) Momma, K.; Izumi, F. *J Appl Crystallogr* **2008**, *41*, 653-658.
(208) Pennington, W. *J Appl Crystallogr* **1999**, *32*, 1028-1029.
(209) Schefer, J.; Könnecke, M.; Murasik, A.; Czopnik, A.; Strässle, T.; Keller, P.; Schlumpf, N. *Physica B: Condensed Matter* **2000**, *276-278*, 168-169.
(210) Fischer, P. *Physica B: Condensed Matter 234-236*, 1202-1208, 1997.
(211) Kumazawa, S.; Kubota, Y.; Takata, M.; Sakata, M.; Ishibashi, Y. *j. appl. crystallopgr.* **1993**.
(212) Izumi, F.; Dilanian, R. A. *transworld Research Nework, Trivaladium* **2002**, *3*, 699-726.
(213) Izumi, F.; Dilanian, R. A. *IUCr Newslett.* **2005**, 59-63.
(214) *Journal of Applied Crystallography* **2008**, *41*, 653-658.
(215) Vigliante, A.; von Zimmermann, M.; Schneider, J. R.; Frello, T.; Andersen, N. H.; Madsen, J.; Buttrey, D. J.; Gibbs, D.; Tranquada, J. M. *Phys. Rev. B* **1997**, *56*, 8248.
(216) Wochner, P.; Tranquada, J. M.; Buttrey, D. J.; Sachan, V. *Phys. Rev. B* **1998**, *57*, 1066.
(217) Le Dréau, L. *Structure and oxygen mobility investigations of La2CuO4+d*; PSI: Villigen, Switzerland, 2007.
(218) Choudhury, N.; Rao, K.; Chaplot, S. *Physica C: Superconductivity* **1990**, *171*, 567-581.
(219) Villesuzanne, A.; Paulus, W.; Cousson, A.; Hosoya, S.; Dréau, L.; Hernandez, O.; Prestipino, C.; Ikbel Houchati, M.; Schefer, J. *J Solid State Electrochem* **2010**, *15*, 357-366.
(220) Frayret, C. Application de la DFT à la modélisation de la diffusion de l'ion oxygen dans des electrolytes solides modèles et des conducteurs mixtes, 2004.
(221) Minervini; Grimes, R.; Kilner, J. A.; Sickafus, K. *J Mater Chem* **2000**, *10*, 2349.
(222) Smaalen, S. V. *Incommensurate crystallography*; Oxford University Press, 2007.
(223) Yamamoto, A. *Acta Crystallogr A Found Crystallogr* **1996**, *52*, 509-560.

(224) Kushima, A.; Parfitt, D.; Chroneos, A.; Yildiz, B.; Kilner, J. A.; Grimes, R. W. *Phys Chem Chem Phys* **2010**.
(225) Yashima, M.; Sirikanda, N.; Ishihara, T. *Journal of the American Chemical Society* **2010**, *132*, 2385-2392.
(226) Betteridge; Carruthers; Cooper, R.; Prout, K.; Watkin, D. J. *J Appl Crystallogr* **2003**, *36*, 1487-1487.
(227) Kimura, H.; Hirota, K.; Lee, C. H.; Yamada, K.; Shirane, G. *Journal of physical societey of japan* **2000**, *69*, 851-857.
(228) Tolédano, P.; Dmitriev, V. *Reconstructive phase transitions: in crystals and quasicrystals*; World Scientific, 1996.
(229) Grzechnik, A. *Phys. Rev. B* **2002**, *65*.
(230) Sawada, A. Dans *ferroelectrics*; Taylor & Francis, Colchester, ROYAUME-UNI: Giens, France, 2003; Vol. 291, p. 257.
(231) Steurer, W. *Acta Crystallogr A Found Crystallogr* **2004**, *61*, 28-38.
(232) Hanson, R. C.; Fjeldly, T. A.; Hochheimer, H. D. *phys. stat. sol. (b)* **1975**, *70*, 567-576.
(233) Sahu, D.; George, T. F. *Solid State Communications* **1988**, *65*, 1371-1373.
(234) Pintschovius, L.; Bassat, J.; Odier, P.; Gervais, F.; Hennion, B.; Reichardt, W. *Physica C* **1988**, *153-155*, 276-277.
(235) Shirane, G. *Rev. mod. phys.* **1974**, *46*.
(236) Aramburu, I.; Friese, K.; Perez-Mato, J. M.; Morgenroth, W.; Aroyo, M.; Breczewski *Phys. Rev. B* **2006**, *73*.
(237) Allan, N. L.; Stølen, S.; Mohn, C. E. *J. Mater. Chem.* **2008**, *18*, 4124.
(238) Stølen, S.; Mohn, C. E.; Ravindran, P.; Allan, N. L. *J Phys Chem B* **2005**, *109*, 12362-12365.
(239) Stolen, S.; Tronnes, R. G. *Physics of the Earth and Planetary Interiors* **2007**, *164*, 50–62.
(240) Binder, K. *Rep. Prog. Phys.* **1987**, *50*, 783-859.
(241) Hosoya, S.; Takei, H. *Journal of Crystal Growth* **1982**, *57*, 343-348.
(242) Zaliznyak, I. A.; Hill, J. P.; Tranquada, J. M.; Erwin, R.; Moritomo, Y. *Phys. Rev. Lett.* **2000**, *85*, 4353.

Acknowledgments

First of all, I would like to thank Professor Werner Paulus not only for having introduced me into the fascinating world of crystallochemistry, but also for encouraging me to open my mind through several travels around the world dedicated to scientific collaborations with people I will never forget. I am also extremely thankful to Dr. Jürg Schefer for his support, his kindness and for his constructive critics which have been essential in the course of this thesis. Dr. Olivier Hernandez has been involved day by day in this project, and I would especially like to show him all my gratitude for systematically devoting time to explain things in details, notably about diffraction by twinned and modulated structures and subsequent treatments of experimental data by adapted softwares. I am also very thankful to Dr. Carmelo Prestipino for his involvement in the project. He has been at the origin of many progresses particularly on account of his sharp computational skills.

This thesis would not have been the same without the precious help of Professor Shoichi Hosoya from the University of Yamanashi whose extraordinary advises concerning crystal growth were essential for obtaining samples of high quality. I would also like to thank him for his kindness, his open mind and for his warm welcome. I am also grateful to Professor Yuichi Shimakawa from the University of Kyoto who also took care of me with great attention during my stays in Japan.

I greatly appreciated the help provided by the beamline scientists during synchrotron and neutron experiments: Dr. Gavin Vaughan from ID11 beamline, Dr. Tsu-Chien Weng from the ID26 beamline, both at ESRF. I would also like to acknowledge people from ILL: Dr. Gary McIntyre from Vivaldi Laue diffractometer, Dr. Antoine Raymond from IN12 spectrometer. There are many people I am thankful too at the Paul Scherrer Institute; I already named Dr. Jürg Schefer but I have to thank him again for his active participation in the numerous experiments we carried out on the 4-circle diffractometer TriCS at SINQ. I am very pleased to show all my gratitude to Dr. Kazimierz Conder and Dr. Ekaterina Pomjakushina, from the LDM group at the PSI, who have not only contributed to this work but who have also been the supervisors of my master thesis in 2007 that decided me to continue in this field. My thanks are also dedicated to Dr. Volodja Pomjakushin from the LNS team. And I am grateful to Professor Juan-Manual Perez-Mato from the University of Bilbao for fruitful discussions.

Particular thanks also go to my occasional flatmates Ruggero Frison and Nikolay Tsyrulin who became two exceptional friends. Thanks also go to Krunoslav Prša, Gelu Marius Rotaru, Guochu Deng, Johann Gironnet, Mohamed Zayed, Yasmine Sassa, Marian Stingaciu, Gwendolyn Pascua, Juan Pablo Urrego-Blanco, Florian Moreau, Aphex Twin, Olivia Wahyudi and Ksenia Raspopina for the enjoyable time I spent with them.

My special thanks go to my parents Martine and Christian, my brother Kevin and to the rest of my family and friends for their unwavering support. My warmest thanks go to Morwenna who has encouraged me day after day and who took the time to proofread my work. She has continuously been my source of motivation not only for my work but also in my life in general.

Despite the fact that I received help and advises from many people, there might still be mistakes or misunderstandings in this thesis, for which I take the entire responsibility.

This thesis has been co-financed by:

CNRS (Centre National de Recherche Scientifique, France)

and,

ESM (Entswicklungsfonds Seltene Metalle, Switzerland)

VU :

Le directeur de thèse
(Prof. Werner Paulus)

VU

Le responsable de l'École Doctorale

VU pour autorisation de soutenance

Rennes, le

Le Président de l'Université de Rennes 1

Guy CATHELINEAU

VU après soutenance pour autorisation de publication :

Le Président du Jury,